Optical grating coupler biosensor and biomedical applications

Lorena Diéguez Moure

Optical Grating Coupler Biosensor and Biomedical Applications

LORENA DIÉGUEZ MOURE

Department of Electronics, UB
Nanobioengineering, IBEC
Barcelona, Spain

Tesi doctoral

Optical grating coupler biosensor and biomedical applications

Memòria presentada per

Lorena Diéguez Moure

per optar al grau de **doctor en Nanociències**

Departament d'Electrònica

Universitat de Barcelona

Programa de doctorat de Nanociències

Tesi doctoral dirigida per: **Dr. Mauricio Moreno Sereno**
Dra. Elena Martínez Fraiz

Barcelona, 2012

ACKNOWLEDGEMENTS

Dicen que el que la sigue la consigue, y también dicen que nunca es tarde si la dicha es buena… Tendría que hacer un par de comentarios al respecto de estas dos frases, pero la realidad es que finalmente este día ha llegado! No puedo describir con palabras la alegría (y el cansancio) que esto supone. Y es que ya dicen que el doctorado es una carrera de fondo… ni un ironman diría yo!

Supongo que este es el espacio para reflexionar sobre todo lo que ha ocurrido durante estos últimos años. Si se trata de agradecer, creo que las primeras personas a las que debo el placer de depósitar esta tesis es a mis directores. Mauricio y Elena, no sabéis lo agradecida que estoy! Son tantas las cosas que he aprendido de vosotros! En lo profesional y en lo personal, caminar a vuestro lado (o de vuestra mano) todos estos años ha sido una experiencia fantástica. Me llevo admiración y respeto, además de muy buenos recuerdos… a pesar de la caña que me habéis dado, jeje. Y espero volver a trabajar con vosotros en el futuro.

Nunca habría llegado a este punto si no hubiese sido por los profesores de la especialidad de optoelectrónica de la facultad de física de la Universidade de Santiago de Compostela. Vicente Moreno, Salvador Bará y Suso Liñares especialmente. De alguna manera nos picaron con la curiosidad de aquello que llamaban investigación y que parecía un mundo mágico, lleno de posibilidades y de cosas nuevas por descubrir. A mis compis de Compostela, muchos de ellos doctores, les debo muchas horas de duras críticas al sistema, que animan a cualquier doctorando frustrado. Miqui, Silviña, Iván, Manuela, Sara, Martín, Pablo, Carlos, Gabi, Fran, Marta, Olalla, Vicen, Kike, y Dani: non haberá unha promoción coma a nosa!

Cuando me mudé a Barcelona para empezar la tesis nunca imaginé que iba a tener tanta suerte. Por circunstancias, y gracias a Mauri, acabé compartiendo piso, barrio y experiencias vitales con los mejores amigos. Susa, Clara, Carmen, Paz, Mariano, Romén, María, Natxo, Braulio, Alicia, Giulia, Simo, Santi y Cyn: gracias por ser mi familia! Y por seguir estando al otro lado del teléfono (o del skype) ahora que ya no vivimos en la ciudad más guapa del mundo. Ojalá se alineen los astros y algún día volvamos a vivir todos cerquita.

Con la llegada a Barcelona vino la llegada al departamento de electrónica. Y vaya primera impresión! (y yo que pensaba que estaba curtida de los 6 años en física…). A los profes, Cornet, Ángel, Blas, Romano, Pepe, Paqui, Atilà, Manel López, Anna, Chema, Gabriel y Manel Puig. Moltes gràcies per fer-me sentir a casa a la feina, per fer-me riure al passadís, per estar sempre disponibles per ajudar en qualsevol cosa (ni que sigui cuinar pop al office), i per fer del departament aquesta gran família que estic trobant tant a faltar. Aquí no fan calçotades! A los compañeros de laboratorio, a Nasser y a Fono, gracias por ayudarme en los comienzos. Gracias por las peleas por elegir la música, por las discusiones científicas y por las que no lo fueron. Y a todos los becarios y becarias que pasaron en un momento u otro por allí. Javi, Héctor, Andreu, Alicia, Òscar, Lluis, Eva, Canals, Toset, Brufau, Josep, Culu e Ivón. Por los cafés de cada día y las cervezas de los viernes. Por las fiestas y las excursiones. Mención especial merecen mi trío calavera: Sergio, Otero y Gonzalo, porque más que compañeros se convirtieron en mis hermanos mayores. Os echo de menos!

Si se puede decir que hubo un antes y un después en mi doctorado, ese ecuador coincidió con las estancias en el ETH. Perdonadme todos por las veces que me habéis escuchado decir "en Suiza el laboratorio funcionaba así…". Pero es todavía en día en que me considero muy afortunada de haber tenido la oportunidad de haber trabajado en el Laboratory of Biosensors and Bioelectronics. Y todo gracias a János! Que grande trabajar con Tomaso! Y qué especial conocer a Marta, Orane y Anna!

A la vuelta de Zürich y con la entrada de mi locura bio, empecé a trabajar más con el laboratorio de Nanobio. Tengo que agradecer al Prof. Josep Samitier que me acogiese en su laboratorio y pusiera a mi disposición tantas instalaciones. Pero trabajar en el Nanobio no sólo es un privilegio en términos de recursos, pero también por su material humano. A Xavi, Anna, Bea, Juanjo y Patrizia, gracias por iluminar mis carencias en biología y en química. Pero lo mejor del laboratorio sin duda son los becarios y los técnicos. A David Caballero, Miriam, Maruxa, Sabine, Marilia, Coco, Jordi, Óscar, Juan Pablo, Elio, Patricia y Marta. Qué juergas nos pasamos dentro y fuera del lab!

Y entre experimento y experimento, se fue pasando el tiempo. Y el tiempo de escribir llegó y me mandaron a las Torres de Mordor. Y me aconsejaron que fuese echando currículums para postdocs. No sabía dónde me estaba metiendo! Pero así, sin avisar, nos vinimos a Australia.

Mudarse tan lejos no es fácil, pero he tenido la suerte de encontrarme con un grupo de gente genial, que ha hecho que me empezase a sentir en casa. A Mélanie, Tom, Muireann, Jarrad, Céline, Régis, Malou, Erwin, Vane y Guille. Thank you guys for making the experience of living in Adelaide such a good one! A Eva, que también se vino a este lado del mundo (aunque a la otra punta) por todos los momentos compartidos, buenos y malos.

No debo olvidar a los amigos de siempre, mis Vigueses: Lucía, Paula, Rebeca, Álex, Marga, Leví, Lorena, María; Compostelanos: Javi, Sabela, Iria y Ángel; Barceloneses: Clara, Lete e Isa; y Suizos: Manuela y Nicole. Siempre ahí para cuando pueda ir a verles!

Y a mis padres y hermanas, que después de todo este tiempo todavía me preguntan cada vez que llaman por teléfono "y qué tal va la tesis?".

He dejado lo mejor para el final, a Sam. Por unirse a mí en esta locura y por dejarlo todo y cruzar el mundo decidido a pasar esta gran aventura juntos. Por ayudarme a levantarme cada mañana y arroparme cada noche. Por entenderme mejor que nadie, por animarme en todo y por ser el mejor compañero de viaje. El único.

Y a Maia, a la que todavía no conozco, pero ya sé que será lo más importante de mi vida.

Gracias!

Optical Grating Coupler Biosensor and Biomedical Applications

LIST OF PUBLICATIONS

Journal articles

Optical gratings coated with thin Si_3N_4 layer for efficient immunosensing by Optical Waveguide Spectroscopy.
L. Diéguez, D. Caballero, J. Calderer, M. Moreno, E. Martínez, J. Samitier
Biosensors 2, 114-126, 2012

Deposition of ITO thin films onto PMMA substrates for waveguide based biosensing devices
S. Azevedo, L. Diéguez, P. Carvalho, J. O. Carneiro, V. Teixeira, E. Martínez, J. Samitier
Journal of Nano Research 17, 75-83, 2012

Effect of the Refractive Index of Buffer Solutions in Evanescent Optical Biosensors
L. Diéguez, N. Darwish, M. Mir, E. Martínez, M. Moreno, J. Samitier
Sensor Letters 7, 851-855, 2009

Electrochemically controlled deposition and dissolution of PLL/DNA multilayers
L. Diéguez, N. Darwish, N. Graf, J. Vörös, T. Zambelli
Soft Matter 5, 2415 – 2421, 2009

Second order effects of aspect ratio variations in high sensitivity grating couplers
N. Darwish, L. Diéguez, M. Moreno, F. Muñoz, R. Mas, J. Mas, J. Samitier, B. Nilsson, G. Petersson; *Microelectronics Engineering 84, 1775-1778, 2007*

Conference Communications

High Efficiency capture of Circulating Tumor Cells from cell mixture using new approaches in microfluidics (Oral Communication)
L. Diéguez, B. Thierry
ICONN 2012 (Perth, Australia)

Robust Fabrication of Chemical Micropatterns for Tumor Spheroid Preparation and Study of Nanoparticles Intratumoral Transport (Oral Communication)
T. Liu, L. Diéguez, B. Thierry
ICONN 2012 (Perth, Australia)

An overview of top-down silicon nanowire fabrication and their applications in cancer research (Oral Communication)
D. Tran Phu, L. Diéguez, H. Duy Tong, B. Thierry
IWNA 2011 – International Workshop on Nanotechnology and Applications (Ho Chi Minh, Vietnam)

Fabrication of different optical gratings for efficient biosensing by Optical Waveguide Spectroscopy (Oral Communication)
L. Diéguez, S. Acevedo, M. Moreno, E. Martínez, V. Teixeira, J. Samitier
MPA meeting 2010 - Materials, Processing and Applications of emerging technologies. (Braga, Portugal)

Fabrication of optical gratings coated with Si_3N_4 for efficient immunosensing monitored by Optical Waveguide Spectroscopy (Poster-flash presentation)
L. Diéguez, D. Caballero, J. Calderer, M. Moreno, E. Martínez, J. Samitier
NanoSpain 2010 (Málaga, Spain)

Inmobilization of nanovesicles carrying Olfactory Receptors and detection via Optical Spectroscopy (Poster)
L. Diéguez, M. Mir, N. Darwish, E. Martínez, J. Samitier
ESF Research Conferences – 2009 – Biological surfaces and interfaces (Sant Feliu de Guixols, Spain)

Influence of the Buffer Refractive Index in Optical Biosensing (Poster)
L. Diéguez, N. Darwish, M. Mir, E. Martínez, M. Moreno, J. Samitier
6ª Reunión Española de Optoelectrónica, OPTOEL 2009 (Málaga, Spain)

Optical Waveguide Lightmode Spectroscopy for Detection of Olfactory Receptor (Poster)
L. Diéguez, N. Darwish, M. Moreno, E. Martínez, J. Samitier
Nanotech Insight 2009 (Barcelona, Spain)

Optical Waveguide Lightmode Spectroscopy for Detection of Olfactory Receptor (Oral communication)
L. Diéguez, M. Mir, S. Rodríguez-Seguí, A. Errachid, E. Martínez, J. Samitier
MADICA 2008 (Rabat, Marocco)

Optical Waveguide Lightmode Spectroscopy for Detection of Olfactory Receptor (Oral communication)
L. Diéguez, M. Mir, S. Rodríguez-Seguí, A. Errachid, E. Martínez, J. Samitier
XXIV Trobades Científiques de la Mediterrània: La física a les ciències de la vida. 2008 (Maó, Spain)

Electronically Controlled Growth and Release of Polyelectrolyte/DNA Multilayers for Drug Delivery (Poster)
L. Diéguez, T. Zambelli, N. Darwish, J. Vörös
ESF Research Conferences – 2007 – Biological surfaces and interfaces (Sant Feliu de Guixols, Spain)

Optical Active Structures Patterned in Polymeric Waveguides (Poster)
L. Diéguez, N. Darwish, M. Moreno, M. J. López, J. Samitier
5ª Reunión Española de Optoelectrónica, OPTOEL 2007 (Bilbao, Spain)

Electrochemically controlled growth and dissolution of PLL/DNA multilayers for tailored DNA release studied by EC-OLWS and in-situ AFM (Poster)
Lorena Diéguez, Tomaso Zambelli, Janos Vörös
AFM BioMed Conference 2007 (Barcelona, Spain)

Electrochemically tailored stability of PLL/DNA multilayers for controlled DNA release: a study by EC-OWLS (Poster)
L. Diéguez, T. Zambelli, J. Vörös
Annual Meeting of the Swiss Physical Society 2007 (Zürich, Switzerland)

Polymer Optical Waveguides Fabrication and Test (Poster)
L. Diéguez, N. Darwish, M. Moreno, M.J. López, J. Samitier,
Nanoelectronic and Photonic Systems Workshop, 2006 (Tarragona, Spain)

Optical sub-micron grating-waveguides for biosensing applications (Poster)
N. Darwish, L. Diéguez, M. Moreno, F. Muñoz, R. Mas, J. Mas J. Samitier, B. Nilsson, G. Petersson
MNE 2006: 32nd International Conference on Micro- and Nano- Engineering 2006 (Barcelona, Spain)

Polymer and dielectric grating couplers for biosensing applications (Poster)
N. Darwish, L.Diéguez, M. Moreno, J. Samitier, F. Muñoz, R. Mas,
3rd NanoSpain Workshop, 2006 (Pamplona, Spain)

Optical Grating Coupler Biosensor and Biomedical Applications

PREFACE

Biosensors are nowadays a powerful tool to enable the detection of specific biological interactions and to evaluate the concentration dependence in the response. A biosensor usually consists of three different parts: the sample to be measured, the transducer and the electronic system that amplifies the signal, analyzes the data and brings a result to the final user. The transducer includes the bioreceptor (which specifically interacts with the sample) and the interface that transforms the recognition from the bioreceptor into a measurable signal. When the analyte interacts with the bioreceptor, the transducer sends a signal that is processed by the electronics. All this process occurs in an efficient, quick, cheap, easy, simple and specific way. Regarding the type of the transductor, the biosensors can be electrochemical, optical, acoustic, magnetic or thermometric; but overall the most powerful ones are the optical biosensors, and among them the grating coupler. As a technique for investigating processes at the solid/liquid interface, presents high mechanical stability, immunity to electromagnetic interferences and pushes the sensitivity to levels even higher than other techniques and allows for the direct monitoring of macromolecular adsorption. Taking advantage of the last advances in nanotechnology, the goal of this thesis is to study the versatility of an Optical Grating Coupler Biosensor. The design of new grating sensor chips will be investigated, a new calibration technique for the sensors will be proposed and, taking advantage of the technique, different biomedical scenarios will be tested.

In Chapter 1: An introduction on the state of the art of biosensing is presented and the current most common techniques are compared. Evanescent field optical biosensors are label free sensors that measure the variation of the refractive index of the adsorbed layer onto a chip surface and translate this variation into surface concentration of the adsorbed molecule.

In Chapter 2: The design and fabrication of grating coupler sensor chips is explored through different approaches. Low cost sensors in polymer substrates were investigated, as well as novel coatings for commercial sensors with different sputtered and evaporated materials. These new sensors will allow quick quantitative studies of the adsorption of biomolecules onto their surfaces, to be used in calibration of other techniques.

In Chapter 3: The evanescent field based techniques depend on a theoretical model of the waveguide to determine the desired parameters of the adsorbed layer. As this layer is not only composed by the biomolecules, but also by some amount of the buffer solution, in this study, we have developed a new calibration method to take into account the refractive index buffer changes. We report a new methodology to characterize each sensor chip before the measurements and we present the refractive indexes of different buffer solutions considering the most common ones used in biosensor applications. This work will set the calibration bases for any optical grating biosensor instrument.

In Chapter 4: The immobilization of liposomes from yeast cells containing the olfactory receptor OR17-40 onto sensor surfaces has been characterized by means of optical waveguide spectroscopy. The objective of this work is to take advantage of the optical biosensing technique to optimize the functionalization strategy of the sensor surface, leading to the effective attachment of the liposomes. The size and homogeneity of nanosized vesicles containing olfactory receptors are also characterized in solution and the efficiency of the immobilization strategy of nanosomes onto sensing surfaces is studied.

In Chapter 5: Taking advantage of the electrochemical Optical Waveguide Lightmode Spectroscopy technique, the kinetics of formation and electrochemically induced dissolution of polyelectrolyte multilayers containing DNA was studied. Experiments were carried out in a specially modified cell for the optical spectroscopy to be operated in electrochemical conditions. The optical waveguides were covered with a thin layer of Indium Tin Oxide, which acted as the working electrode of a three-electrodes cell. Dissolution of the polyelectrolyte films was observed for potentials above 1.8 V.

In the Appendix: As an experimental handbook, a summary of the different fabrication and characterization techniques has been compiled at the end of this thesis.

Optical Grating Coupler Biosensor and Biomedical Applications

ABBREVIATIONS

μCP	micro-Contact Printing
AFM	Atomic Force Microscopy
BSA	Bovine Serum Albumin
BSE	Back-Scattered Electrons
cAMP	Cyclic Adenosine Monophosphate Assay
CCD	Charge-Couple Device
CV	Cyclic Voltammetry
CVD	Chemical Vapor Deposition
DLS	Dynamic Light Scattering
DNA	Deoxyribonucleic Acid
DRIE	Deep Reactive Ion Etching
EC-OWLS	Electrochemical OWLS
EDTA	Ethylenediaminetetraacetic Acid
EIA	Enzyme Immuno-Assay
EIS	Electrochemical Impedance Spectroscopy
ELA	Equivalent Layer Approximation
ELISA	Enzyme-Linked Immunosorbent Assay
FET	Field Effect Transistor
FITC	Fluorescein Isothiocyanate
FWHM	Full Width at Half-Maximum
GC	Grating Coupler
GPCRs	G-Protein Coupled Receptors
GST	Glutathione-S-Transferase
GTP	Guanosine Triphosphate
HSA	Human Serum Albumin
ITO	Indium Tin Oxide
LAPS	Light-Addressable Potentiometric Sensor
LbL	Layer by Layer
LOD	Limit of Detection
LPCVD	Low-Pressure CVD
MZI	Mach Zehnder Interferometer
NIL	Nano Imprint Lithography
OGCB	Optical Grating Coupler Biosensor
OR	Olfactory Receptor
OSN	Olfactory Sensory Neuron
OWLS	Optical Waveguide Lightmode Spectroscopy
PAH	Poly(allylamine) hydrochloride
PBS	Phosphate Buffered Saline
PDMS	Polydimethylsiloxane
PEG	Poly(ethylene) glycol
PEM	Polyelectrolyte Multilayer
PLL	Poly-(L-Lysine)
PMMA	Polymethylmetacrilate
PMSF	Phenylmethanesulfonylfruoride

PSS	Poly(sodium 4-styrene sulfonate)
QCM	Quartz Crystal Microbalance
QCM-D	QCM with Dissipation
RI	Refractive Index
RIE	Reactive Ion Etching
RIU	Refractive Index Units
SAM	Self-Assembled Monolayer
SAR	Scanning Angle Reflectometry
SμCP	Submerged micro-Contact Printing
SEI	Secondary Electron Imaging
SEM	Scanning Electron Microscopy
SPM	Scanning Probe Microscopy
SPR	Surface Plasmon Resonance
TE	Transverse Electric
TEA	Triethoxysilane Aldehyde
TEM	Transmission Electron Microscopy
TGA	Thin Grating Approximation
TIR	Total Internal Reflection
TM	Transverse Magnetic
UHV	Ultra High Vacuum
WLI	White Light Interferometer
XPS	X-Ray Photoemission Spectroscopy

CONTENTS

CHAPTER 1: BIOSENSORS

1   INTRODUCTION & STATE OF THE ART

In recent times it has become apparent that more sophisticated rapid measurements devices are necessary to collect real-time or in-line information from a variety of environments, from bioprocessing to healthcare. It is hoped that pressure to meet these demands will be answered by the development of biosensors. Their development is currently one of the most active areas of analytical research. A biosensor is an analytical device consisting on three individual parts: an immobilized biological sensitive material, which roles the recognition element (enzyme, antibody, antigen, organelles, DNA, cells, tissues or organic molecules) integrated within a physicochemical transducer and an electronic part. It ultimately converts the biological information into a quantitatively measurable signal usually in the form of optical, acoustic, electrical or magnetic response (Figure 1.1) [1]. Such devices can be used for direct measurements of analytes in a complex sample matrix. Modern biosensors have evolved from the marriage of different disciplines: physics, electronics, chemistry and biology. The two formers provide a transducer, the two latters, the biomolecules forming a sensing layer that will be used to detect specific analytes [2].

The path towards modern-day sensor technology began in the mid-1950's with L.C. Clark Jr. He invented an electrode to measure the dissolved oxygen in the blood of patients undergoing surgery [3]. A modification of this system led to the first blood glucose sensing device, an area of diagnostics now dominated by miniaturized biosensors [4]. The glucose oxidase sensor is still the most widely used, although many improvements have been added since the 1960's. During the past decade, manufacturing techniques, initially developed for integrated circuits, have made possible the production of sensor electrodes hundreds or thousands of times smaller, under 100 μm [5].

The biosensor's market represent a rapidly expanding field, at the present time, with an estimated 60% annual growth rate; the major impetus coming from the health-

care [6-9] industry but with some pressure from other areas, such as food quality [10-12] and environmental monitoring [13-15].

Biosensors, in particular immunosensors, are used to study antibody-antigen interactions and provide a promising means of analysis owing to their specificity and sensitivity. High specificity is achieved by the molecular recognition of target analytes (usually the antigens) by antibodies to form a stable complex on the surface of an immunoassay system or an immunosensor [16]. To fully exploit the specific interaction through biorecognition, the surface architecture of the sensor also must suppress any non-specific interaction. A tremendous research effort has been invested to find surface modifications with specific interaction capabilities over prolonged periods of time in biological fluids.
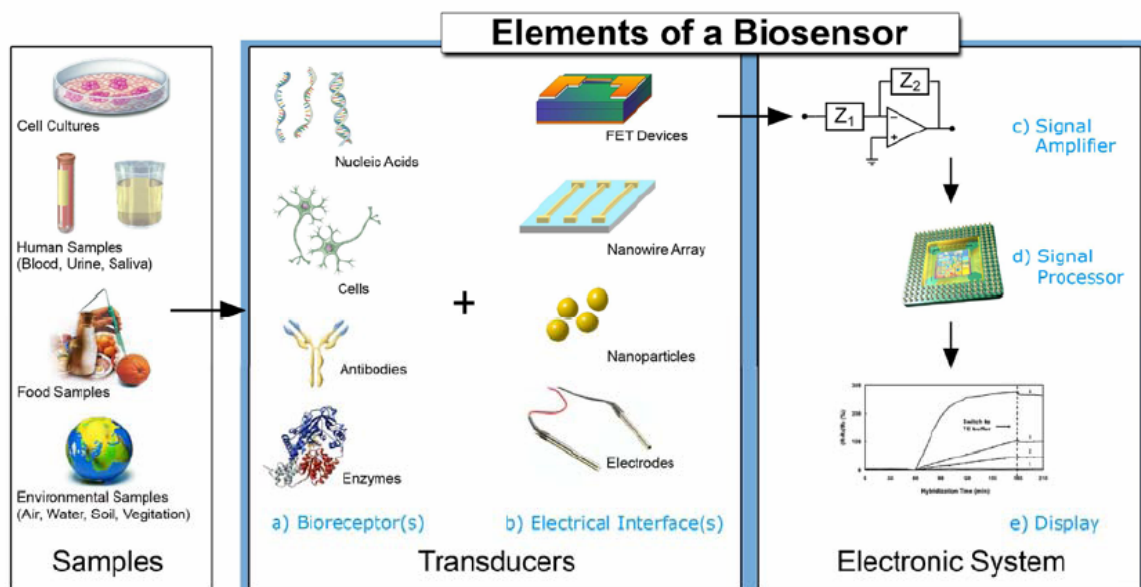
Figure 1.1.- Elements and selected components of a typical biosensor [1].

Antibodies or antibody derivatives (antigens or haptens) usually serve as the biological recognition elements, which are either integrated within or intimately associated with a physicochemical transducer. This recognition reaction defines the high selectivity and sensitivity of the transducer device. The electronic part is used to amplify and digitalize the physicochemical output signal from the transducer devices. On the other hand, sensitivity depends on several factors including the use of high affinity analyte-specific antibodies, their orientation after being immobilized on the

immunoassay or immunosensor surface and the appropriate detection system for measuring the analytical signal [17].

A successful biosensor must accomplish the following features:

- The biorecognition layer must be highly specific for the purpose of the analyses.

- The reaction should be as independent of such physical parameters as stirring, pH and temperature as is manageable.

- The response should be accurate, precise, reproducible and linear over the useful analytical range, without dilution or concentration. It should also be free from electrical noise.

- If the biosensor is to be used for invasive monitoring in clinical situations, the probe must be tiny and biocompatible.

- The complete biosensor should be cheap, small, portable and capable of being used by semi-skilled operators.

- There should be a market for the biosensor.

The figures of merit to evaluate the success in the performance of a biosensor are the sensitivity and the limit of detection (LOD) (Figure 1.2). The LOD is the smallest concentration of analyte detectable with a specified precision or reproducibility. It can be determined by extrapolating a plot of concentration (x) versus measurement unit (y) to the x-axis in logarithmic scale. The intercept is the lower limit of detection and the sensitivity is the smallest concentration change that the biosensor is capable of detecting. It is determined from the slope of the previously described plot. The range in which the sensor is sensitive (from the limit of detection to the saturation) is called the dynamic range.
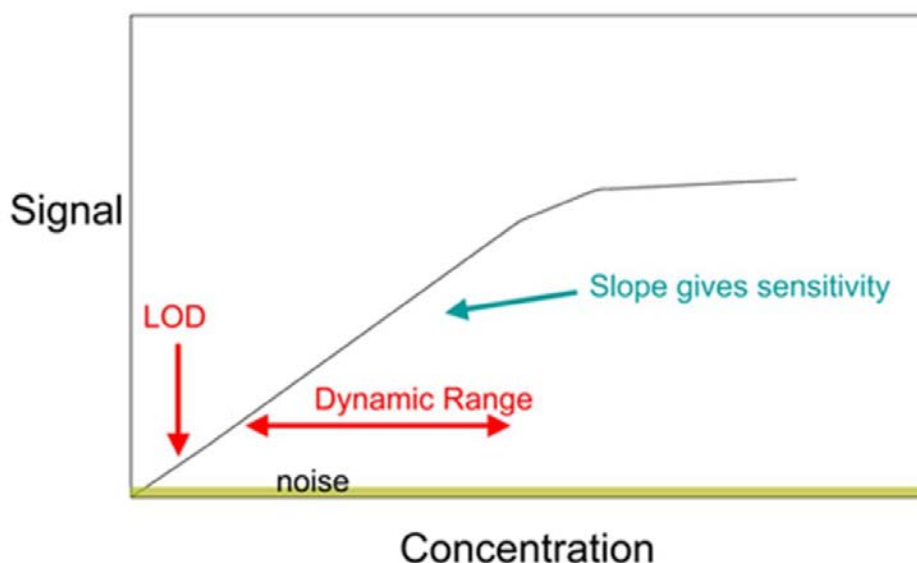
Figure 1.2.- Response of a biosensor. Limit of detection and sensitivity.

This chapter aims to describe the different types of mostly used biosensors, their working principle and their advantages and disadvantages over one another. Special attention has been brought to the review of electrochemical and optical biosensors. A comparative of the different biosensors aims to justify the election of the grating coupler biosensor as the case of study of this thesis.

1.1 CLASSIFICATION

Biosensor classification depends on different factors, as the used receptor, the methodology for the immobilization of such receptor or the kind of transducer used; being this last the most used criteria [18]. The transducer devices can be such as microgravimetric devices (quartz crystal microbalance), electrochemical (potentiometric, conductometric, capacitative, impedance, amperometric) and optical (fluorescence, luminescence, refractive index, absorbance, reflectance, optothermal effect, light scattering).

Probably the most typical transducers are the outlined:

- Effects due to the mass of the reactants or products (**piezo-electric biosensors**).

- Changes in the distribution of charges causing an electrical potential to be measured (**potentiometric biosensors**).

- Movement of electrons produced in a redox reaction (**amperometric biosensors**).

- Changes in the electrical impedance of an interface in AC steady state with constant DC bias conditions (**impedance biosensors**).

- Light output during the biorecognition reaction or light absorbance difference between the reactants and products (**fluorescence, absorbance, luminescence, among others**).

- Coupling or outcoupling conditions in a waveguide - grating vary upon biomolecule adsorption (**refractive index**, **evanescent wave sensors**).

2   PIEZOELECTRIC BIOSENSORS

Quartz is one member of a family of crystals that experience the piezoelectric effect. The piezoelectric effect has found applications in high power sources, sensors, actuators, frequency standards, motors, etc., and the relationship between applied voltage and mechanical deformation is well known; this allows probing an acoustic resonance by electrical means. Applying alternating current to the quartz crystal will induce oscillations. With an alternating current between the electrodes of a properly cut crystal, a standing shear wave is generated. The Q factor, which is the ratio of frequency and bandwidth, can be as high as 10^6. Such a narrow resonance leads to highly stable oscillators and a high accuracy in the determination of the resonance frequency. The QCM exploits this ease and precision for sensing.

2.1 QUARTZ CRYSTAL MICROBALANCE

A quartz crystal microbalance (QCM) measures changes in the mass adsorbed per unit area of an electrode by measuring the change in frequency of a quartz crystal resonator. The QCM can be used under vacuum, in gas phase and more recently in liquid environments [19]. Frequency measurements are easily made to high precision; hence, it is easy to measure mass densities down to a level of below 1 μg/cm^2 (see example at figure 1.3). In addition to measuring the frequency, the dissipation is often measured to help analysis. The dissipation is a parameter quantifying the damping in the system, and is related to the viscoelastic properties of the sample.

With its ability to simultaneously detect mass and viscoelastic property changes, the quartz crystal microbalance with dissipation monitoring (QCM-D) is a good tool to study biological interactions. In liquid, it is highly effective at determining the affinity of molecules (proteins, in particular) to surfaces functionalized with recognition sites. A typical setup for the QCM (Q-Sense, Biolin Scientific AB, Sweeden) reaches nanogram sensitivity [20] and contains water cooling tubes, the retaining unit, frequency sensing equipment through a microdot feed-through, an oscillation source, and a measurement and recording device. These studies have included protein-protein and protein-surface interactions as well as conformational changes in protein films [21-24]. A particular 2001 study by Höök et al. is notable for characterizing the structural transformation of a mussel adhesive protein adsorbed onto a hydrophobic methyl-terminated surface. It is an ideal example to demonstrate the usefulness of simultaneous detection of mass and viscoelastic property changes to characterize a dynamic, multistep biological process. The adsorption kinetics of the protein and subsequent structural transformation induced by cross-linking are monitored in terms of frequency and dissipation changes in order to understand the film properties [25]. Larger entities such as viruses or polymers are investigated, as well. For instance it is useful to determine adhesion of proteins on polymers. Lord et al. [26] used QCM-D to study adsorption of biomolecules on the PHEMA based hydrogels and found most biomolecules can be adsorbed on the hydrogel surfaces causing increases in mass and dissipation upon adsorption. With use of QCM-D technique, Welle [27] found that the quantity and viscosity of surface bound albumin on polystyrene can be lowered after the substrate is UV (185 nm) treated.

More recently, QCM is also considered an emerging tool for the study of cell biology. It was then recognized that the adhesion of cells to the quartz surface also induced a shift in resonance frequency that was shown to be linearly correlated with the fractional surface coverage [28, 29]. Time-resolved measurements of the resonance frequency were then used to follow the attachment and spreading of cells to the quartz surface, with extraordinary time resolution. Comparison with established cytological techniques has proven that the QCM readout reports reliably on the number of cells on the surface and the time course of adhesion [28, 30, 31]. A few studies have been published in which the QCM is used as a transducer in cell-based drug testing assays [32-34].
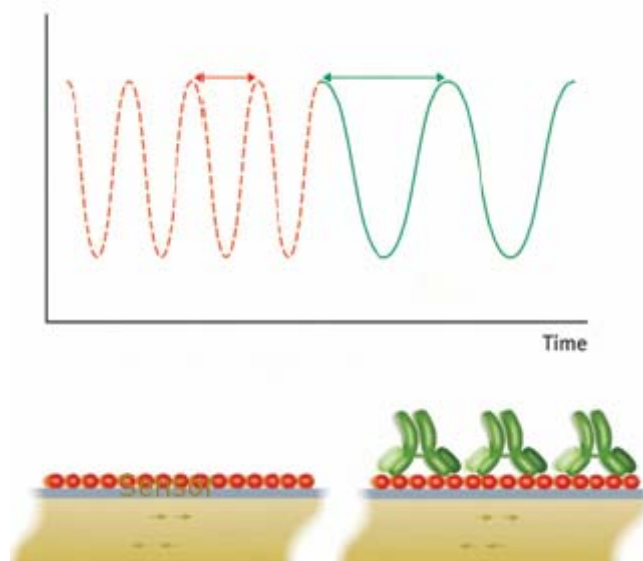
Figure 1.3.- Quartz Crystal Microbalance. The top diagram illustrates how the frequency of the oscillating sensor crystal (gold) changes when the mass is increased by addition of a molecular layer. Here antibodies (green) are added to a layer of protein (red) [35].

The frequency of oscillation of the quartz crystal is partially dependent on the thickness of the biofilm adsorbed on the electrode. During normal operation, all the other influencing variables remain constant; thus a change in thickness correlates directly to a change in frequency. As mass is deposited on the electrode surface, the thickness increases; consequently the frequency of oscillation decreases from the initial value. With some simplifying assumptions, this frequency change can be quantified and correlated precisely to the mass change using Sauerbrey's equation [36]:

$$\Delta f = -\frac{2f_0^2}{A\sqrt{\rho_q \mu_q}} \Delta m \qquad (1.1)$$

where f_0 is the resonant frequency, A is the area of the piezoelectrically active crystal and ρ_q and μ_q are the density and the shear modulus of the quartz.

The QCM can be combined with other surface-analytical instruments. The electrochemical QCM (EC-QCM) is particularly advanced [37-39]. Using the EC-QCM, one determines the ratio of mass deposited at the electrode surface during an electrochemical reaction to the total charge passed through the electrode. This ratio is called the current efficiency.

QCM-D produces measured values of wet mass. This means that the mass calculated from the resonance frequency shift includes both protein mass and water that binds or hydrodynamically couples to the protein adlayer. The analysis of the energy dissipation in the adlayer and its magnitude in relation to the frequency shift (c.f.

adsorbed mass) provides insight about the mechanical/structural properties such as viscoelasticity [40].

3 ELECTROCHEMICAL BIOSENSORS

3.1 OVERVIEW

Electrochemical immunosensors, in which an electrode is used as the transduction element, represent an important subclass of (bio)chemical immunosensors. Such devices hold a leading position among sensors presently commercially available and have found a vast range of important applications in the fields of clinical, industrial, environmental and agricultural analyses. Electrochemical detection of antibody-antigen interactions is claimed to overcome the problems associated with other detection approaches, such as detection speed, simplicity, economy and limits of detection [41]. Furthermore, electrochemistry is an interfacial process in which the relevant reactions take place at the electrode–solution interface, rather than in bulk solution.

Electrochemical biosensors do not suffer the drawback of high sensor setup complexity and cost. This is due to their close link to developments in low-cost production of microelectronic circuits and their easy interface with normal electronic read-out and processing. Other inherent advantages of electrochemical biosensors are their robustness, easy miniaturization, excellent detection limits, even with small analyte volumes and ability to be used in turbid biofluids with optically absorbing and fluorescent compounds, thus providing an opportunity to analyze complex multicomponent mixtures for diagnosing diseases or monitoring the status of patients. Despite these advantages, electrochemical biosensors suffer from poor stability, low signal-to-noise ratio, limited dynamic range, signal reproducibility and reliability, and do not allow unique identification of response with the biochemical event [1].

The principle of their operation is based on the electrochemical detection of the labelled immunoagents or markers such as enzymes, metal ions or other electroactive compounds [42]. An electrical excitation is produced on the working electrode and the system response is monitored. As the analyte is being deposited on this electrode, the response signal changes. According to the type of signal measured, electrochemical immunosensors can be subdivided into potentiometric, voltammetric, amperometric, and more recently, electrochemical impedance spectroscopic (EIS) biosensors.

3.2 ELECTROCHEMICAL TECHNIQUES

3.2.1 Cyclic Voltammetry

The cyclic voltammetry (CV) is one of the most versatile electrochemical techniques for the study of the oxidation and reduction processes in different mediums, adsorption processes over surfaces and electron transference mechanisms in chemical modified electrodes [43]. In a cyclic voltammetry experiment the working electrode potential with respect to the reference electrode is ramped linearly versus time as shown in figure 1.4. This ramping is known as the experiment's scan rate (V/s).
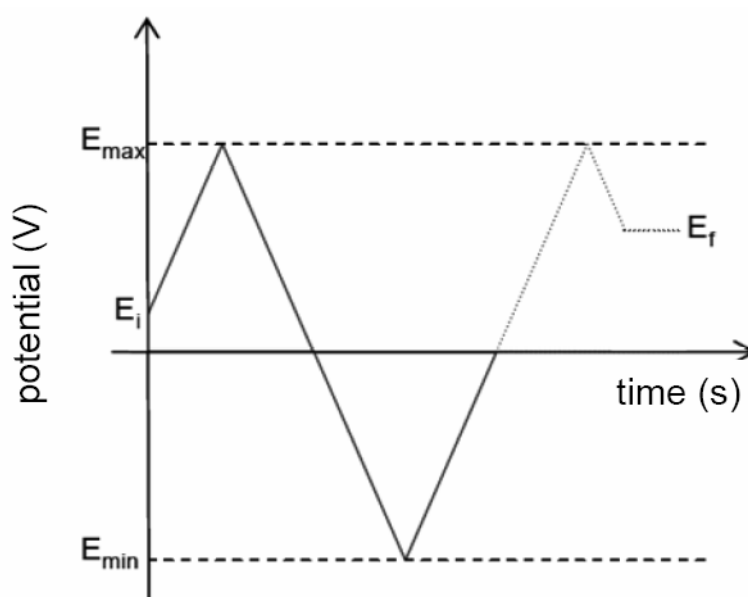
Figure 1.4.- Graphic of the potential variation vs time in a cyclic voltammetry experiment. E_i is the initial potential, E_f the final potential and E_{max} and E_{min} are the maximum (anodic) and minimum (cathodic) potential, respectively.

The potential is measured between the reference and the working electrodes and the current is measured between the working electrode and the counter electrode. The output data is then plotted as current (I) vs. potential (V) (Figure 1.5). As the waveform shows, the forward scan produces a current peak for analytes that can be reduced (or oxidized depending on the initial scan direction) through the range of the potential scanned. The current will increase as the potential reaches the reduction potential of the analyte (E_{pa}), but then falls off as the concentration of the analyte is depleted close to the electrode surface. If the redox couple is reversible then when the applied potential is reversed, it will reach the potential that will re-oxidize the product formed in the first

reduction reaction, and produce a current of reverse polarity from the forward scan (E_{pc}). This oxidation peak will usually have a similar shape to the reduction peak. As a result, information about the redox potential and electrochemical reaction rates of the analytes is obtained.
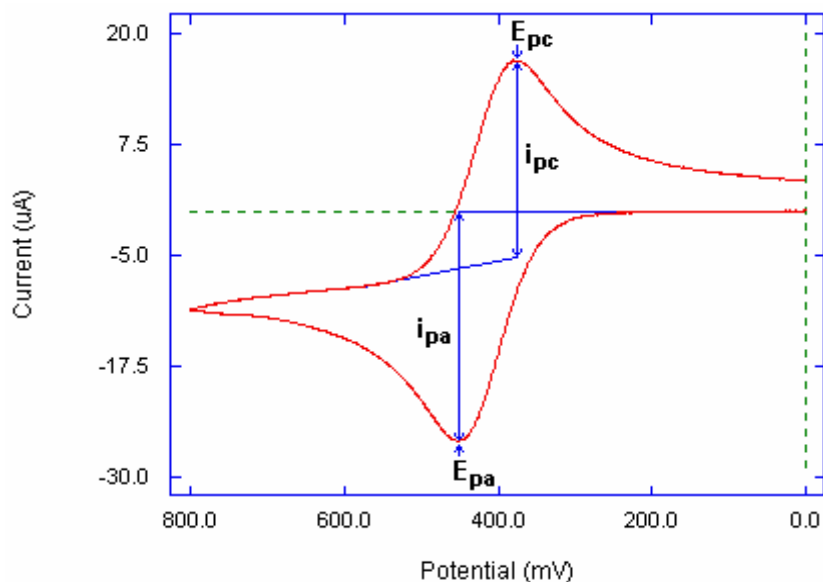
Figure 1.5.- Typical cyclic voltammetry I vs. V curve. Where Ipc, Ipa, Epc and Epa are the intensities and potentials of reduction and oxidation respectively.

The utility of cyclic voltammetry technique is highly dependent on the analyte being studied. The analyte has to be redox active within the experimental potential window. It is also highly desirable for the analyte to display a reversible wave. A reversible wave takes place when an analyte is reduced or oxidized on a forward scan and is then re-oxidized or re-reduced in a predictable way on the return scan. Cyclic voltammetry is useful to obtain quantitative information about electrochemical processes, such as the redox potential, the reaction rate of an analyte solution, the electron stoichiometry of a system, the diffusion coefficient of an analyte and also the concentration of an unknown solution can be determined by generating a calibration curve of current vs. concentration.

3.2.2 Amperometry

In amperometry, the current produced by the oxidation or reduction of electroactive analyte species at an electrode surface is monitored under controlled

potential conditions. The magnitude of the current is then related to the amount of analyte present. In electrochemical immunosensors, as both antibody and antigen are usually not intrinsically electroactive, a suitable label (such an enzyme) must be introduced to promote an electrochemical reaction. This kind of immunosensor usually uses a complex three-electrode measuring system consisting of a working electrode (e.g. gold, glassy carbon, or carbon paste), a reference electrode (e.g. Ag/AgCl), and a conducting counter electrode (e.g. platinum) [44].

A typical electrochemical cell is depicted in figure 1.6. The reference electrode acts as a reference in measuring and controlling the working electrode potential and the counter electrode passes all the current needed to balance the current observed at the working electrode.
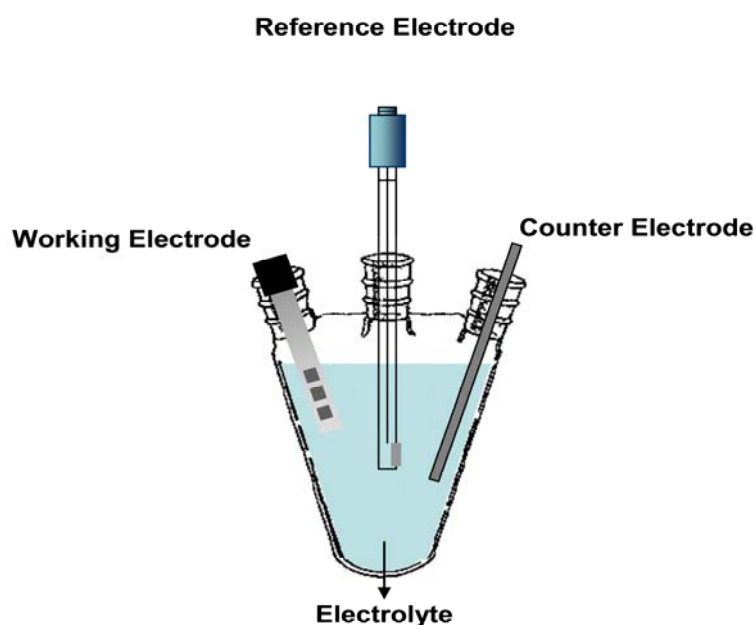
Figure 1.6.- A cartoon of a three electrode electrochemical cell.

3.2.3 Potentiometry (Voltammetry)

Potentiometric immunosensors rely upon a change in potential that occurs between a working and a reference electrode as a result of specific interaction between an antibody and its antigen. A voltammetric sensor utilizes the concentration effect on the current-potential relationship. This relationship depends on the rate by which the analyte is brought to the electrode surface (mass transfer) and the kinetics of transfer

reaction at the electrode surface. One of the main disadvantages of this type of detection is the relatively small change in potential that arises from the interaction between an antibody and its antigen, in the order of tens of millivolts [45]. Moreover, interferences from the sample matrix may prevent this small signal from being successfully detected. Thus such sensors often have a compromised reliability and sensitivity.

3.2.4 Electrochemical Impedance Spectroscopy

Electrochemical Impedance Spectroscopy (EIS) immunosensing is based on the determining small changes of capacitance at the electrode – electrolyte interface after the interaction between an antibody and an antigen. The change of capacitance is due to the change of the thickness and/or dielectric behaviour after the analyte binds to the biorecognition layer on the electrode surface according to the electrical double-layer theory [46]. Immunosensors based on EIS have good characteristics as high sensitivity and they are label-free.

EIS is a powerful technique that allows detecting small changes in a liquid media and/or in the electrode surface, that can be related to several phenomena. For example, a change in the specimen concentration, an affinity biding, a selective recognition or many other events that may be difficult to "observe" can be detected with this technique. It is a versatile electrochemical tool to characterize intrinsic electrical properties of any material or solution and their interface. It analyzes the impedance ($Z=V/I$) of the observed system as a function of the frequency and amplitude of the exciting signal. This analysis provides quantitative information about the conductance, the dielectric constant and the static properties of the interfaces of a system, and its dynamic change due to adsorption or change-transfer phenomena.

Electrochemical impedance is usually measured by applying an AC sine wave potential with low amplitude (5 to 10 mV peak-to-peak) superimposed on a DC potential to the electrochemical system. The AC signal scans the frequency domain, allowing the individual excitation of different processes with different time constants. Therefore, slow processes like chemical reactions and fast processes like ionic conduction can be studied independently this way.

The system impedance $Z(w)$ can be expressed in terms of a real and an imaginary part. If the real part is plotted on the X-axis and the imaginary part is plotted

on the Y-axis of a chart, we get a *Nyquist Plot* (Figure 1.7a). In this plot each point is the impedance of the system at one given frequency and it is represented as a vector of length $|Z|$. The angle between this vector and the X-axis, commonly called the 'phase angle', is φ (=*arg Z*).
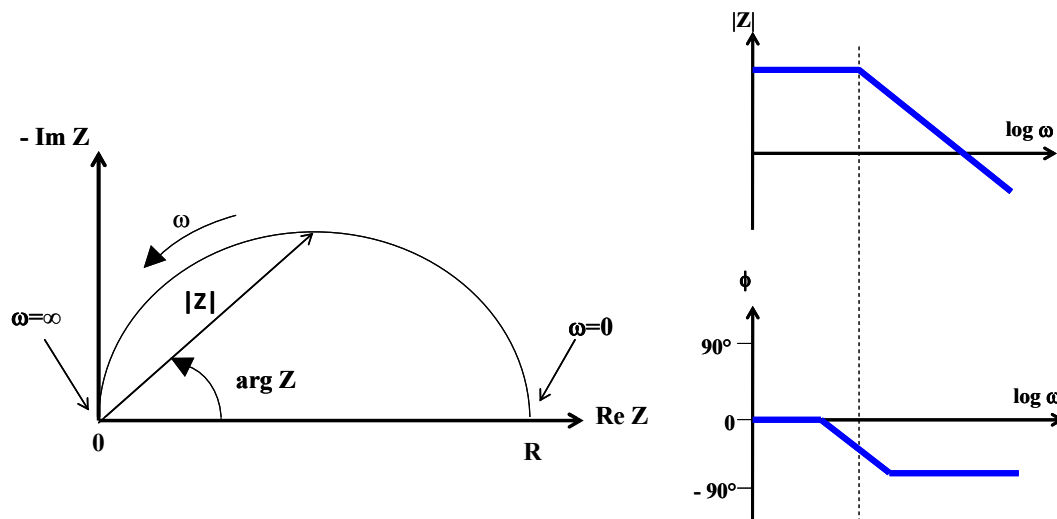
Figure 1.7.- (a) Nyquist plot with impedance vector. (b) Bode plot with one time constant.

The Nyquist Plot is usually complemented by the *Bode Plots* (Figure 1.7b), where the impedance modulus and the phase angle are plotted as a function of the frequency (in a *log* scale). From these graphs is possible to determine the characteristics of the sensor. The electrode – solution interface can be represented by an equivalent circuit (Figure 1.8) where R_s denotes the ohmic resistance of the electrolyte solution, R_{ct} the charge (or electron) transfer resistance that exists if a redox probe is present in the electrolyte solution, Z_w the Warburg impedance arising from the diffusion of redox probe ions from the bulk electrolyte to the electrode interface, and C_{dl}, the double layer capacitance (formed by two parallel layers of charge onto the sensor surface, the first comprised by ions adsorbed onto the sensor and the second composed of ions attracted to the first layer due to coulomb forces)..
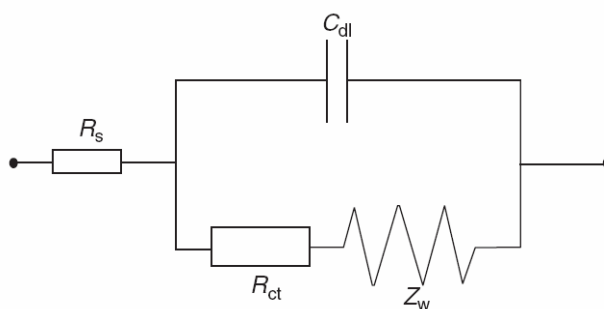
Figure 1.8.- An equivalent circuit representing the interfacial features of an electrochemical immunosensor in the presence of a redox probe.

The most promising applications of electrochemical impedance biosensors are situations where low cost, small instrument size, speed of analysis and sensitivity are crucial. EIS is especially suited for multiplexed sensing, as it allows monitoring different processes with various time constants in the electrode/electrolyte interface in a single experiment. Clinical diagnostics, biowar agent detection, consumer test kits, bioprocess monitoring, and food and water quality testing are some of the promising applications where electrochemical impedance biosensors can be applied with high sensitivity and selectivity.

4   OPTICAL BIOSENSORS

Since almost all optical phenomena at surfaces (e.g. adsorption, fluorescence, changes in refractive index, etc.) can be used as transduction elements in a biosensor, optical immunosensors are considered as one of the most promising alternatives to the traditional immunoassays in clinic diagnosis and environmental analysis. Optical biosensors present the advantages of applying visible electromagnetic radiation, non-destructive operation mode, rapid signal generation and reading, immunity to electromagnetic interference, possible use in aggressive environments and, in general, a high sensitivity [47, 48]. Commonly, in optical transducers, the chemical or biological stimuli produce changes in the characteristics of the medium in contact with the light path, such as variation in its emission or absorption properties (luminescence, fluorescence) or in its refractive index. This deviation will modify the light propagation (wavelength, intensity, polarisation, phase velocity, etc) that can be measured under several sensor schemes and techniques.

4.1 COLORIMETRIC AND FLUORESCENT BIOSENSORS

Fluorescent ELISA (Enzyme-linked immunosorbent assay) is probably the most widely used fluorescent biosensor assay. Although not a biosensor itself, this assay can be incorporated as the transducer in a biosensor. ELISA, also known as an enzyme immunoassay (EIA), is a biochemical technique used mainly in immunology to detect the presence of an antibody or an antigen in a sample. The ELISA has been used as a

diagnostic tool in medicine, as well as a quality control check in various industries. In simple terms, in ELISA, an unknown amount of antigen is affixed to a surface, and then a specific antibody is washed over the surface so that it can bind to the antigen. This antibody is linked to an enzyme, and in the final step a substance is added that the enzyme can convert to some detectable signal. Thus in the case of fluorescence ELISA, when light of the appropriate wavelength is shone upon the sample, any antigen/antibody complexes will fluoresce so that the amount of antigen in the sample can be inferred through the magnitude of the fluorescence.

Performing an ELISA involves at least one antibody with specificity for a particular antigen. The sample with an unknown amount of antigen is immobilized on a solid support (usually a polystyrene microtiter plate) either non-specifically (via adsorption to the surface) or specifically (via capture by another antibody specific to the same antigen, in a "sandwich" ELISA). After the antigen is immobilized the detection antibody is added, forming a complex with the antigen. The detection antibody can be covalently linked to an enzyme, or can itself be detected by a secondary antibody which is linked to an enzyme through bioconjugation. Between each step the plate is typically washed with a mild detergent solution to remove any proteins or antibodies that are not specifically bound. After the final wash step the plate is developed by adding an enzymatic substrate to produce a visible signal, which indicates the quantity of antigen in the sample. The procedure is described in figure 1.9.
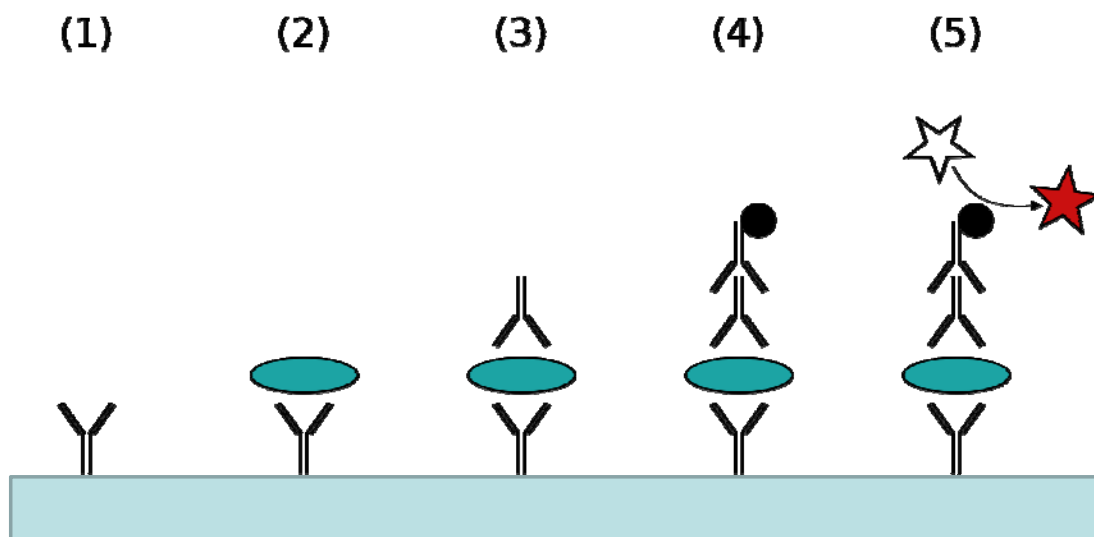
Figure 1.9.- A sandwich ELISA. (1) Plate is coated with a capture antibody; (2) sample is added, and any antigen present binds to capture antibody; (3) enzyme linked capture antibody used as detecting antibody is added, and binds to antigen; (4) substrate is added, and is converted by enzyme to detectable form. Modified from [49].

Traditional ELISA typically involves chromogenic reporters which produce some kind of observable color change to indicate the presence of antigen or analyte. Newer ELISA-like techniques utilize fluorogenic, electrochemiluminescent, and real-time PCR reporters to create quantifiable signals. These new reporters can have various advantages including higher sensitivities and multiplexing [50, 51]. Technically, newer assays of this type are not strictly ELISAs as they are not "enzyme-linked" but are instead linked to some non-enzymatic reporter. However, given that the general principles in these assays are largely similar, they are often grouped in the same category as ELISAs.

4.2 EVANESCENCE FIELD SENSORS

Optical biosensing methods based in the so-called evanescent wave technique use evanescent field to probe the surface of a sensing site for the presence of bound or absorbed analytes. Optical waveguides are used as the basic element of these sensors, as they provide structures for light propagation. An optical waveguide is formed by a core layer of material of certain refractive index surrounded by two other media with lower refractive indexes. Light is confined within the core layer by successive total internal reflections at the core-cladding media interfaces. However, although light travels confined within the core layer, there is a part of the guided light (evanescent field) that travels through a region that extends outside, around hundred of nanometres, into the media surrounding the waveguide. When there is a change in the optical characteristics of the outer medium (i.e. refractive index change), a modification in the propagation of the light (phase velocity) is induced via the evanescent field.

Evanescent Wave Optical Biosensors are comprised of optical fibers with an evanescent wave [52], resonant mirror [53], surface plasmon resonance [54], Mach-Zender interferometer [55], and grating coupler biosensors [56].

4.2.1 Surface Plasmon Resonance

One of the most relevant optical techniques for biosensing is the change in Surface Plasmon Resonance (SPR) properties [57]. SPR is a powerful technique to

measure biomolecular interactions in real-time in a label free environment. The Surface Plasmon Resonance is a physical process that can occur when plane-polarized light hits a metal film under total internal reflection conditions [58]. When a light beam hits a metal (usually gold), most of the incoming light gets reflected. But at incident angles bigger than the critical angle, all the incoming light is reflected, this is called total internal reflection (TIR). In TIR, the reflected photons create an electric field on the opposite side of the interface. When the energy of the photon electrical field of this evanescent wave is just right it can interact with the free electron constellations in the gold surface. These are the outer shell and conduction-band electrons. The incident light photons are absorbed and the energy is transferred to the electrons, which convert into surface plasmons. Therefore, when in a TIR situation the quantum energy of the photons is right, the photons are converted to plasmons, leaving a 'gap' in the reflected light intensity. The plasmons create a comparable field that extends into the medium on either side of the film. This field is called the evanescent wave [59]. The depth of the evanescent wave which is useful for measurements is within ~300 nm of the sensor surface [60]. The velocity (and therefore the momentum) of the plasmons is changed when the composition of the medium changes. Because of the change in momentum, the angle of incident light at which the resonance occurs changes. This can be measured very precisely [61]. This type of SPR is known as resonant angle or angular SPR and is commonly used [62]. On the other hand, at a fixed angle of incident light, the wavelength can be varied until resonance occurs [63]. This is known as resonant wavelength SPR or spectral SPR and is not used widely.

A scheme showing the working principle of a SPR biosensor is shown in figure 1.10. In this setup a fluidic system carries the sample in contact with the gold coated sensor. If a prism is in close contact with the sensor, it can be used to meet the resonance conditions and couple the light into the surface modes of the metal surface. Since in experiments the metal film, the incident light and temperature are kept constant, the SPR signal is directly dependent on the change of the refractive index of the medium on the sensor side of the SPR surface. The binding of biomolecules results in the change of the refractive index on the sensor surface, which is measured as a change in resonance angle or resonance wavelength. This resonance shift can be monitor overtime creating a kinetics representation of the events taking place on the sensor surface.
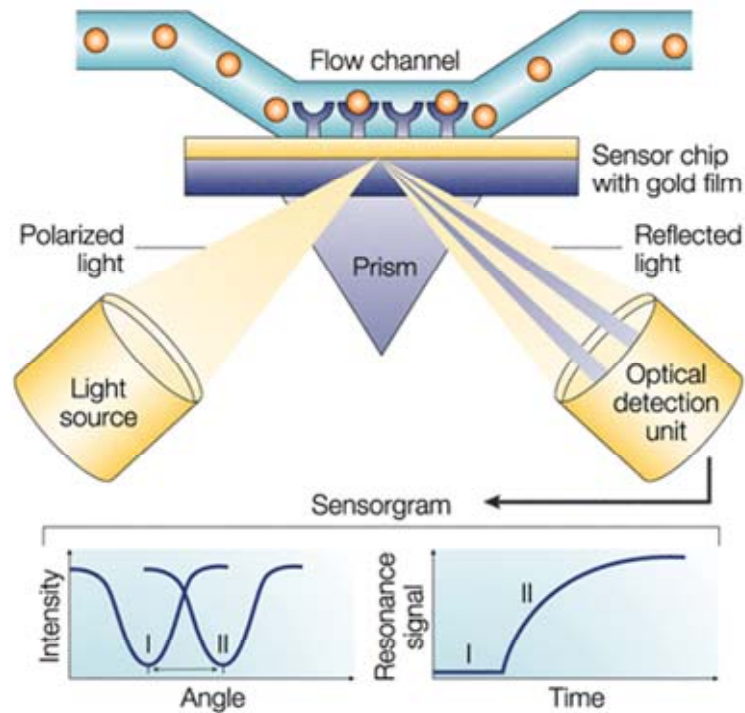
Figure 1.10.- Working principle of a SPR biosensor. [64]

This sensing method has been greatly improved and it is being used in commercial devices. Probably the most popular commercial version of SPR is the BIACORE system (BIAcoreTM, SpreetaTM, QuantechTM), shown in figure 1.11:

Figure 1.11.- Biacore T100 [65]

Optical Grating Coupler Biosensor and Biomedical Applications

As the SPR senses directly changes in the refractive index in the vicinity of the sensor surface, labelling of the analytes is not required, which is often a labour and cost intensive procedure. Also, as the penetration depth of the surface plasmon is so small, bulk effects coming from the analyte solution can be neglected. The responses to changes in refractive index are so fast that real time and kinetic experiments are possible. The change in resonance angle can be translated into a variation in refractive index that successively can render a value of adsorbed mass onto the sensing surface. But the analysis of the data is a key part of the experiment that can lead to wrong interpretations of the results. This problem gets more complicated as the data to analyse increases dramatically in a real time experiment. In addition reagents and buffers need to be carefully prepared and calibrated, as well temperature and gas bubbles must be controlled to avoid instrument noise. Despite the high costs of the sensors, the set up and its maintenance, the SPR biosensor is very useful to study analytes with concentrations higher that 1µg/ml, where the dynamic range is reproducible.

4.2.2. Mach-Zehnder Interferometry

In a Mach Zehnder Interferometer (MZI) two light beams of equal intensity are made to travel across two areas of a waveguide (one is the sensor and the other is the reference) and finally they are combined, creating an interference pattern (see Figure 1.12)
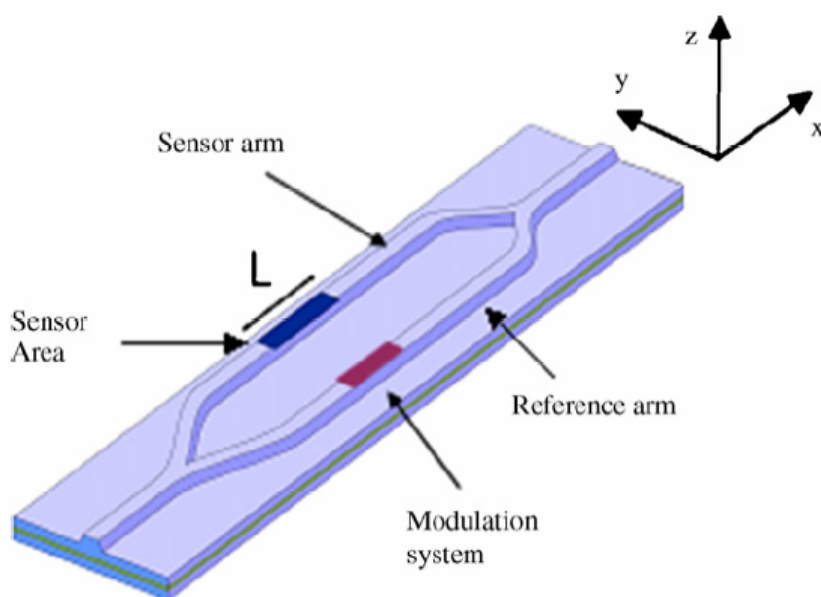
Figure 1.12.- Mach-Zehnder interferometer. [66]

When a biochemical reaction takes place in the sensor area, only the light that travels through this arm will experience a change in its effective refractive index. At the sensor output, the intensity (I) of the light coming from both arms will interfere, showing a sinusoidal variation that depends on the difference of the effective refractive indexes (to be defined in the next chapter) of the sensor and reference arms (ΔN_{eff}) and on the interaction length (L) and can directly related to the concentration of the analyte to be measured:

$$I \propto \left[1 + V \cdot \cos \Delta \Phi \right] \tag{1.2}$$

where V is the visibility factor and $\Delta \Phi = \left(\Phi_r - \Phi_s \right)$ is the phase shift between guided modes in the reference and sensing arm:

$$\Delta \Phi = \frac{2\pi}{\lambda} \cdot L \cdot \Delta N_{eff} \tag{1.3}$$

where λ is the wavelength. This sinusoidal variation can be directly related to the concentration of the analyte to be measured [67].

The interferometric sensor platform is highly sensitive and is the only one that provides with an internal reference for compensation of refractive index fluctuations and unspecific adsorption. Interferometric sensors have a broader dynamic range than most other types of sensors and show higher sensitivity as compared to other integrated optical biosensors. Due to the high sensitivity of the interferometer sensor the direct detection of small molecules would be possible with this device [68]. Detection limit is generally limited by electronic and mechanical noise, thermal drift, light source instabilities and chemical noise. But the intrinsic reference channel of the interferometric devices offers the possibility of reducing common mode effects like temperature drifts and non-specific adsorptions. Detection limit of 10^{-7} in refractive index (or better) can be achieved with these devices which opens the possibility of development of highly sensitive devices, for example, for extreme protein concentration determination (femtomolar) in a direct way [67].

The MZI has been widely used as a biosensor [69] and some groups have even reported the possibility to build such a system in polymer technology [70].

4.2.3. Grating coupler

By using the physics of a diffraction grating, an optical grating coupler biosensor (OGCB) measures the concentration of an analyte by detecting changes in the angle at which light couples into a waveguide as the analyte is being deposited. Biological receptors on the surface of the waveguide capture the molecules of interest, which affect the refractive index seen by the evanescent wave on the vicinity of the sensor surface (Figure 1.13).
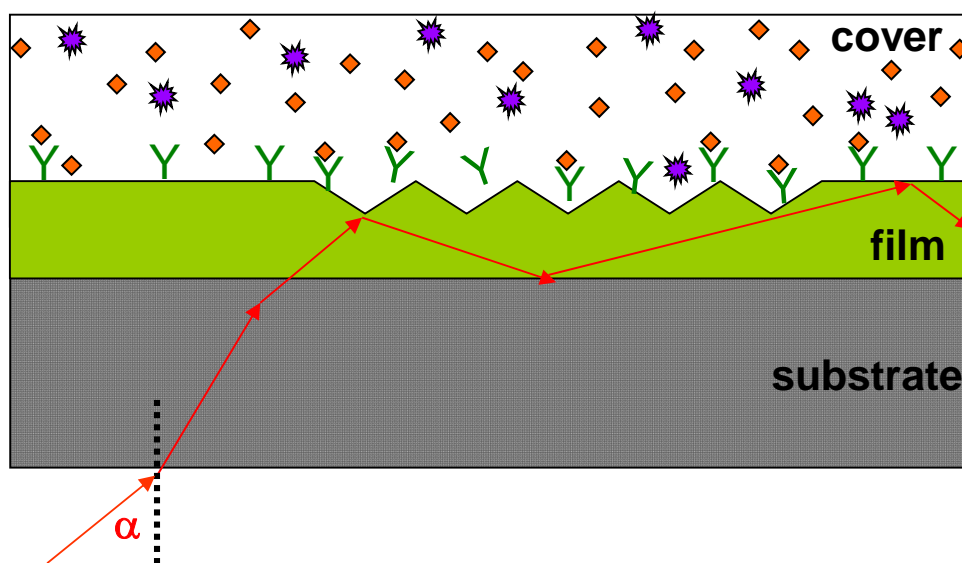
Figure 1.13.- Input grating coupler scheme. When an analyte adsorbs onto the sensor surface, the angle where the light gets coupled varies.

As a technique for investigating processes at the solid/liquid interface, it pushes the sensitivity to levels even higher than the already impressive achievements of older techniques such as ellipsometry [71], scanning angle reflectometry (SAR) [72] and SPR [73]. Theory, methods and application examples from the very beginning of the history of grating coupler waveguide sensors up to 1995 have been reviewed by Lukosz [74].

The effective refractive index, N_{eff} of the GC will change depending on the concentration of particles within a sample. To determine N_{eff} the coupling angle is monitored. Light couples into a dielectric waveguide at a well-specified angle with the use of a GC; therefore, the coupling angle allows an accurate determination of N_{eff}. A spectrum of the coupling angles is shown in figure 1.14.
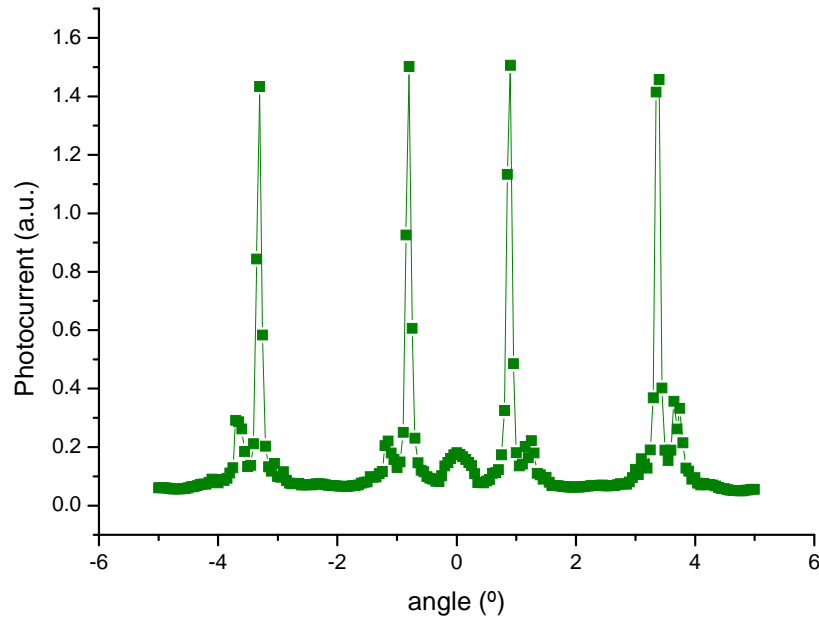
Figure 1.14.- A typical lightmode spectrum

Waveguides consists of a very thin (generally 150-250 nm) layer of a high refractive index material, deposited on a substrate with lower refractive index. On the upper side, the waveguide may be exposed to air or to other material (e.g aqueous solution). The coupling of light into a waveguide by means of a grating coupler occurs at angles α according to:

$$N_{eff} = n_C \sin\alpha + m\frac{\lambda}{\Lambda} \qquad (1.4)$$

where Neff is the effective refractive index of the waveguide mode excited by the input coupling. The refractive index of the external medium, vacuum wavelength and grating constant are denoted by n_C, λ, and Λ, respectively. The diffraction order is denoted by *m*. From the former calculation, it should be obvious that accurate particle detection requires a fine resolution of the coupling angle. This is made easier by using light sources with small spectral line widths, such as lasers. These light sources possess a small range of angles for which waveguide coupling will occur. The chemical absorption of molecules from the sample into the GC will affect therefore the incoupling angle.

There are grating coupler biosensors commercially available, such as the Optical Waveguide Lightmode Spectroscopy (OWLS; MicroVacuum, Budapest, Hungary). The OWLS instrument uses an optical grating for the incoupling of a He-Ne laser into a planar waveguide (figure 1.15). It measures precisely the change in the coupling angle

of the zeroth transverse electric and magnetic polarization modes of the laser upon adsorption of macromolecules. The optical thickness and the refractive index of thin and homogeneous adsorbed layers can be determined from the coupling angle shifts [75]. Since the refractive index is a linear function of the concentration or mass density [76], the absolute amount of the adsorbed molecules can be calculated using Feijter's Formula [77]:

$$M = d_A \frac{n_A - n_C}{dn/dc}$$ (1.5)

where d_A is the thickness of the adsorbed layer and dn/dc is the refractive index increment of the media with the concentration of molecules, which can be measured using a refractometer. The surface adsorbed mass densities determined from Eq. 1.5 depend only on the difference in the refractive index of the adsorbed molecules (n_A) and the cover medium (n_C); thus the solvent molecules will not contribute to the mass. This model is also applicable to the SPR or any other evanescent wave sensor.

Figure 1.15.- Commercial set-up of the OWLS system (Microvacuum Ltd., Hungary)

The OWLS technique offers a resolution of 10^{-6} in the effective refractive index change, is therefore highly sensitive (i.e., ~ 1 ng/cm^2) and allows for the direct online monitoring of macromolecular adsorption. The OWLS system is particularly valuable for the detailed analysis of binding processes, with a view to elucidate the underlying physico-chemical mechanisms. Its high sensitivity, coupled with the easy-to-run under controlled hydrodynamic conditions, enables many crucial details to be revealed, which remain hidden when investigated using less-advanced methods. Thus, OWLS is an extremely valuable tool in different areas, from fundamental biological research

Optical Grating Coupler Biosensor and Biomedical Applications

(biomolecular interactions [78], living cells [79], membrane protein-lipid bilayer interactions [80], nucleic acids [81]), bionanotechnology [82], biocompatibility [83] and drug discovery [34] to research aimed at developing diagnostic biosensors and immunosensors [84].

The EC-OWLS instrument shown in Figure 1.16, includes an electrochemical flow cell where the sensor (OW 2400c Sensor Chip, MicroVacuum), a waveguide coated by a 10 nm indium tin oxide layer (ITO), roles the working electrode. A potential difference is applied between the ITO and a Pt counter electrodes, and the ITO potential is determined vs. an Ag/AgCl reference electrode.
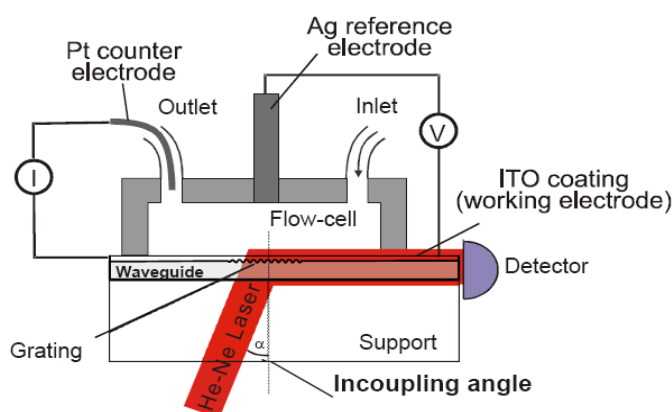
Figure 1.16.-   Schematic of EC-OWLS setup comprising a three-electrode configuration within a waveguide spectrometer with a 15 μL cell. The waveguide was coated with ITO to allow for potential control (working electrode). A silver wire inserted into the top of the cell served as a reference electrode and a platinum wire in export tubing served as a counter electrode.

This technique allows applying an external electric field into the flow cell. The electric field dependence of the adsorption/desorption of proteins or other biomolecules can be studied qualitatively and quantitatively by controlled potential OWLS measurement [85]. Also, with the addition of electrical field stimulation in EC-OWLS systems, living cell behaviour under electrical field can be studied [86].

Incoupled light intensity versus angle of incidence spectra can be measured by the two photodiodes placed at both end of the waveguide. As in figure 1.14, the photocurrent versus angle can be plotted. From these peaks, the refractive index (n_F) and the thickness (d_F) of the waveguide layer and the temperature (T) can be calculated.

The refractive index measurement allows to measure time dependent surface processes. Peak measurements are repeated either continuously or at a given repeating frequency. In this way, the kinetics of the adsorption of molecules onto the sensor

surface can be monitored. An example of this type of measurements is showed in figure 1.17.
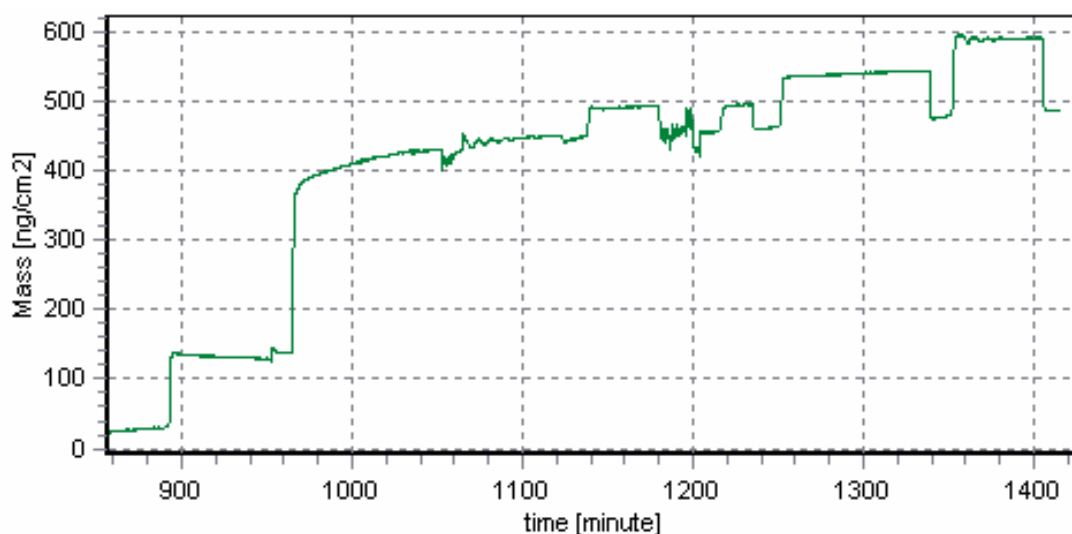
Figure 1.17.- A typical kinetic curve of effective refractive index.

5 COMPARATIVE

From all the above described biosensors, optical biosensors are an excellent candidate for study and development, as they exhibit high sensitivity, high mechanical stability, are immune to electromagnetic interferences and permit no destructive measurements. While the QCM measures the wet mass deposited on the surface, SPR and waveguide grating couplers sense dry mass adsorbed onto the sensor; which discriminates de sole effect of the analyte from effects from the buffer solution. Electrochemical sensors on the other hand are so sensible to any change happening in the surface of the working electrode that makes it very difficult to differentiate the individual influence from independent events. From the great variety of optical methods that can be employed for the detection, those which can give a direct signal after a molecular interaction (without the use of labels) have attracted quite attention, as for example Surface Plasmon Resonance, Grating Coupler or Interferometers. In table 1.1, a comparison of the different sensor technologies as a function of the limit of detection (in ng/cm^2) is presented [67].

Table 1. Comparison of sensitivities for different integrated optical biosensors

Sensing principle	Limit of detection (ng/cm^2)	Manufacter	REF
SPR	0.2 - 0.5	Aviv Instruments Biacore Graffinity Pharmaceuticals HTS Biosystems IBIS Nippon Lasers Prolinx	[73]
Grating Coupler Waveguide	0.1 - 1	Farfield Sensors Microvacuum Luna Analytics	[87]
Mach-Zehnder interferometer	0.01	--	[88, 89]

Interferometric biosensors arrangement is highly sensitive and provides with an internal reference for compensation of refractive-index fluctuations and unspecific adsorption. Interferometric sensors have a broader dynamic range than most other types of sensors and show higher sensitivity as compared to other integrated scheme as it is shown in Table 1. Due to the high sensitivity of the interferometer sensor, the direct detection of small molecules (as for example environmental pollutants where concentrations down to 0.1 ng/ml must be detected) would be possible with this device. Detection limit of 10^{-7} in refractive index (or better) can be achieved with these devices [90], but it is generally limited by electronic and mechanical noise, thermal drift, light source instabilities and chemical noise. Even though, the Mach-Zehnder interferometer sensor seems to be one of the more promising concepts for detection of low concentration of small molecules without labels (10^{-12} M or even lower) [91], the main problem in the development and possible commercialization of the MZI device is the complexity of the design, fabrication and optical adjustments. The overall procedure for MZI fabrication is rather laborious and monomode waveguides are required, increasing even more the complexity of the technology.

The main advantage of planar dielectric waveguides over SPR devices for label-free detection lies in the enhanced degrees of freedom for sensor design. In both technologies, the penetration depth of guided waves at the sensor interface is directly related to the geometrical extent of the measurement volume, where sensitivity is high. For SPR systems, this parameter is given by the material properties, with a typical penetration depth of around 200 nanometers [92]. In the case of planar dielectric waveguides, this property can be chosen by design, enhancing the application fields to the detection of relatively large objects in the micrometer range, such as cells [93].

Furthermore, the absence of a metal film can be an advantage, for instance when combining label-free with luminescent detection. Energy transfers to the metal film (which is called quenching effect) make the combination of luminescence and SPR sensors impractical at least in the classic configuration, while dielectric waveguides are used successfully to enhance the sensitivity of fluorescent sensors [94].

Another advantage of biochemical sensors based on waveguide gratings is their suitability for building sensor arrays with a high number of different sensing regions present on the same chip. This facilitates the detection of several target molecule types simultaneously present in an analyte solution, which is a key requirement for biochemical sensors in all application fields [95].

For all these reasons, waveguide grating coupler based biosensors will be our technique of choice for the studies and developments carried out in this thesis.

6 SUMMARY

Taking advantage of the last advances in nanotechnology, the goal of this thesis is to study the versatility of an Optical Grating Coupler Biosensor. Towards this purpose, new and robust grating coupler sensor chips will be developed in different materials presenting high sensitivity, fast response, stability, reproducibility, small size and low cost; suitable for different applications. This will be the objective of chapter number 2. In the third chapter, a new calibration method to individually characterize the sensor chip, the analytes and the buffer solutions before performing biosensing measurements, will be investigated. In the fourth chapter, the potential of the grating coupler technique is applied to optimize the immobilization of liposomes carrying olfactory receptors onto the sensor surface. Last, in chapter number five, the grating

coupler biosensor will be combined with electrochemical techniques to get a deeper understanding in the mechanisms ruling the stability of polyelectrolyte multilayers.

7 REFERENCES

[1]   D. Grieshaber, R. MacKenzie, J. Vörös, and E. Reimhult, "Electrochemical Biosensors - Sensor Principles and Architectures," in *Sensors*. vol. 8, 2008, pp. 1400-1458.

[2]   J. S. Schultz, "Biosensors," *Scientific American,* vol. 265, pp. 64-9, 1991.

[3]   L. C. Clark, R. Wolf, D. Granger, and Z. Taylor, "Continuous Recording of Blood Oxygen Tensions by Polarography." vol. 6, 1953, pp. 189-193.

[4]   L. C. Clark and C. Lyons, "Electrode systems fro continuous monitoring in cardiovascular surgery," *Annals of the New York Academy of Sciences,* vol. 102, pp. 29-45, 1962.

[5]   R. M. Guijt, J. P. Armstrong, E. Candish, V. Lefleur, W. J. Percey, S. Shabala, P. C. Hauser, and M. C. Breadmore, "Microfluidic chips for capillary electrophoresis with integrated electrodes for capacitively coupled conductivity detection based on printed circuit board technology," *Sensors and Actuators B: Chemical,* vol. 159, pp. 307-313.

[6]   Y.-H. Yun, A. Bhattacharya, N. Watts, and M. Schulz, "A Label-Free Electronic Biosensor for Detection of Bone Turnover Markers," in *Sensors*. vol. 9, 2009, pp. 7957-7969.

[7]   A. Rasooly and J. Jacobson, "Development of biosensors for cancer clinical testing," *Biosensors and Bioelectronics,* vol. 21, pp. 1851-1858, 2006.

[8]   S. Kumbhat, K. Sharma, R. Gehlot, A. Solanki, and V. Joshi, "Surface plasmon resonance based immunosensor for serological diagnosis of dengue virus infection," *Journal of Pharmaceutical and Biomedical Analysis,* vol. 52, pp. 255-259, 2010.

[9]   S. K. Arya, M. Datta, and B. D. Malhotra, "Recent advances in cholesterol biosensor," *Biosensors and Bioelectronics,* vol. 23, pp. 1083-1100, 2008.

[10]   C. Situ, M. H. Mooney, C. T. Elliott, and J. Buijs, "Advances in surface plasmon resonance biosensor technology towards high-throughput, food-safety analysis," *TrAC Trends in Analytical Chemistry,* vol. 29, pp. 1305-1315, 2010.

[11]   T. B. Goriushkina, A. P. Soldatkin, and S. V. Dzyadevych, "Application of Amperometric Biosensors for Analysis of Ethanol, Glucose, and Lactate in Wine," *Journal of Agricultural and Food Chemistry,* vol. 57, pp. 6528-6535, 2009.

[12]   J. Giné Bordonaba and L. A. Terry, "Development of a Glucose Biosensor for Rapid Assessment of Strawberry Quality: Relationship between Biosensor Response and Fruit Composition," *Journal of Agricultural and Food Chemistry,* vol. 57, pp. 8220-8226, 2009.

[13]   A. Sabelnikov, V. Zhukov, and R. Kempf, "Probability of real-time detection versus probability of infection for aerosolized biowarfare agents: A model study," *Biosensors and Bioelectronics,* vol. 21, pp. 2070-2077, 2006.

[14]   M. Nayak, A. Kotian, S. Marathe, and D. Chakravortty, "Detection of microorganisms using biosensors--A smarter way towards detection techniques," *Biosensors and Bioelectronics,* vol. 25, pp. 661-667, 2009.

[15]   M. A. Andersson, R. Mikkola, S. Rasimus, D. Hoornstra, P. Salin, R. Rahkila, M. Heikkinen, S. Mattila, J. Peltola, S. Kalso, and M. Salkinoja-Salonen, "Boar spermatozoa as a biosensor for detecting toxic substances in indoor dust and aerosols," *Toxicology in Vitro,* vol. 24, pp. 2041-2052, 2010.

[16]   A. J. Killard, B. Deasy, R. O'Kennedy, and M. R. Smyth, "Antibodies: production, functions and applications in biosensors," *TrAC Trends in Analytical Chemistry,* vol. 14, pp. 257-266, 1995/7// 1995.

[17]   L. Lechuga, "Micro- and nanoimmunosensors: technology and applications," *Analytical and Bioanalytical Chemistry,* vol. 384, pp. 44-46, 2006.

[18]   S. Ghoshal, D. Mitra, S. Roy, and M. D. Dutta, "Biosensors and biochips for nanomedical applications: a review," *Sens. Transducers J.,* vol. 113, pp. 1-17, 2010.

[19]   T. Nomura and A. Minemura, "Behavior of a piezoelectric quartz crystal in an aqueous solution and its use for the determination of minute amounts of cyanide," *Nippon Kagaku Kaishi,* pp. 1621-5, 1980.

[20]   J. Xu, K.-W. Liu, K. S. Matthews, and S. L. Biswal, "Monitoring DNA Binding to Escherichia coli Lactose Repressor Using Quartz Crystal Microbalance with Dissipation," *Langmuir,* vol. 27, pp. 4900-4905, 2011.

[21]   S. Belegrinou, I. Mannelli, P. Lisboa, F. Bretagnol, A. Valsesia, G. Ceccone, P. Colpo, H. Rauscher, and F. o. Rossi, "pH-Dependent Immobilization of Proteins on Surfaces Functionalized by Plasma-Enhanced Chemical Vapor Deposition of Poly(acrylic acid)- and Poly(ethylene oxide)-like Films," *Langmuir,* vol. 24, pp. 7251-7261, 2008.

[22]   C. Fant, H. Elwing, and F. Höök, "The Influence of Cross-Linking on Protein-Protein Interactions in a Marine Adhesive: The Case of Two Byssus Plaque Proteins from the Blue Mussel," *Biomacromolecules,* vol. 3, pp. 732-741, 2002.

[23]   S. Boujday, A. Bantegnie, E. Briand, P.-G. Marnet, M. l. Salmain, and C.-M. Pradier, "In-Depth Investigation of Protein Adsorption on Gold Surfaces: Correlating the Structure and Density to the Efficiency of the Sensing Layer," *The Journal of Physical Chemistry B,* vol. 112, pp. 6708-6715, 2008.

[24]   H. Chen, X. Su, K.-G. Neoh, and W.-S. Choe, "Context-Dependent Adsorption Behavior of Cyclic and Linear Peptides on Metal Oxide Surfaces," *Langmuir,* vol. 25, pp. 1588-1593, 2008.

[25]   F. Höök, B. Kasemo, T. Nylander, C. Fant, K. Sott, and H. Elwing, "Variations in Coupled Water, Viscoelastic Properties, and Film Thickness of a Mefp-1 Protein Film during Adsorption and Cross-Linking:â€‰ A Quartz Crystal Microbalance with Dissipation Monitoring, Ellipsometry, and Surface Plasmon Resonance Study," *Analytical Chemistry,* vol. 73, pp. 5796-5804, 2001.

[26]   M. S. Lord, M. H. Stenzel, A. Simmons, and B. K. Milthorpe, "The effect of charged groups on protein interactions with poly(HEMA) hydrogels," *Biomaterials,* vol. 27, pp. 567-575, 2006.

[27]   A. Welle, "Competitive plasma protein adsorption on modified polymer surfaces monitored by quartz crystal microbalance technique," *Journal of Biomaterials Science -- Polymer Edition,* vol. 15, pp. 357-370, 2004.

[28]   D. M. Gryte, M. D. Ward, and W. S. Hu, "Real-time measurement of anchorage-dependent cell adhesion using a quartz crystal microbalance," *Biotechnology Progress,* vol. 9, pp. 105-108, 1993.

[29]   J. Redepenning, T. K. Schlesinger, E. J. Mechalke, D. A. Puleo, and R. Bizios, "Osteoblast attachment monitored with a quartz crystal microbalance," *Analytical Chemistry,* vol. 65, pp. 3378-3381, 1993.

[30] J. Li, C. Thielemann, U. Reuning, and D. Johannsmann, "Monitoring of integrin-mediated adhesion of human ovarian cancer cells to model protein surfaces by quartz crystal resonators: evaluation in the impedance analysis mode," *Biosensors and Bioelectronics,* vol. 20, pp. 1333-1340, 2005.

[31] J. Wegener, A. Janshoff, and H. J. Galla, "Cell adhesion monitoring using a quartz crystal microbalance: comparative analysis of different mammalian cell lines," *European Biophysics Journal,* vol. 28, pp. 26-37, 1998.

[32] T. Zhou, K. A. Marx, M. Warren, H. Schulze, and S. J. Braunhut, "The Quartz Crystal Microbalance as a Continuous Monitoring Tool for the Study of Endothelial Cell Surface Attachment and Growth," *Biotechnology Progress,* vol. 16, pp. 268-277, 2000.

[33] K. A. Marx, T. Zhou, A. Montrone, H. Schulze, and S. J. Braunhut, "A quartz crystal microbalance cell biosensor: detection of microtubule alterations in living cells at nM nocodazole concentrations," *Biosensors and Bioelectronics,* vol. 16, pp. 773-782, 2001.

[34] T. S. Hug, "Biophysical Methods for Monitoring Cell-Substrate Interactions in Drug Discovery," in *ASSAY and Drug Development Technologies*. vol. 1, 2003, pp. 479-488.

[35] "http://www.q-sense.com/qcm-d-technology." Retrieved on the 23rd April 2011.

[36] G. Sauerbrey, "Verwendung von Schwingquarzen zur Wägung dünner Schichten und zur Mikrowägung," *Zeitschrift für Physik A Hadrons and Nuclei,* vol. 155, pp. 206-222, 1959.

[37] R. Schumacher, "The Quartz Microbalance: A Novel Approach to the In-Situ Investigation of Interfacial Phenomena at the Solid/Liquid Junction [New Analytical Methods (40)]," *Angewandte Chemie International Edition in English,* vol. 29, pp. 329-343, 1990.

[38] S. Bruckenstein and M. Shay, "An in situ weighing study of the mechanism for the formation of the adsorbed oxygen monolayer at a gold electrode," *Journal of Electroanalytical Chemistry and Interfacial Electrochemistry,* vol. 188, pp. 131-136, 1985.

[39] D. A. Buttry and M. D. Ward, "Measurement of interfacial processes at electrode surfaces with the electrochemical quartz crystal microbalance," *Chemical Reviews,* vol. 92, pp. 1355-1379, 1992.

[40] F. Höök, J. Vörös, M. Rodahl, R. Kurrat, P. Böni, J. J. Ramsden, M. Textor, N. D. Spencer, P. Tengvall, J. Gold, and B. Kasemo, "A comparative study of protein adsorption on titanium oxide surfaces using in situ ellipsometry, optical waveguide lightmode spectroscopy, and quartz crystal microbalance/dissipation," *Colloids and Surfaces B: Biointerfaces,* vol. 24, pp. 155-170, 2002.

[41] H. Wang, G. Shen, and R. Yu, *Aspects of recent development of immunosensors, in Electrochemical Sensors, Biosensors and their Biomedical Applications.* San Diego: Academic Press, 2008.

[42] E. P. Medyantseva, E. V. Khaldeeva, and G. K. Budnikov, "Immunosensors in Biology and Medicine: Analytical Capabilities, Problems, and Prospects," *Journal of Analytical Chemistry,* vol. 56, pp. 886-900, 2001.

[43] J. Heinze, "Cyclic Voltammetry—"Electrochemical Spectroscopy". New Analytical Methods (25)," *Angewandte Chemie International Edition in English,* vol. 23, pp. 831-847, 1984.

[44] J. M. Fowler, D. K. Y. Wong, H. B. Halsall, and W. R. Heineman, *Recent developments in electrochemical immunoassays and immunosensors.*

Electrochemical sensors, biosensors and their biomedical applications. Amsterdam, Boston Academic Press, 2008.

[45]   Q. Xue, C. Bian, J. Tong, J. Sun, H. Zhang, and S. Xia, "A micro potentiometric immunosensor for hemoglobin-A1c level detection based on mixed SAMs wrapped nano-spheres array," *Biosensors and Bioelectronics,* vol. 26, pp. 2689-2693.

[46]   A. Gebbert, M. Alvarez-Icaza, W. Stoecklein, and R. D. Schmid, "Real-time monitoring of immunochemical interactions with a tantalum capacitance flow-through cell," *Analytical Chemistry,* vol. 64, pp. 997-1003, 1992.

[47]   X. Fan, I. M. White, S. I. Shopova, H. Zhu, J. D. Suter, and Y. Sun, "Sensitive optical biosensors for unlabeled targets: A review," *Analytica Chimica Acta,* vol. 620, pp. 8-26, 2008.

[48]   M. A. González-Martínez, R. Puchades, and A. Maquieira, "Optical immunosensors for environmental monitoring: How far have we come?," *Analytical & Bioanalytical Chemistry,* vol. 387, pp. 205-218, 2007.

[49]   "http://en.wikipedia.org/wiki/File:ELISA-sandwich.svg ": from Jeffery M. Vinocur (Multi-license with GFDL and Creative Commons CC-BY 2.5), Retrieved on the 23rd April 2011.

[50]   S. X. Leng, J. E. McElhaney, J. D. Walston, D. Xie, N. S. Fedarko, and G. A. Kuchel, "ELISA and multiplex technologies for cytokine measurement in inflammation and aging research," *The journals of gerontology. Series A, Biological sciences and medical sciences,* vol. 63, pp. 879-84, 2008.

[51]   M. Adler, S. Schulz, and M. Spengler, "Cytokine Quantification in Drug Development: A comparison of sensitive immunoassay platforms," Chimera Biotech. (Report), 2009.

[52]   T. Giallorenzi, J. Bucaro, A. Dandridge, G. Sigel, J. Cole, S. Rashleigh, and R. Priest, "Optical fiber sensor technology," *Quantum Electronics, IEEE Journal of,* vol. 18, pp. 626-665, 1982.

[53]   R. Cush, J. M. Cronin, W. J. Stewart, C. H. Maule, J. Molloy, and N. J. Goddard, "The resonant mirror: a novel optical biosensor for direct sensing of biomolecular interactions Part I: Principle of operation and associated instrumentation," *Biosensors and Bioelectronics,* vol. 8, pp. 347-354, 1993.

[54]   J. Homola, J. Ctyroky, M. Skalsky, J. Hradilova, and P. Kolarova, "A surface plasmon resonance based integrated optical sensor," *Sensors and Actuators B: Chemical,* vol. 39, pp. 286-290, 1997.

[55]   R. G. Heideman, R. P. H. Kooyman, and J. Greve, "Performance of a highly sensitive optical waveguide Mach-Zehnder interferometer immunosensor," *Sensors and Actuators B: Chemical,* vol. 10, pp. 209-217, 1993.

[56]   A. Brandenburg and A. Gombert, "Grating couplers as chemical sensors: a new optical configuration," *Sensors and Actuators B: Chemical,* vol. 17, pp. 35-40, 1993.

[57]   D. Erickson, S. Mandal, A. Yang, and B. Cordovez, "Nanobiosensors: optofluidic, electrical and mechanical approaches to biomolecular detection at the nanoscale," *Microfluidics and Nanofluidics,* vol. 4, pp. 33-52, 2008.

[58]   Biacore, *BIAtechnology Handbook, version AB*, 1998.

[59]   K. Nagata, H. Handa, and Editors, *Real-Time Analysis of Biomolecular Interactions: Applications of BIACORE*: Springer-Verlag, 2000.

[60]   P. A. van der Merwe, " Surface Plasmon Resonance. ," 2003, p. 50.

[61]   F. Markey, "What is SPR anyway?," *Bia Journal,* vol. 1, pp. 14-17, 1999.

[62]   T. Akimoto, S. Sasaki, K. Ikebukuro, and I. Karube, "Effect of incident angle of light on sensitivity and detection limit for layers of antibody with surface plasmon resonance spectroscopy," *Biosensors and Bioelectronics,* vol. 15, pp. 355-362, 2000.

[63]   J. G. Quinn, S. O'Neill, A. Doyle, C. McAtamney, D. Diamond, B. D. MacCraith, and R. O'Kennedy, "Development and Application of Surface Plasmon Resonance-Based Biosensors for the Detection of Cell-Ligand Interactions," *Analytical Biochemistry,* vol. 281, pp. 135-143, 2000.

[64]   M. A. Cooper, "Optical biosensors in drug discovery," *Nat Rev Drug Discov,* vol. 1, pp. 515-528, 2002.

[65]   "http://www.biacore.com/lifesciences/products/systems_overview/t100/," Retrieved on the 23rd April 2011.

[66]   B. Sepúlveda and et al., "Optical biosensor microsystems based on the integration of highly sensitive Mach-Zehnder interferometer devices." vol. 8, 2006, p. S561.

[67]   L. M. Lechuga, "Interferometric Biosensors for environmental pollution detection," in *Optical Sensors for Industrial, environmental and diagnostic applications*, E. R. N. a. O. S. Wolfbeis., Ed.: Springer, 2003.

[68]   L. M. Lechuga, E. Mauriz, B. Sepúlveda, J. Sánchez del Río, A. Llobera, A. Calle, and C. Domínguez, "Optoelectronics sensors applied to biology," *Opt. Pura Apl.,* vol. 39, pp. 129-133, 2006.

[69]   B. J. Luff, J. S. Wilkinson, J. Piehler, U. Hollenbach, J. Ingenhoff, and N. Fabricius, "Integrated optical Mach-Zehnder biosensor," *Lightwave Technology, Journal of,* vol. 16, pp. 583-592, 1998.

[70]   D. Esinenco, S. D. Psoma, M. Kusko, A. Schneider, and R. Muller, "SU-8 micro-biosensor based on Mach-Zehnder interferometer " *Rev.Adv.Mater.Sci.(RAMS),* vol. 10, pp. 295-299 2005.

[71]   H. Elwing, "ChemInform Abstract: Protein Adsorption and Ellipsometry in Biomaterial Research," *ChemInform,* vol. 29, pp. no-no, 1998.

[72]   P. Huetz, P. Schaaf, J. C. Voegel, E. K. Mann, B. Miras, V. Ball, M. Freund, and J. P. Cazenave, "Reactivity of Antibodies on Antigens Adsorbed on Solid Surfaces," in *Proteins at Interfaces II*. vol. 602: American Chemical Society, 1995, pp. 334-349.

[73]   J. Homola, S. S. Yee, and G. Gauglitz, "Surface plasmon resonance sensors: review," *Sensors and Actuators B: Chemical,* vol. 54, pp. 3-15, 1999.

[74]   W. Lukosz, "Integrated optical chemical and direct biochemical sensors," *Sensors and Actuators B: Chemical,* vol. 29, pp. 37-50, 1995.

[75]   K. Tiefenthaler and W. Lukosz, "Sensitivity of grating couplers as integrated-optical chemical sensors," *J. Opt. Soc. Am. B* vol. 6, p. 209, 1989.

[76]   K. Sato, D. Kodama, Y. Naka, and J. i. Anzai, "Electrochemically Induced Disintegration of Layer-by-Layer-Assembled Thin Films Composed of 2-Iminobiotin-Labeled Poly(ethyleneimine) and Avidin." vol. 7, 2006, pp. 3302-3305.

[77]   J. A. D. Feijter and J. B. F. A. Veer, "Ellipsometry as a tool to study the adsorption behavior of synthetic and biopolymers at the air-water interface," *Biopolymers,* vol. 17, pp. 1759-1772, 1978.

[78]   H. M. Grandin, B. Stadler, M. Textor, and J. Voros, "Waveguide excitation fluorescence microscopy: A new tool for sensing and imaging the biointerface," *Biosensors and Bioelectronics,* vol. 21, pp. 1476-1482, 2006.

[79]   C. R. Wittmer, J. A. Phelps, W. M. Saltzman, and P. R. Van Tassel, "Fibronectin terminated multilayer films: Protein adsorption and cell attachment studies," *Biomaterials,* vol. 28, pp. 851-860, 2007.

[80]   A. Lukács, G. Garab, and E. Papp, "Measurement of the optical parameters of purple membrane and plant light-harvesting complex films with optical waveguide lightmode spectroscopy," *Biosensors and Bioelectronics,* vol. 21, pp. 1606-1612, 2006.

[81]   B. Städler, D. Falconnet, I. Pfeiffer, F. Höök, and J. Vörös, "Micropatterning of DNA-Tagged Vesicles," *Langmuir,* vol. 20, pp. 11348-11354, 2004.

[82]   V. Ball, M. Michel, F. Boulmedais, J. Hemmerle, Y. Haikel, P. Schaaf, and J. C. Voegel, "Nucleation Kinetics of Calcium Phosphates on Polyelectrolyte Multilayers Displaying Internal Secondary Structure," *Crystal Growth & Design,* vol. 6, pp. 327-334, 2006.

[83]   T. M. Blättler, S. Pasche, M. Textor, and H. J. Griesser, "High Salt Stability and Protein Resistance of Poly(l-lysine)-g-poly(ethylene glycol) Copolymers Covalently Immobilized via Aldehyde Plasma Polymer Interlayers on Inorganic and Polymeric Substrates," *Langmuir,* vol. 22, pp. 5760-5769, 2006.

[84]   D. Grieshaber, E. Reimhult, and J. Voros, "Enzymatic Biosensors towards a Multiplexed Electronic Detection System for Early Cancer Diagnostics," in *Nano/Micro Engineered and Molecular Systems, 2007. NEMS '07. 2nd IEEE International Conference on*, 2007, pp. 402-405.

[85]   J. P. Bearinger, J. Vörös, N. D. Spencer, J. A. Hubbel, and M. Textor, "Nanoscale Bio-Molecular Control Using EC-OWLS," in *NSTI Natonech -The Nanotechnology Conference and Trade Show* Santa Clara, 2007.

[86]   N. Adányi, E. Németh, A. Halász, I. Szendro, and M. Váradi, "Application of electrochemical optical waveguide lightmode spectroscopy for studying the effect of different stress factors on lactic acid bacteria," *Analytica Chimica Acta,* vol. 573-574, pp. 41-47, 2006.

[87]   M. Wiki, H. Gao, M. Juvet, and R. E. Kunz, "Compact integrated optical sensor system," *Biosensors and Bioelectronics,* vol. 16, pp. 37-45, 2001.

[88]   B. H. Schneider, E. L. Dickinson, M. D. Vach, J. V. Hoijer, and L. V. Howard, "Optical chip immunoassay for hCG in human whole blood," *Biosensors and Bioelectronics,* vol. 15, pp. 597-604, 2000.

[89]   A. Brandenburg, R. Krauter, C. Künzel, M. Stefan, and H. Schulte, "Interferometric Sensor for Detection of Surface-Bound Bioreactions," *Appl. Opt.,* vol. 39, pp. 6396-6405, 2000.

[90]   L. M. Lechuga, A. T. M. Lenferink, R. P. H. Kooyman, and J. Greve, "Feasibility of evanescent wave interferometer immunosensors for pesticide detection: chemical aspects," *Sensors and Actuators B: Chemical,* vol. 25, pp. 762-765, 1995.

[91]   E. F. Schipper, A. M. Brugman, C. Dominguez, L. M. Lechuga, R. P. H. Kooyman, and J. Greve, "The realization of an integrated Mach-Zehnder waveguide immunosensor in silicon technology," *Sensors and Actuators B: Chemical,* vol. 40, pp. 147-153, 1997.

[92]   W. Lukosz, "Principles and sensitivities of integrated optical and surface plasmon sensors for direct affinity sensing and immunosensing," *Biosensors and Bioelectronics,* vol. 6, pp. 215-225, 1991.

[93]   R. Horváth, H. C. Pedersen, N. Skivesen, D. Selmeczi, and N. B. Larsen, "Optical waveguide sensor for on-line monitoring of bacteria," *Opt. Lett.,* vol. 28, pp. 1233-1235, 2003.

[94]   P. N. Zeller, G. Voirin, and R. E. Kunz, "Single-pad scheme for integrated optical fluorescence sensing," *Biosensors and Bioelectronics,* vol. 15, pp. 591-595, 2000.

[95]   N. Darwish, D. Caballero, M. Moreno, A. Errachid, and J. Samitier, "Multi-analytic grating coupler biosensor for differential binding analysis," *Sensors and Actuators B: Chemical,* vol. 144, pp. 413-417, 2010.

Optical Grating Coupler Biosensor and Biomedical Applications

CHAPTER 2: OPTICAL GRATING COUPLER SENSOR CHIP DESIGN AND FABRICATION

1 INTRODUCTION & STATE OF THE ART

An optical waveguide is a structure which confines and guides the light beam by the process of total internal reflection. The most extensively used optical waveguide is the optical fibre which consists of a cylindrical central core, clad by a material of slightly lower refractive index.

The simplest optical waveguide to analyse is the planar waveguide which consists of a thin film (of refractive index n_F) sandwiched between materials of slightly lower refractive indexes. Such planar waveguides are important components in integrated optics with applications in sensing and optical communications.

In integrated optics, several kinds of waveguides are used; these are the planar, strip and rib guides. In planar waveguides (see figures 2.1), the confinement of the light energy is only along one transverse dimension and the light energy can diffract in the other transverse dimension. In contrast to planar waveguides, strip (see figure 2.2) and rib waveguides confine the light energy in both transverse dimensions; this confinement is a desirable feature for the fabrication of devices such as amplitude or intensity modulators, directional couplers, optical switches etc.
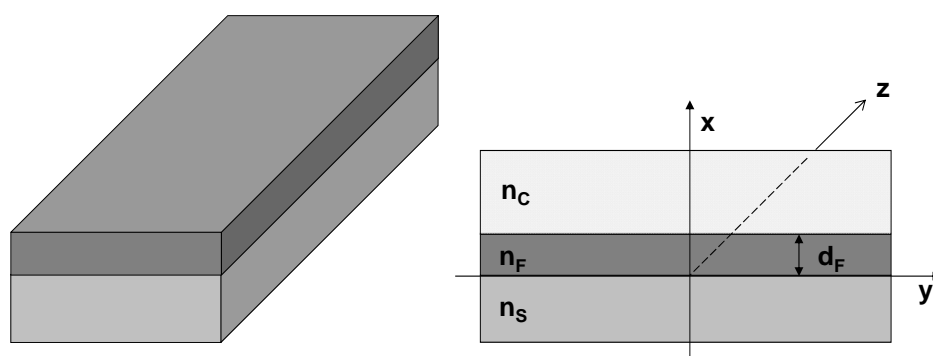

Fig. 2.1.- **(a)** A planar waveguide consisting of a film of refractive index n_F deposited on a substrate of refractive index n_S and with a cover of refractive index n_C. The refractive index varies only along the x-direction: light can diffract in the y-z plane. **(b)** Transverse cross section of the waveguide.
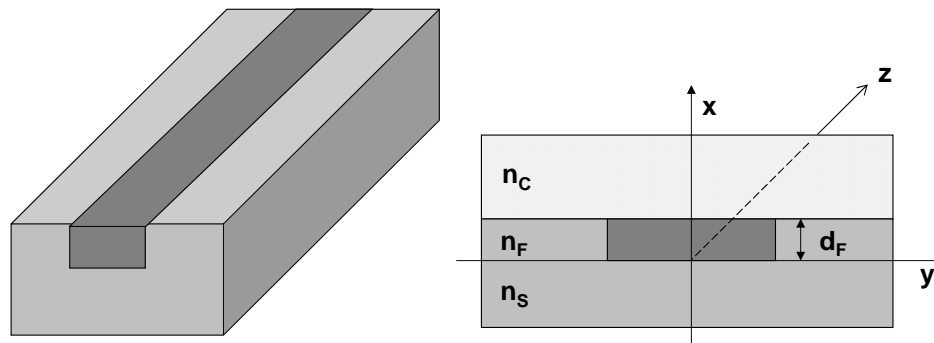
Fig. 2.2.- **(a)** A strip waveguide consisting of a high index region of refractive index n_F surrounded by media of lower refractive indexes. The light confinement is along both the x and y-directions; the direction of propagation is the z-direction. **(b)** Transverse cross section of the waveguide.

The planar waveguides are widely used as the transducer in label-free optical biosensors. Although the most widespread planar waveguide-based detection system found in the market is the surface plasmon resonance (SPR), there are several techniques using dielectric planar waveguides in biosensing, including Optical Waveguide Lightmode Spectroscopy (OWLS) [1-3], Mach-Zehnder [4] and Young interferometers [5, 6]. The main advantage of planar dielectric waveguides over SPR devices for label-free detection lies in the enhanced degrees of freedom for sensor design. In both technologies, the penetration depth of the evanescent field of the guided waves at the sensor interface is directly related with the extent of the molecules to analyze, where the sensitivity is high. For SPR systems, this parameter is given by the material properties, with a typical penetration depth of around 200 nm [7]. Although long-range SPR is currently an emerging topic of research [8, 9], the technique is still at early stages of its development. In the case of planar dielectric waveguides, this property can be chosen by design, enhancing the application fields to the detection of relatively large objects in the micrometer range, such as cells [10]. Furthermore, the absence of a metal film can be an advantage, for instance when combining label-free with luminescence detection. Energy transfers to the metal film (quenching effect) make the combination of luminescence and SPR impractical, while dielectric waveguides are used successfully to enhance the sensitivity of fluorescent sensors [11]. Among all the different biochemical sensors based on dielectric waveguides, the grating couplers present a big advantage as they are suitable for building sensor arrays with a high number of different sensing regions present on the same chip. This facilitates the detection of several target molecule types simultaneously present in an analyte solution,

which is a key requirement for biosensors in all application fields. Also, grating coupler (GC) biosensors allow that two parameters: the thickness (d_A) and the refractive index (n_A) of the adsorbed layer can be simultaneously determined from the two measured parameters using the mode equations [12]. Without making any assumption, the absolute values for the surface adsorbed mass density can be directly calculated [13].

The use of waveguide gratings as integrated optical sensors started in the 80's when Lukosz and Tiefentaler reported their application as humidity and gas sensing [14]. In the sight of achieving a highly sensitive, fast, small and low cost device, Kunz developed the use of chirped gratings, replicated polymer substrates and the "wavelength-interrogated optical sensor" [15-18]. Grating couplers have been widely used to investigate a broad range of biological applications: protein-DNA interactions, lipid bilayers, environmental pollution, biomaterials and interactions with cells. GCs have been applied to study protein association and dissociation kinetics [19], to determine the optical anisotropy of phospholipids bilayers [20], to study membrane-protein solubilization and incorporation [21], contribution of forces to the binding of proteins to lipid layers [22], to investigate antigen-antibody interactions [23], for affinity-based pesticide sensing [24], to study the effect of oxygen plasma treatment of polyethylene on the protein adsorption kinetics [25], to investigate the stability of polyelectrolyte multilayers [26], to study the resistance to protein adsorption of poly (ethylene glycol) layers [27] and to monitor living animal cell adhesion and spreading [28].

The fabrication of a cheap, reliable, reproducible grating coupler waveguide sensor requires efficient manufacturing of two components: a low-loss optical waveguiding layer and a low-modulation, high-frequency grating. Good optical waveguiding films are usually made from metal oxides that have a high-optical refractive index in the visible range. The required thin and low-loss waveguiding layers need to be deposited on glass or plastic substrates with high reproducibility.

Although dielectrics are the classical material for waveguide fabrication, the natural length scales of polymer chains and their morphologies in the bulk, which lie in the nanometer domain, make polymers also ideal building blocks for nanotechnology [29]. There are a number of recent developments in the use of polymers for the fabrication of nanostructures via lithographic and self-assembling strategies, such as

nano-imprint lithography and soft lithography, that make the use of polymers in waveguides not only cheap but reliable. Dielectrics are very stable and high quality while polymers are easy to handle and low cost. Moreover the polymer is a biocompatible material and is also very well developed for biosensing applications. A highly effective method has been used to fabricate waveguides at low cost, overcoming this drawback presented by evaporators and sputtering systems. The so call sol-gel technique [30] produces uniform and smooth solid layers from metal alkoxides or colloidal solutions after a heat treatment.

Usual methods to fabricate the high sensitive, high-periodicity grating are conventional photolithographic, holographic and laser ablation techniques, but they are quite costly. Instead, a polymer waveguide will allow the fabrication of a refractive grating on the film layer by embossing techniques, saving time, money and resources on the fabrication process [31]. Commercially available grating-coupler waveguide sensors have been made from SiO_2, Ta_2O_5 and SiO_2/TiO_2.

Grating couplers allow adapting the sensor chip surface chemistry to the particular needs of an application, by coating the sensor with a thin transparent film presenting low optical loss. For this purpose, the coating layer should be thin enough not to alter the optical parameters of the grating coupler sensor significantly, but thick enough to cover the sensor completely. Metal oxides coatings are common (SiO_2, TiO_2, Ta_2O_5, ZrO_2, Nb_2O_5.) [32], but even electrically conductive transparent oxide layers can be applied as coatings on the grating coupler sensor chip.

This chapter aims to design and, in section 2, fabricate different grating coupler sensor chips through different approaches. We have investigated in section 3 the replication of optical gratings in spun polymer substrates, to achieve new low cost sensors. We have also studied in section 4, the coating of commercial sensors with different sputtered and evaporated materials, to allow quick quantitative studies of the adsorption of biomolecules onto their surfaces, to be used in calibration of other techniques.

2 THEORETICAL BACKGROUND

2.1 PLANAR WAVEGUIDE THEORY

In order to understand the behaviour of a planar waveguide as the transducer in optical biosensors, it is necessary to understand the guiding properties of waveguides quantitatively. In this section is presented a detailed electromagnetic analysis of a planar asymmetric waveguide [33] for which the refractive indices of the materials on the top and bottom of the film are assumed to be different. In this case, the waveguide (figure 2.1) can be characterized by a refractive index variation of the form:

$$n(x) = \begin{cases} n_C; & x > 0, \ \text{cover} \\ n_F; & -d < x < 0, \ \text{film} \\ n_S; & x < -d, \ \text{substrate} \end{cases} \tag{2.1}$$

The above refractive index variation corresponds to a thin film of refractive index n_f and thickness d deposited on a transparent substrate of refractive index ns ($n_S < n_F$). The region above the film is referred to as the cover and has a refractive index n_C (which is also less than n_F).

We will assume without any loss of generality that $n_F > n_S \geq n_C$. Light guidance in such planar waveguides can easily be understood on the basis of total internal reflection (TIR). Consider a light wave incident on the film-cover interface subtending an angle θ with the normal to the interface (see Fig.2.3) For small values of θ which are less than the critical angle for TIR between the film and the cover, i.e., for $\theta < \theta_C$ where $\theta_C = \sin^{-1}(n_C/n_F)$, only a part of the energy is reflected, the remaining portion is transmitted. Since we have assumed $n_C < n_S$, the reflected portion is incident on the film-substrate interface at an angle less than the corresponding critical angle $\theta_S = \sin^{-1}(n_S/n_F)$, and again the wave undergoes only a partial reflection at the film-substrate boundary. Thus the wave is not guided in the film but loses its energy to the substrate and cover; these correspond to what are referred to as *cover modes*. If we start increasing θ, we will reach a condition when θ will be just greater than θ_C but still less than θ_s. For such a case the wave is total internal reflected at the film-cover boundary but is transmitted at the film-substrate interface; these correspond to what are known as *substrate modes*. Both cover and substrate modes belong to a class of modes referred to

as *radiation modes*, which refer to the fact that the waves associated with these modes are not guided in the film. On further increase of θ when θ>θ$_S$, the light wave is total internal reflected at both the film-cover and film-substrate interfaces (Fig. 2.3) and the wave is said to be guided in the film. Such a wave corresponds to what is known as a *guided mode*. Thus:

$$\theta > \theta_S = \sin^{-1}[\max(n_C, n_S)/n_F] \Leftrightarrow \text{guided modes} \qquad (2.2)$$
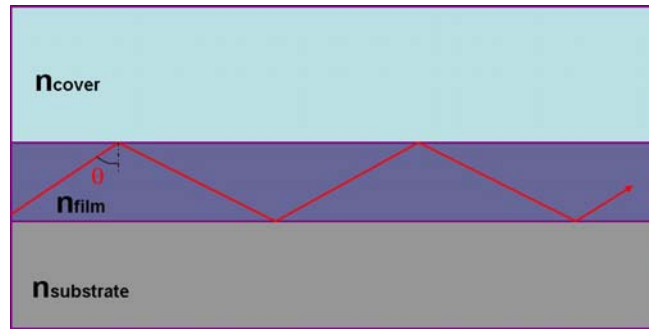
Fig. 2.3.- A ray incident on the film-substrate interface at an angle θ bigger than the critical angle between the film and the cover (θ > θ$_C$) undergoes TIR. The ray is also incident on the film-substrate interface at an angle greater than the critical angle θ$_S$, then the ray undergoes TIR at both the film-substrate and film-cover boundaries. Such rays correspond to the guided modes of the waveguide.

As in a planar waveguide the refractive index depends only on the x-coordinate, the electric and magnetic fields associated with a propagating electromagnetic wave can be written in the form [33]:

$$E_j = E_j(x)e^{i(\omega t - \beta z)}; \ j = x, y, z \qquad (2.3)$$

$$H_j = H_j(x)e^{i(\omega t - \beta z)}; \ j = x, y, z \qquad (2.4)$$

where ω represents the angular frequency of the wave and β is known as the propagation constant. Corresponding to a specific value of β, there is a specific field distribution described by E(x) and H(x) and for these specific distributions, the nature of the distributions remains unchanged with propagation along the guide; such distributions are referred to as *modes* of the waveguide. A study of the propagation characteristics and the corresponding field distributions of these modes is of primary importance in the design of efficient integrated optic devices.

The Maxwell's equations for an isotropic, linear, non-conducting and non-magnetic medium take the form:

$$\nabla x E = -\partial B / \partial t = -\mu_0 \partial H / \partial t \tag{2.5}$$

$$\nabla x H = -\partial D / \partial t = \varepsilon_0 n^2 \partial E / \partial t \tag{2.6}$$

$$\nabla \cdot D = 0 \tag{2.7}$$

$$\nabla \cdot B = 0 \tag{2.8}$$

where we have used the constitutive relations:

$$B = \mu_0 H \tag{2.9}$$

$$D = \varepsilon E = \varepsilon_0 n^2 E \tag{2.10}$$

in which E, D, B and H represent the electric field, electric displacement, magnetic induction and magnetic intensity respectively, $\mu_0 = 4\pi \cdot 10^{-7} Ns^2/C^2$ represents the free space magnetic permeability and $\varepsilon = \varepsilon_0 K = \varepsilon_0 n^2$ represents the dielectric permittivity of the medium, $K(x) = n^2(x)$, and n are respectively the dielectric constant and the refractive index and $\varepsilon_0 = 8.854 \cdot 10^{-12} C^2/Nm^2$ is the permittivity of free space.

If we substitute the above forms of the electric and magnetic fields in Maxwell's equations (2.5 and 2.6), it can easily be shown that the different components of the electric and magnetic fields are related through the following equations:

$$H_x = -\frac{\beta}{\omega\mu_0} E_y \tag{2.11}$$

$$H_z = \frac{i}{\omega\mu_0} \frac{\partial E_y}{\partial x} \qquad \text{TE modes} \tag{2.12}$$

$$-i\beta H_x - \frac{\partial H_z}{\partial x} = i\omega\varepsilon_0 K(x) E_y \tag{2.13}$$

$$E_x = \frac{\beta}{\omega \varepsilon_0 K(x)} H_y \qquad (2.14)$$

$$E_z = \frac{1}{i\omega \varepsilon_0 K(x)} \frac{\partial H_y}{\partial x} \left.\begin{array}{c} \\ \\ \\ \\ \end{array}\right\} \text{TM modes} \qquad (2.15)$$

$$i\beta E_x + \frac{\partial E_z}{\partial x} = i\omega \mu_0 H_y \qquad (2.16)$$

As it can be seen, the first three equations involve only E_y, H_x and H_z and the last three equations involve only E_x, E_z and H_y. Thus for such a waveguide configuration, Maxwell's equations reduce to two independent set of equations. The first set corresponds to what are known as transverse electric (TE) modes because the electric field has only a transversal component. The second set corresponds to what are known as transverse magnetic (TM) modes because the magnetic field now has only a transverse component. The propagation waves in such planar waveguides may thus be described in term of TE and TM modes.

First we consider TE modes: we substitute H_x and H_z from Eqs. (2.11) and (2.12) in Eq. (2.13) to obtain:

$$\frac{d^2 E_y}{dx^2} + \left[k_0^2 n^2(x) - \beta^2 \right] E_y(x) = 0 \qquad (2.17)$$

where

$$k_0 = \omega(\varepsilon_0 \mu_0)^{1/2} = \omega / c \qquad (2.18)$$

is the free space wave number and c is the speed of light in free space.

We will now carry out a modal analysis of waveguides characterized by Eq. (2.1) and highlight some interesting features associated with them. We discuss first TE modes and then TM modes. For TE modes, E_y satisfies the equation (2.17), thus the field component E_y satisfies the following equations in the three media:

$$\frac{d^2 E_y}{dx^2} - \gamma_C^2 E_y = 0; \ x > 0, \ \text{cover} \qquad (2.19a)$$

$$\frac{d^2 E_y}{dx^2} + \kappa_F^2 E_y = 0; \ 0 > x > -d, \ \text{film} \qquad (2.19b)$$

$$\frac{d^2 E_y}{dx^2} - \gamma_S^2 E_y = 0; \; x < -d, \text{ substrate} \qquad (2.19c)$$

where

$$\gamma_C^2 = \beta^2 - k_0^2 n_C^2 \qquad (2.20)$$
$$\kappa_F^2 = k_0^2 n_F^2 - \beta^2 \qquad (2.21)$$
$$\gamma_S^2 = \beta^2 - k_0^2 n_S^2 \qquad (2.22)$$

For guided modes, we require that the field should decay in the cover and substrate so that most of the energy associated with the mode lies inside the film. Thus, for guided modes γ_C^2 and γ_S^2 must be positive, so that Eqs. (2.19a) and (2.19c) may yield exponentially decaying solutions rather than oscillatory solutions. Thus for guided modes (since $n_S \geq n_C$)

$$k_0^2 n_S^2 < \beta^2$$

Also, since the fields have to be oscillatory inside the film, κ_F^2 must be positive and hence from Eq. (2.21) we get

$$\beta^2 < k_0^2 n_F^2$$

Hence for guided modes:

$$k_0^2 n_S^2 < \beta^2 < k_0^2 n_F^2 \qquad (2.23)$$

and we obtain for the solution of the scalar wave equation in the three regions:

$$E_y = \begin{cases} A e^{-\gamma_C x}; & x > 0 \\ B e^{i\kappa_F x} + C e^{-i\kappa_F x}; & 0 > x > -d \\ D e^{\gamma_S x}; & x < -d \end{cases} \qquad (2.24)$$

where A, B, C and D are constants. To determine them, we use the boundary conditions, namely the continuity of E_y and dE_y/dx at x=0 and x=-d to obtain:

$$A = B + C \qquad (2.25)$$
$$B e^{-i\kappa_F d} + C e^{i\kappa_F d} = D e^{-\gamma_S d} \qquad (2.26)$$
$$-\gamma_C A = i\kappa_F B - i\kappa_F C \qquad (2.27)$$
$$i\kappa_F B e^{-i\kappa_F d} - i\kappa_F C e^{i\kappa_F d} = \gamma_S D e^{-\gamma_S d} \qquad (2.28)$$

Eliminating A from Eqs. (2.25) and (2.27) we get

$$(\gamma_C + i\kappa_F) B + (\gamma_C - i\kappa_F) C = 0 \qquad (2.29)$$

Similarly eliminating D from Eqs. (2.26) and (2.28) we obtain

$$\left(\gamma_S - i\kappa_F\right)Be^{-i\kappa_F d} + \left(\gamma_S + i\kappa_F\right)Ce^{i\kappa_F d} = 0 \tag{2.30}$$

From Eqs. (2.29) and (2.30) we get

$$\tan \kappa_F d = \frac{\dfrac{\gamma_C}{\kappa_F} + \dfrac{\gamma_S}{\kappa_F}}{1 - \left(\dfrac{\gamma_C}{\kappa_F}\right)\left(\dfrac{\gamma_S}{\kappa_F}\right)} \qquad \text{TE modes} \tag{2.31}$$

which represents the transcendental equation determining the propagation constant, β, of the TE mode. Eq (2.31) can be written in the following convenient form:

$$\tan\left[V\left(1-b\right)^{1/2}\right] = \frac{\left(\dfrac{b}{1-b}\right)^{1/2} + \left(\dfrac{b+a}{1-b}\right)^{1/2}}{1 - \dfrac{\left[b\left(b+a\right)\right]^{1/2}}{\left(1-b\right)}} \qquad \text{TE modes} \tag{2.32}$$

where

$$\left.\begin{array}{l} b = \dfrac{\dfrac{\beta^2}{k_0^2} - n_S^2}{n_F^2 - n_S^2} = \dfrac{N_{eff}^2 - n_S^2}{n_F^2 - n_S^2}; \quad N_{eff} = \dfrac{\beta}{k_0} \\[4mm] V = k_0 d\left(n_F^2 - n_S^2\right)^{1/2}; \quad a = \dfrac{n_S^2 - n_C^2}{n_F^2 - n_S^2} \end{array}\right\} \tag{2.33}$$

The parameters b, V and a are known as the normalized propagation constant, the normalized waveguide parameter and the asymmetry parameter respectively; N_{eff} is called the effective index of the mode. Observe that since for guided modes $\max\left(n_C, n_S\right) < N_{eff} < n_F$, b lies between 0 and 1. The asymmetry parameter a may vary from zero (for symmetric waveguides, $n_S = n_C$) to very large values for highly asymmetric waveguides (with $n_S \neq n_C$ and $n_S \rightarrow n_F$).

Using Eqs. (2.29) and (2.30) we obtain the following expression for the field pattern:

$$E_y = \begin{cases} A e^{-\gamma_C x}; & x \geq 0 \\ A\left[\cos \kappa_F x - \left(\gamma_C / \kappa_F\right) \sin \kappa_F x\right]; & 0 \geq x \geq -d \\ A\left[\cos \kappa_F x + \left(\gamma_C / \kappa_F\right) \sin \kappa_F x\right] e^{\gamma_S(x+d)}; & x \leq -d \end{cases} \qquad (2.34)$$

In a similar manner we can obtain the transcendental equation which determines the propagation constant for TM modes. The procedure is similar to the one used for TE modes. The final result is:

$$\tan\left[V\left(1-b\right)^{\frac{1}{2}}\right] = \dfrac{\dfrac{1}{\gamma_1}\left(\dfrac{b}{1-b}\right)^{\frac{1}{2}} + \dfrac{1}{\gamma_2}\left(\dfrac{b+a}{1-b}\right)^{\frac{1}{2}}}{1 - \dfrac{1}{\gamma_1 \gamma_2}\dfrac{\left[b\left(b+a\right)\right]^{\frac{1}{2}}}{\left(1-b\right)}} \qquad \text{TM modes} \qquad (2.35)$$

where

$$\gamma_1 = \left(n_S / n_F\right)^2, \qquad \gamma_2 = \left(n_C / n_F\right)^2 = \gamma_1 - a\left(1-\gamma_1\right) \qquad (2.36)$$

The corresponding field pattern is given by:

$$H_y = \begin{cases} A e^{-\gamma_C x}; & x \geq 0 \\ A\left[\cos \kappa_F x - \dfrac{n_F^2}{n_C^2}\dfrac{\gamma_C}{\kappa_F}\sin \kappa_F x\right]; & 0 \geq x \geq -d \\ A\left[\cos \kappa_F x + \dfrac{n_F^2}{n_C^2}\dfrac{\gamma_C}{\kappa_F}\sin \kappa_F x\right] e^{\gamma_S(x+d)}; & x \leq -d \end{cases} \qquad (2.37)$$

Depending on the fabrication parameters of the waveguide, only a definite number of guided modes may propagate. The mode number m corresponds to the number of times the field crosses the axis, as can be seen in figure 2.4. It is also important that higher order modes penetrate deeper into the substrate and cover than lower order modes.
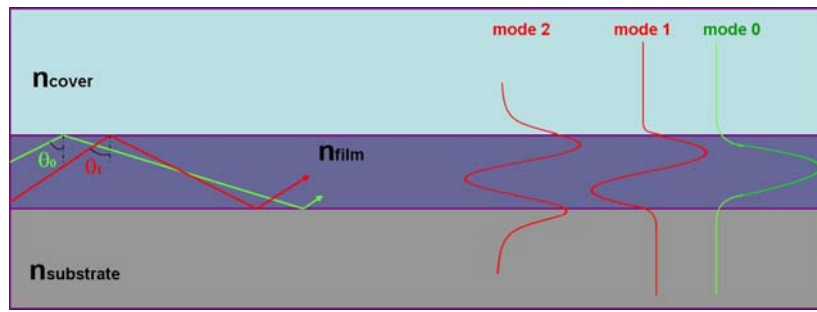
Fig. 2.4.- Schematic of the field distribution of the TE modes corresponding to m=0, 1 and 2 in a planar waveguide.

The cut-off condition where the modes are not anymore guided, but radiated is given by:

$$\beta/k_0 = n_s \implies b = 0 \tag{2.38}$$

If we substitute this expression in Eqs. (2.32) and (2.35), we will get the following expressions for the cut-off frequencies:

$$V_c^{TE} = \tan^{-1} a^{1/2} + m\pi \qquad \text{TE modes} \tag{2.39}$$

$$V_c^{TM} = \tan^{-1}\left(a^{1/2}/\gamma_2 \right) + m\pi \qquad \text{TM modes} \tag{2.40}$$

The cut-off frequencies of TM modes are greater than the corresponding cut-off frequencies of TE modes. Considering the fundamental mode (m=0), we will only have the TE mode and the waveguide is usually referred to as absolutely single polarization single moded. Anyway, in most practical single mode waveguides, there is one TE mode and one TM mode; however the incident field is usually linearly polarized at 45º in order to excite both the TE and the TM modes at the same time.

2.2 LIGHT COUPLING

To build an integrated waveguide sensor, it is necessary to incorporate an element to couple the light beam into the waveguide. There are different methods that allow the light coupling: butt coupling, prism coupling and grating coupling.

Butt coupling (or lateral coupling) is the simplest solution, mostly used to couple light into an optical fiber if the source size equals the fiber core size. If the source size is different from the fiber size, a lens system designed with the appropriate magnification can change the image of the source so that its size matches the size of the fiber, but this method can produce serious loses. Due to the additional optical components and rigorous alignment needed, this technique is only used basically in the laboratory.

Prism coupling is widely used with the aim of coupling the light into a waveguide. For a particular angle, total internal reflection is produced at the prism base, creating an evanescent wave on the other side. If the prism is tightly pressed against the waveguide, the evanescent wave can travel through the air gap exciting a guided mode into the waveguide. Since the pressure point is very small, when the light beam travels back to the waveguide-prism interface, the air gap is big again and the light remains trapped.

In the grating couplers a diffractive grating is patterned on the sensor surface forming a series of periodic fine corrugations etched into the waveguide surface. Under some constructive interferences in the diffracted mode by the grating and the film-substrate interface, the light is coupled into the waveguide. The area of the grating must be carefully controlled to avoid the light to be uncoupled.
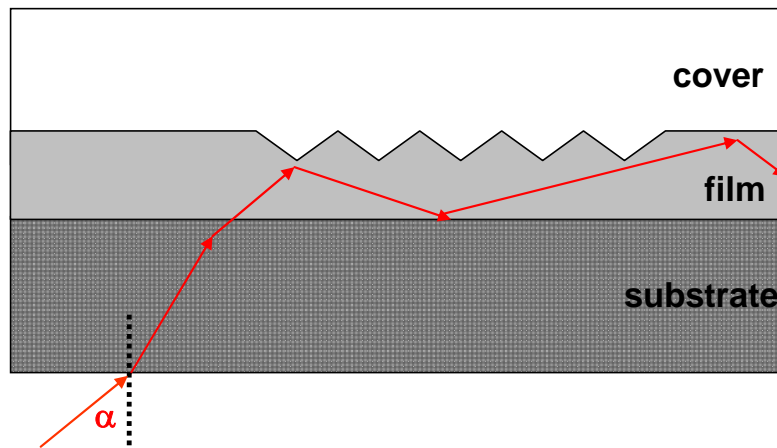

Fig. 2.5.- Input grating coupler scheme.

As shown in Fig. 2.5, the grating facilitates the direct input of the laser light at an angle that excites a guided mode, following the next equation:

$$N_{eff} = n_C \sin \alpha + m \frac{\lambda}{\Lambda}$$ (2.41)

where N_{eff} is the guided mode effective index, α the incoupling angle, m the diffractive order and Λ the grating period. The change produced in the coupled angle as a consequence of the sensing reaction onto the grating can be measured.

Among these three methods, the latter alone does not require additional optical components, but only correct alignment of the laser onto the diffractive grating. Therefore, we will use this approach in our setup. The grating coupling method allows the integration of the coupling element into the waveguide, providing a very easy plug-and-play configuration of the biosensor, once the grating is fabricated.

3 POLYMER-BASED GRATING COUPLER BIOSENSOR DESIGN

In this section, the replication of optical gratings in polymer substrates will be studied to achieve new low cost sensors. For the design and analysis of waveguide-grating devices, efficient modelling tools are required. Analytical approximations are sufficient for many practical questions, such as resonance peak position, sensitivity or temperature drift (see chapter 3). Other tasks, such as the determination of fabrication tolerances require more detailed modelling techniques. As an example, it has been observed [34] that extremely small non-uniformities due to fabrication errors can significantly distort the signal shapes, a phenomenon which cannot be predicted with the above mentioned approximations. More sophisticated numerical methods are required for explaining these phenomena and for adjusting fabrication parameters.

3.1 *WAVEGUIDE SENSITIVITY*

The main parameter to take into account when designing a waveguide based biosensor is its sensitivity, defined as the capacity to detect variations of the refractive index of the cover media. Through the equation 2.41, N_{eff} is related with the coupling angle. When an adlayer of biomolecules forms onto the sensor surface, the sensitivity is defined by the dependence of the effective refractive index on the refractive index of the cover media, n_C, and on the refractive index and the thickness of the adlayer (n_A, d_A):

$$dN_{eff} = \frac{\partial N_{eff}}{\partial n_C} dn_C + \frac{\partial N_{eff}}{\partial n_A} dn_A + \frac{\partial N_{eff}}{\partial d_A} dd_A \tag{2.42}$$

For a particular case where the adlayer is only formed by one substance, we can assume that the refractive index of the adlayer is constant and that the sensitivity only depends on the cover media and the thickness of the adlayer:

$$dN_{eff} = \frac{\partial N_{eff}}{\partial n_C} dn_C + \frac{\partial N_{eff}}{\partial d_A} dd_A \qquad (2.43)$$

The sensitivity of the waveguide can be tuned by changing the fabrication parameters. To estimate the sensitivity, we calculate the effective refractive indexes for small changes in the refractive index (dimensionless) of the cover solution and in the adlayer thickness (in RIU/nm). For this particular case, we chose a glass substrate ($n_S = 1.47$). If we plot the sensitivity against the thickness of the waveguide film for different film materials, Fig. 2.6, we will clearly see that for a monomode waveguide, the bigger the contrast between the refractive indexes of substrate and film, the better the sensitivity.
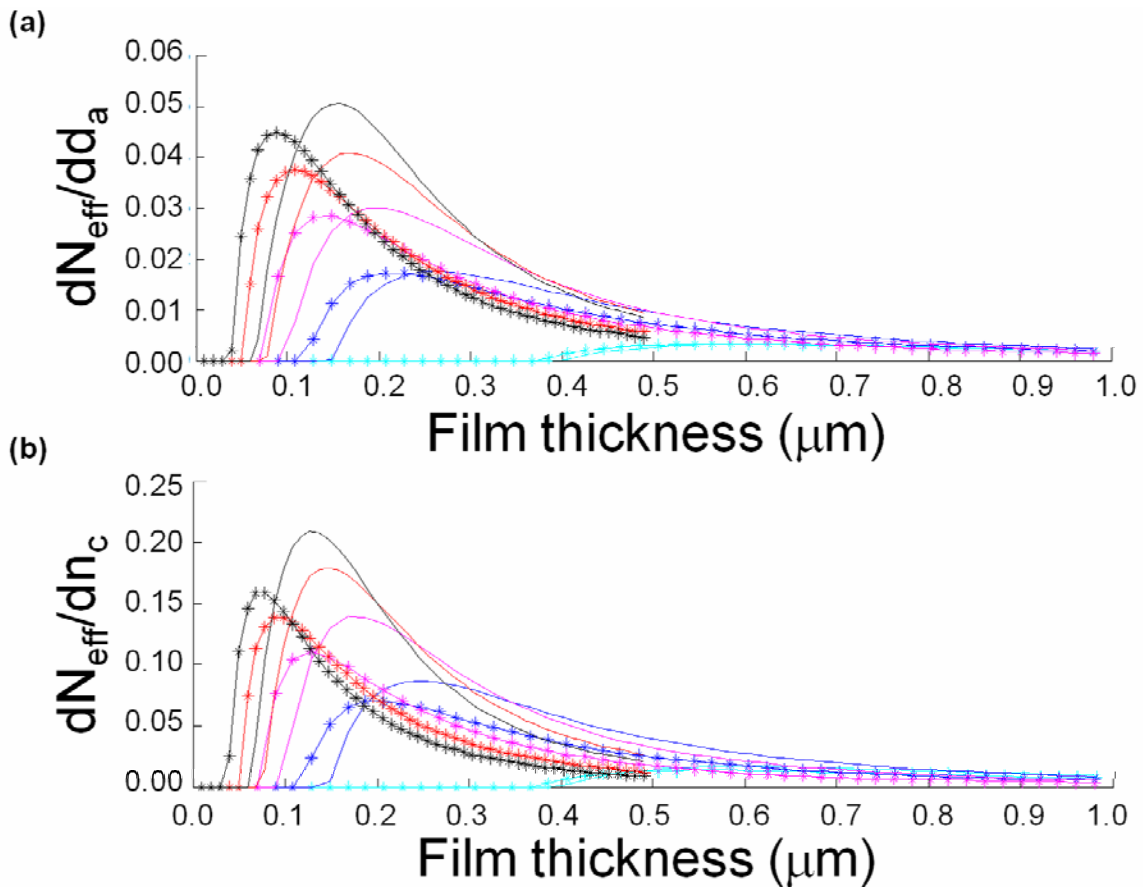

Fig. 2.6.- Sensitivity for TE (-*-) and TM (---) modes a) to the thickness of the adsorbed layer, b) to the refractive index of the cover media, for different waveguide materials with refractive indexes: 1.9 (black), 1.8 (red), 1.7 (pink), 1.6 (blue) and 1.5 (cyan).

Therefore, choosing the appropriate materials for the waveguide is an important step in the design. Silicon nitride, with a refractive index of 2 is a good choice for a waveguide film.

3.1.1 Polymer over glass

Polymethylmetacrilate (PMMA) is a thermoplastic transparent polymer. Its low glass transition temperature at Tg = 105 ºC, make it a great candidate for imprinting techniques [35]. These characteristics allow a thin layer of PMMA to be used as the film in an optical waveguide, where the grating is patterned by replica-molding techniques. However the PMMA refractive index, 1.492, is quite low compare to that of glass, 1.453, making waveguides based on PMMA over glass not very sensitive.

In the figure 2.7, a zoom in from figure 2.6 is presented, for the particular case of the sensitivity of a PMMA film over PYREX vs. PMMA thickness. The simulations were performed using the classical transfer-matrix method to solve a 4 layer structure [36].
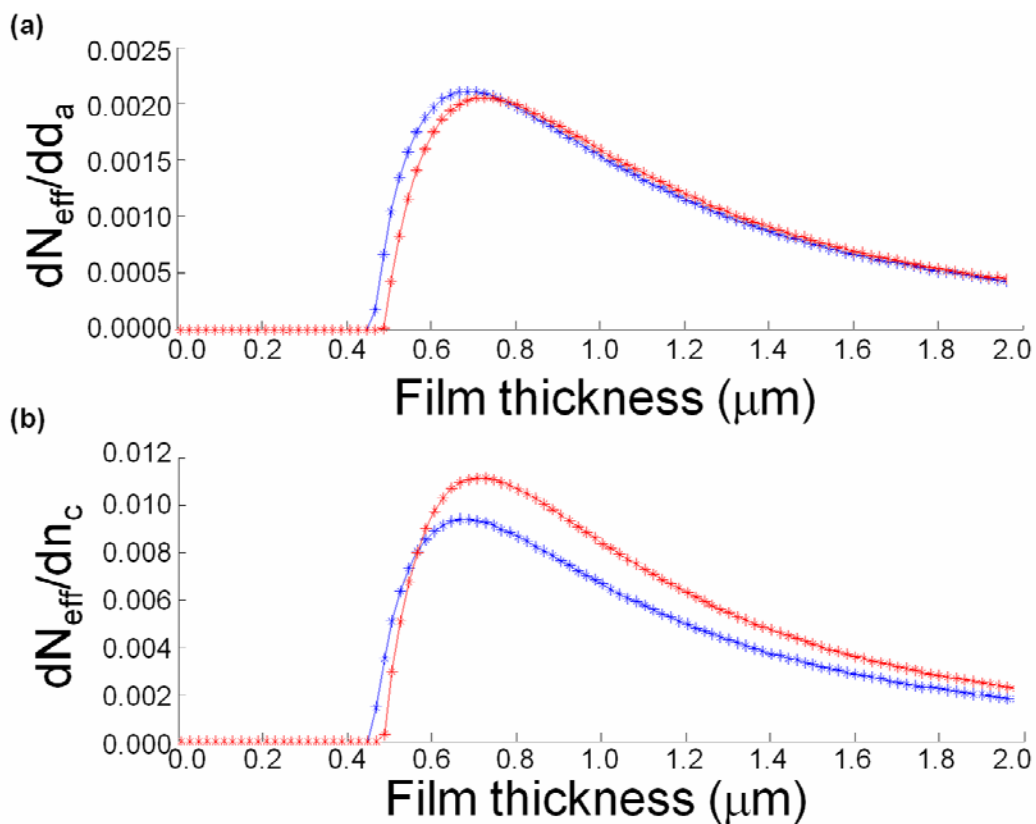

Fig. 2.7.- PMMA waveguide sensitivity for TE (blue) and TM (red) coupled modes: Variation of the effective refractive index sensitivity with the a) thickness of the adsorbed layer and b) the cover refractive index, vs. film thickness.

From the simulation, we see that to build a PMMA waveguide propagating the fundamental TE and TM modes, a minimum thickness of 500 nm is necessary. Moreover, if we fine-tune the thickness of the PMMA waveguide film and set it to 650 nm, we will get a sensor with the maximum sensitivity, but this is still very low compared to what we could get by using a film material with higher refractive index. Even though the poor sensitivity of the PMMA waveguide does not make it a good candidate as a sensor, it is still a good option for the grating embossing. Using the PMMA as a substrate on top of which another film with higher refractive index is deposited, would allow the easy grating embossing and at the same time guaranty a good sensitivity.

3.1.2 ITO over PMMA

There are several transparent dielectrics with high refractive index that could act as a waveguide film; but for label free biosensing, a combination of lightmode spectroscopy and electrochemical techniques offer higher sensitivity and versatility for the detection of biomolecules. Transparent Conducting Oxides are transparent thin films in the visible region of electromagnetic spectrum (>80%) and conductors of electrical current ($<10^{-3}\Omega$cm), therefore making an interesting alternative to the metallic transparent thin films, because of their high transparency and good conductivity. The most widely used transparent conducting coating is Indium Tin Oxide (ITO) [37]. With a high refractive index of 1.94, the attractiveness of ITO relies on its low sheet resistance and high optical transmittance in the visible region. However this properties are very hard to attain because are strongly dependent of the growth conditions such as oxygen partial pressure, bias voltage and substrate temperature.

In the present work, the waveguide will consist of a SnO_2 doped In_2O_3 (ITO – Indium Tin Oxide) thin film deposited by DC reactive magnetron sputtering.

A simulation showing the sensitivity of an ITO waveguide over PMMA to the thickness of the adlayer against the film thickness is presented at figure 2.8. In this case we have chosen a constant value for the refractive index of the cover of 1.33.
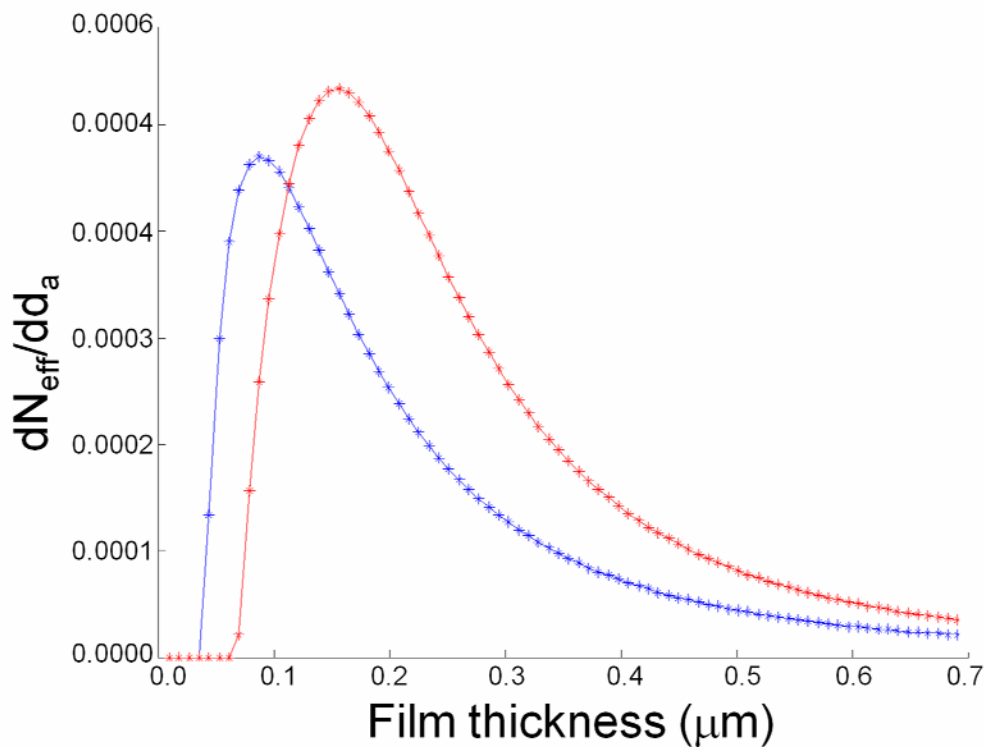
Fig. 2.8.- The figure shows the sensitivity of the effective refractive index to the thickness of the adsorbed layer, in front of the film thickness for a ITO waveguide onto PMMA for TE (blue) and TM (red) coupled modes.

3.2 WAVEGUIDE FABRICATION PARAMETERS

To design a waveguide there are some parameters to adjust, such as thickness and refractive index of the different layers. In this case, it is described the design for a three-layer configuration. The cover and the substrate thickness should be infinite in comparison with the film thickness and the refractive index of the film should be bigger that the other two. Moreover, to fabricate a monomode waveguide, it is necessary to reach a compromise between the film thickness and the contrast between indexes.

3.2.1 Film thickness

To find out the optimal film thickness to build a monomode waveguide we need to look at the film thickness that brings better sensitivity to the structure. Looking at the figure 2.8, the optimal ITO thickness should be between 120 to 200 nm. It is also important to ensure that, at the chosen film thickness the waveguide is monomode. To do so, we will use the three layer waveguide composed by water, ITO and PMMA and

we will calculate the thickness at which the fundamental and first TE and TM modes apperar using equations 2.33, 2.39 and 2.40. As already shown in figure 2.8, the fundamental TE mode will be excited when the film thickness is 40.5 nm, and the fundamental TM mode, when it is 69.8 nm. The first TE mode will not appear when the film thickness is thinner than 295.7 nm. In this way we can be sure that a waveguide constructed with 120 nm of ITO over PMMA will be sensitive and monomode.

3.2.2 Grating geometry

Also the parameters of the grating play a very important role on the sensor sensitivity. The geometry of the gratings, duty cycle and depth, and their influence on the sensitivity have been widely studied at [38]. For low duty cycles or high etching depths the grating has more of its volume occupied by the external fluid, so the mean index is closer to this one, and while sensitivity decays the field penetration depth grows. For a good incoupling of the light into the waveguide the duty cycle should be 50% with a depth of about 20nm.

4 THIN FILM COATED GRATING COUPLER BIOSENSORS

In order to adapt the sensor chip to the requirements of specific applications, thin coatings can be made onto waveguides with different transparent materials without affecting their sensitivity and allowing simulating the surface properties of the material of interest [39, 40]. The coating of commercial silicon-titanium oxide sensors with different materials will allow quick quantitative studies of the adsorption of biomolecules onto their surfaces, to be used in calibration of other techniques.

Being silicon nitride one of the most widely used insulators in Field Effect Transistors [41] and broadly exploited in optical waveguides due to its high refractive index [42, 43], it is of great interest to provide a technology that will allow quantifying the adsorption of biomolecules onto the gate of nitride-based transistors. Also, among the different materials for the grating-coupled sensors, silicon nitride offers superior optical properties and a number of fabrication advantages such as the absence of undesirable impurities and the good control of the film composition and thickness,

which is especially important for ultrathin layers used in optical spectroscopy measurements.

Although silicon nitride-based immunosensors are widely reported [44-46], this is the first time that optical gratings are coated with a thin layer of silicon-nitride to allow quick quantitative studies of the absorption of biomolecules onto its surface, to be used in calibration of other techniques, such as Field Effect Transistor based biosensor.

A major challenge is the represented by gold, as the ultimate sensor material. We propose creating an extremely thin gold coating onto silicon-titanium oxide waveguides to be able to monitor the adsorption of biomolecules onto gold, as a universal calibration for other techniques.

5 EXPERIMENTAL

5.1 MATERIALS AND REAGENTS

PMMA 11% was purchased from Microchem (Germany). Sodium cyanoborohydride, Triethanolamine, Glycine and HSA (Albumin solution from human serum 30% in 0.85% sodium chloride) were purchased from Sigma-Aldrich (USA). The triethoxysilane aldehyde (TEA), which was obtained from United Chemical Technologies (USA), was stored in the dark, under argon and at room temperature. Alpha-Methoxy-omega-amino poly (ethylene glycol) (PEG-NH$_2$ MW 750 Dalton) was purchased from IRIS Biotech (Germany). Anti-HSA rabbit monoclonal antibodies (IgG) having a molecular weight of about 150 kDa were purchased from AntibodyBcn (Spain). Antibodies were prepared in phosphate buffer saline solution (0.01 M phosphate buffer, 0.0027 M potassium chloride and 0.137 M sodium chloride, PH 7.4). Sodium hydroxide was purchased from Sigma-Aldrich (USA), Hydrochloric acid was purchased from Merck (Germany).

5.2 GRATING SUBSTRATES

Silicon-titanium oxide grating substrates (depth 20 nm, period 2400 lines/mm) were supplied by MicroVacuum Ltd (Budapest, Hungary) and consist on a 170 nm thick

silicon-titanium oxide layer (n_F = 1.77) onto a glass substrate (n_S= 1.53). The optical grating coupler (see figure 2.9) is prepared by the SOL-GEL method [30]. The grating area dimensions were 2 mm in width per 12 mm in length on a total chip size of 12 mm in length, 8 mm in width and 0.5 mm thick. Previously to be coated, the gratings were thoroughly cleaned with organic solvents and Milli-Q water.
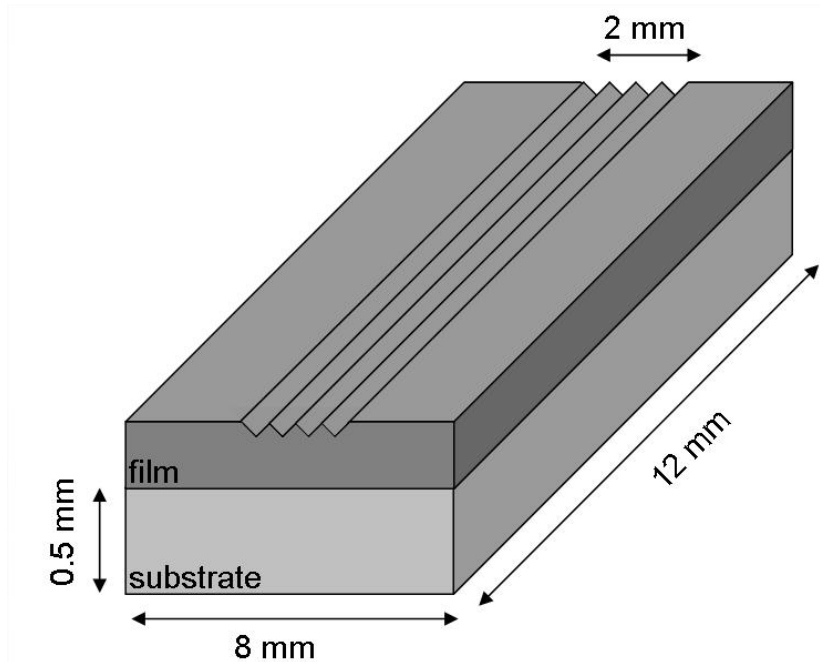
Fig. 2.9.- Commercial optical waveguide featuring a diffractive grating patterned in its surface (Microvacuum, Budapest, Hungary).

5.3 OWLS MEASURING PRINCIPLE

The structure and measuring principle of the optical grating coupler sensor chip are depicted in Fig. 2.5. A He-Ne laser (λ = 632.8 nm) is diffracted by the grating and, at a characteristic incident angle (α), there is a constructive interference (phase shift of the internal reflection is zero) that excites a guided mode, then the light propagates through the waveguide via total internal reflection and an evanescent field is generated onto the covering medium. The change in the refraction index of the covering layer produced by the analyte recognition can be monitored on line by measuring the changes in the incoupling angle [47-49]. In this case, a commercial OWLS instrument from MicroVacuum Ltd. (Budapest, Hungary) was used. This system software measures the effective refractive index on the zero transverse electric and magnetic modes and

converts them to adsorbed layer mass and thickness by assuming an optical uniform layer and a refractive index varying linearly with mass density [12] upon using Feijter's Formula [13].

5.4 POLYMER GRATING IMPRINTING

To integrate the polymer waveguides in an optical biosensor is needed to replicate the grating onto the polymer surface, reducing the fabrication costs and therefore achieving the manufacturing of disposable one use chips.

A thick layer of 3 μm of PMMA is spin coated onto 500 μm fused silica substrates of 8 x 12 mm, used as support. After curing the sample at 180ºC for 60 seconds, it is ready for imprinting. As masters we used Si_3N_4 gratings fabricated with standard micro and nanoelectronic techniques (RIE and ebeam): 20 nm depth, 0.5 μm period and 50% duty cycle [38]. Before imprinting, the master was cleaned and silanized, reducing adhesion between the master and the polymer [50, 51]. Finally, the Nano Imprint Lithography (NIL) process is carried out in two steps: from the nitride master to a 125 μm thick poly(ethylene naphthalate) sheet (PEN, Goodfellow Ltd. Cambridge, UK), and from the PEN replica to the spun PMMA [52, 53], as presented in table 2.1.

Table 2.1   NIL parameters to print the grating on PMMA

Step	Si_3N_4 to PEN			PEN to PMMA		
	Temp (ºC)	Pressure (bar)	t (s)	Temp (ºC)	Pressure (bar)	t (s)
1	50	0	30	50	0	30
2	80	0	100	80	0	100
3	225	70	600	140	30	600
4	80	0	10	80	0	10
5	80	0		80	0	

5.5 THIN LAYER DEPOSITION AND CHARACTERIZATION

5.5.1 Indium Tin Oxide sputtering

Sputtering processes are normally carried out at high substrate temperatures (>200ºC) to allow good results in terms of transparency and conductivity. For this

particular application is required low deposition temperature to preserve the grating structure patterned in the polymer substrate. Indium tin oxide thin films were deposited on PMMA and glass substrates using DC reactive magnetron sputtering. Before deposition, the sputtering chamber was pumped down to $3.5 \cdot 10^{-5}$ mbar using a combinatory system of a rotary pump (Alcatel ANNECY Ty-2033, PS – 33 m^3/h) and a diffusion pump (Edwards Vapour Pump EO4, PS – 600 l/s), which work together to maintain high vacuum. To define the best deposition parameters, several sets of experiments were performed at different substrate temperatures (25, 80, 90 and 100 ºC) and at different oxygen content, achieving the best results when depositing at room temperature and 0.5sccm oxygen during 350 seconds with a deposition rate of 0.4 nm/s [54, 55].

5.5.2 Silicon Nitride sputtering

Silicon nitride thin films were deposited by r.f. magnetron sputtering (Edwards Coating System ESM100) onto the SOL-GEL gratings and also onto silicon wafer substrates (to help in the layer characterization process) [56]. Film deposition was carried out by sputtering of a pure Si_3N_4 target with an r.f. input power of 100 W. The cathode magnetron was 100 mm in diameter, the substrate was rotated in relation with the target and the substrate-target distance was kept at 5 cm. Before deposition, the chamber was evacuated to $1.5 \cdot 10^{-5}$ mbar and then, backfilled to a working pressure of $5.0 \cdot 10^{-3}$ mbar. Film thickness and refractive index of the film were determined by ellipsometry (monochrome He-Ne PLASMOS) on the substrates deposited on silicon. The optimal thickness selected for the silicon nitride coating is 10nm, in order to get a layer thick enough to be uniform and at the same time, thin enough to be transparent and to avoid changing significantly the effective refractive index of the waveguide [57]. For the film required thickness of 10 nm, the sputtering deposition time was established at 3 minutes.

Silicon nitride coated optical grating coupler sensor chips were characterized by X-Ray Photoemission spectroscopy (XPS) after their activation to be used in immunosensing. XPS spectra were recorded in a Perkin-206 Elmer PHI 5500 Multitechnique System from Physical Electronics (Waltham, MA, USA) with a

monochromatic X-ray source (Aluminum KR line of 1486.6 eV energy and 350 W), placed perpendicular to the analyzer axis and calibrated using the 3d5/2 210 line of Ag with a full width at half-maximum (FWHM) of 0.8 eV. The resolution selected for the spectra was 187.5 eV of pass energy and 0.8 eV/step. All measurements were taken in an ultra high vacuum (UHV) chamber pressure between $5 \cdot 10^{-9}$ and $5 \cdot 10^{-8}$ mbar. When necessary, a low energy electron flood gun (0-3 eV) was used to discharge the samples. Peak fitting was performed using MultiPak 220 V6.0A software from Physical Electronics Inc. (Chanhassen,MN, USA).

5.5.3 Gold Thermal Evaporation

Gold transparent thin films deposited on commercial chips where produced using thermal evaporation. The evaporation chamber was pumped down to 10^{-5} mbar before deposition by a combinatory system of two pumps: a rotary pump (Alcatel Pascal 2010D) and a diffusion pump (Genavac Oil Diffusion Pumd ODP150). A gold wire of 99.9999% purity was used as source material which was melted in a tungsten boat vessel. The deposition parameters were optimized to achieve a thin film transparent in the visible range and with high transmittance at 632.8 nm [54]. A summary of the optimized evaporation parameters is presented in table 2.2.

Table 2.2   Gold film evaporation parameters

Base pressure (mbar)	$4 \cdot 10^{-5}$
Current (mA)	190
Deposition time (s)	25-180
Gold wire diameter (mm)	0.5
Mass (g)	0.9
Vessel-substrate distance (mm)	50

5.6 ATOMIC FORCE MICROSCOPY SURFACE CHARACTERIZATION

Atomic Force Microscopy (AFM) was used to characterize the topography of the optical gratings before and after the silicon nitride deposition. The measurements were performed in a Dimension 3100 AFM instrument (Veeco Instruments, USA) equipped with a rectangular silicon AFM tip (MikroMasch NSC18/AlBS) with a spring constant

of 3.5 N/m, a radius of curvature about 10 nm and a resonance frequency around 75 kHz. The instrument was operated in Tapping mode, in air media and room temperature. The topographic images obtained were analyzed by using the free WSxM software (Nanotec Electrónica, Spain).

5.7 IMMUNOSENSING ANALYTICAL PROCEDURE

To test the capability of the new structures to work as an immunosensor, standard antibody-antigent detention experiments were performed. The pair anti-HSA/HSA was selected for this purpose, as a model. In order to functionalize the silicon nitride coated OWLS chips for the antibody immobilization, the procedure described by Caballero et al. was followed [58] (Fig. 2.10).
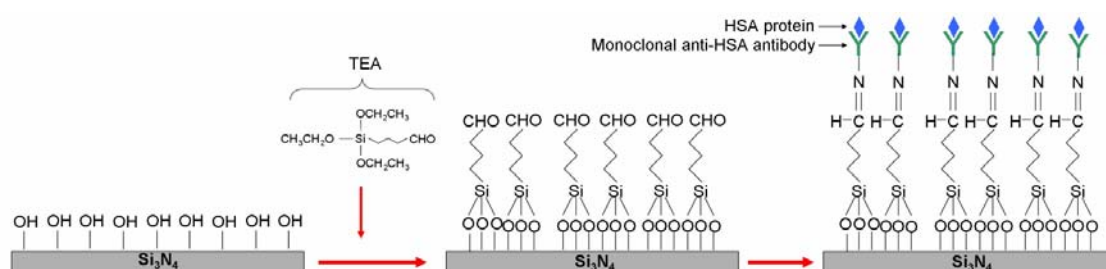

Fig.2.10.- Scheme of the silicon nitride surface functionalization of the direct immobilization of anti-HSA antibodies.

Briefly, after cleaning with organic solvents and Milli-Q water, the silicon nitride coated chip was immersed in Piranha solution (1:3 v/v H_2O_2:$H_2SO_{4;}$ *Caution: Piranha is an extremely strong oxidant and should be handled very carefully*) at 90 ºC for 30 min. Afterwards, sequential immersion in aqueous solutions of NaOH (0.5 M) for 20 min., HCl (0.1 M) for 10 min. and a final immersion in NaOH (0.5 M) solution for 10 min. were performed to activate the surface. The samples were then rinsed thoroughly with HCl and Milli-Q water and dried in an oven at 100 ºC for 20 min. Then, the chip was functionalized with triethoxysilane aldehyde (TEA) by the vapour-phase method for 1 hour and cured into the oven for 1 hour at 100 ºC. Afterwards, the samples were rinsed with absolute ethanol and dried under nitrogen. Once functionalized with the organosilane, the antibodies were immobilized on the chip surface by immersing it into a 10^{-7} M anti-HSA monoclonal antibody PBS solution

(0.01 M phosphate buffer, $2.7 \cdot 10^{-3}$ M potassium chloride and 0.137 M sodium chloride, pH 8.4), containing 4 mM sodium cyanoborohydride and allowed to react for 1 hour at 37ºC. Afterwards, it was thoroughly rinsed with PBS to remove antibody excess. Subsequently, the aldehyde free surface groups were blocked by a solution of ethanolamine (100 mM ethanolamine in 10 mM PBS, pH 8.4) in the presence of 4 mM cyanoborohydride for 1-2 hours at room temperature. Finally, the surface was thoroughly rinsed with PBS, pH 8.4. These antibodies will later recognize the HSA protein from the flowing solution.

The OWLS immunosensor system was operated in a continuous flow mode during sample measurement. For the sensing experiments, 500 μl of increasing concentrations (from 10^{-13} M to 10^{-3} M) of the HSA in PBS buffer were injected into the OWLS flow cell. The flow rate of the solution was kept at 30.4 μl/min and the on line sensor response was continuously collected as a surface mass change (ng/cm^2). After the injection of each analyte concentration, the system was kept in stop-flow mode to favour the analyte incubation for 30 min. Then, the sample was rinsed by flowing PBS solution for 20 min to eliminate unspecific HSA adsorption. The changes of the surface mass during the measurement cycles were automatically calculated by the software implemented in the measurement system through the experimental values of the incoupling angles of the zero transverse electric and magnetic modes.

6 RESULTS AND DISCUSSION

6.1 POLYMER BASED WAVEGUIDES

A low cost polymer based sensor chip is produced by patterning an optical grating on PMMA substrates and coating with a film layer of ITO.

6.1.1 Polymer layer fabrication and test

To test the refractive index and to optimize the fabrication parameters of the polymer layer, PMMA waveguides (n_F = 1.492 over PYREX, n_S = 1.47) of different thicknesses were fabricated. The prism coupling method will then allow us, upon measuring the incoupling angle of the laser into the waveguide, to calculate the

refractive index and the thickness of the PMMA layer. The film has to be thick enough to allow two propagation modes.

The PMMA is deposited by spin coating. The spin coating technique allows depositing uniform micrometer thick polymer layers. The polymer dissolution is dispensed over the substrate and, as it spins at high speed, it results in an even distribution of polymer on the surface from which any excess was eliminated [59]. Finally, the solvent is eliminated by warming the sample; this process is called soft-bake. The final polymer thickness depends on its viscosity and on the spin speed. Table 2.3 shows the estimated PMMA thickness versus the spin speed, according to the supplier. Finally, the sample is soft-baked at 180 ºC for 60 seconds

Table 2.3 Expected PMMA Thickness vs. Spin Speed

Spin Speed (rpm)	Film Thickness (μm)
1000	5
1500	3.7
2000	3
3500	2

To determine the thickness and the refractive index of a waveguide film, we have used the prism coupler technique described in Fig. 2.10. Both parameters are obtained simultaneously by measuring the coupling angles and fitting them with a theoretical dispersion curve [60]. Removing the air gap between the prism and the guide ensures that the evanescent field passes through the film, so it is necessary to press the film mechanically against the prism. For a determined angle Total Internal Reflection (TIR) is produced.

By measuring the coupling angles, θ_m, that verify the guide conditions, we can experimentally find the propagation constants following the next equation:

$$\tilde{N}_m = \frac{c}{\upsilon_m} = n_p \sin\theta_m \qquad (2.44)$$

where υ_m is the phase speed for the mode m (m=0,1,2...) and n_p is the refractive index of the prism. Since we can also calculate these constants with a theoretical-based method, we only need a computational program to iteratively fit both parameters,

refractive index (n) and film thickness (W), until the theoretical values fit to the experimental, $\bar{n}$ and $\bar{W}$.
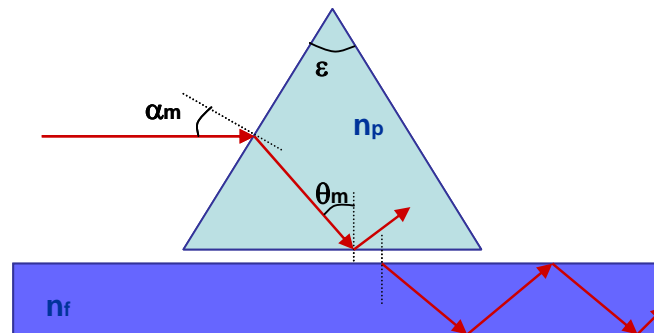

Fig. 2.10.- Prism coupler technique for inserting the light into the waveguide.

We have mounted the prism over a XY platform on a goniometer, with an arch minute resolution (Newport). We placed the sample in contact with the equilateral prism (SF11, n_p=1.779, Thorlabs) and upon pressing the two of them together appeared a dark spot that will be the coupling point. The He-Ne laser (λ=633nm) is polarized TE and focalized on the spot.

We have measured the PMMA samples and input them into our MATLAB program that gives us a numerical solution showed in Table 2.4. The program objective is to reduce the dispersion, $\sigma(n,w)$, in between the fitted, $N_m(n,w)$, and the experimental, $\tilde{N}_m$, values of the effective refractive index:

$$\sigma(n,w) = \sum_m \left[\tilde{N}_m - N_m(n,w) \right]^2 \qquad (2.45)$$

where n and w are the refractive index and the thickness of the waveguide film. The obtained results fit perfectly to the expected as we can see in the Fig. 2.11. So we can conclude that the film refractive index is n_F = 1.4886.

Table 2.4 PMMA Fit Results

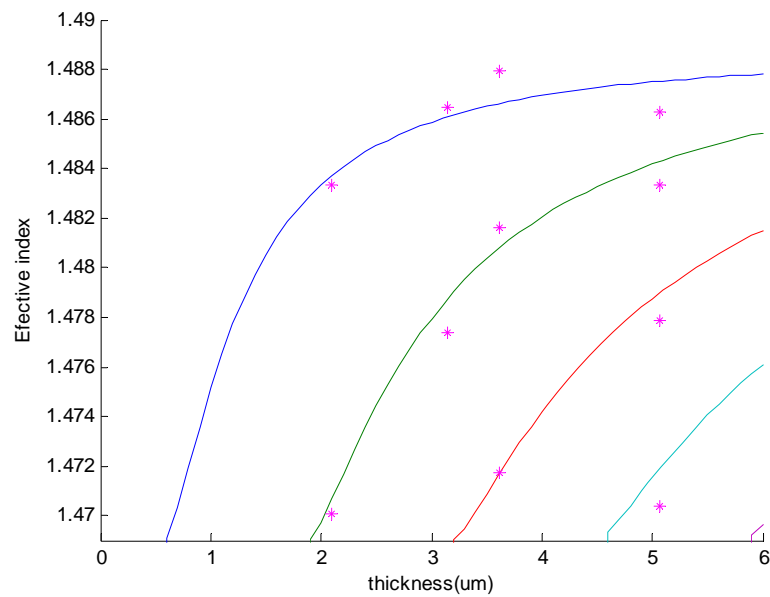| $W_{theoretical}$ (µm)	$\bar{n}$	$\bar{w}$ (µm)	$\sigma(n,W)$
5	1.4871	5.0687	$4.72 \cdot 10^{-7}$
3.7	1.4895	3.6187	$6.78 \cdot 10^{-7}$
3	1.4886	3.1392	$2.15 \cdot 10^{-5}$
2	1.4886	2.0967	$1.38 \cdot 10^{-5}$

Fig.2.11.- Theoretical refractive index curves and observed effective refractive index values for PMMA waveguides.

The refractive index of the waveguide film materials must be carefully controlled for adjusting to the different requirements of the different devices, in this case to provide single-mode high efficiency light transmission [28]. An attempt to fine tune the refractive index of PMMA was carried out changing the softbake treatment after spin coating. A change is expected because the molecular weight of the resist, M, increases after thermal treatment, as indicated by the Lorentz-Lorentz equation:

$$\frac{n^2 - 1}{n^2 + 2} = \frac{N}{3M\varepsilon} \rho\beta \qquad (2.46)$$

where N is the Avogadro's number, ρ the density, ε the permittivity, and β the mean polarizability of the molecules, which is almost constant upon polymerization.

We have softbaked the PMMA layers at 65 ºC during different times and evaluated the refractive index of the resulting layers by ellipsometry at 632.8 nm. In figure 2.12 we can see how the refractive index changes during the first minutes of softbake as the polymer loses solvent. This preliminary result suggests that is should be possible to establish a fine control of the refractive index of the polymer only by fine tuning the fabrication protocol.
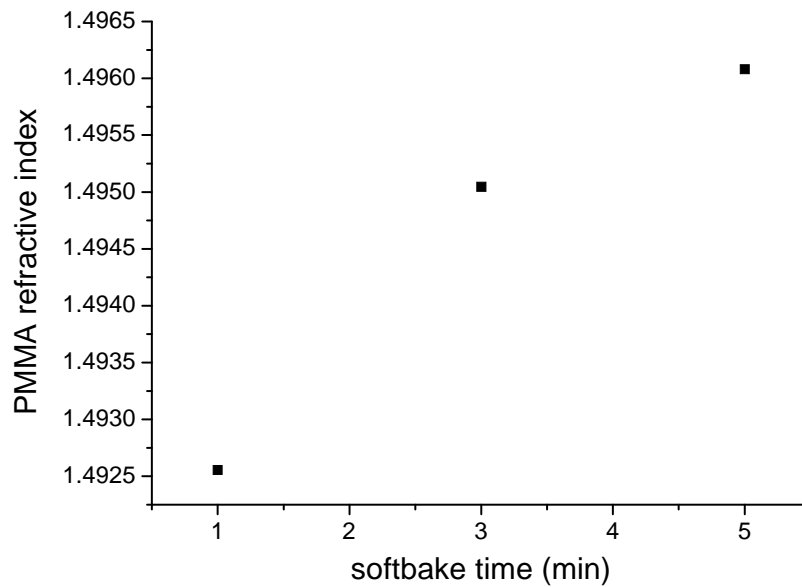
Fig.2.12.- PMMA refractive index evolution with the softbake time.

6.1.2 Grating replication in polymer

Unlike conventional lithography methods, imprint lithography itself does not use any energetic beams. In this way, NIL is not limited by wave diffraction effects, scattering and interference in the resist and backscattering from a substrate. Also, all the nanosized features of a given sample are replicated at once instead of in a serial process, making the lithographic process much faster. Figure 2.13 shows the surface quality of the master used to replicate the optical grating.
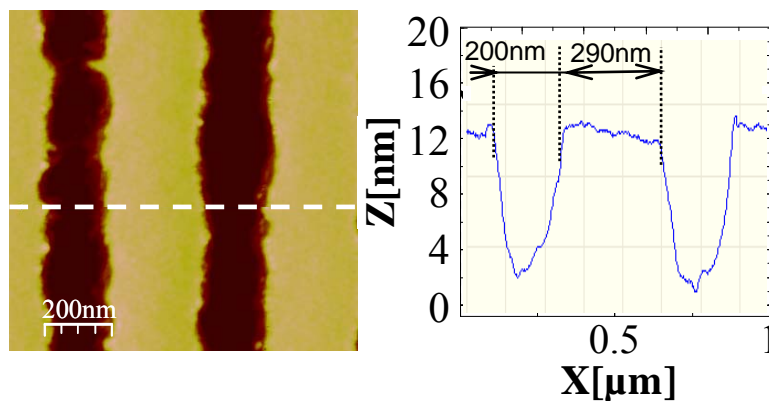

Fig. 2.13.- AFM image of the master used to nanoimprint the polymer gratings.

As it can be seen, the grating has a period of 500 nm and apparent depth of around 11 nm. Due to the AFM tip convolution, it is likely that the measured depth of the grating is underestimated.

This master was used to replicate the grating onto a PEN sheet and then from the PEN master to the PMMA spun coated glass substrates. After the NIL process, Figure 2.14, it can be noticed that surface roughness has increased up to 2 nm, while the grating structure remained barely altered.
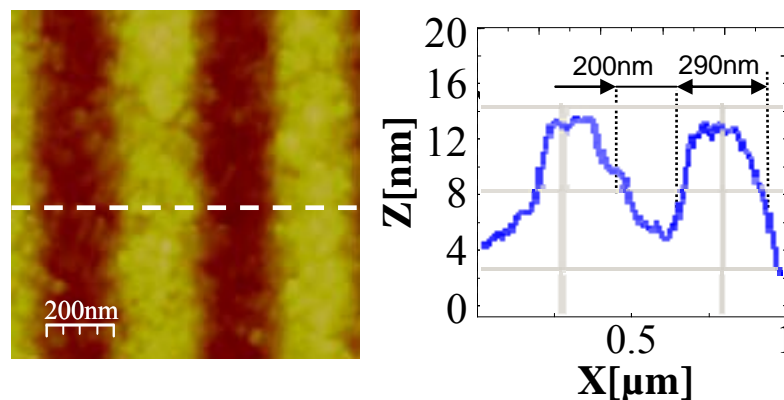

Fig. 2.14.- AFM image of the grating imprinted onto the PMMA substrates.

It is possible to conclude that NIL is suitable to replicate structures on polymer substrates with good dimensional definition. Not only the refractive grating replication is successful when it comes to the geometry, but also the polymer gratings are able to couple laser light into the polymer-glass waveguide, as clearly shown in figure 2.15.
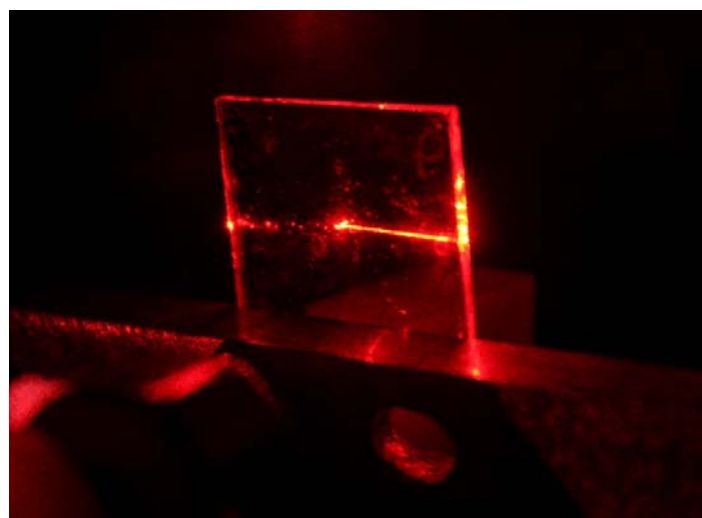

Fig. 2.15.- An He-Ne laser is coupled into the polymer waveguide through the printed grating tested on the optical bench.

6.1.3 ITO coating

Optimal thin layers of 120 nm of amorphous ITO onto PMMA were achieved depositing at room temperature at a rate of 0.4 nm/s with an oxygen content of 0.5 sccm during 300 seconds [55]. This thickness has been found as the optimal because it is very close to the maximum sensitivity of both the TE and the TM modes, as it can be seen is figure 2.8. This is the zone of interest as the OWLS works at 45º of polarization, meaning exciting both modes at the simultaneously.

To investigate the characteristics of the ITO film, sacrificial samples of sputtered ITO onto flat coated PMMA substrates were fabricated. The sheet resistance of the ITO thin film was characterized by Hall Effect measurements using the van der Pauw method and obtaining an electrical resistivity of 7.12E-4 Ω/cm. The optical parameters were also investigated. In the transmittance spectrum included in figure 2.16, the ITO thin film shows a transmittance of about 80% at 632.8nm. At the same wavelength the sample has a refractive index of 1.932 (figure 2.17).
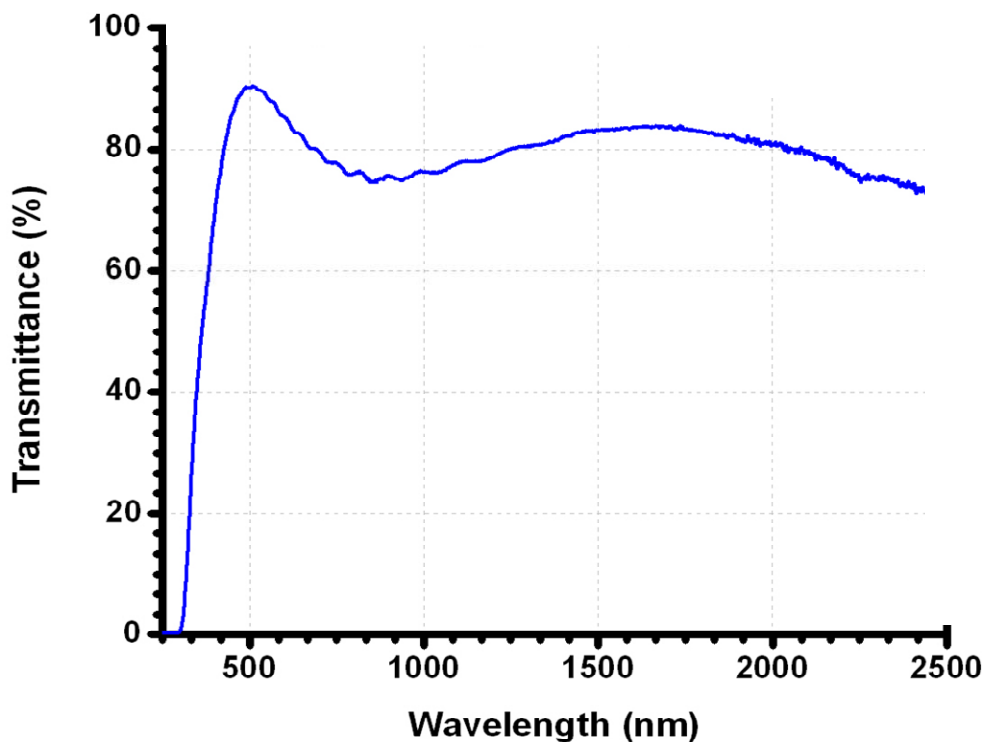
Fig. 2.16.- Transmittance spectrum of a 120nm ITO thin film.
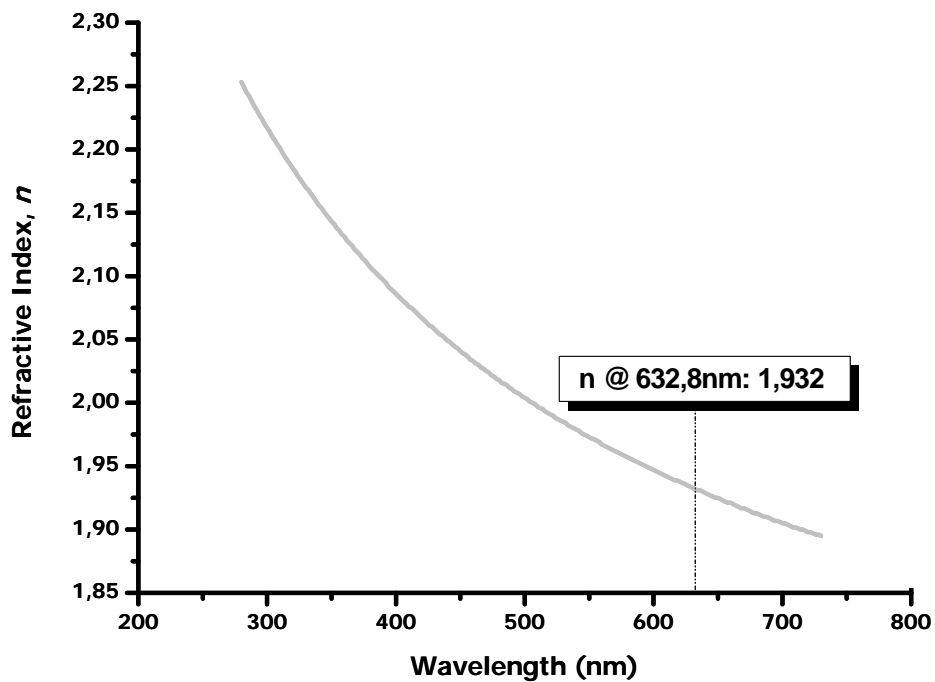
Fig. 2.17.- Ellipsometry measurement of refractive index.

The thickness of the deposited ITO thin films was confirmed to be around 110 nm, as measured with SEM (figure 2.18).
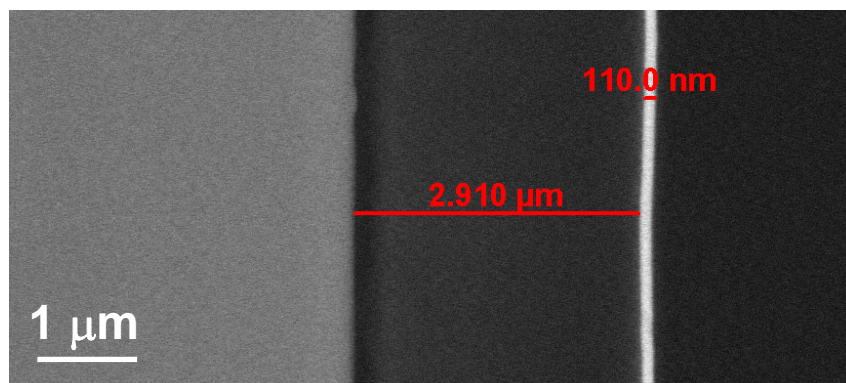
Fig. 2.18.- SEM cross section image of the ITO thin film onto a 3µm layer of PMMA onto glass.

Once the sputtering parameters were optimized, a layer of 120 nm of Indium Tin Oxide was sputtered onto the PMMA gratings. AFM measurements were made to investigate the surface quality of the ITO-PMMA waveguides. Figure 2.19 shows surface images of ITO films deposited at room temperature onto the PMMA gratings.
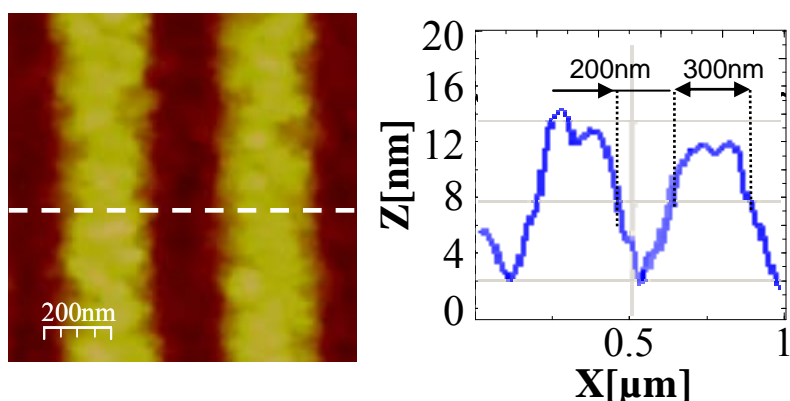
Fig. 2.19.- AFM image of the ITO coated PMMA grating.

The period of the grating is maintained at 500 nm and the apparent grating depth is 10 nm, while the roughness measurement out of the grating zone showed a roughness of only of about 1.3nm.

6.1.4 ITO Coated Polymer Gratings Characterization

Once the ITO coated polymer sensor was fabricated, the performance of the polymer-based chip in the OWLS instrument was tested. Figure 2.20 shows the coupled angle spectra of the ITO/PMMA sensor chip.
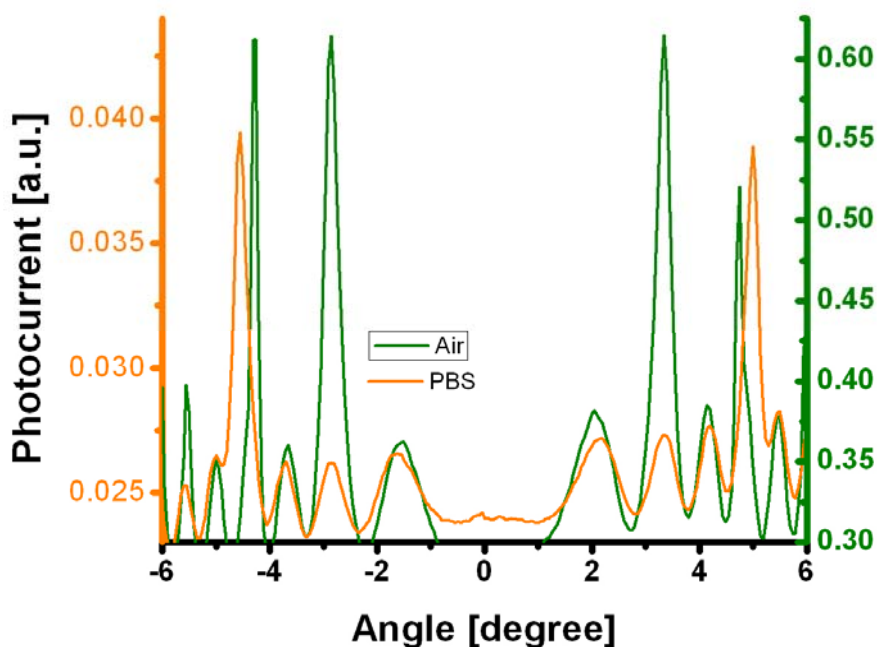
Fig. 2.20.-. The laser beam is coupled inside the waveguide at different incoupling angles. The green line shows the incoupling spectra of the ITO/PMMA chip in air, while the orange line shows the incoupling spectra in PBS.

Even though the polymer-based chip presents good performance when is tested in air, only two peaks are found when trying the sensor in PBS. This might be due to the fact that the coupling loses are so high that we are unable to excite both TE and TM modes at the same time. When polarizing the light at 0º and at 90º, we are able to find the TE and TM coupling modes, respectively; but their intensity is still very low. To solve this issue, it would be necessary to reduce the coupling loses. One way of achieving this purpose would be, for example, to decrease even further the roughness of the polymer layer. The ITO coated polymer gratings will obviously need further optimization in the future.

6.2 THIN FILM COATED COMMERCIAL OPTICAL GRATINGS

6.2.1 Commercial SOL-GEL waveguides

Before the gold layer deposition, the grating substrate was characterized by AFM. Figure 2.21 shows topographic images of the grating and a line profile. As it can be seen, the grating has a period of 480 nm, an apparent depth of around 10 nm and a RMS value on the flat top surfaces of 0.7 nm. Due to the AFM tip convolution, it is likely that the measured depth of the grating is underestimated.
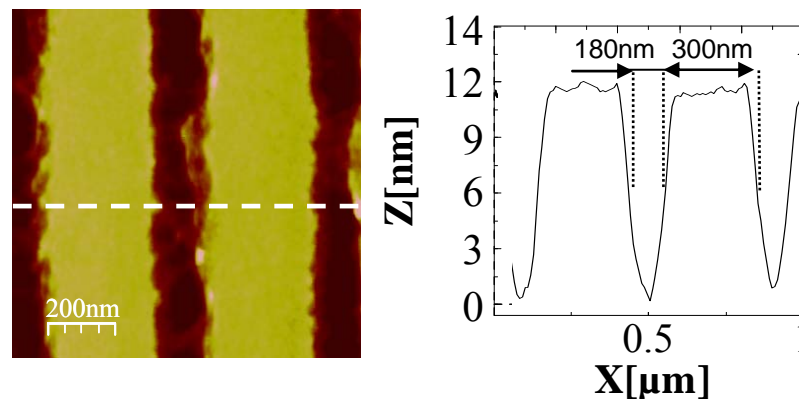
Fig. 2.21.- AFM image and profile of the SOL-GEL grating chip before gold thin layer deposition.

6.2.2 Gold coated sensors

6.2.2.1 Gold layer characterization

Thin films of gold were evaporated having a high purity gold wire as source material. As it can be seen in figure 2.22, the transmittance of the gold film decreases

with the deposition time, that is, decreases as the gold thickness increases. After optimizing the deposition parameters, gold thin films were deposited on three commercial chips during 25 seconds. With these conditions it was possible to produce a gold thin film with a transmittance of 83.43% at 632.8nm.
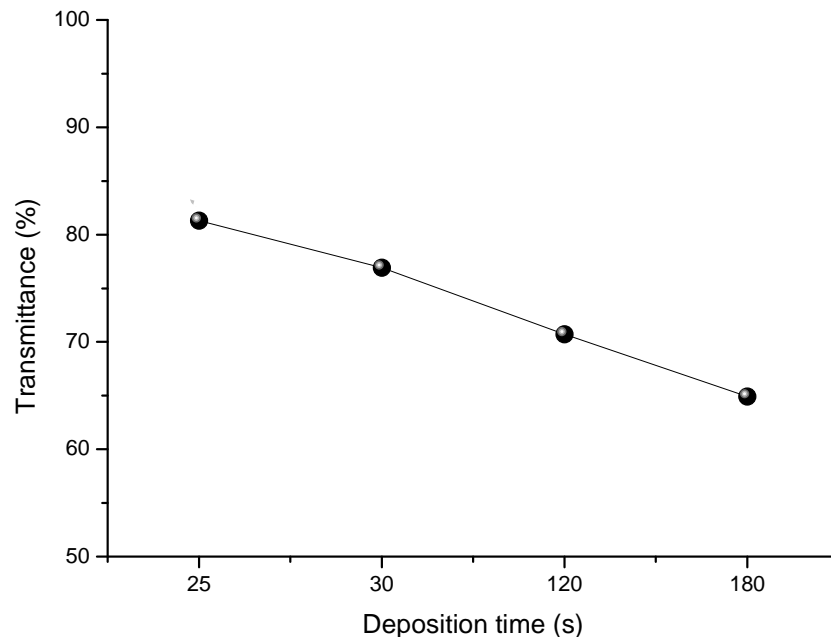
Fig. 2.22.- Gold thin films transmittance at 632.8 nm.

The topography of the gold coated sensors was evaluated by AFM analysis and the results are presented in figure 2.23. The roughness of the gold layer increases up to 2 nm, making the grating depth a bit smaller, around 5 nm.
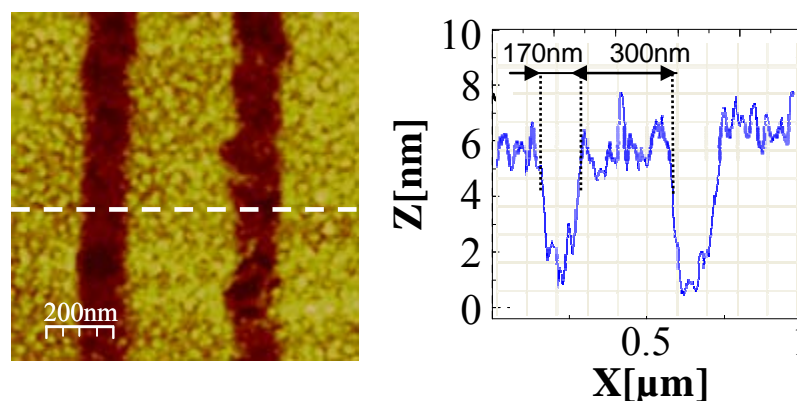
Fig. 2.23.- AFM image of the grating chip after gold thin layer deposition

6.2.2.2. Gold coated sensor performance

To test the performance of the gold coated sensor, an OWLS experiment was carried out in air. The result is presented in figure 2.24.
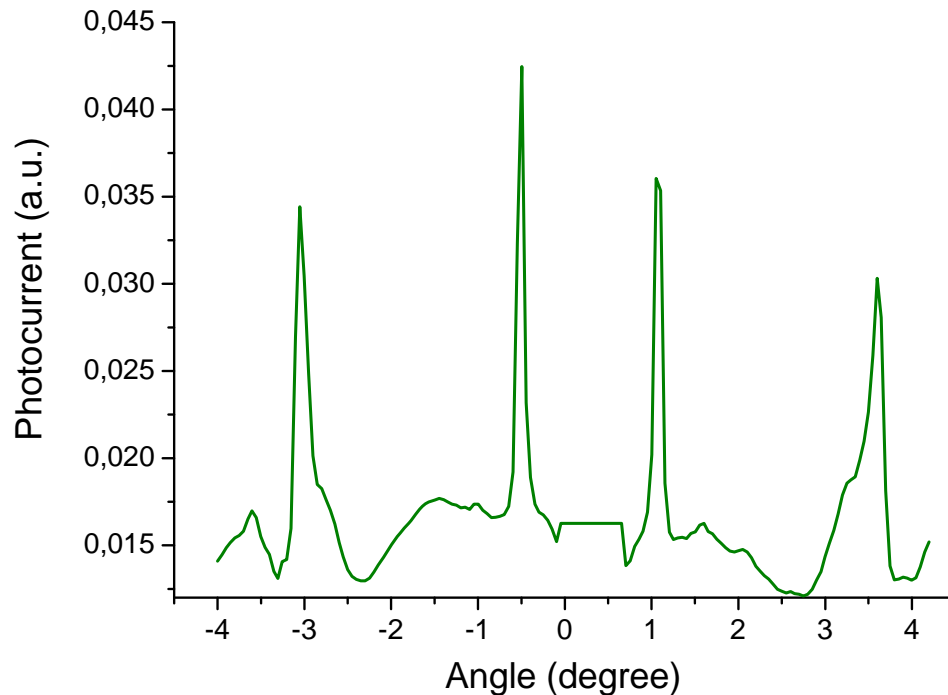
Fig. 2.24.- The OWLS response shows the incoupling spectrum of a gold coated sensor.

The figure 2.24 confirms the performance of the gold-coated grating sensor in air, showing well defined incoupling peaks corresponding to the fundamental TE and TM modes. Unfortunately, the quality of the adhesion of the gold layer onto the SOL-GEL sensor was poor and detached from the surface when brought in contact with solution. Additional work must be done in order to improve the adhesion of the gold nanofilms to the sensor. This could be done depositing a very thin layer of about 5nm of chromium prior to gold deposition.

6.2.3 Silicon Nitride

6.2.3.1 Silicon Nitride layer characterization

The deposition time and the applied bias of the sputtering process were optimized in order to obtain the best nitride layer in terms of high transmittance in the

visible range and in terms of surface smoothness. After deposition, silicon nitride film thickness and refractive index were determined by ellipsometry measurements as 10.3 (± 0.1) nm and 2.22 (± 0.10), respectively. This refractive index value is in agreement with the corresponding stoichiometric one, which is 2.05 at 300 K [43].

The effects in the chemical composition of the outmost part of the silicon nitride layer produced by the chemical activation process with the NaOH were investigated by means of XPS. Figure 2.25a plots the surface full XPS spectrum of the activated layer, where it can be observed that the there is a huge content of oxygen (up to 34% in atomic content). Moreover, it can be also observed that the ratio Si:N does greatly exceed the stoichiometric ratio of the silicon nitride, being in this case $Si_{6.8}N_4$. In order to investigate this in more detail, a high-resolution spectrum of the 2p Si peak was performed and analyzed. The peak could be deconvoluted into three contributions (Fig. 2.25b), coming from three different oxidation states corresponding to silicon nitride, silicon oxide and silicon. These results prove the presence of an oxygen-rich surface that will be then further functionalized by the TEA reagent [56].
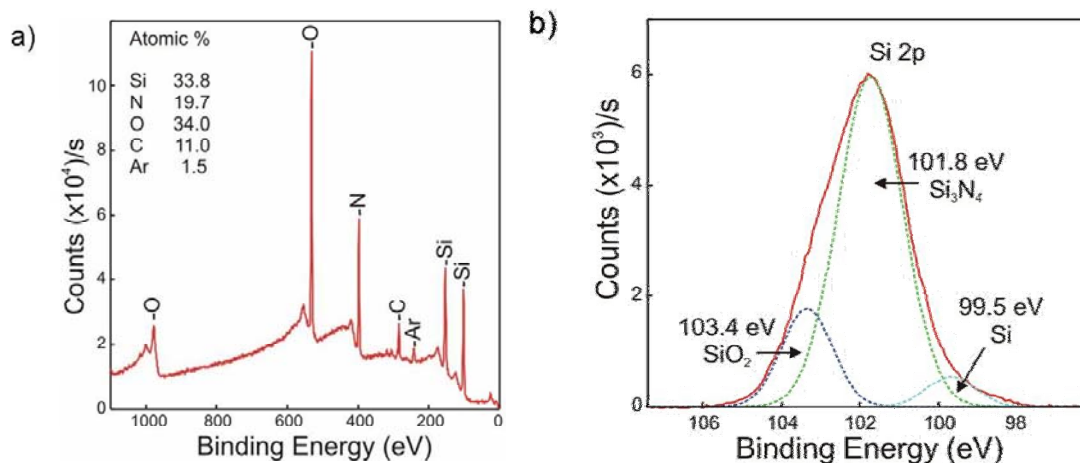
Fig. 2.25.- XPS spectra of the activated silicon nitride coated OWLS chip (a) full energy range spectrum and (b) high resolution spectrum of the Si 2p peak, showing its deconvolution into three contributions. After the chemical activation procedure with NaOH solution a high content of O can be observed, which is in accordance with the presence of SiO_2.

6.2.3.2. Silicon Nitride coated sensor performance

Prior to the silicon nitride layer deposition, the grating substrate was characterized by means of AFM. Figure 2.26 shows 2D topography AFM images of the

grating and a line profile. As it can be seen, the grating has a period of 450 nm, an apparent depth of around 7 nm and a RMS value on the flat top surfaces of 0.7 nm. Due to the AFM tip convolution, it is likely that the measured depth of the grating is underestimated.
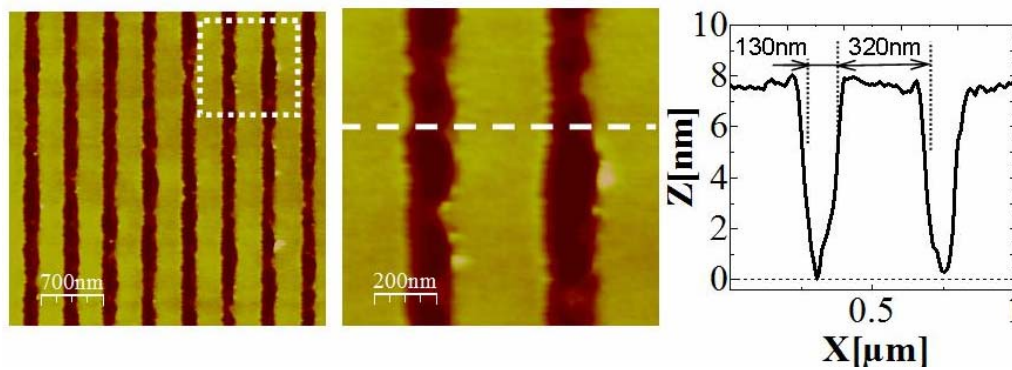
Fig. 2.26.- AFM images of the grating chip before silicon nitride thin layer deposition

After the deposition of the 10.3 nm of silicon nitride, Figure 2.27, it can be noticed that surface roughness has increased up to 2.6 nm (RMS value), presenting a grainier morphology, while the grating structure remained barely altered (period of 450 nm and apparent depth of 7 nm).
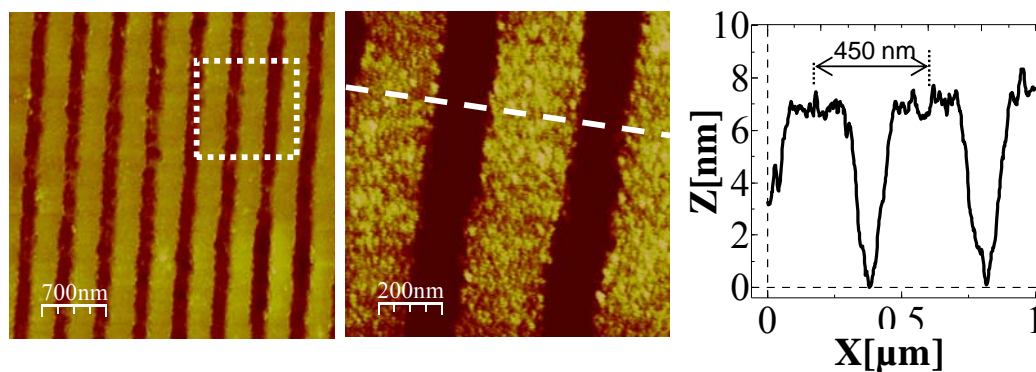
Fig. 2.27.- AFM images of the grating chip after silicon nitride thin layer deposition

Once the chip was functionalized with the anti-HSA antibodies, the morphology of the grating was again characterized by the AFM technique. Figure 2.28 shows the changes produced by the organic layer: the grating structure period remains unaltered (450 nm) but the structure depth decreases slightly (5-6 nm) and the surface becomes again smoother, with RMS values around 1.8 nm.
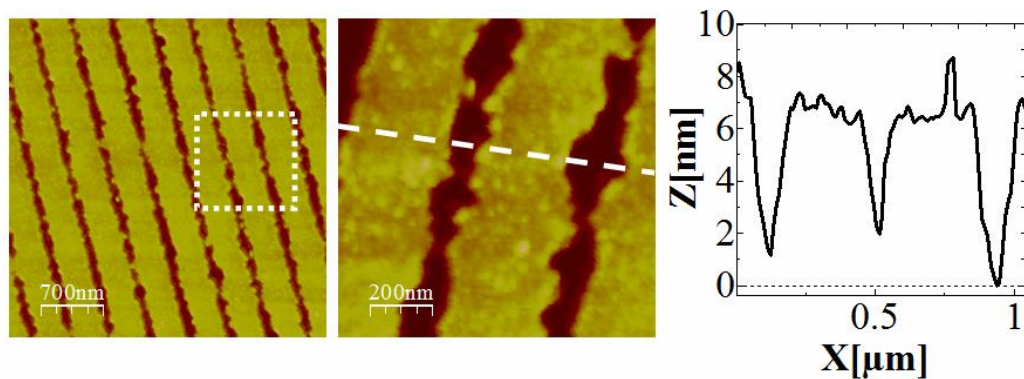
Fig. 2.28.- AFM images of the grating chip after antibody functionalization. The grating structure is maintained after the organic layer deposition.

Once fabricated, the functionalized silicon nitride chip performance in the OWLS instrument was checked. Figure 2.29 shows the plot of OWLS incoupling angle spectra after the silicon nitride layer deposition. It can be seen that both TE and TM peaks are perfectly visible after the silicon nitride deposition and the signal to noise ratio increases from 41 to 56 in the OWLS spectra when the chip is functionalized with antibodies with respect to the bare Si_3N_4 coated chip. This is related to the decrease in the roughness as a flatter surface avoids scattering during the incoupling of the laser. The same figure shows the OWLS incoupling angle peaks after the chip functionalization with the anti-HSA antibody layer. Worth noticing, the functionalization of the chip did not affect the chip structure neither covered the whole chip surface, allowing the coupling of the laser.
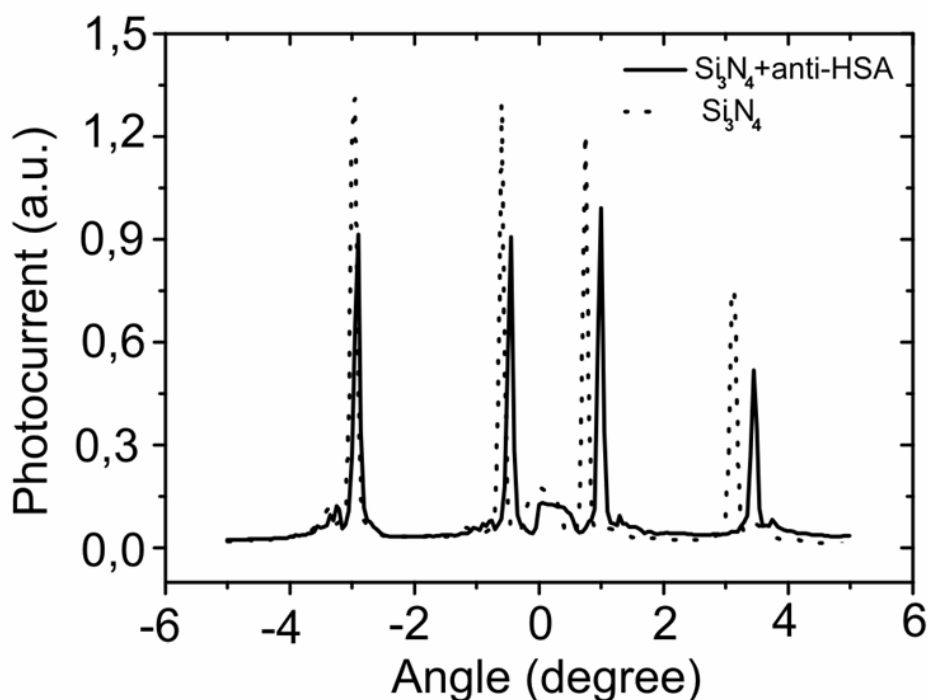
Fig. 2.29.- The laser beam is coupled inside the waveguide at different incoupling angles (depending on the covering layer). The spectrum is followed by the photodiodes placed at each end of the waveguide. The dash line shows the incoupling spectra of the bare chip covered with silicon nitride, and the continuous line after antibody functionalization.

6.2.3.3. Silicon Nitride coated as an immunosensor: proof of concept

Human serum albumin detection experiments were performed in order to establish the biosensing viability of the whole developed system. The albumin concentration in the blood serum of an average adult human is 42.0 ± 3.5 mg/mL, (~0.6 mM) with an interval of 35-50 mg/mL [61, 62]. Hyperalbuminemia and hypoalbuminemia are pathogenesis related with high or low HSA concentrations in body fluids, respectively. The immunosensing experiments have been specifically designed to show high sensitivity and dynamic range performance in the range of interest. HSA was recognized by the anti-HSA antibody attached to the silicon nitride coated OWLS waveguide chip. The system proved to be stable; responses did not decrease significantly during the measurement. A typical curve of the measurements performed with the system is shown in Figure 2.30. Measurements started by stabilizing the system by flowing PBS for two hours approximately in order to obtain a steady baseline. Then, solutions with increasing HSA protein concentrations ranging from 10^{-13} M to 10^{-3} M were injected in the cell. After each injection, the system was kept in stop-

flow mode. In order to stabilize the signal, and then it was thoroughly rinsed with PBS in order to remove all the protein non-specifically adhered to the chip surface. The system response was sigmoidal with the protein concentration, as predicted by the Nerst equation and the Langmuir adsorption theory [63]. Considering the amount of antibody captured probes used on the immobilization procedure (equivalent to 104 pmol/cm^2) and taking into account that an antibody perfect monolayer would have a density of 1.7 pmol/cm^2 (antibodies are around 10 nm in diameter [64]) the antibody amount used in the immobilization process is well in excess. If the recognition ratio between the protein and the antibody is 0.37:1 [65], the maximum saturation value of protein to be recognised for an ideal antibody monolayer would be 336 ng/cm^2. Thus, the experimental data measured for the adsorbed protein in the detection range assayed, shown in figure 2.31, is far from saturation, therefore confirming that the biosensing system is well design to work in the desired range.
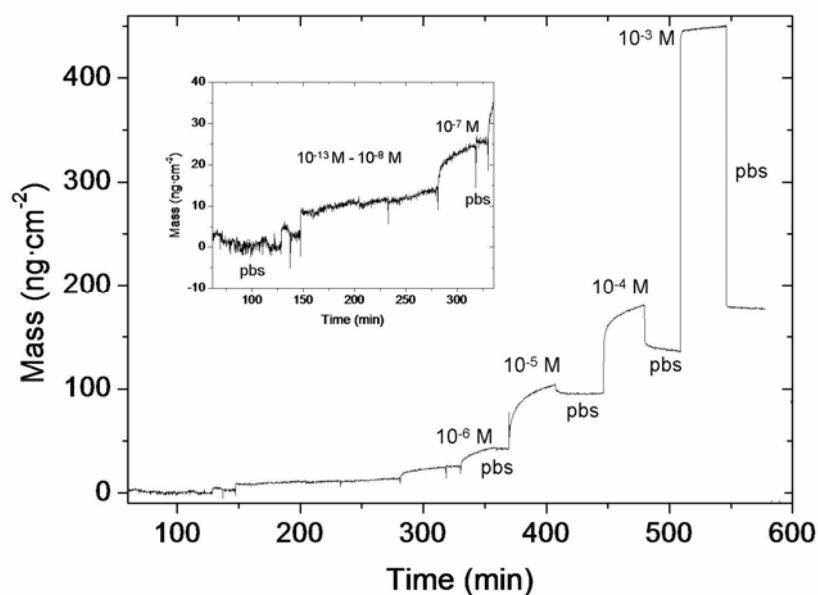
Fig. 2.30.- OWLS graphic showing the mass of HSA protein at different concentrations adsorbed on the Si$_3$N$_4$ functionalized chip after washing with PBS.

The relationship between the adsorbed mass, attributed to the HSA protein and the protein concentration plotted in a semi-logarithmic scale is shown in Figure 2.31. The experimental mass values were fitted using a sigmoidal fit with a correlation factor of R^2=0.9969. The graphic also suggests a linear fit within the range of 10^{-3} M to 10^{-6} M

with a R^2 value of 0.99689. The sensitivity of the system within the dynamic range is 34 ng·cm^{-2} for the HSA detection.

These results show a biosensing system with a dynamic working range particularly well fitted and designed for the specific application, with a LOD that, despite not reaching the values reported by similar studies [66], is three orders of magnitude better than needed for diagnosis of hyper/hypoalbuminemia and far more stable. Furthermore, our system presents a very good sensitivity and the possibility of extracting values of adsorbed mass.
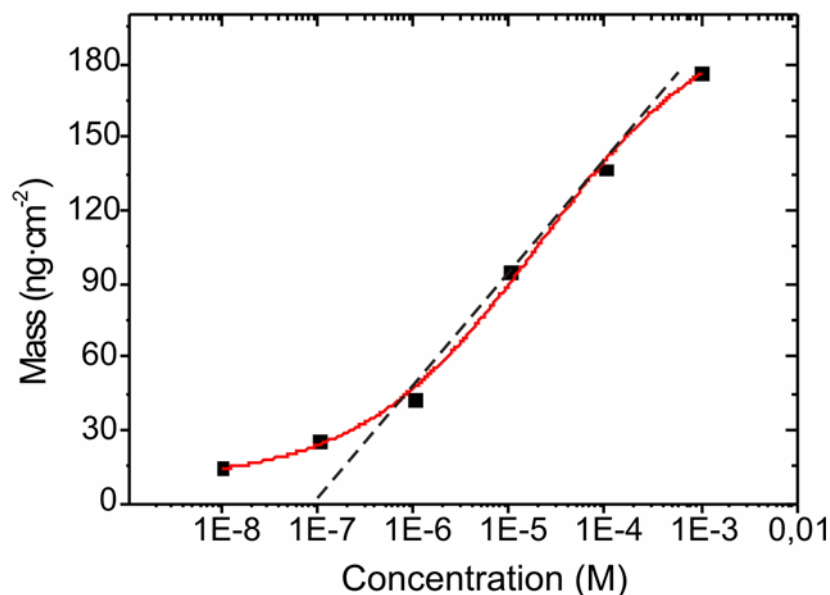
Fig. 2.31.- Relationship between the adsorbed mass of HSA protein in the surface and the HSA solution concentration.

This model study of the detection and quantification of HSA, demonstrate the potential of the Si_3N_4 covered grating sensor chips [56]. The ability of the silicon nitride to be the functional layer in a real-time biosensor renders it a promising material for integration of optical waveguides with microelectronics; for instance, the integration of optical waveguides into printed-circuit boards, or into field effect transistors.

7 CONCLUSIONS AND FUTURE WORK

An OWLS chip with a silicon nitride grating surface has been fabricated by coating a diffraction grating with a 10 nm thin layer of Si_3N_4 by sputtering deposition, confirmed by AFM, ellipsometry and XPS measurements. A novel protocol was used for the direct immobilization of biomolecules onto the silicon nitride optical immunosensor and a self-assembled monolayer of anti-human serum albumin antibodies were directly immobilized on the functionalized Si_3N_4 OWLS chip for the detection of different concentrations of HSA proteins, as a proof of concept. Results show that the adsorbed mass of protein can be easily measured, giving extra information about the molecular interactions processes compared with the previous detection techniques; for instance the amount of protein immobilized in the surface. The potential of the Si_3N_4 covered grating sensor chips opens new ways in biosensing, allowing the integration of optical biosensors with microelectronics.

After an extensive study of how the waveguide film thickness affects the sensitivity of polymer waveguides, a polymer-based grating sensor chip has been fabricated by Nano Imprint Lithography, featuring as a substrate for an ITO waveguide featuring high sensitivity. Even though the sensitivity of this polymer-based waveguide was maximized, optical loses interfered in its performance. Also, gold coated commercial gratings have been fabricated with good optical characteristics, but poor adhesion. Although we have demonstrated the validity of these new approaches, further work needs to be done to achieve solid proof of concept. Nevertheless, we have set the basis for polymer-based gratings and for the first time developed gold substrates for optical spectroscopy.

8 REFERENCES

[1]   R. Horváth, J. Vörös, R. Graf, G. Fricsovszky, M. Textor, L. R. Lindvold, N. D. Spencer, and E. Papp, "Effect of patterns and inhomogeneities on the surface of waveguides used for optical waveguide lightmode spectroscopy applications," *Applied Physics B: Lasers and Optics,* vol. 72, pp. 441-447, 2001.

[2]   W. Lukosz and K. Tiefenthaler, "Sensitivity of integrated optical grating and prism couplers as (bio)chemical sensors," *Sensors and Actuators,* vol. 15, pp. 273-284, 1988.

[3]   P. M. Nellen, K. Tiefenthaler, and W. Lukosz, "Integrated optical input grating couplers as biochemical sensors," *Sensors and Actuators,* vol. 15, pp. 285-295, 1988.

[4]   R. G. Heideman, R. P. H. Kooyman, and J. Greve, "Performance of a highly sensitive optical waveguide Mach-Zehnder interferometer immunosensor," *Sensors and Actuators B: Chemical,* vol. 10, pp. 209-217, 1993.

[5]   A. Brandenburg, R. Krauter, C. Künzel, M. Stefan, and H. Schulte, "Interferometric Sensor for Detection of Surface-Bound Bioreactions," *Appl. Opt.,* vol. 39, pp. 6396-6405, 2000.

[6]   A. Ymeti, J. S. Kanger, R. Wijn, P. V. Lambeck, and J. Greve, "Development of a multichannel integrated interferometer immunosensor," *Sensors and Actuators B: Chemical,* vol. 83, pp. 1-7, 2002.

[7]   W. Lukosz, "Principles and sensitivities of integrated optical and surface plasmon sensors for direct affinity sensing and immunosensing," *Biosensors and Bioelectronics,* vol. 6, pp. 215-225, 1991.

[8]   R. Slavík and J. Homola, "Ultrahigh resolution long range surface plasmon-based sensor," *Sensors and Actuators B: Chemical,* vol. 123, pp. 10-12, 2007.

[9]   V. N. Konopsky and E. V. Alieva, "Long-range plasmons in lossy metal films on photonic crystal surfaces," *Opt. Lett.,* vol. 34, pp. 479-481, 2009.

[10]   R. Horváth, H. C. Pedersen, N. Skivesen, D. Selmeczi, and N. B. Larsen, "Optical waveguide sensor for on-line monitoring of bacteria," *Opt. Lett.,* vol. 28, pp. 1233-1235, 2003.

[11]   P. N. Zeller, G. Voirin, and R. E. Kunz, "Single-pad scheme for integrated optical fluorescence sensing," *Biosensors and Bioelectronics,* vol. 15, pp. 591-595, 2000.

[12]   J. Ramsden, "Review of New Experimental techniques for Investigating Random Sequential Adsorption," *Journal of Statistical Physics,* vol. 73, p. 853, 1993.

[13]   J. A. D. Feijter and J. B. F. A. Veer, "Ellipsometry as a tool to study the adsorption behavior of synthetic and biopolymers at the air-water interface," *Biopolymers,* vol. 17, pp. 1759-1772, 1978.

[14]   W. Lukosz and K. Tiefenthaler, "Directional switching in planar waveguides effected by adsorption-desorption processes," in *IEE Conference Publication*, 1983, pp. 152-155.

[15]   R. E. Kunz, J. Edlinger, P. Sixt, and M. T. Gale, "Replicated chirped waveguide gratings for optical sensing applications," *Sensors and Actuators A: Physical,* vol. 47, pp. 482-486, 1995/4//.

[16]   M. Wiki, H. Gao, M. Juvet, and R. E. Kunz, "Compact integrated optical sensor system," *Biosensors and Bioelectronics,* vol. 16, pp. 37-45, 2001.

[17]   K. Cottier, M. Wiki, G. Voirin, H. Gao, and R. E. Kunz, "Label-free highly sensitive detection of (small) molecules by wavelength interrogation of integrated optical chips," *Sensors and Actuators B: Chemical,* vol. 91, pp. 241-251, 2003.

[18]   M. Wiki and R. E. Kunz, "Wavelength-interrogated optical sensor for biochemical applications," *Opt. Lett.,* vol. 25, pp. 463-465, 2000.

[19]   J. J. Ramsden and J. r. Dreier, "Kinetics of the Interaction between DNA and the Type IC Restriction Enzyme EcoR124IIâ€ " *Biochemistry,* vol. 35, pp. 3746-3753, 1996.

[20]   J. J. Ramsden, "Molecular orientation in lipid bilayers," *Philosophical Magazine Part B,* vol. 79, pp. 381-386, 2011/08/14 1999.

[21]   G. Csúcs and J. J. Ramsden, "Solubilization of planar bilayers with detergent," *Biochimica et Biophysica Acta (BBA) - Biomembranes,* vol. 1369, pp. 304-308, 1998.

[22]   J. J. Ramsden and G. Vergères, "Nonelectrostatic Contributions to the Binding of MARCKS-Related Protein to Lipid Bilayers," *Archives of Biochemistry and Biophysics,* vol. 371, pp. 241-245, 1999.

[23]   J. J. Ramsden and P. Schneider, "Membrane insertion and antibody recognition of a glycosylphosphatidylinositol-anchored protein: an optical study," *Biochemistry,* vol. 32, pp. 523-529, 1993.

[24]   J. Piehler, A. Brandenburg, A. Brecht, E. Wagner, and G. Gauglitz, "Characterization of grating couplers for affinity-based pesticide sensing," *Appl. Opt.,* vol. 36, pp. 6554-6562, 1997.

[25]   M. R. Widmer, M. Heuberger, J. Vörös, and N. D. Spencer, "Influence of polymer surface chemistry on frictional properties under protein-lubrication conditions: implications for hip-implant design," *Tribology Letters,* vol. 10, pp. 111-116, 2001.

[26]   L. Diéguez, N. Darwish, N. Graf, J. Voros, and T. Zambelli, "Electrochemical tuning of the stability of PLL/DNA multilayers," *Soft Matter,* vol. 5, pp. 2415-2421, 2009.

[27]   G. L. Kenausis, J. Vörös, D. L. Elbert, N. Huang, R. Hofer, L. Ruiz-Taylor, M. Textor, J. A. Hubbell, and N. D. Spencer, "Poly(l-lysine)-g-Poly(ethylene glycol) Layers on Metal Oxide Surfaces:â€‰ Attachment Mechanism and Effects of Polymer Architecture on Resistance to Protein Adsorptionâ€ " *The Journal of Physical Chemistry B,* vol. 104, pp. 3298-3309, 2000.

[28]   J. J. Ramsden, S. Y. Li, E. Heinzle, and J. E. Prenosil, "Optical method for measurement of number and shape of attached cells in real time," *Cytometry,* vol. 19, pp. 97-102, 1995.

[29]   H. Li and W. T. S. Huck, "Polymers in nanotechnology," *Current Opinion in Solid State and Materials Science,* vol. 6, pp. 3-8, 2002.

[30]   B. E. Yoldas, "Deposition and properties of optical oxide coatings from polymerized solutions," *Appl. Opt.,* vol. 21, pp. 2960-2964, 1982.

[31]   W. Lukosz and K. Tiefenthaler, "Embossing technique for fabricating integrated optical components in hard inorganic waveguiding materials," *Opt. Lett.,* vol. 8, pp. 537-539, 1983.

[32]   R. Kurrat, M. Textor, J. J. Ramsden, P. Böni, and N. D. Spencer, *Instrumental improvements in optical waveguide light mode spectroscopy for the study of biomolecule adsorption* vol. 68: AIP, 1997.

[33]   A. K. Ghatak and K. Thyagarajan, *Optical electronics.* Cambridge, New York: Cambridge University Press, 1989.

[34] C. Kaspar, E. K. Rino, V. Guy, and W. Max, "Thickness-modulated waveguides for integrated optical sensing," in *Optical Fibers and Sensors for Medical Applications II*, San Jose, CA, USA, 2002, pp. 53-63.

[35] C. A. Mills, E. Martinez, F. Bessueille, G. Villanueva, J. Bausells, J. Samitier, and A. Errachid, "Production of structures for microfluidics using polymer imprint techniques," *Microelectronic Engineering,* vol. 78-79, pp. 695-700, 2005.

[36] A. Ghatak, K. Thyagarajan, and M. Shenoy, "Numerical analysis of planar optical waveguides using matrix approach," *Lightwave Technology, Journal of,* vol. 5, pp. 660-667, 1987.

[37] M. Tadatsugu, "Present status of transparent conducting oxide thin-film development for Indium-Tin-Oxide (ITO) substitutes," *Thin Solid Films,* vol. 516, pp. 5822-5828, 2008.

[38] N. Darwish, L. Diéguez, M. Moreno, F. Muñoz, R. Mas, J. Mas, J. Samitier, B. Nilsson, and G. Petersson, "Second order effects of aspect ratio variations in high sensitivity grating couplers," *Microelectronic Engineering,* vol. 84, pp. 1775-1778, May-August 2007 2007.

[39] R. Kurrat, M. Textor, J. J. Ramsden, P. Boni, and N. D. Spencer, "Instrumental improvements in optical waveguide light mode spectroscopy for the study of biomolecule adsorption," *Review of Scientific Instruments,* vol. 68, p. 2172, 1997.

[40] K. Schmitt, K. Oehse, G. Sulz, and C. Hoffmann, "Evanescent field Sensors Based on Tantalum Pentoxide Waveguides – A Review," *Sensors,* vol. 8, pp. 711-738, 2008.

[41] T. P. Ma, "Making silicon nitride film a viable gate dielectric," *Electron Devices, IEEE Transactions on,* vol. 45, pp. 680-690, 1998.

[42] K. Schmitt and C. Hoffmann, "High-refractive-index waveguide platforms for chemical and biosensing," *Springer Ser. Chem. Sens. Biosens.,* vol. 7, pp. 21-54, 2010.

[43] E. Palik, *Handbook of Optical Constants of Solids*. Orlando, Florida: Academic Press, 1985.

[44] O. Hofmann, G. Voirin, P. Niedermann, and A. Manz, "Three-Dimensional Microfluidic Confinement for Efficient Sample Delivery to Biosensor Surfaces. Application to Immunoassays on Planar Optical Waveguides," *Analytical Chemistry,* vol. 74, pp. 5243-5250, 2002.

[45] S. Busse, J. Kaeshammer, S. Kraemer, and S. Mittler, "Gold and thiol surface functionalized integrated optical Mach-Zehnder interferometer for sensing purposes," *Sens. Actuators, B,* vol. B60, pp. 148-154, 1999.

[46] V. A. Nabok, F. N. Starodub, K. A. Ray, and K. A. Hassan, "Registration of immunoglobuline AB/AG reaction with planar polarization interferometer," in *Biochemical and Biomolecular Sensing*, Boston, MA, USA, 2000, pp. 1-9.

[47] J. Vörös, J. J. Ramsden, G. Csúcs, I. Szendro, S. M. De Paul, M. Textor, and N. D. Spencer, "Optical grating coupler biosensors," *Biomaterials,* vol. 23, pp. 3699-3710, 2002.

[48] A. Brandenburg and A. Gombert, "Grating couplers as chemical sensors: a new optical configuration," *Sensors and Actuators B: Chemical,* vol. 17, pp. 35-40, 1993.

[49]   K. Tiefenthaler and W. Lukosz, "Sensitivity of grating couplers as integrated-optical chemical sensors," *J. Opt. Soc. Am. B* vol. 6, p. 209, 1989.

[50]   C. A. Mills, J. Escarr, E. Engel, E. Martinez, A. Errachid, J. Bertomeu, J. Andreu, J. A. Planell, and J. Samitier, "Micro-and nanostructuring of poly(ethylene-2,6-naphthalate) surfaces, for biomedical applications, using polymer replication techniques," 2005, p. 369.

[51]   C. A. Mills, E. Martinez, F. Bessueille, G. Villanueva, J. Bausells, J. Samitier, and A. Errachid, "Production of structures for microfluidics using polymer imprint techniques," *Microelectronic Engineering,* vol. 78-79, pp. 695-700, 2005.

[52]   J. P. B. a. T. Lebey, "On some dielectric properties of PEN," *Journal of Physics D: Applied Physics,* vol. 29, p. 2052, 1996.

[53]   C. A. Mills, J. G. Fernandez, A. Errachid, and J. Samitier, "The use of high glass temperature polymers in the production of transparent, structured surfaces using nanoimprint lithography," *Microelectronic Engineering,* vol. 85, pp. 1897-1901, 2008.

[54]   C. S. L. Azevedo, "Development of Nanostructured Materials for Medical Nanobiosensors," in *Sciences School.* vol. Master: University of Minho, 2009.

[55]   S. Azevedo, L. Diéguez, P. Carvalho, J. O. Carneiro, V. Teixeira, E. Martínez, and J. Samitier, "Deposition of ITO thin films onto PMMA substrates for waveguide based biosensing devices," *Journal of Nano Research,* vol. 17, pp. 75-83, 2012.

[56]   L. Diéguez, D. Caballero, J. Calderer, M. Moreno, E. Martínez, and J. Samitier, "Optical Gratings Coated with Thin Si3N4 Layer for Efficient Immunosensing by Optical Waveguide Lightmode Spectroscopy." *Biosensors,* vol. 2, 2012, pp. 114-126.

[57]   R. Kurrat, M. Textor, J. J. Ramsden, P. Boni, and N. D. Spencer, "Instrumental improvements in optical waveguide light mode spectroscopy for the study of," *Review of Scientific Instruments,* vol. 68, p. 2172, 1997.

[58]   D. Caballero, J. Samitier, J. Bausells, and A. Errachid, "Direct Patterning of Anti-Human Serum Albumin Antibodies on Aldehyde-Terminated Silicon Nitride Surfaces for HSA Protein Detection," *Small,* vol. 5, pp. 1531-1534, 2009.

[59]   D. C. O'Shea, T. J. Suleski, A. D. Kathman, and D. W. Prather, *Diffractive Optics. Design, Fabrication and Test.* vol. TT62, 2004.

[60]   R. Ulrich and R. Torge, "Measurement of Thin Film Parameters with a Prism Coupler," *Applied Optics,* vol. 12, pp. 2901-2908, 1973.

[61]   M. Hassan, E. Azzazy, and R. H. Christenson, "All About Albumin: Biochemistry, Genetics, and Medical Applications. ," in *Academic Press.* vol. 43, J. Theodore Peters, Ed. San Diego, CA, 1997, p. 432.

[62]   S. Curry, H. Mandelkow, P. Brick, and N. Franks, "Crystal structure of human serum albumin complexed with fatty acid reveals an asymmetric distribution of binding sites," *Nat Struct Mol Biol,* vol. 5, pp. 827-835, 1998.

[63]   G. Fleer, *Adsorption from solution at the solid/liquid interface*, ed. G. D. Porfitt and C. H. Rochester ed. London: Academic Press, 1983.

[64]   W. K. Hartmann, N. Saptharishi, X. Y. Yang, G. Mitra, and G. Soman, "Characterization and analysis of thermal denaturation of antibodies by size

exclusion high-performance liquid chromatography with quadruple detection," *Analytical Biochemistry,* vol. 325, pp. 227-239, 2004.

[65]   S. Lin, C.-C. Lu, H.-F. Chien, and S.-M. Hsu, "An on-line quantitative immunoassay system based on a quartz crystal microbalance," *Journal of Immunological Methods,* vol. 239, pp. 121-124, 2000.

[66]   N. Darwish, D. Caballero, M. Moreno, A. Errachid, and J. Samitier, "Multi-analytic grating coupler biosensor for differential binding analysis," *Sensors and Actuators B: Chemical,* vol. 144, pp. 413-417, 2010.

CHAPTER 3: EFFECT OF THE REFRACTIVE INDEX OF BUFFER SOLUTIONS IN EVANESCENT OPTICAL BIOSENSORS

1 INTRODUCTION & STATE OF THE ART

Evanescent optical biosensors, like Surface Plasmon Resonance (SPR) or Optical Waveguide Lightmode Spectroscopy (OWLS), are label-free sensors able to follow *in situ* the immobilization kinetics of an analyte by monitoring the local refractive index change. Upon this measurement, it is possible to obtain highly accurate quantitative information about the thickness and the mass of the adsorbed film or the surface coverage of a substrate sample [1].

As stated in chapter 2, a grating coupler sensor chip, such as the one used in the OWLS technique, usually consists in three different layers: substrate, waveguide film and cover (see figure 3.1). The cover layer is the sample solution which is formed by a buffer solution containing biomolecules that will be adsorbed on the surface of the sensor. When an adsorbed layer is created onto the surface, the coupling conditions change, therefore allowing to follow up the real time immobilization. Moreover, the variation of the refractive index of the adsorbed layer onto the chip surface upon changing biomolecule solution concentrations is translated into surface concentration of the adsorbed molecule [1-4]. It is important to take into account that the adsorbed layer is not a dry layer only composed by biomolecules, but they are also hydrated with some buffer solution.
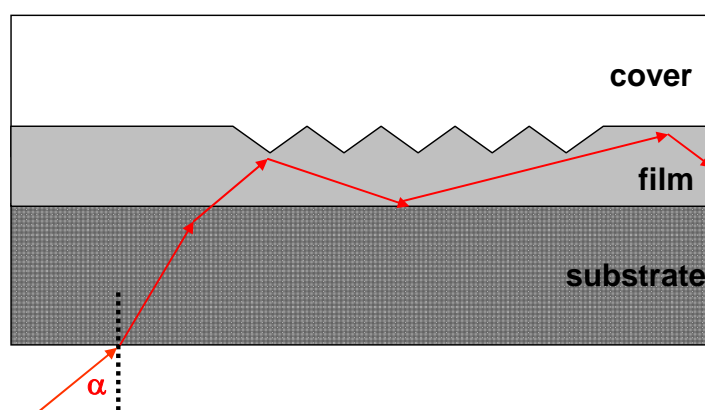

Fig. 3.1.- Scheme of a three layer grating coupler. The waveguide film is sandwiched between the glass substrate and the cover media.

In fact, some works point out that the refractive index increment produced in an evanescent optical biosensor by a protein solution is not only due to the protein, but also to the solvent itself [5]. This was demonstrated by Ball and co-workers in 1998 [5]. Not only the solvent nature is relevant, but it is also of great importance to study the dependence of the refractive index of the different buffers with other parameters, such as temperature [6] and pH. In this respect, Kroslak et al. published a work studying the deposition kinetics of β-lactoglobulin at a solid-liquid interface over a range of temperatures, pH and NaCl buffer concentrations, by means of OWLS [7]. They found that the obtained surface coverage increased by 10% when corrections on the refractive index value were made taking into account the variations of the refractive index with the temperature change. This is in agreement with our premise that an accurately optical characterization of the buffer solution used is, in fact, essential for the final fine modelling of the system. Of course, the buffer influence in the final refractive index increment will be also dependant on the hydrating degree of the protein or biomolecule layer deposited on the biosensor surface [5, 8, 9].

Since the invention of the grating coupler biosensor in the eighties decade, hundreds of studies have been published regarding different biosensing applications. Despite this fact, there are not many publications concerning how external parameters, as temperature or pH, affect the output measurement or how to obtain the input parameters (refractive index involved) needed for the calculations. Probably the most important parameter to define is the refractive index of the adsorbate, referring as adsorbate the protein layer hydrated deposited on the surface of the sensor from a protein solution of concentration c. Although for proteins the values for the refractive index increment of the adsorbate, dn/dc have been tabulated [10], most researchers in the field use a dn/dc value of 0.18 ± 0.03 cm^3/g, regardless of the identity of the protein and the actual electrolyte or buffer solution. This value was obtained measuring different concentrations of protein solutions, up to 0.05 wt %, in white light using an Abbé refractometer [11]. Although this "universal" value fits relatively well for some common protein solutions (i.e. bovine serum albumin, BSA), it does not always hold (dn/dc = 0.272 cm^3/g for hen egg white lysozyme –HEL- in 10 mM Sodium thiocyanate (NaSCN) 10 mM 4-(2-Hydroxyethyl)piperazine-1-ethanesulfonic acid sodium salt), especially when dealing with highly specific buffers [5, 12]. This difference in the dn/dc

values, could lead to up to 10% error when calculating the protein mass adsorbed onto the chip surface. Hence, there is obviously a need to measure the refractive index increment of the solution one wishes to work with in order to calculate true biomolecule surface concentrations.

In order to obtain accurate quantitative measurements of the adsorbed layer and its dependence on the buffer solution and on external parameters, it is of crucial importance a previous characterization of the waveguide chip parameters (waveguide film thickness and refractive index). This is due to the fact that these parameters may vary slightly depending on the fabrication conditions. Also the working conditions, such as the temperature, may influence the measurements and therefore need to be evaluated before each experiment.

In this chapter, we describe a new calibration method to individually characterize each sensor chip and each buffer solution before performing biosensing measurements with the OWLS technique (figure 3.2). This novel protocol will allow performing kinetic experiments with great accuracy, regardless the working conditions. Firstly, for a specific sensor chip, the incoupling angle will be measured in air and in water to obtain, after simulations, the intrinsic parameters of the waveguide film (refractive index n_F and film thickness d_F). The waveguide parameter characterization will then add to the analyses of the refractive index of buffer solutions of interest to get more accurate values of the properties of the adsorbed layer (refractive index n_A and film thickness d_A) on a biosensing experiment, and therefore to calculate the real surface coverage of the sensing surface. Moreover, studies at different concentrations and temperatures within the physiological pH have been attempted.
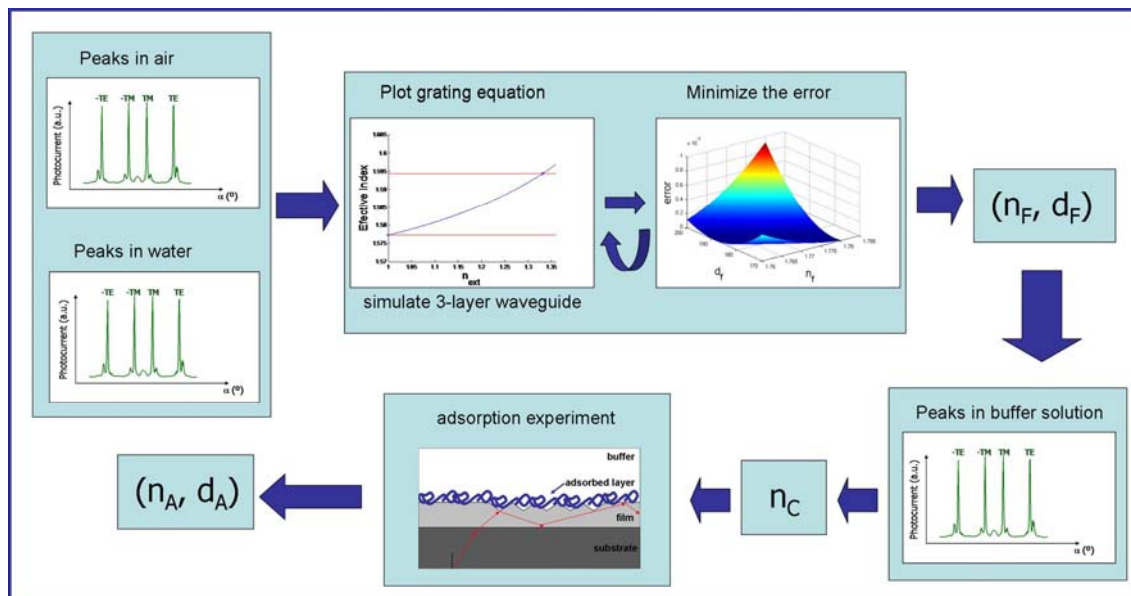
Fig. 3.2.- Flow chart for the calibration process. This figure describes the standard procedure for calibrating each sensor chip, the buffer solutions and finally calculating the parameters of the adsorbed layer. Upon measuring the coupling spectra in two known media, and minimising the error between the grating equation and the dispersion equation, the intrinsic parameters of the waveguide (n_F, d_F) can be obtained. In a second step, the coupling spectrum is measured in the buffer solution of interest and its refractive index, n_C, is calculated. Last, with all the parameters characterized, a kinetic experiment can be carried out.

Following the flow chart in figure 3.2, to calculate the intrinsic parameters of a specific waveguide we need to define a theoretical model. In section 3.3 of this chapter we will discuss the different approaches to model our system. The equations will be solved with numerical methods using as initial conditions the nominal parameters of the waveguide. The solutions that minimize the error in the simulations will be chosen as the intrinsic parameters of the waveguide (n_F, d_F). Setting these calculated values as constants, and with the measurements obtained for the different buffer solutions, in section 4.2 we will reverse our model to calculate the refractive index of the media with no proteins dissolved, n_C. Once the whole system is characterized, we could use our model to monitor with great accuracy an adsorption experiment. All this work will set the calibration bases for any optical grating biosensor instrument.

2   THEORETICAL BACKGROUND: MODEL OF A 3-LAYER WAVEGUIDE SYSTEM

Quantitative results derived from measurements by evanescent field based techniques depend on a theoretical model of the waveguide film. Taking into account that the biomolecule adsorbed layer onto the sensing grating surface is not only composed by the biomolecules, but also by some amount of the buffer solution [5], the refractive index of this adsorbed layer, n_A, is:

$$n_A = n_C + \frac{dn}{dc} c_A \qquad (3.1)$$

where c_A is the concentration of adsorbed molecules, n_C is the refractive index of the buffer solution and dn/dc is the refractive index variation of the adsorbed layer due to the variation in the amount of adsorbed biomolecules (see Fig.3.3).

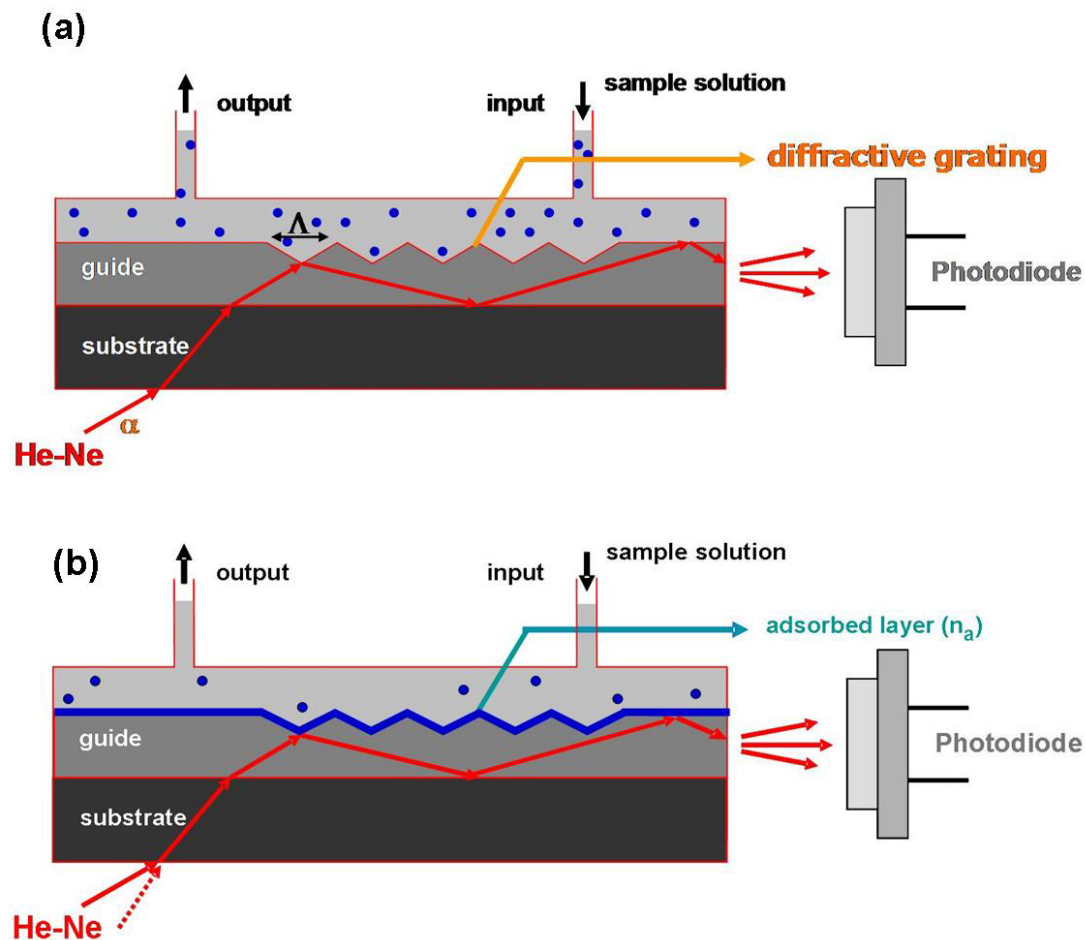Fig. 3.3.- Grating coupler scheme. α is the incoupling angle and Λ is the grating period. (a) The cover layer is the sample solution. (b) When an adsorbed layer is created onto the surface (shown in blue), the coupling conditions change.

If the adsorbed layer forms an isotropic and homogeneous layer, the surface concentration of the absorbate can be defined by the Gibbs equation [5]:

$$M = c_A d_A \qquad (3.2)$$

where d_A is the thickness of the biolayer. Taking into account the relationship of the concentration of the adsorbed layer with its refractive index from equation 3.1, the mass adsorbed on the surface, measured in ng/cm^2, can be calculated by equation (3.3):

$$M = d_A \frac{n_A - n_C}{dn/dc} \qquad (3.3)$$

Thus, the changes in the refractive index and in the thickness of the adsorbed layer (n_A and d_A, respectively) measured by the optical methods (variation of the incoupling angle upon immobilization of molecules onto the sensor surface) [13] should be modelled taking into account this "hybrid adsorbed monolayer." These outputs are extremely relevant, since they address us to calculate the surface coverage percentage upon comparison with the theoretical thickness of a monolayer.

The effective refractive index (N_{eff}) is a parameter extracted from the grating equation (3.8) and it is also related to the parameters of the waveguide. Upon measuring the incoupling angle for two known cover media, the characteristic parameters of the waveguide, film refractive index (n_F) and thickness (d_F), can be extracted from the 3-layer model (substrate, film and cover, from figure 3.1) using the Thin Grating Approximation (TGA) that does not consider the grating as a layer:

$$N_{eff} = f(n_F, d_F, n_C) \qquad (3.4)$$

$$\pi m = \frac{2\pi}{\lambda}\sqrt{n_F^2 - N_{eff}^2}\,d_F - \arctan\left[\left(\frac{n_F}{n_S}\right)^{2\rho}\sqrt{\frac{N_{eff}^2 - n_S^2}{n_F^2 - N_{eff}^2}}\right] - \arctan\left[\left(\frac{n_F}{n_C}\right)^{2\rho}\sqrt{\frac{N_{eff}^2 - n_C^2}{n_F^2 - N_{eff}^2}}\right]$$

$$(3.5)$$

$$\text{where} \quad \begin{cases} \rho = 1 \text{ and } N_{eff} = N_{eff}^{TM}, \text{ for TM mode} \\ \rho = 0 \text{ and } N = N_{eff}^{TE}, \text{ for TE mode} \end{cases}$$

where $N_{eff}{}^{TE}$ and $N_{eff}{}^{TM}$ are the effective refractive indexes for the coupled modes TE and TM respectively and n_S is the index of the substrate. By determining these

parameters (n_F, d_F) and setting them as constants, the refractive index of the cover media can be studied reversing the 3-layer model (equation 3.5).
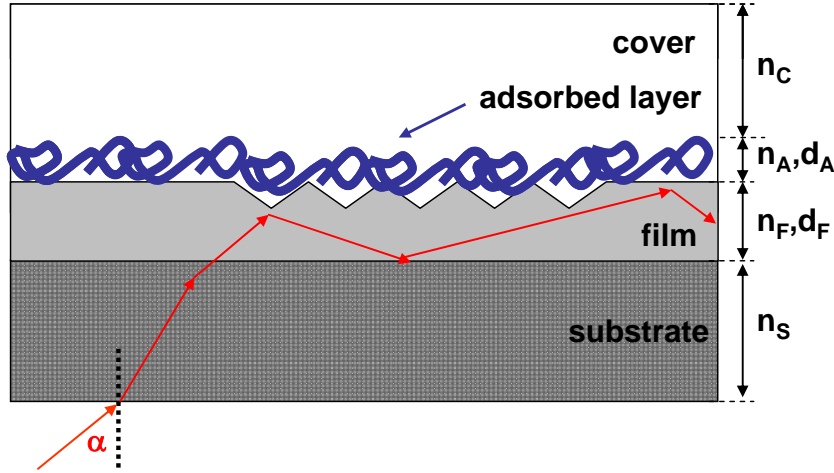

Fig. 3.4.- Grating coupler scheme. 4-layer model

Once the waveguide intrinsic parameters (n_F, d_F) and the cover media (n_C) are properly characterised, the properties of the adsorbed layer (n_A, d_A) can be studied through a 4-layer waveguide model (substrate, film, adsorbed layer and cover, from figure 3.4) [14]:

$$N = f\,(n_A, d_A) \tag{3.6}$$

$$\pi m = \frac{2\pi}{\lambda}\sqrt{n_F^2 - N_{eff}^2}\left(d_F + d_A\,\frac{n_A^2 - n_C^2}{n_F^2 - n_C^2}\left[\frac{\left(N_{eff}/n_C\right)^2 + \left(N_{eff}/n_A\right)^2 - 1}{\left(N_{eff}/n_C\right)^2 + \left(N_{eff}/n_F\right)^2 - 1} \right]^{\rho} \right)$$

$$- \arctan\left[\left(\frac{n_F}{n_S}\right)^{2\rho}\sqrt{\frac{N_{eff}^2 - n_S^2}{n_F^2 - N_{eff}^2}} \right] - \arctan\left[\left(\frac{n_F}{n_C}\right)^{2\rho}\sqrt{\frac{N_{eff}^2 - n_C^2}{n_F^2 - N_{eff}^2}} \right] \tag{3.7}$$

$$\text{where}\quad \begin{cases} \rho=1 \text{ and } N=N_{eff}^{TM},\ \text{for TM mode} \\ \rho=0 \text{ and } N=N_{eff}^{TE},\ \text{for TE mode} \end{cases}$$

In this case, when describing the previous equations, 3.4 to 3.7, we have assumed that the refractive grating is infinitely thin, and therefore does not behave like a

layer (TGA model). The effective refractive index is obtained from the in-coupling angle of the laser into the refractive grating ruled by the grating equation:

$$N_{eff} = n_C \sin\alpha + \frac{m\lambda}{\Lambda} \qquad (3.8)$$

where N_{eff} is the effective refractive index, α is the incoupling angle, n_C is the refractive index of the cover, m is the diffractive order, λ is the wavelength of the laser and Λ the grating periodicity.

3 EXPERIMENTAL

3.1 PREPARATION OF BUFFER SOLUTIONS

Hydrochloride acid (HCl), 4-(2-Hydroxyethyl)piperazine- 1-ethanesulfonic acid sodium salt (HEPES), sodium chloride (NaCl), sodium hydroxide (NaOH), tris(hydroxymethyl)aminomethane (Trizma base), polyethylene glycol sorbitan monolaurate (tween), ethylenedinitril tetraacetic acid (EDTA), tris(hydroxymethyl)aminomethane hydrochloride acid (Tris-HCl) and phosphate buffered saline (PBS) were purchased from Sigma Aldrich (Spain). Dulbecco's Modified Eagle Medium was purchased from Invitrogen (Spain).

All the buffer solutions were prepared in MilliQ water and set at physiological pH 7.5 (at 25ºC) with HCl or NaOH. Table 3.1 summarizes the buffer solutions used in this chapter and their acronym.

Table 3.1   List of buffer solutions

Buffer solution	Acronym
Milli Q purified water	MilliQ
4-(2-Hydroxyethyl)piperazine-1-ethanesulfonic acid sodium salt	HEPES
50 mM Hepes solution, 50 mM NaCl solution, 1 mM EDTA	HEPES hybridization
tris(hydroxymethyl)aminomethane hydrochloride acid	Tris-HCl
0.0165 mol tris-HCl, 0.0034 mol trizma base, 0.013 mol NaCl	Trizma
Phosphate buffered saline	PBS
0.1M PBS, 0.5% Tween20	PBS + tween
Dulbecco's Modified Eagle Medium	DMEM

1 tablet of PBS is dissolved in 200 ml of water to obtain 10 mM PBS (PBS tablets contain 0.0003 mol of sodium phosphate monobasic, 0.0016 mol of sodium phosphate dibasic, 0.022 mol of NaCl and 0.00054 mol of KCl). HEPES hybridization buffer was prepared with a mixture of 50 mM of HEPES solution, 50 mM NaCl solution and 1 mM concentration of EDTA. The mixture was sonicated until EDTA was completely solubilized. 200 mL of 100 mM Trizma buffer contains 0.0165 mol of tris-HCl, 0.0034 mol of trizma base and 0.013 mol of NaCl.

3.2 OWLS MEASUREMENTS

The OWLS instrument (MicroVacuum, Budapest, Hungary) measures the effective refractive index on the zeroth transverse electric (TE) and magnetic (TM) modes of a He-Ne laser coupled at specific angles onto a waveguide by an optical grating. Then, the software converts these angles into adsorbed layer mass and thickness by assuming an optical uniform layer and a refractive index varying linearly with mass density [13] upon using Feijter's Formula [11]. For details, see chapter 1 of this manuscript, section 3.2.1. The optical grating coupler sensor chip employed here (OWLS2400, MicroVacuum, Budapest, Hungary) is described in chapter 2 of this manuscript, section 5.2. Prior to the measurements, the chip surfaces were ultrasonically cleaned in isopropanol, dried with N_2 and then subjected to oxygen plasma for 2 min, which results in removal of low molecular weight species and oxidation of the chip surfaces. Therefore, a hydroxide layer (with reactive -OH groups) was produce on the surface layer, improving its adhesion properties and hydrophilicity.

Buffer sample solutions were injected using syringes into a liquid cell (~10 µl) at controlled temperature. A volume of 2 ml of each buffer was necessary to avoid bubbles in series of five measurements. Then, the incoupling angles were measured in each case and these data were ready to start the calibration in MATLAB® following the procedure schematized in Fig. 3.2. The temperature was controlled with accuracy better than ± 0.1ºC.

3.3. OPTICAL GRATING PARAMETER CALIBRATION

The OWLS instrument provides a software tool to characterize the intrinsic parameters of the chip sensors (n_F, d_F) automatically. This software combines the waveguide 3-layer model (3.5) with the grating equation (3.8). Then, upon measuring in air the incoupling angle for the TE and TM modes, the parameters of the waveguide (n_F and d_F) are calculated numerically using the N_{eff}^{TE} and N_{eff}^{TM} equations, using the nominal parameters of the waveguide as the initial conditions for the simulation. Once the waveguide is well characterized, it is possible to use the system as a refractometer, by measuring the coupling spectra in different conditions to obtain the refractive index of different buffer solutions and its dependence with the concentration of the analyte and with the temperature.

Modelling the grating analytically is a computing intensive task, requiring the use of descriptions like the coupled wave analysis or the integral method [15]. There is another issue to take into account when modelling the different layers of waveguides with a refractive grating patterned on the top. The waveguide can be modelled using the Thin Grating Approximation (TGA), which considers the grating thickness equal to zero (see fig 3.5a) and therefore evaluates the waveguide with the 3-layer model. Instead, the Equivalent Layer Approximation (ELA) considers the grating as an independent layer, and uses then a 4-layer model [14] described by the dispersion equation 3.9:

$$\pi m = \frac{2\pi}{\lambda}\sqrt{n_F^2 - N_{eff}^2}\left(d_F + d_G\,\frac{n_G^2 - n_C^2}{n_F^2 - n_C^2}\left[\frac{\left(N_{eff}/n_C\right)^2 + \left(N_{eff}/n_G\right)^2 - 1}{\left(N_{eff}/n_C\right)^2 + \left(N_{eff}/n_F\right)^2 - 1}\right]^{\rho}\right)$$

$$- \arctan\left[\left(\frac{n_F}{n_S}\right)^{2\rho}\sqrt{\frac{N_{eff}^2 - n_S^2}{n_F^2 - N_{eff}^2}}\right] - \arctan\left[\left(\frac{n_F}{n_C}\right)^{2\rho}\sqrt{\frac{N_{eff}^2 - n_C^2}{n_F^2 - N_{eff}^2}}\right] \qquad (3.9)$$

$$\text{where} \quad \begin{cases} \rho = 1 \text{ and } N = N_{eff}^{TM}, \text{ for TM mode} \\ \rho = 0 \text{ and } N = N_{eff}^{TE}, \text{ for TE mode} \end{cases}$$

As shown in figure 3.5b, this additional layer would have a thickness equal to that of the grooves depth, and a refractive index dependent on the indices of the materials involved (material of the grating and buffer solution) and on the duty cycle, τ, of the structure [16]:

$$n_G = \sqrt{\tau n_F^2 + (1-\tau) n_C^2}$$ (3.10)

A description based on TGA provides parameters slightly dependent on the buffer ($n_F = f(n_C)$, $d_F = f(n_C)$), but the ELA approach is buffer independent [16] and, for square shaped gratings, leads to more accurate predictions, as demonstrated in a previous work [17].
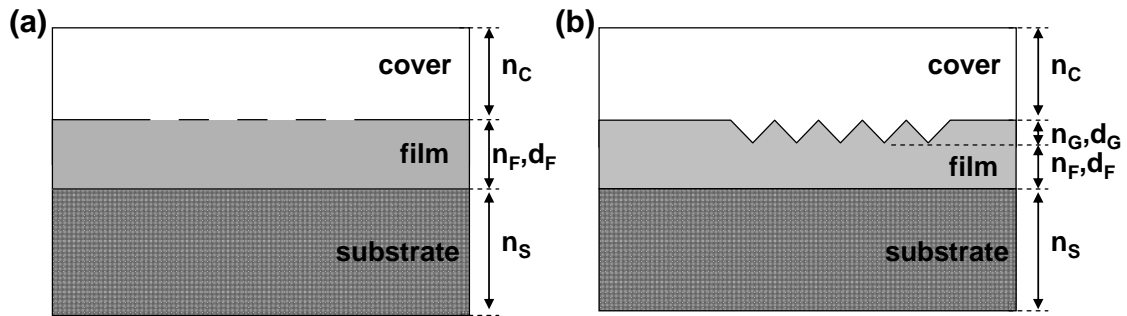

Fig. 3.5.- (a) Thin Grating Approximation (TGA), and (b) Equivalent Layer Approximation (ELA).

The OWLS software uses the Thin Grating Approximation (TGA) to model the waveguide, which usually leads to good results regarding the chip characterization and even the biochemical response, but for measuring refractive indices with precisions better than 0.1% the more accurate ELA procedure is needed.

To evaluate the influence of the two models and since we need two equations to resolve the two parameters (n_F, d_F), instead of using the dispersion equation for TE and TM modes, we will use only the TE model but in two different conditions corresponding to two different cover media. Since most of the buffers employed in characterizations are manually prepared except the air and the MilliQ water, these two media would be taken as calibration points (figure 3.6).
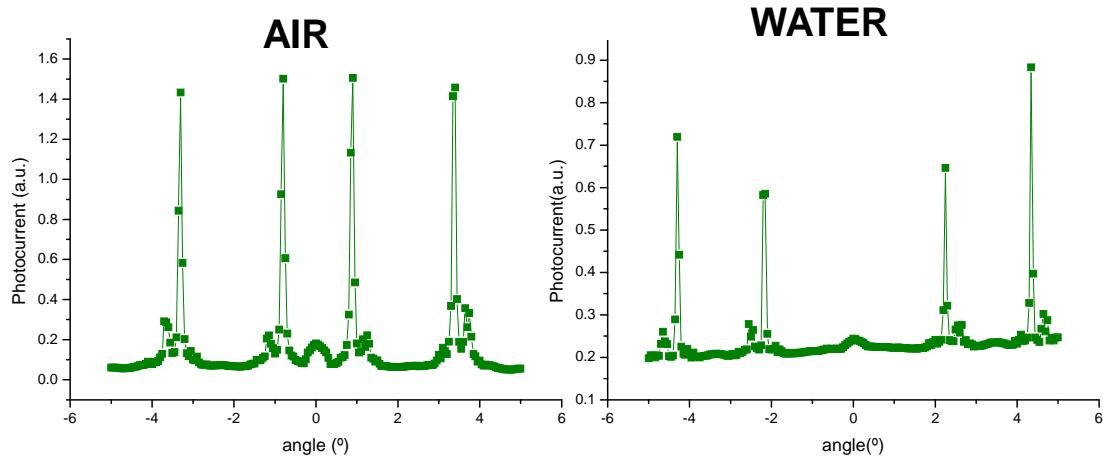
Fig. 3.6.- Air and MilliQ water incoupling spectra measured with an OWLS grating coupler. By assuming that the refractive index of air and water are 1.000000 and 1.331144 respectively, we can calculate the intrinsic parameters of this specific sensor chip.

The angles at where the TE polarized light is coupled into the waveguide for air and water are translated into the effective refractive indices, N_{air}^{TE} and N_{water}^{TE}, through the grating equation (3.8). The functional dependence is fixed from the waveguide dispersion equation for the 3-layer model –TLA- (3.5) or the 4-layer model –ELA- (3.9). The TGA model is solved through the normalized dispersion equation [18] and the ELA model is solved using a transfer matrix approach [19].

Setting the nominal parameters of the sensor chip as initial conditions and, minimizing the error when sweeping across thicknesses and refractive indices of the waveguide, the film parameters (n_F, d_F) are calculated (see figures 3.7 and 3.8). The objective is to find the values of (n_F, d_F) that reduce the dispersion $\sigma(n,d)$, in between the measured, $N^{grating}$, and the calculated, $N^{dispersion}$, values of the effective refractive index:

$$\sigma(n,d) = \sum_c \left[N_c^{grating} - N_c^{dispersion} \right]^2 \qquad (3.11)$$
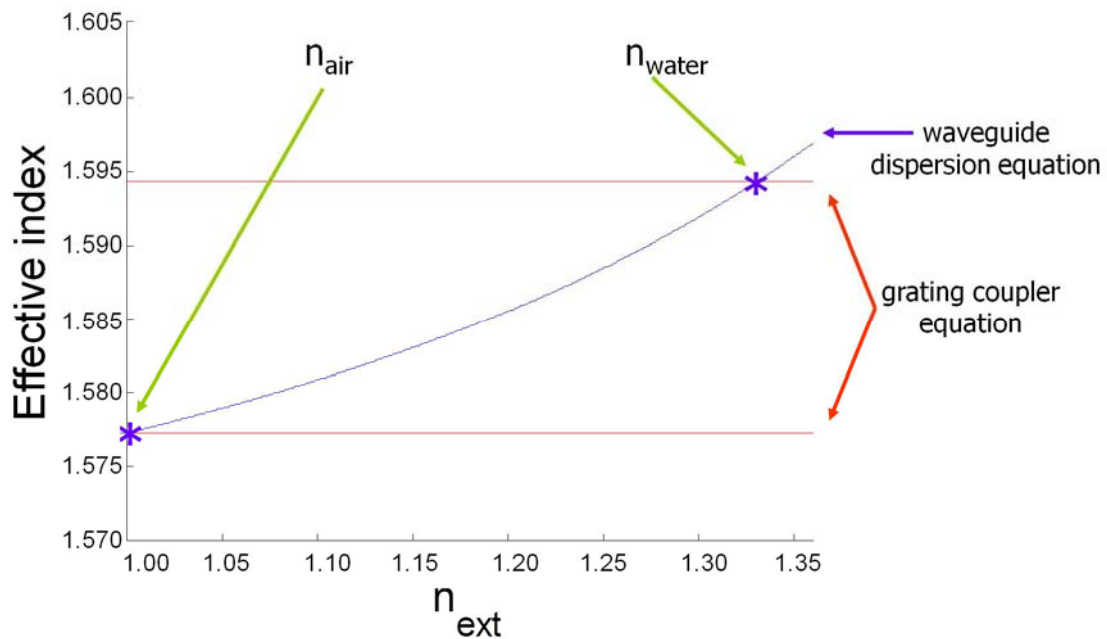
Fig. 3.7.- Calibration of the parameters of a waveguide chip. The angles at which the light is coupled for air and water are measured and included in the grating equation (eq. 3.8) to calculate the effective refractive index, $N^{grating}$ (red lines). Then, sweeping across the thickness and refractive index of the waveguide (taking the nominal parameters as initial conditions) the dispersion equations (TGA eq. 3.5 and ELA eq. 3.9) are used to calculate the effective refractive index, $N^{dispersion}$ with the refractive index of the buffer solution, n_{ext} (blue curve).

Fig. 3.8.- Plot of the error in the calculation of the effective refractive index for given pairs (n_F, d_F). Minimizing the difference between the $N^{grating}$ calculated through the grating coupler equation and the $N^{dispersion}$ calculated through the dispersion equation for the two calibration points, it is possible to obtain the parameters of the waveguide.

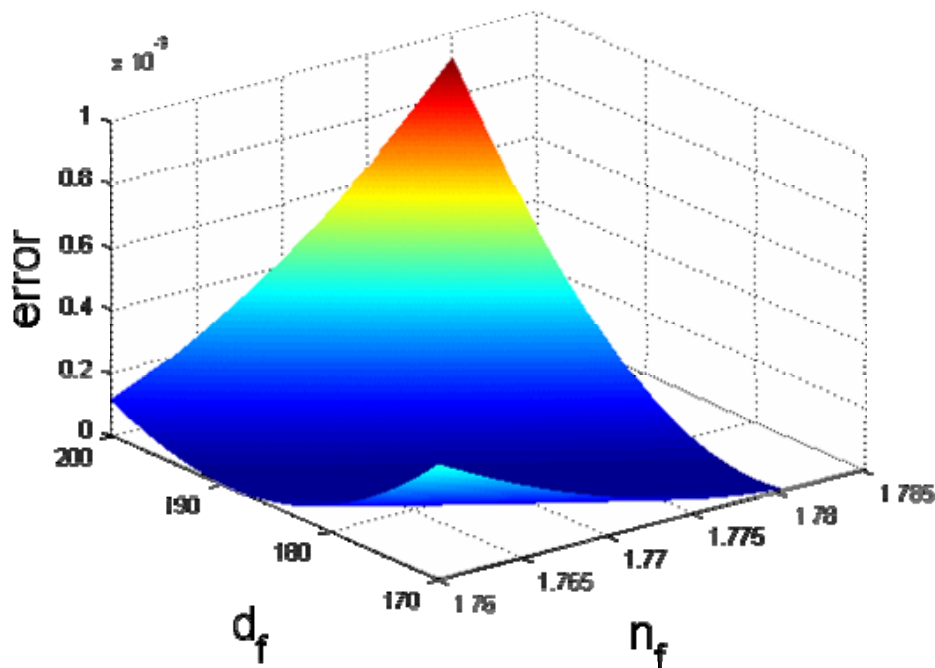Once the waveguide parameters are calibrated, we can set them as constants in the dispersion equation (3.5 and 3.9). Then, upon measuring the incoupling angle, it would be possible to calculate the refractive index of unknown buffer solutions and their variation with the external conditions.

4   RESULTS & DISCUSSION

4.1.   WAVEGUIDE PARAMETER CALCULATION

To understand the influence that using the 3-layer model (TGA) or the 4-layer model (ELA) have in the calculation of the waveguide parameters (n_F, d_F), we have characterized several chips using the calibration protocol described in section 3.3, using the two models. The obtained results for the characterization of a model waveguide (the behaviour of all measured sensors was equivalent) with the two approaches, TGA and ELA, are shown at Table 3.2.

Table 3.2   Values of the film parameters (n_F, d_F) for a particular chip

Method	$\overline{n}_F$ [a]	$\overline{d}_F$ (nm)[a]	var(n_F)[b]	var(d_F)[b]	S(n_F, d_F)[c]	n_C
TGA	1.7803	171.86	$1.18 \cdot 10^{-6}$	86.99	0.0674	$1.331563 \pm 7 \cdot 10^{-6}$
ELA	1.7828	174.445	$2.46 \cdot 10^{-7}$	1.32	$3.87 \cdot 10^{-4}$	$1.321567 \pm 2 \cdot 10^{-6}$

Notes: [a] mean values, [b] variances, [c] covariance.

The obtained film refractive indices only vary in a 0.14% and the film thickness in a 1.5%. The small difference in the values obtained for the waveguide parameters rely on the fact that the real refractive grating depth of these waveguides is really small (< 10 nm). These slightly different values hold the statement that the presence of the grating modifies the behaviour of the OWLS sensor chips, but they also suggest a more surprising conclusion: both the TGA and the ELA characterizations lead to equivalent behavioural descriptions. Although the calculated film parameters are different, the two methods bring on equal results -within the permitted accuracy- when calculating the refractive index of the cover upon new measurements. The first idea is held by the evidence that depending on the grating thickness, the TGA parameters (n_F, d_F) calibrating the waveguide change, while the second relies on the fact that regardless the model, once the grating depth is set to a fixed value (selected from physical

measurements or from the specifications of the manufacturer), a set of parameters can be found that provide the same characterization curve. Meaning that, if we calculate the parameters through the TGA approximation and then we calculate the cover refractive index through the 3-layer model, we obtain the same results than calculating it through the 4-layer model, when the parameters are obtained through the ELA approximation.

Finally, the more simple method, TGA, is chosen as the standard calibration procedure for the data treatment. With such calibration and precise measurement of the refractive index of the buffer and its variation with the concentration of the analyte, it is possible to predict an adjustment of about 10% in the calculation of the pair (n_A, d_A) and therefore in the calculation of the surface coverage [7].

4.2. MEASUREMENT OF BUFFER SOLUTION REFRACTIVE INDEX

An accurate measurement of the refractive index of the buffer solutions is necessary to be able to quantitatively evaluate the surface concentrations of adsorbed species [20]. A good characterization of the buffer solution is necessary when performing kinetic experiments as, to be able to calculate the surface coverage of a biomolecule adsorbed onto the sensor, it is essential to know how the refractive index of the solution changes with the concentration of the analyte (equation 3.3). Precision of 10^{-6} on the value of the buffer refractive index will lead to an appropriated buffer differentiation [5]. The refractive index increment parameter is $dn/dc = 0.153$ cm^3/g for a typical protein solution in MilliQ water, but this value has been reported to change until 0.182 cm^3/g in the case of using a buffer solution that has a refractive index different than the water on the third decimal [5, 11]. To overcome this problem, in this section we have precisely characterized the refractive index of different buffer solutions commonly used in biological and biosensing experiments.

Once the waveguide chip has been calibrated and its intrinsic parameters (n_F, d_F) calculated, it is possible to directly calculate the refractive index of the buffer just by measuring the incoupling angle of the system and applying reversely the 3-layer model (3.5). As shown in figure 3.9, when having the real parameters of the chip it is possible to establish a linear fit between the incoupling angle and the refractive index of the buffer media.
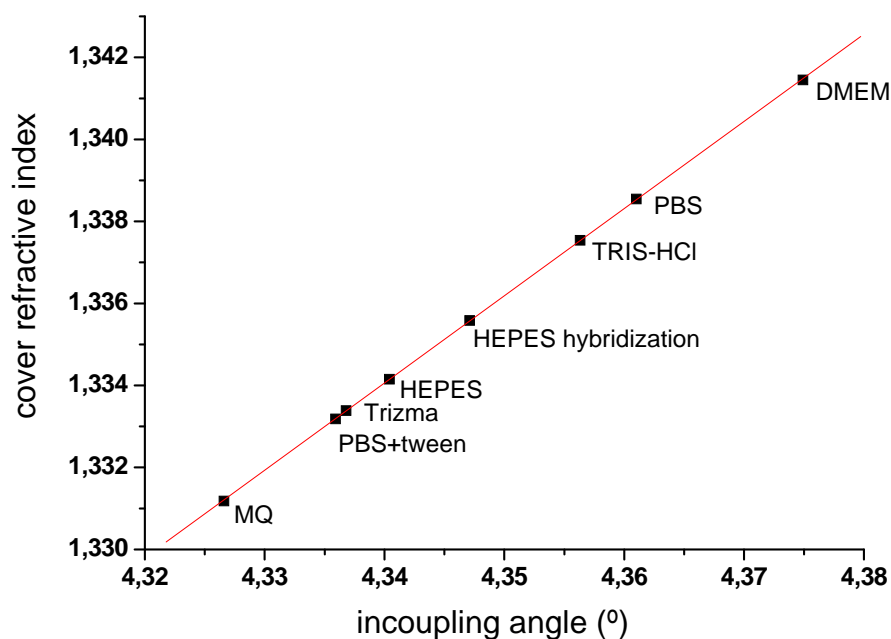
Fig. 3.9.- Refractive index of common buffer solutions (Table 3.1) measured by the OWLS system. The linear fit sets the refractive index of the cover upon measuring the incoupling angle.

The OWLS measurements together with our calibration are able to distinguish solutions with the requested precision of 10^{-6} on the refractive index. The OWLS instrument warranties the 10^{-6} precision and the calibration assures that the relative difference between one measurement and another is only due to the buffer solution. On the contrary, in the literature we can find values for the refractive index of buffer solutions very inaccurate and very uneven. For instance, when looking up the refractive index of the PBS, it is possible to find values such as: 1.3338 [21], 1.365 [22], 1.333 [23], 1.33 [24], 1.334 [25] among others, in opposition to our value: 1.3385. Our accurate definition of the refractive index will allow us to distinguish between different proteins in the solutions, or different concentrations of the same protein, even when the variation on the refractive index will be very smooth. Another issue is that the same solution prepared in different conditions, in a different day, or analysed at different temperature would have a different refractive index. This calibration allows calculating, not an absolute refractive index, but the particular refractive index right before the experiment. This precise control of the buffer solution regardless the working conditions, ensures high precision in the further analysis of an adsorbed layer.

4.3. DETERMINING THE CONCENTRATION OF AN ANALYTE IN SOLUTION BY OWLS

Taking into account the highly sensitive method developed for the determination of the buffer refractive index, the OWLS instrument should be valid to measure very small variation in analyte concentrations. As a practical example, the refractive indices of PBS solutions containing different concentrations of nano-size liposomes (nanosomes) were measured and correlated to the concentration of proteins expressed in their membrane (as the concentration of nanosomes itself is unknown). By the previous method, the refractive index value of PBS buffer was determined as 1.3385, and used as the one corresponding to a solution with zero nanosome concentration. Then, the refractive index of several nanosome's solutions were measured and plotted against the known parameter, which happened to be their protein concentration (Figure 3.10). As a result of these measurements, the parameter dn/dc, indicating the refractive index variation with the protein concentration, was extracted by fitting the experimental results to a linear function. The refractive index increment parameter extracted is dn/dc = 1.33·10^3 cm^3/g. This new value is going to be of great influence when calculating the characteristics of the nanosome adsorbed layer in a kinetic experiment and will be further used in the kinetics experiments in chapter 5 of this thesis.
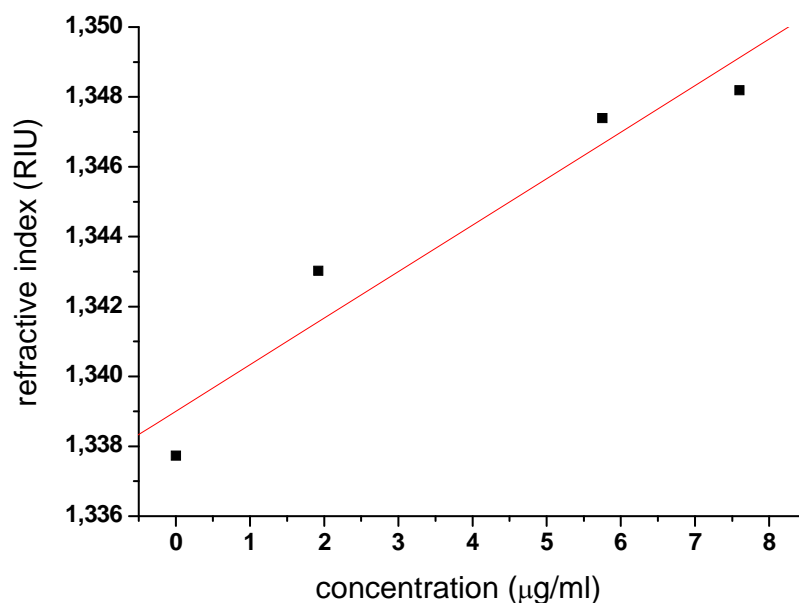

Fig. 3.10.- Refractive index of different concentrations of protein in a nanosome solution. The incoupling angle is measured for each concentration to calculate the refractive index of the solution. The slope of the linear fit is the variation of the refractive index of the solution with the concentration (dn/dc = 1.33·10^{-3} RIU ml/µg, R=0.97).

4.4. DEPENDANCE OF THE BUFFER REFRACTIVE INDEX ON THE SALT CONCENTRATION

Since some properties of the buffer solutions, such as salt concentration, temperature or pH will change depending on the experiment performed, it is of great interest to obtain a model describing the buffer refractive index variation as a function of these parameters. To use an accurate value of the refractive index of the buffer solution will ensure that any change in the refractive index measured during the kinetic experiments is independent of the buffer and only due to the adsorption of biomolecules onto the surface. It is well known than the refractive index of aqueous solutions is a linear function with the solute content over a wide range of concentrations relevant in physiology. Fig. 3.11 shows the water refractive index variation with salt concentration measured at 18 ºC (blue line) [26]. To test whether other buffers would follow similar behaviour, we have measured at 25 ºC different concentrations of PBS solution (10 mM, 20 mM and 40 mM) (Fig. 3.11, red line), obtaining the expected linear dependence with R better than 0.999.
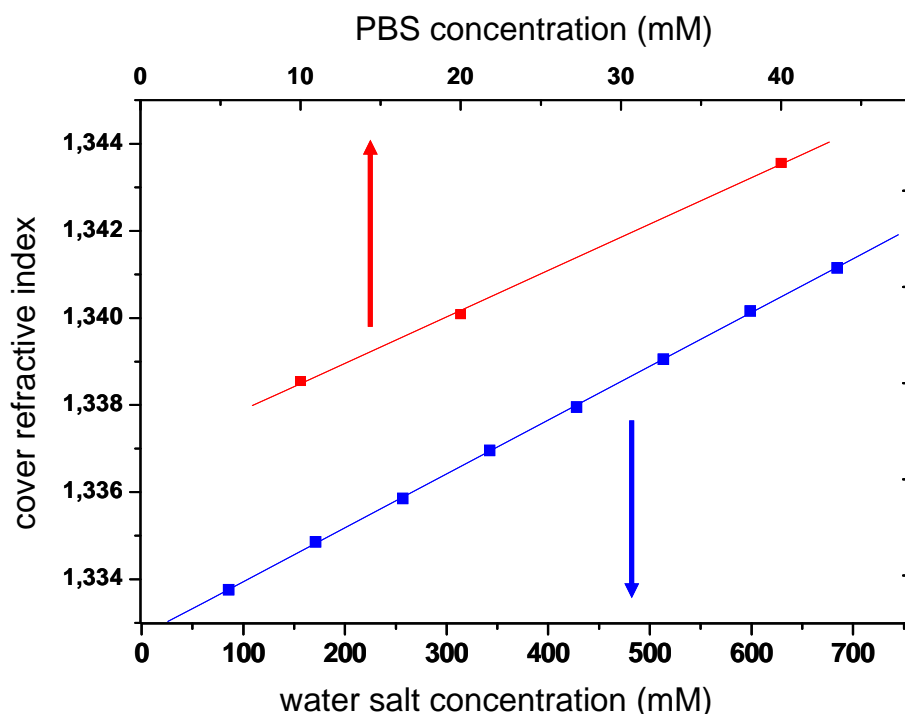

Fig. 3.11.- Refractive index of different PBS concentrated solutions (10 mM, 20 mM and 40 mM) measured at 25ºC [experimental values obtained in this work] and refractive index variation of the water with the salt content [26].

PBS is a water-based salt solution containing a mixture of different salts: sodium chloride, sodium phosphate, and, in our formulation, potassium chloride and potassium phosphate. The linear dependence of the refractive index of water and PBS with the salt concentration is as follows:

$$n(PBS) = 1.33681 + 0.00168 * [PBS (mM)], R=0.9996$$
$$n(water) = 1.33275 + 0.00001 * [water (mM)], R=0.9999$$

These results can be used to easy calculate the influence of the salt concentration of the buffer in an adsorption experiment, and to discriminate this effect from the real kinetics of the adsorption.

4.5. DEPENDANCE OF THE BUFFER REFRACTIVE INDEX ON THE TEMPERATURE

Another important external parameter to take into account when performing biosensing experiments is the temperature. The two typical working temperatures are the room temperature (25 ºC) and the physiological temperature (37 ºC). At figure 3.12, a study among this range of temperatures is presented for MilliQ water, standard 10 mM PBS and HEPES buffer solutions. The refractive indices of the buffers at the different temperatures were extracted from their incoupling angles, after calibration of the sensor chip following the procedure previously established.
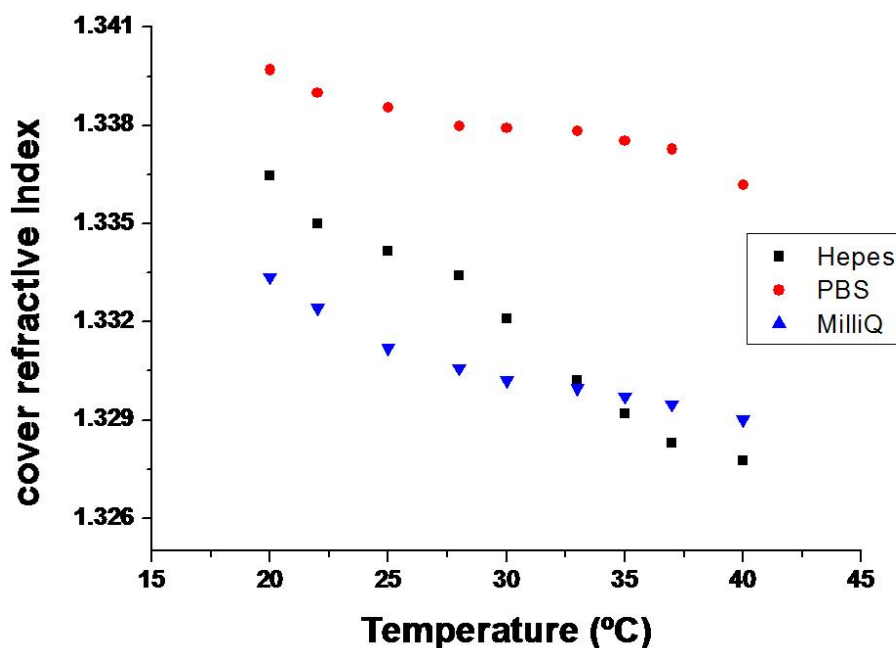

Fig. 3.12.- Refractive index of PBS and HEPES solutions measured at different temperatures.

Both behaviours are linear-like, as expected upon observation of the water dependence with the temperature [27]. Even though, the dependency is not perfectly linear, this can be due to the fact that the refractive index of the materials composing the waveguide also changes upon temperature variation. The substrate is made out of glass and its refractive index varies around $10^{-6}/°C$ [28], but the guide film index dependence would be the most important. Such a variation on the refractive indices would produce a great influence on the buffer index calculation. In order to clarify this point, the air and the water refractive index dependence with the temperature have been measured using the OWLS instrument to allow discriminating both influences, the effect of the waveguide materials and the one of the solvent. Using the tabulated values for the refractives indices of air and water, and following the procedure previously explained in section 4.1, the variation of the film refractive index with the temperature was calculated and it is represented in figure 3.13.
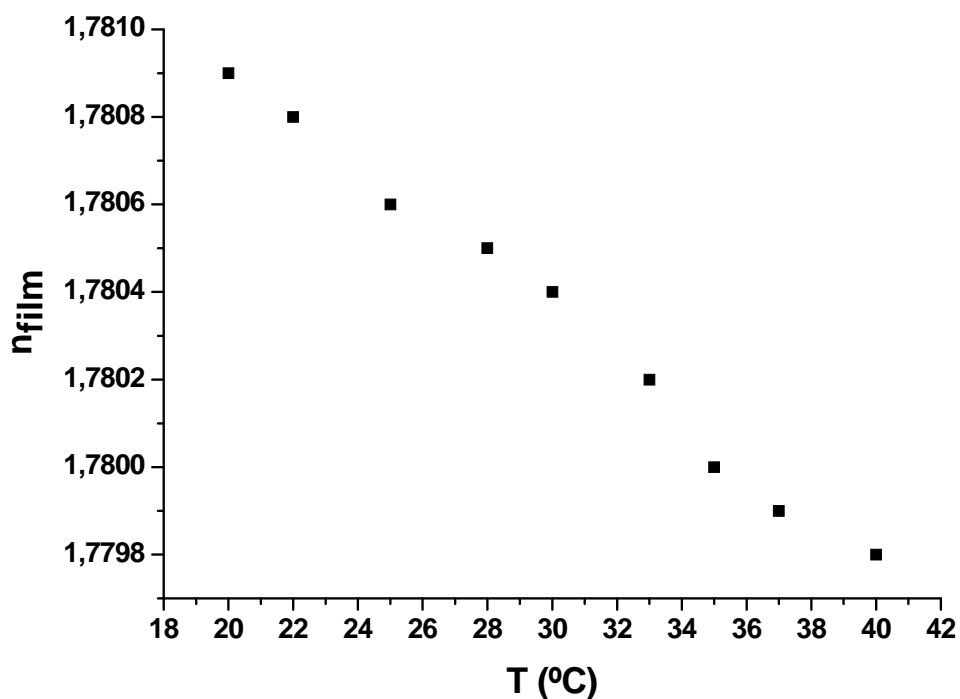

Fig. 3.13.- Variation of the refractive index of the waveguide film with the temperature.

As expected, the refractive index of the waveguide film is affected highly by temperature changes, around $5 \cdot 10^{-5}/°C$. This influence shall also be taken into account when carrying out a kinetic experiment to avoid errors in the measured values.

5 CONCLUSIONS

In this chapter a new calibration protocol has been established for experiments requiring high precision measurements. This routine includes an individual modelling of each sensor chip and considers, in a very precise way, parameters that are normally not taken into account, such as the buffer's nature, its composition and the working temperature. In this way, the particular refractive indices of buffer solutions can be measured with great accuracy before each experiment regardless the working conditions, ensuring high precision of the kinetics measurements and in the further analysis of an adsorbed layer. The TGA approximation allows modeling our waveguide with all the required precision, avoiding the need of using a more complicated ELA model.

6 REFERENCES

[1]   J. Vörös, *et al.*, "Optical grating coupler biosensors," *Biomaterials,* vol. 23, pp. 3699-3710, 2002.

[2]   X. H. Wang and S. Wang, "Sensors and biosensors for the determination of small molecule biological toxins," *Sensors,* vol. 8, pp. 6045-6054, 2008.

[3]   X. Fan, *et al.*, "Sensitive optical biosensors for unlabeled targets: A review," *Analytica Chimica Acta,* vol. 620, pp. 8-26, 2008.

[4]   P. Kozma, *et al.*, "Grating coupled optical waveguide interferometer for label-free biosensing," *Sensors and Actuators B: Chemical,* vol. 155, pp. 446-450, 2011.

[5]   V. Ball and J. J. Ramsden, "Buffer dependence of refractive index increments of protein solutions," *Biopolymers,* vol. 46, pp. 489-492, 1998.

[6]   S. Saini and et al., "Temperature dependence of pyrolysed sol-gel planar waveguide parameters," vol. 27, ed, 1994, p. 1134.

[7]   M. Kroslak, *et al.*, "Effects of Temperature, pH, and Salt Concentration on Î²-Lactoglobulin Deposition Kinetics Studied by Optical Waveguide Lightmode Spectroscopy," *Biomacromolecules,* vol. 8, pp. 963-970, 2007.

[8]   G. Velicelebi and J. M. Sturtevant, "Thermodynamics of the denaturation of lysozyme in alcohol-water mixtures," *Biochemistry,* vol. 18, pp. 1180-1186, 1979.

[9]   S. Bhattacharjya and P. Balaram, "Effects of organic solvents on protein structures: Observation of a structured helical core in hen egg-white lysozyme in aqueous dimethylsulfoxide," *Proteins: Structure, Function, and Bioinformatics,* vol. 29, pp. 492-507, 1997.

[10]   G. D. Fasman, "Practical Handbook of Chemistry and Molecular Biology," *Ed. CRC Pres Boston,* pp. 536-544, 1990.

[11]   J. A. D. Feijter and J. B. F. A. Veer, "Ellipsometry as a tool to study the adsorption behavior of synthetic and biopolymers at the air-water interface," *Biopolymers,* vol. 17, pp. 1759-1772, 1978.

[12]   Z. Heiner and K. Osvay, "Refractive index of dark-adapted bacteriorhodopsin and tris(hydroxymethyl)aminomethane buffer between 390 and 880 nm," *Appl. Opt.,* vol. 48, pp. 4610-4615, 2009.

[13]   K. Tiefenthaler and W. Lukosz, "Sensitivity of grating couplers as integrated-optical chemical sensors," *J. Opt. Soc. Am. B* vol. 6, p. 209, 1989.

[14]   J. Ramsden, "Review of New Experimental techniques for Investigating Random Sequential Adsorption," *Journal of Statistical Physics,* vol. 73, p. 853, 1993.

[15]   S. T. Peng, "Rigorous formulation of scattering and guidance by dielectric grating waveguides: general case of oblique incidence," *J. Opt. Soc. Am. A,* vol. 6, pp. 1869-1883, 1989.

[16]   R. E. Kunz*, et al.*, "Finite grating depth effects for integrated optical sensors with high sensitivity," *Biosensors and Bioelectronics,* vol. 11, pp. 653-667, 1996.

[17]   N. Darwish*, et al.*, "Second order effects of aspect ratio variations in high sensitivity grating couplers," *Microelectronic Engineering,* vol. 84, pp. 1775-1778, May-August 2007 2007.

[18]   A. K. Ghatak and K. Thyagarajan, *Optical electronics*. Cambridge, New York: Cambridge University Press, 1989.

[19]   J. Chilwell and I. Hodgkinson, "Thin-films field-transfer matrix theory of planar multilayer waveguides and reflection from prism-loaded waveguides.," *J. Opt. Soc. Am. A,* vol. 1, pp. 742- 753, 1984.

[20]   H. Zhao*, et al.*, "On the Distribution of Protein Refractive Index Increments," *Biophysical Journal,* vol. 100, pp. 2309-2317, 2011.

[21]   Y.-C. Lin*, et al.*, "An Enhanced Optical Multimode Fiber Sensor Based on Surface Plasmon Resonance With Cascaded Structure," *Photonics Technology Letters, IEEE,* vol. 20, pp. 1287-1289, 2008.

[22]   W. Z. Song*, et al.*, "Refractive index measurement of single living cells using on-chip Fabry-P[e-acute]rot cavity," vol. 89, ed: AIP, 2006, p. 203901.

[23]   J. Ingenhoff*, et al.*, "Biosensors using integrated optical devices," *Fresenius' Journal of Analytical Chemistry,* vol. 346, pp. 580-583, 1993.

[24]   M. B. Christiansen*, et al.*, "Polymer photonic crystal dye lasers as label free evanescent cell sensors," vol. 7402, A. D. Elizabeth and A. E. Louay, Eds., ed: SPIE, 2009, p. 74020L.

[25]   F. C. Chien and S. J. Chen, "Direct determination of the refractive index and thickness of a biolayer based on coupled waveguide-surface plasmon resonance mode," *Opt. Lett.,* vol. 31, pp. 187-189, 2006.

[26]   N. E. Dorsey and O. Krummel, "Properties of ordinary water-substance," *Hafner Publishing Company,* p. 295, 1940.

[27]   P. Schiebener*, et al.*, "Refractive index of water and steam as function of wavelength, temperature and density," *NIST,* vol. 19, pp. 677-717, 1990.

[28] G. Ghosh, "Dispersion-equation coefficients for the refractive index and birefringence of calcite and quartz crystals," *Optics Communications,* vol. 163, pp. 95-102, 1999.

CHAPTER 4: MONITORING THE IMMOBILIZATION OF OLFACTORY RECEPTORS ONTO SENSING SURFACES

1 INTRODUCTION & STATE OF THE ART

The olfactory system has the ability to discriminate and identify thousands of odorant compounds at very low concentrations. Recently, many researchers have been trying to develop artificial sensing devices that are based and mimic the performance of the natural mammal olfactory system [1-4]. A bioelectronic nose, which uses olfactory receptors (ORs) as sensing elements, would benefit naturally optimized molecular recognition (figure 4.1). A bioelectronic nose consists of a biological recognition part and a non-biological sensor platform part. Bioelectronic noses can be classified into cell-based and protein-based biosensors. Cell-based biosensors use living cells that express olfactory receptors as the biological sensing elements while protein-based biosensors use the olfactory receptor proteins. Various cell-based odorant detection methods, such as the cAMP (cyclic adenosine monophosphate) assay, Ca_{2+} imaging, microelectrode, SPR, and other sensing systems have recently been developed [5-16]. These cell-based biosensors offer noninvasive, easy operating, low cost, and long-term methods to measure cellular signalling triggered by ligands interacting with receptors on the cell membrane. Receptor protein-based bioelectronic noses have also been developed to directly detect odorant-receptor binding. In this case, the development of protein-based olfactory systems has been attempted using ORs as the sensing elements. This type of bioelectronic nose integrates individual secondary transducers with olfactory receptors anchored to it. These methods have the potential to detect odorant binding in a more stable manner, which is a prerequisite for high throughput screening.

Bioelectronic noses can be developed by combining the biological sensing elements with non-biological devices that could measure the binding of odorant molecules to the ORs. The application of bioelectronic nose in a wide range of different scientific and medical fields is essentially dependent on the development of highly sensitive and selective biosensors able to detect very low molecular weight compounds, down to 100 g/mol. These sensor systems for the rapid detection of specific odorants are crucial for environmental monitoring, anti-bioterrorism, disease diagnostics, and food

safety. Thus, in the near future, it will be a necessary requirement for its practical application in the industry that are the miniaturization for portable bioelectronic nose, sensor array for the multiplex detection of various compounds, and simultaneous data processing technique for the analysis of massive signals from sensor array. Recently, the European project, named "Bioelectronic Olfactory Neuron Device" (BOND, http://bondproject.org/), has started in an attempt of develop a bioelectronic nose based on the electrical properties of OR [17].
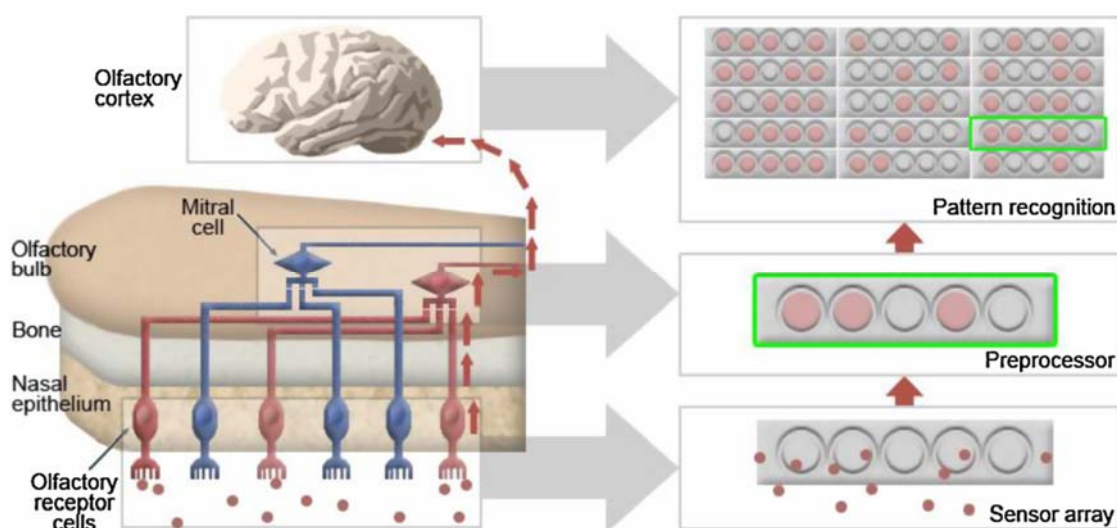

Fig.4.1.- Artificial nose devices mimic the human olfactory system. The electronic and bioelectronic nose systems simulate each stage of the human olfactory system, resulting in the recognition of volatile molecules by pattern analysis. Reproduced from [18].

The interaction of odorant molecules to ORs can be measured using various methods such as piezoelectric [4], optic [19], and electric devices [20]. In this introduction are reviewed the most recent bioelectronic noses that use ORs as the biological sensing elements and the various sensing devices that have been used as the non-biological sensor platform, such as quartz crystal microbalance (QCM) [21], surface plasmon resonance (SPR) [22], microelectrodes [21], and nanotube-based field effect transistor (FET) sensor [23].

To date, the many efforts that have been conducted in the design and development of the bioelectronic nose have led to significant improvements in this field. However, there are still some challenging aspects in the fabrication of the bioelectronic nose. First of all, only a few cognate ligands exist in the currently available odorant repertoire in mammal's OR. So, to produce the desired olfactory receptor, various OR

genes have to be cloned and expressed. Second, the low expression yield of recombinant ORs in heterologous cell systems can act as a bottleneck. Many attempts using numerous expression systems have been made to increase the level of expression, although adequate expression systems for the functional expression of ORs is still required. Third, concerning the anchoring of ORs on the solid surface of sensor, this is still an important factor in the field of biosensor development.

Although many studies on olfaction have been performed, an understanding of olfactory receptor (OR) function has progressed slowly due to the lack of appropriate heterologous systems for expressing and assaying odorant responses. The primary requirement to the development of a bioelectronic nose is an adequate expression system for ORs. Recently, various studies on cell-based bioelectronic noses have been conducted. Liu et al. developed an olfactory neuron-based neurochip using a light-addressable potentiometric sensor (LAPS). A LAPS is a silicon-based detector that allows one to measure the electric potential distribution along its surface. Olfactory sensory neurons (OSNs) were cultured on the silicon electrode and the response of the ORs with the environment were monitored by measuring the electric surface potential when illuminating a small spot of the sensor surface with a focused pulsed lightpointer [15, 16]. After exposing the cells to different concentrations of a neurotransmitter (glutamic acid), the receptor channels of the neurons opened and an extracellular potential signal was recorded. Furthermore, when stimulated by odorants a reversible signal was achieved at a specific frequency that was concentration dependant. However, the expression level of olfactory receptors in OSNs is very low (with a probability $P <$ 0.05 [24]) and it is somewhat difficult to culture olfactory sensory neurons (their survival rate is very low [25]). Thus, several attempts have been made to achieve functional expression of ORs in various heterologous systems; E. coli, yeast, and mammalian cells including Sf9, HeLa, HEK-293, PC12, and CHO cells [11-14, 17]. But ORs do not have an N-terminal import sequence, making it difficult to be expressed on the plasma membrane of heterologous cell systems. Even when OR expression is achieved on plasma membranes, the localization is also an issue, as ORs are continuously internalized [26]. Nanometer-scale sensors based on the nanotube (NT) - FET have been used for highly sensitive chemical sensing. Yoon et al. [27] described the integration of a human olfactory receptor protein (hOR2AG1) and conducting polymer nanotubes into a FET platform (CPNT-FET) suitable for electronic

measurement. Field-induced sensitivity was observed, eventually leading to the recognition of a target odorant at a remarkably low concentration. The hOR2AG1 was expressed in E. coli as a fusion protein with a glutathione-S-transferase (GST) tag at its N-terminus [11]. Their results showed the specific response of CPNT-FET to the target odorant, amyl butyrate. It is known that hOR2AG1 specifically responds to amyl butyrate, a common reagent for fruit flavor [28]. The FET showed a concentration-dependent increase in current change when exposed to amyl butyrate.

A second school is the one focused in studying OR-based bioelectronic noses. It is of high interest to establish solid supports capable of immobilising membrane proteins such as the ORs in a functional conformation, allowing high throughput ligand screening. ORs belong to the family of G-protein coupled receptors (GPCRs) and are very susceptible to denaturation, as they are composed of hydrophobic residues destabilised in aqueous environments. Supported or free spanning lipid bilayers, as well as vesicles or lipoprotein particles offer friendly interfaces to express OR receptors. This allows for an easier handling and stability of the ORs, but when it comes to odorant detection, the molecular pathway provided by the cell machinery is inexistent. Therefore, instead of the signal transduction provided by olfactory cells, the detection mechanism relies on a conformational change of the ORs upon odorant binding.

OR-based odorant detection has been electronically performed using electrochemical impedance spectroscopy (EIS) measurements [29]. The OR I7, which was expressed in yeast, was immobilized on a gold electrode as a multilayer through a mixed self-assembled monolayer (SAM). The electrode was functionalized with the biotinylated OR I7-specific antibody and then exposed to OR I7 in its membrane fraction. This method allowed for well-controlled immobilization of the receptor protein within a lipid environment. After measuring the variation of the polarization resistance with the odorant concentration, they reported a dose-dependent detection of odorants in solution demonstrating that well-controlled immobilization of OR proteins on a surface can provide for reliable and reproducible results by OR-odorants. However, some issues with non-specific adsorption and stability remained to be solved. Recently, the selectivity and sensitivity of SPR in detecting the binding between ORs and odorants has been examined. Rat OR I7 or hOR17-40 was co-expressed with $G_{\alpha olf}$ in a yeast expression system. Nanosomes containing ORs were obtained by mechanical disruption and immobilized on the surface of SPR. Vidic et al. immobilized nanosomes containing

hOR17-40 on the SPR surface and monitored the binding of OR-odorants by measuring the desorption of the $G_{\alpha olf}$ subunit from the lipidic bilayer [30]. No SPR signal was detected when helional, which is a specific odorant for hOR17-40 [31], or GTP (guanosine triphosphate) alone was incubated with the nanosomes. However, an SPR signal was induced after the injection of helional and GTP together. In addition, the sensitivity increased when GTP was replaced with a non hydrolysable analogue, $GTP_\gamma S$. These results demonstrated that ORs in nanosomes could discriminate a specific odorant ligand among odorants with similar structure and they were able to quantitatively evaluate the concentration of odorants. Last, the QCM has also been used in the development of conventional and OR-based electronic noses. As a piezoelectric crystal sensor, QCM can detect the interaction between various odorants and chemicals that have been coated on the crystal surface of the QCM. Ko and Park demonstrated this by using QCM coated with crude membrane extracts, containing the expressed receptor protein ODR-10 as the sensing component [4]. ODR10, which is an olfactory receptor from C. elegans, was expressed in E. coli. This system was shown to have high sensitivity and specificity against the specific odorant diacetyl.

But even though the functioning of OR-based bioelectronic noses has been already proved, a better understanding of the mechanism of OR-odorant binding on the molecular level is required for the development of a more efficient bioelectronic nose. To this purpose, a very robust sensing system is required that could enlighten the underlying mechanisms of the odorant-receptor interaction. Optical Waveguide Lightmode Spectroscopy is a perfect candidate as, taking advantage of the in-situ combination of optical and electrochemical techniques can ultimately allow getting a better understanding of the OR-odorant binding on the molecular level.

Efficient immobilization of ORs or cells on solid surfaces is the first step towards reliable and reproducible binding monitoring. Different functionalization techniques have been used so far in the literature to immobilize membrane fraction containing ORs onto sensing surfaces. Thiol-based chemistries are very popular for OR immobilization onto gold electrodes [10, 20, 22, 32-35], while silane-based approaches are the choice when using silicon-based FETs [21].

OWLS is a fine optical biosensing technique, that combined with electrochemistry (in the so called EC-OWLS) would allow to achieve a better insight into the receptor-odorant recognition process. Comparing the kinetics of the recognition

together with the associated electrochemical signal will enlighten the recognition process that, even though is thought to be a conformational changed, is not yet fully understood.

To find a robust and specific functionalization strategy that could be used in the characterization process (by EC-OWLS) and in the ultimate bioelectronic nose consisting in an electrochemical sensing device, would obviously be an advantage. Polyelectrolyte-based SAMs have also been used to act as an interface between the sensor surfaces and ORs carried in liposomes [36]. This approach based on electrostatic interactions would work with similar efficiency onto gold electrodes and transparent conductive waveguides.

In this chapter, the immobilization of liposomes from yeast cells containing the olfactory receptor OR17-40 onto sensor surfaces has been characterized by means of OWLS. The objective of this work is to optimize the functionalization strategy of the sensor surface, leading to the effective attachment of the liposomes. In section 3.1 the size and homogeneity of nanosized vesicles containing ORs are characterized in solution and the efficiency of the immobilization strategy of nanosomes onto sensing surfaces is studied. In section 3.2, the number and availability of ORs on the surface is investigated. In summary, olfactory receptors carried by nanosomes were successfully immobilized specifically onto biosensor surfaces functionalized by mixed self-assembled monolayers, although the number of available olfactory receptors remains too low.

2 EXPERIMENTAL

2.1 CHEMICALS AND REAGENTS

The reagents were obtained from different companies: poly(L-lysine)-grafted-poly(ethylene glycol)/biotinylated (PLL(20)-g[3.5]-PEG(2)/PEG(3.4)-Biotin(50%)), was purchased in SuSoS (Switzerland) and prepared at 0.1 mg/ml in PBS. Streptavidin and Streptavidin-Texas Red were purchased in Cultek (Spain) and prepared at 0.1mg/ml in PBS. Anti-c-myc-biotin and Anti-c-myc-FITC, were purchased from Sigma Aldrich (Spain). c-myc and c-myc-FITC were obtained from Affinity Bioreagents (USA).

The buffer solution, phosphate buffered saline (PBS), was purchased from Sigma Aldrich (Spain) and prepared at a concentration of 10 nM in Milli Q water. It was filtered prior to use. Lysis buffer was prepared by dissolving 2,2 g sorbitol in 20 ml milliQ water, adding 2,5 ml 1M Tris/HCl pH7.5 (from Merck, Spain), and 50 μl 1M Ethylenediaminetetraacetic acid (EDTA, from Panreac, Spain). Then 50 μl of 100 mM phenylmethanesulfonylfruoride (PMSF, from Sigma, Spain) stock solution (in ethanol) was added. In the meantime, 1 tablet of Protease Inhibitor Cocktail (from Roche, Spain) in 1 ml milliQ water was dissolved and added to the total volume. Later milliQ water was added until 50 ml of total buffer lysis was obtained.

Bovin Serum Albumin (BSA) was obtained from Sigma (Spain) and prepared 1% in Milli Q water. Nanosomes containing olfactory receptors OR17-40 were a gift from INRA (France).

2.2 SUBSTRATES

In order to achieve a similar nanosome's immobilization efficiency onto the working electrode of the ultimate electrochemical biosensor and onto the indium tin oxide (ITO) coated waveguide of the OWLS system, the experiments of functionalization and absorption of nanosomes were performed on two different substrates, gold and ITO.

The gold was obtained from NTB Buchs (Switzerland). Optical grating coupler sensor chips coated with a thin layer of 10 nm of ITO (OWLS2400, MicroVacuum, Budapest, Hungary) were used as the so-called ITO substrate. Prior to the measurements, both types of substrates were ultrasonically cleaned in isopropanol, dried with N_2 and then subjected to oxygen plasma for 2 min, which results in removal of low molecular weight species and oxidation of the chip surfaces. Worth is noticing that the RMS roughness of the gold substrates is 0.8 nm, while that of the ITO coated waveguides is 2.2 nm.

2.3 YEAST CELLS CULTURE AND ISOLATION OF NANOSOMES

Saccharomyces cerevisiae cells expressing the Olfactory Receptor OR17-40 were cultured in Sabouraud Broth media at 30ºC at the French National Institute for

Agricultural Research (INRA, France), in collaboration within the BOND project framework. Starting from 108 h growth of yeast cell culture (second part of exponential growth), the sample was washed twice in cold water (2 centrifugations at 5000G, during 5 min, at 4ºC). The pellet of cells was resuspended in the same volume of lysis buffer. Then, the cells are broken in a cell disrupter (Constant System LTD, Basic Z Model) at 2,5 Kbar, during 1 minute. Later, the cells are centrifuged again at 5000G, during 30 min at 4ºC. Around 500 μl of supernatant is recovered in a clean tube, and the same volume of lysis buffer is added. The solution is centrifuged again at 40000G, during 1 h at 4ºC. The supernatant is removed and the pellet containing the yeast membranes is resuspended in the same volume of lysis buffer + 10% glycerol (from Sigma).

To homogenize the sample, a Pellet Pestle Motor is used (Kontes, VWR, USA. Ref motor: 431-0100, Ref arm 0,5ml: 431-0095, Ref arm 1,5 ml: 431-0094). Then, the total protein concentration is quantified by BCA kit protein assay (Pierce, USA) using bovine serum albumin as a standard. To finish, the stock suspension of nanosomes with protein content of 2.5 mg/ml was aliquoted in vials of 25μl, frozen and stored at 80 ºC. A cartoon depicting the nanosomes expressing ORs is included in figure 4.2.
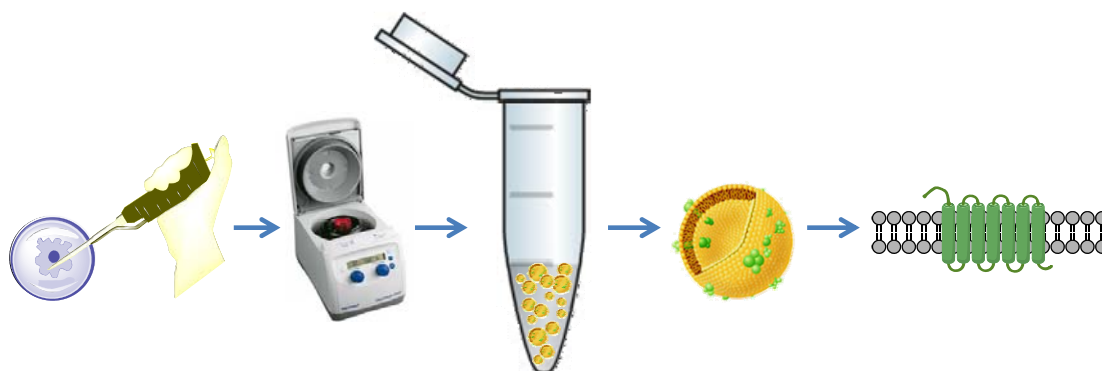

Fig.4.2.- Yeast expressing ORs were broken down and their intracellular content eliminated. The membranes were reorganized in nanosized liposomes expressing not only ORs, but also other membrane proteins from their cellular origin. The total amount of protein expression was quantified via a BCA assay.

Stock suspension of OR17-40 in its natural membrane fraction was thawed and resuspended in PBS on ice up to the desired concentration. The suspension was then treated in the ultrasonic bath in ice-cold water during 2 minutes in order to obtain a homogeneous size of nanosomes in suspension.

2.4. CHARACTERIZATION OF NANOSOMES IN SOLUTION

2.4.1 Light scattering

Dynamic Light Scattering (DLS) is a technique that uses the scattering of light produced by small spherical particles (much smaller than the wavelength) to determine their size distribution profile in suspension. DLS measurements were performed with a Zetasizer-Nano ZS90 (Malvern Instrument Ltd., England). The system was equipped with a He-Ne laser, 4 mW. A plastic cuvette of 1 cm optical length was used as sample container. DLS applications 5.10 software was used to analyze the data. Using the Mie theory and setting the parameters of the suspension, it was possible to translate the scattering intensity into number of particles for each hydrodynamic diameter. In this case PBS was used as the dispersion medium with refractive index 1.3385 and for the refractive index of the nanosomes 1.45 was chosen (as the average between refractive index of lipids and proteins). The average size reported here is expressed in number and fitted to a Gaussian adjustment. For each sample, three DLS measurements were conducted with a fixed 5 runs. In each run, the cuvette containing particles is illuminated by a laser and a frosted glass screen is used to view the sample cell. The rate at which the intensity of the scattered light fluctuates when detected by the optical set up is measured. Each run lasted 5 s. All the measurements were done at room temperature. Detection angle of 90º was chosen for the size measurements.

2.4.2 Cryo-fracture Transmission Electron Microscopy

The liquid specimens are rapidly frozen and fractured to create a metal replica that can be imaged by electron microscopy avoiding the extreme sensitivity of the sample to beam damage, which requires using a low dose mode giving lower image resolution. Freeze-fracture transmission electron microscopy (TEM) study was done according to the procedure described [37]. The nanosomes suspension was sandwiched between two copper platelets using a 400-mesh gold grid as spacer. Then the samples were frozen by liquid propane immersion, at -189ºC and fractured at -150ºC and 10^{-8} mbar in a BAL-TEC BAF 060 freeze-etching system (BAL-TEC, Liechtenstein). The replicas were obtained by unidirectional shadowing at 45º with 2 nm of Pt/C and at 90º with 20 nm of carbon. Later, the replicas were floated on distilled water during 5 min and observed in a Jeol 1010 TEM (Jeol, USA) at 80 kV, allowing magnification from

50x to 500000X. With the SIS MegaView III CCD camera we were able to investigate the size and shape of the nanosomes in suspension.

2.5. NANOSOMES IMMOBILIZATION

To immobilize our nanosomes onto gold and ITO surfaces two techniques have been used: direct unspecific adsorption of the nanosomes onto the surfaces and specific surface functionalization. For the specific surface functionalization procedure (Figure 4.3), the Au or ITO surface is activated by oxygen plasma during 1 minute at low power (Harrick Plasma, USA). Then, the hydrophilic surfaces are stabilized in PBS buffer solution during 10 minutes and further dipped into the PLL-g-PEG-biotin solution during 30 minutes to allow the polymer form a stable self assembled monolayer (SAM). After rinsing with PBS, the sample is dipped into a streptavidin solution during 1 hour. The sample is then rinsed to remove the unbounded streptavidin from the surface and further dipped into an anti-cmyc biotinylated antibody solution and left react during 1 hour. After incubation of the antibody, the sample is rinsed again with PBS as ready to react with the cmyc-tag coupled to the membrane proteins present in the nanosomes. A cartoon depicting the scheme of the functionalization process is included in figure 4.3.
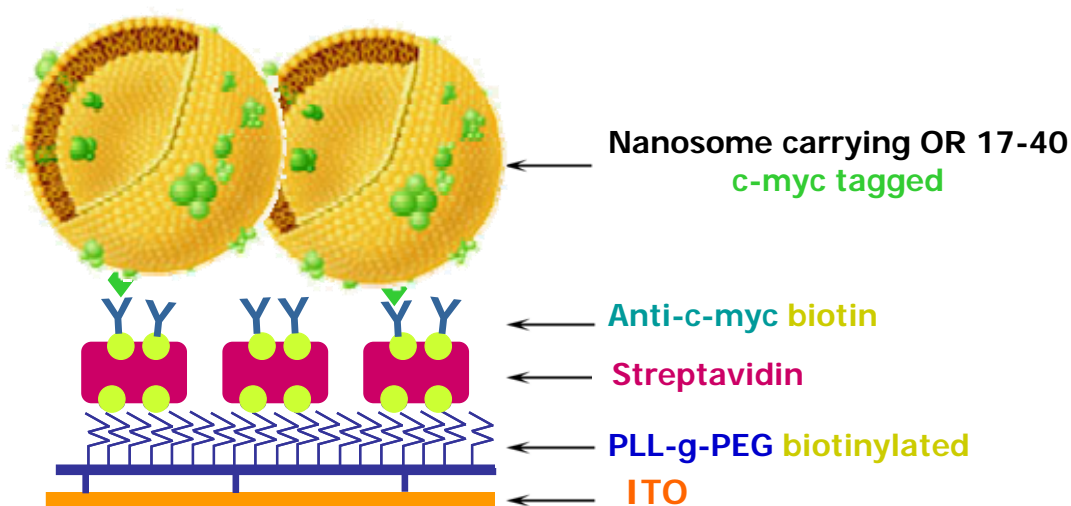

Fig. 4.3.- Scheme of the functionalization of the ITO substrate.

2.6. CHARACTERIZATION TECHNIQUES OF NANOSOMES ON SURFACES

2.6.1 Cryo-fixation Scanning Electron Microscopy

The immobilization of nanosomes onto ITO substrates was characterized by cryo-fixation Scanning Electron Microscopy (SEM). The freeze-drying SEM study was done as follows: the sample was frozen by impact freezing using a cryovacublock (Reichter-Jung, Germany) cooled by liquid nitrogen, and freeze-dried at -90ºC and 10^{-8} mbar in a BAL-TEC BAF 060 freeze-etching system (BAL-TEC, Liechtenstein) during 2 hours. Samples were then coated by unidirectional evaporation with 1 nm of Pt/C at an angle of 45º and with 10 nm of C at an angle of 90º, and they were kept in the same vacuum until the chamber reached room temperature. The samples were studied in a Nova NanoSEM 230 (FEI, USA).

2.6.2 Atomic Force Microscopy

Atomic Force Microscope (AFM) was operated in liquid, in PBS solution. A commercial AFM set-up from Nanotec Electronica™ is used together with Olympus Biolever® probes (nominal force constant 0.03 N/m). The mode operative used is jumping. This mode is an imaging mode that minimizes the lateral and normal forces applied to the sample, hence advantageous to image the nanosomes without modifying their morphology [38]. Applied forces are kept below 40 pN and recalibration is implemented to ensure constant applied force during the entire scan.

Characteristic parameters of the immobilization of nanosomes onto mica, gold and ITO substrates are extracted from the topographic AFM images. Individual nanovesicles are parameterized by height, width and volume; whereas the collective pattern is parameterized by the surface coverage measured using the Flooding algorithm (WSxM free software, http://www.nanotec.es/products/wsxm/ [39]).

2.6.3 Fluorescence microscope and microcontact printing (μCP)

In order to create a micropatterned surface where reactive spots could provide some contrast with non-reactive spots, microcontact printing technique was used in ITO substrates. For this purpose, a silicon master with holes of 5 μm in diameter and 0.8 μm in depth was used to create a replica in polydimethylsiloxane (PDMS) which was used as a stamp for the for μCP (figure 4.4). Prior to use, the stamp was ultrasonically

cleaned in ethanol for 15 min, dried under nitrogen stream and subjected to 1 minute of oxygen plasma.
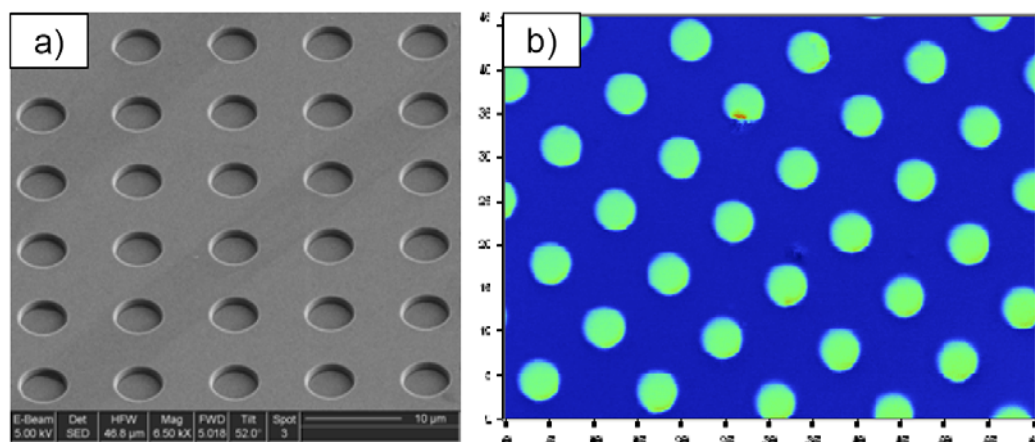

Fig.4.4.- (a) SEM image of the silicon master with holes of 5 μm in diameter and (b) White Light Interferometer (WLI) image of the PDMS replica with posts of 5 μm in diameter.

The PDMS stamp was 'inked' by immersion in the reagent solution for 10 minutes and then dried under a N2 flow. The ITO substrates were cleaned in 2-propanol in an ultrasounds bath for 10 minutes, then dried under nitrogen stream and later subjected to 1 minute of oxygen plasma. Then, the PDMS stamp was directly contacted to the functionalized substrate for 10 seconds, in air, at room temperature for the transfer of reagent to the surface. Immunostaining with fluorescently labelled antibodies was use to visualize the pattern. The surface immobilization efficiency was investigated by fluorescence microscopy (Nikon E1000, Japan).

Two different types of experiments were performed to evaluate the availability of c-myc probes in nanosomes absorbed or functionalized onto ITO substrates. Firstly, a PDMS stamp presenting 5 μm in diameter posts was employed to pattern Bobine Serum Albumin (BSA) onto the ITO surfaces. BSA was used to create passivation regions which avoid further protein adsorption [40]. Subsequently, 200 μl of the nanosome suspension (30 μg/ml of protein content in PBS) were left to adsorb onto the non-passivated areas of the pattern during 1 hour in such a way that a contrast between the areas covered by the nanosomes and the BSA would be created. Then, to detect the presence of the ORs, the sample was incubated with a fluorescently labelled antibody against the c-myc tag (anti-c-myc-FITC) at a concentration of 5 μg/ml in PBS. Once the

sample was rinsed and dried, it was ready to be observed under the fluorescence microscope.

Secondly, for the nanosomes immobilized through a functionalization layer, we followed the procedure described in section 2.5. We coated the ITO surface with a SAM of PLL-g-PEG-biotin and then patterned the surface with a 5 μm post stamp inked with 200 μl of TexasRed-labelled streptavidin (0.1 mg/ml). Afterwards, the streptavidin patterned areas were incubated first with an anti-c-myc biotin antibody (5 μg/ml, 200 μl) and then with a suspension of nanosomes (30 μg/ml of protein content in PBS). After 1 hour, the sample was rinsed with PBS, Milli Q water and dried with nitrogen. In order to avoid non-specific adsorption of the secondary fluorescent antibody on top of the immobilized anti-c-myc-biotin, a passivation step was performed. The sample was incubated with 1% BSA during 1 hour prior to the fluorescent antibody deposition. To detect the presence of tagged OR available for molecular recognition at the nanosome surface after their immobilization, the sample was further incubated with a solution of anti-c-myc-FITC antibody (5 μg/ml, 200 μl). Once the sample was rinsed and dried, it was ready to be observed under the fluorescence microscope.

2.6.4 OWLS

OWLS experiments were carried out to study the efficiency of the nanosomes immobilization onto ITO surfaces and to quantify the resulting surface coverage. The full process of functionalization and immobilization of nanosomes was performed following the description in section 2.5 in a very small flow chamber (volume of 12 μl) at a flow rate of 50 μl/min during depositions, and 200 μl/min while rinsing with buffer solution. Every immobilization step is carried out during 1 hour or longer until the signal is stable and then non-immobilized molecules are rinsed away during 10 minutes until a new baseline is achieved. A solution of 200 μl/ml of PLL-g-PEG-biotin was circulated onto the ITO waveguide to create a self assembled monolayer. After rinsing with PBS, the available biotins were exposed to a 0.1 mg/ml solution of streptavidin in PBS until saturation occurred. Non reacted streptavidin molecules were rinsed away with PBS. A solution of 5 μg/ml of biotinylated anti-c-myc antibody was circulated to react with the streptavidin, and later rinsed with PBS. Then, the immobilized antibodies were exposed to the suspension of nanosomes (30 μg/ml of protein content in PBS) to

react with the c-myc tags attached to the ORs. Not bound nanosomes were rinsed again with PBS.

Monitoring the kinetics of the immobilization of nanosomes onto a functionalized ITO with OWLS, allows us to quantify the efficiency of each step in the nanosome immobilization procedure. We have investigated the grafting efficiency of the antibody monolayer over the streptavidin, the optimal concentration of the nanosome solution and the availability of ORs in immobilized nanosomes. Every experiment was performed a minimum of three times to obtain significant results, presented as media +- standard deviation.

3 RESULTS & DISCUSSION

3.1 NANOSOME CHARACTERIZATION

3.1.1 Size and Morphology in solution

To study the size of the nanosomes and the homogeneity of the nanosome solution, we have performed Dynamic Light Scattering (DLS) measurements. As DLS requires large volume and highly diluted samples (0.0001% to 1% v/v), we have used 1 ml of a nanosome solution with a total protein concentration of 15 μg/ml, measured with a BCA kit protein assay.

The data obtained when analysing a control non-treated nanosome sample (just thawed) is shown in figure 4.5. The collected data (square data points) show two populations of nanosomes. Since the number of nanosomes in the second group is very small, we fit only the first population as a Gaussian plot (red line) following the next equation:

$$y = y_0 + \frac{A}{w\sqrt{\pi/2}} e^{-2\left(\frac{x-x_c}{w}\right)^2} \tag{4.1}$$

The center of the Gaussian, x_C, is the average size of the nanosomes and the polydispersity is obtained as the width, w, of the peak. As shown in figure 4.5, a non-treated sample shows nanosomes with an average size of around 400 nm in diameter, but with very high polydispersity of 178 nm.
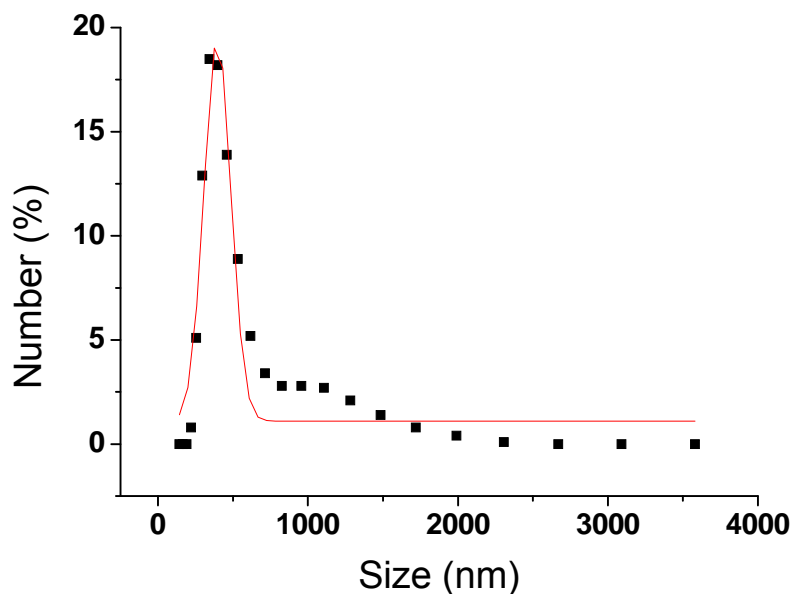
Fig. 4.5.- Dynamic Light Scattering measurement of a freshly thawed nanosome sample (black squares). The nanosome's population fits a very polydispersed Gaussian curve (red line) with center on 400 nm.

It would be ideal to have a homogeneous population of nanosomes with an average diameter below 100 nm, so then the OR are not too far from the sensing surface. In order to reduce the size of the nanosomes and to homogenize the nanosome population, we have sonicated (50 W, 40 Hz) the nanosome suspension in ice cold water during 2 and 20 minutes. The DLS data and correspondent fittings are shown in figure 4.6.
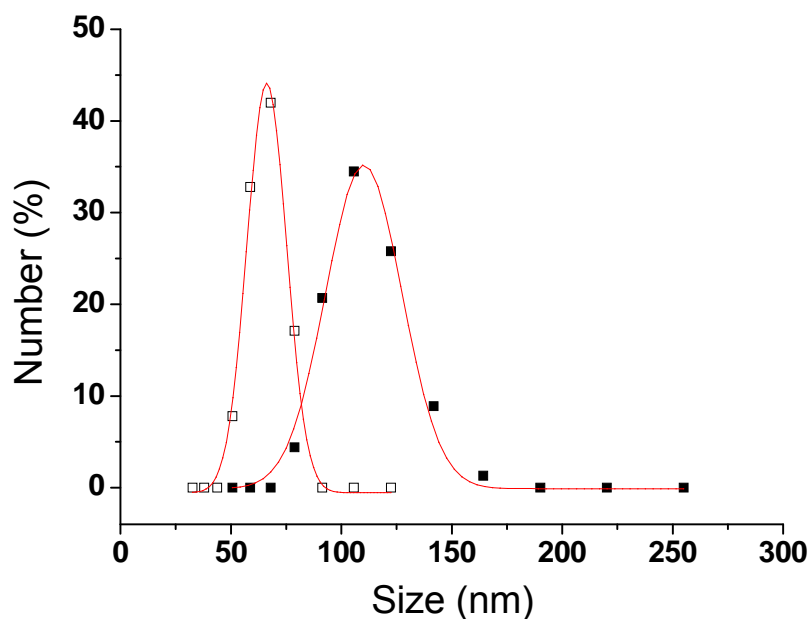

Fig. 4.6.- The DLS measurements for a nanosome sample sonicated during 2 minutes (solid squares) and 20 minutes (hollow squares) are presented together with their Gaussian fitting (red lines).

When the solution was sonicated during 2 minutes (solid squares) the nanosome size was much smaller and homogeneous than in the non-treated sample, with an average nanosome diameter of 110 nm and low polydispersity of 34 nm. But when the solution was sonicated during 20 minutes the average diameter of the nanosomes decreased down to 66 nm and the polydispersity was as small as only 18 nm.

A resume of the Light Scattering parameters for the different sonication times and their standard deviation is presented in table 4.1. The variation of nanosome diameter and the polydispersion of the sample with the sonication time are plot in figure 4.7. There is a big decrease in the average diameter of the nanosomes and a massive breakthrough in the homogeneity of the sample when this is sonicated during 2 minutes. This tendency gets accentuated even further when the sample is subjected to ultrasounds for longer times. As the polydispersity of the sample sonicated during 2 minutes is acceptable and the diameter of the nanosomes, ~100 nm, is good enough for our application, this is the chosen parameter for the homogenization step. A lower sonication time will allow for faster sample preparation at the same time that we ensure that the ORs will be less affected. As a conclusion, according to the DLS results, nanosome samples produced by 2 min of sonication in ice cold water have good characteristics in terms of nanosome size and polydispersity and will be used for further purposes.

Table 4.1 Light Scattering parameters for the different sonication times

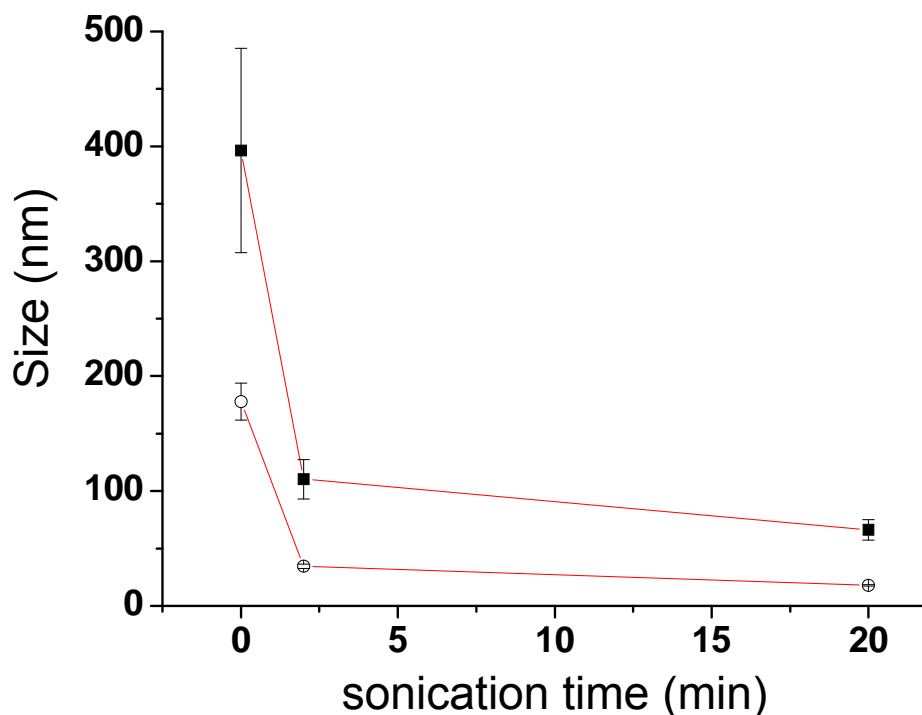| Minutes of sonication	x_c (nm)	w (nm)	Number (%)
0	396 ± 89	178 ± 16	99.9
2	110 ± 17	34.5 ± 1.8	95.7
20	66.2 ± 8.9	17.9 ± 0.7	99.7

Fig. 4.7.- Evolution of the nanosome diameter (solid squares) and the polydispersity of the sample (hollow circles) with the sonication time.

To investigate further the morphology of the nanosomes, imaging of the nanosomes in solution is performed. For this purpose Cryofracture Transmission Electron Microscopy is used. In this case, to allow for an easier localization of nanosomes in the TEM grid, the nanosome concentration was increased 100-folded to a total protein concentration of 2500 μg/ml. Two sets of samples were captured, non-treated nanosome suspension (figure 4.8) and suspension sonicated during 2 minutes (figure 4.9). Cryofracture TEM examination shows a fairly homogeneous nanosome distribution in the sample with a density of nanosomes in the surface estimated as 1 nanosome per 3 μm^2. The TEM micrographs (figures 4.8 and 4.9) show the presence of membrane proteins of around 5 nm size in the nanovesicles membrane regardless the sample treatment, verifying the ability of the cell disruption protocol to maintain the cell membrane integrity for membrane proteins to be present. Some of these membrane proteins are olfactory receptors.
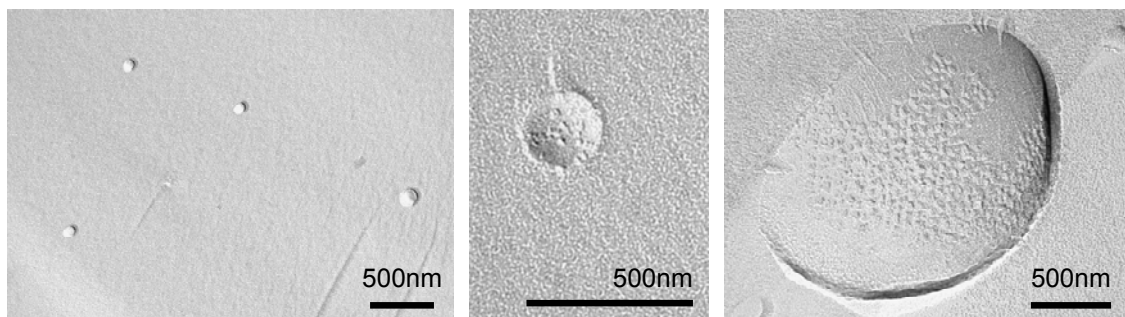
Fig. 4.8.- Cryo-fracture TEM images of a non treated nanosome suspension. Membrane proteins are clearly visible on the vesicle membrane. Nanosomes of a very wide range of sizes can be observed.
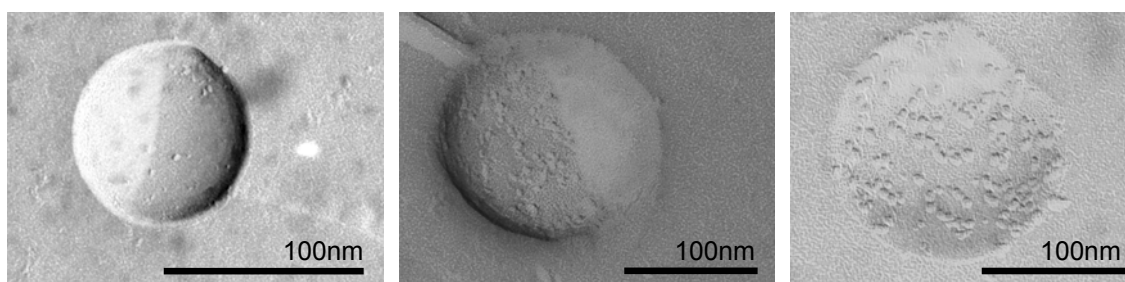

Fig. 4.9.- Freeze fracture TEM micrographs of a nanosome suspension treated with ultrasounds for 2 minutes. Membrane proteins are still clear on the nanovesicles surface, regardless the sonication treatment. The diameter of the nanosomes appears very homogeneous around 100 nm.

It is also clear from the freeze fracture electron microscopy pictures that liposomes with diameters ranging from 200 nm to 2 μm coexist in the non treated suspension, while in the treated sample the vesicles show a homogeneous diameter just above 100 nm. These results are consistent with the DLS data previously showed and confirm that our treatment to homogenize the nanosome suspension is successful.

3.1.2 Nanosome immobilization by physical adsorption

As discussed earlier, the aim of this chapter is to achieve an efficient and robust immobilization of ORs onto sensor surfaces. This is not a trivial process and many attempts have been published to date [10, 20-22, 32-35]. There are basically two ways of accomplishing this task: physical adsorption or chemical bonding. In this section the simplest approach, physisorption will be investigated.

To study the distribution of nanosomes onto a surface and too explore whether they keep the same shape and proportions as in liquid, we have characterised first of all nanosomes adsorbed on a mica substrate. For that purpose, we have deposited a drop of 200 μl of nanosomes suspension (sonicated during 2 minutes) with a concentration of

30 µg/ml during 1 hour on top of a mica substrate. Then we rinsed with PBS to remove unbound nanosomes from the surface, and performed in liquid imaging with the AFM. As can be seen in figure 4.10, nanosomes sit nicely onto the highly hydrophilic mica surface. The nanosomes though do not maintain a spherical structure, but spread forming a "scrambled-egg" shape with an aspect ratio of 1:6. This is basically due to the high attraction between the lipids and the surface, given its high hydrophilicity. The shape of the nanosomes should be tuned depending on the contact angle of the surface used and the immobilization protocol.
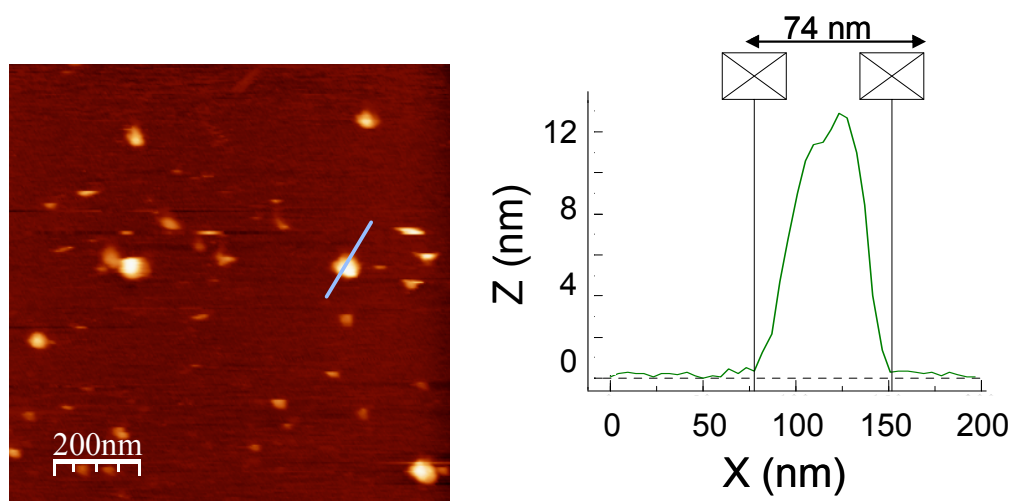

Fig. 4.10.- AFM image of nanosomes adsorbed onto a mica substrate.

Following the same procedure, a drop of nanosomes suspension was also deposited onto a gold surface and it was imaged by AFM operating in liquid environment (PBS) (figure 4.11). Although some nanosomes get adsorbed onto the gold presenting an aspect ratio of 1:7, the surface density is very low (5 nanosomes/μm^2).
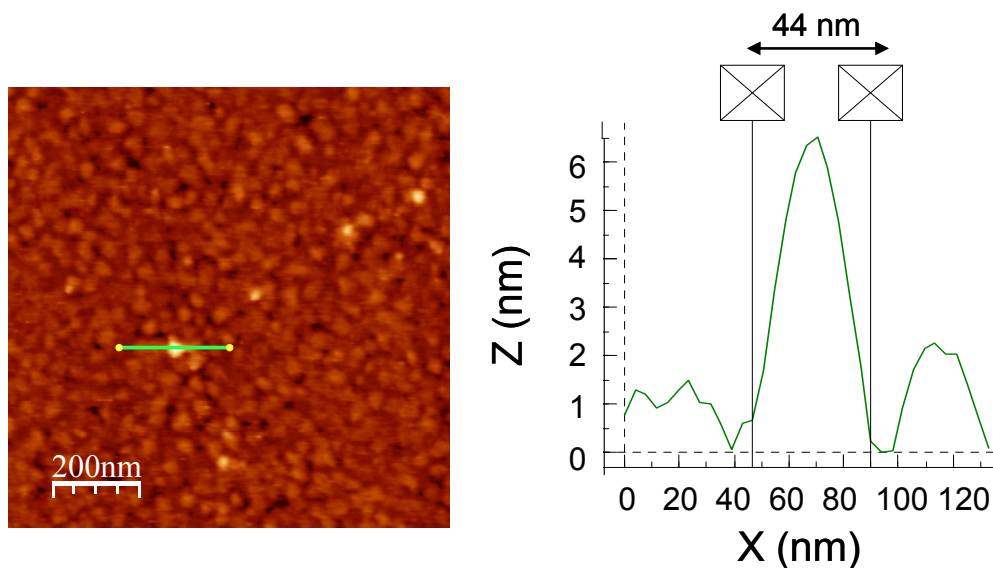
Fig. 4.11.- AFM image of nanosomes adsorbed onto a gold substrate.

A similar situation is found when the nanosomes suspension is left to adsorb onto an Indium Tin Oxide surface (figure 4.12), only a few nanosomes sit onto the ITO surface with an aspect ratio of 1:9.
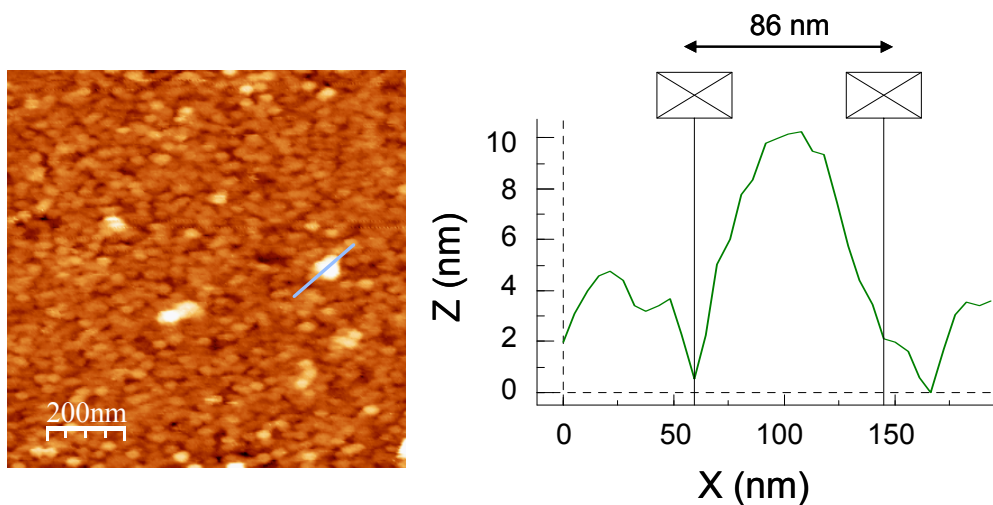

Fig. 4.12.- AFM image of nanosomes adsorbed onto a Indium Tin Oxide.

Table 4.2 Nanosome number and morphology adsorbed in different substrates

Substrate	contact angle (º)	Aspect ratio	Surface coverage (%)
Mica	30	1:6	8.6
Gold	54	1:7	2.5
ITO	65	1:9	2.3

As summarized in table 4.2, it seems that the number of nanosomes adsorbed decreases when increasing the hydrophobicity of the surface (the contact angles of mica, Au and ITO are 30º, 54º and 65º respectively). Also, the nanosomes collapse when adsorbed in either case, thus indicating a similar contact potential in all cases. However, the integrity of the nanosomes in certified, since the height of the immobilized nanovesicles is 10 nm, which is consistent with empty nanosomes with two sides of double lipid layer (5 nm) pilled up. This is not far from the results already reported in the literature, where nanosomes adsorbed onto bare gold surfaces showed a height around 10 nm with widths ranging from 50 to 100 nm and the surface coverage was between 2% to 9% [33]. Also, hydrophilic surfaces proved to achieve better surface coverage with respect to the hydrophobic case.

Concluding, the structure of the nanosomes flattens when immobilized due to the interaction forces with the surface, nevertheless those forces are not strong enough to cause nanovesicle opening. The hydrophilicity of the surface plays an important role in the surface coverage, but it does not affect the nature of the nanosome once is adsorbed. Even so, the physical adsorption of the nanosomes onto the sensor surface does not provide a good methodology for nanosome immobilization, as it provides with very low surface coverage that would negatively influence the response of the potential sensor.

3.1.3 Nanosome immobilization by specific molecular recognition

As the surface density of the nanosomes adsorbed onto bare Au or ITO is very low, a functionalization procedure (described in 2.5) was designed to promote the nanosome anchorage onto surfaces by molecular recognition mechanisms. This would increase the surface coverage and maintain the spherical shape of the nanosomes. In this way, the nanosomes would be specifically immobilized onto the surface through the c-myc tag that is coupled to the olfactory receptor expressed in the nanosomes membrane (Fig. 4.3). This functionalization has also the advantage of working equally either on Au or on ITO, as the SAM is formed through the electrostatic interactions of the negatively charged surface with the polycation Poly-L-Lysine (PLL) upon activation through oxygen plasma. To characterize our functionalization layer (the PLL-g-PEG-biotin, the streptavidin and the biotinylated antibody), a functionalized ITO surface

analyzed by means of AFM. For this purpose the AFM tip was used in liquid to mechanically remove the functionalization layer from the ITO surface. An area of 1x1 μm of the functionalization layer was scratched by pressing the cantilever hard against the surface (increasing the set point) and removing the feedback. Then, a bigger image of 5x5 μm allows measuring the thickness of the functionalization layer. Figure 4.13 shows that the thickness of the functionalization layer composed by the PLL-g-PEG-biotin, the streptavidin and the biotinylated antibody, is about 6 nm thick.
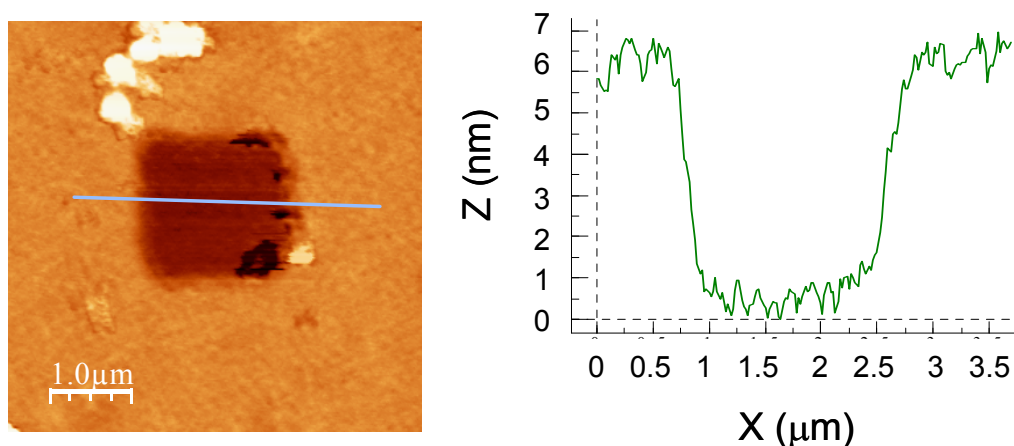

Fig. 4.13.- AFM image of the ITO substrate functionalized with a SAM of PLL-g-biotin, streptavidin and anti-cmyc antibody. A square area (2 x 2 microns) was worn by increasing the set point of the AFM whileworking in contact mode. A profile of the worn area can be seen in the right hand side, where the thinkness of the functionalization layer can be established in 6 +- 0.5 nm, as extracted from the data analysis (WSxM software).

As found in [41], the thickness of our grafted co-polymer when hydrated at a 90% and physisorbed onto the surface at the same conditions is only 4 nm, while the layer thickness of the dry mass is only 1.5 nm. The molecular radius of the streptavidin was reported to be 4.5 nm [42]. Regarding the antibodies, many studies have been published regarding the size of the antibodies, ranging from 4.5 nm [43] to 10 nm [44]. There is a small discrepancy between our 6 nm and the expected 10 nm from the literature, nonetheless there are in the same order of magnitude and we can still confirm that the functionalization layer is well designed and deposited onto the ITO surface.

Once the functionalization layer has been characterized, we deposited a suspension of nanosomes with a protein concentration of 60 μg/ml (200 μl, sample size is 12x8 mm^2), onto the SAM and left it react during 1 hour. We have chosen a much longer time than the 10 minutes reported in the literature [10, 22, 33], to ensure that the anti-cmyc antibody will have time enough to react with the cmyc tagged to the

membrane protein. Is worth to mention that the presence of the cmyc tag and its recognition with the antibody have been previously confirmed with western blot [22]. In the AFM image shown in figure 4.14, we can observed that the number of nanosomes immobilized onto the surface has not increased and that their aspect ratio is still 1:10.
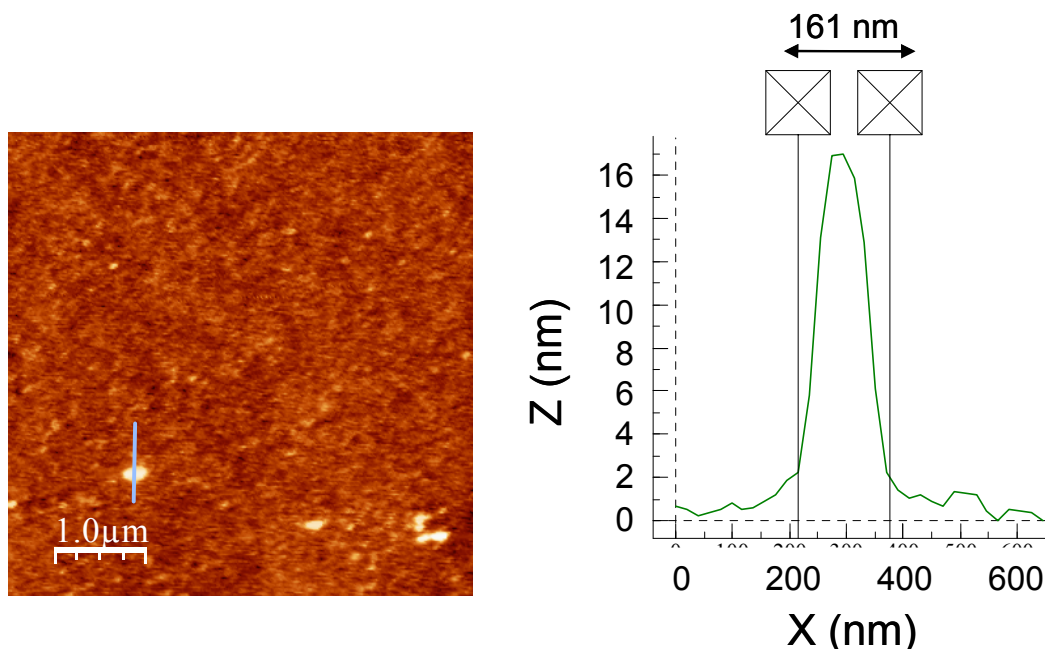

Fig. 4.14.- AFM image of nanosomes immobilized on a functionalized ITO substrate. The sample was functionalized by a drop coating procedure.

As the suspension of nanosomes is quite diluted, to improve the nanosomes mobility and the chance of more nanosomes to be driven towards the surface, we repeated the same procedure above, but this time in flux. Another obvious solution would be to increase the nanosome concentration, but we are interested in using the least amount of sample as possible. The full process of functionalization and immobilization of nanosomes was performed in a very small flow chamber (volume of 12 μl) at a flow rate of 50 μl/min during depositions, and 200 μl/min while rinsing with buffer solution, following the protocol described in 2.6.4.

The resulting sample was analyzed by AFM, as shown in figure 4.15. The image suggests that the number of nanosomes present onto the surface has increased to a surface coverage of about 23%, although the aspect ratio has increased even further to 1:20.
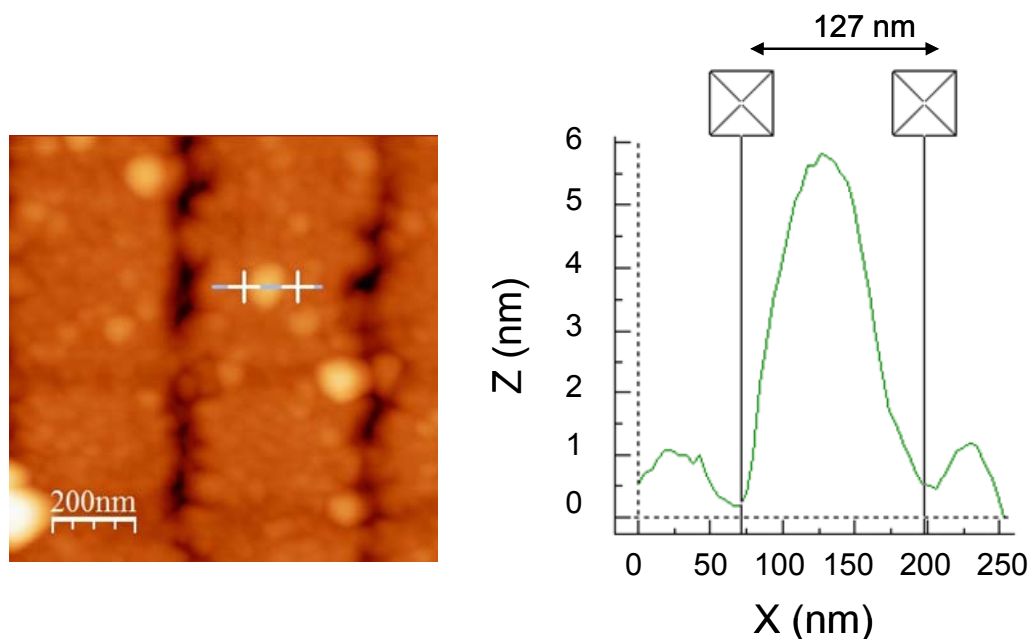
Fig. 4.15.- AFM image of nanosomes immobilized on a functionalized ITO substrate (an OWLS grating coupler). The functionalization was performed in flux.

To fully understand the cause of the nanosomes collapsing further in the funcionalized samples, and to discriminate whether this effect is an artefact induced by the AFM tip while scanning the samples; we decided to image the samples after functionalization and immobilization of the nanosomes (by dipping) by means of cryo-fixation SEM. The results, in figure 4.16, show that the nanosomes diameter is around 100 nm, suggesting that the collapsing effect that appeared in the AFM pictures is an artefact caused by the AFM tip itself. Worth is to comment on the surface coverage observed in the SEM micrograph. Even though the functionalization has not been performed in flux conditions, in this case the surface coverage is 15%. This is due to the fact that this time the functionalization has been done by dipping (instead of using the drop method as in the AFM experiment depicted in figure 4.14), meaning that the substrate has been exposed to a much larger volume (2 ml) of nanosome solution.
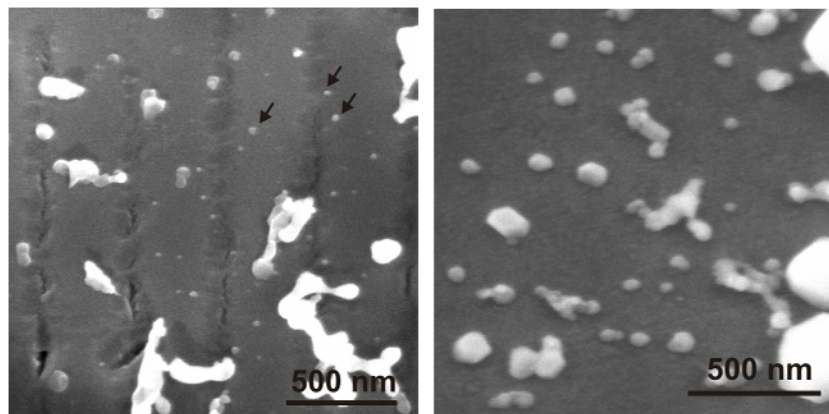
Fig. 4.16.- Cryo-fixation SEM image of the immobilization of nanosomes on functionalized ITO. The sample was functionalized by a dipping procedure.

3.2 NUMBER OF OLFACTORY RECEPTORS PER NANOSOME

In view of the obtained results about the nanosome immobilization process, the low surface coverage reveals as a critical issue. As the procedure used to anchor the nanosomes onto the functionalized surface is based on the capture of cmyc tags incorporated in the olfactory receptors, through the anti-cmyc antibody immobilize on the surface; we wonder whether the number of cmyc tagged OR in the nanosomes is uniform among their population and, if so, if this number is too low to hamper nanosome immobilization.

The micro-contact printing (μCP) technique allows to perform fluorescent microscopy experiments while including the control at the same time in the same substrate, avoiding common issues in fluorescent microscopy, such as the evaluation of signal to noise ratio, background, light intensity and so on (refer to section 2.6.3). Two sets of experiments were performed to evaluate the availability of c-myc probes in nanosomes that have been either absorbed, either functionalized onto an ITO substrate.

Firstly, for the adsorbed nanosomes, BSA was patterned onto the ITO surface to create passivation regions and the remaining surface was left to react with the nanosome suspension. To detect the presence of the ORs, the sample was incubated with anti-cmyc-FITC. A cartoon summarizing this process is depicted in figure 4.17. Once the sample was rinsed and dried, it was ready to be observed under the fluorescence microscope.
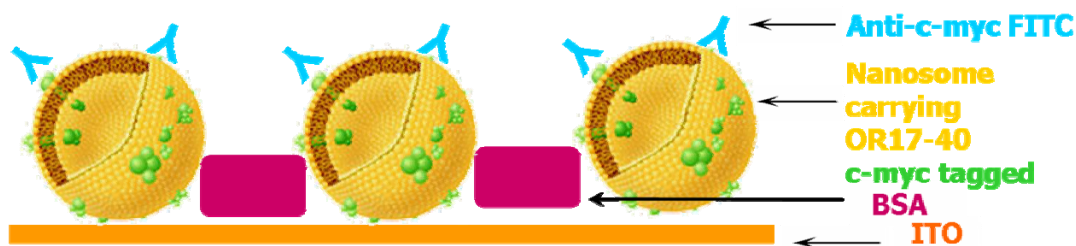
Fig. 4.17.- Squeme of a µCP experiment in which the nanosomes are physically adsorbed onto the ITO surface. Firstly a BSA pattern was created on the surface to prevent protein adsorption, secondly nanosomes were left to adsorb in the remaining areas. Last, a fluorescent antibody was used to identify available ORs in the surface.

The fluorescent dye (fluorescein isothiocyanate, FITC) was excited with a mercury lamp at 490 nm during 300 s, and the emitted fluorescence at 520 nm was recorded with a band pass filter (510 to 550 nm). The resulting image is shown in figure 4.18. As it can be seen, the fluorescence is not present in the area passivated with the BSA pattern, suggesting that there is no non-specific adsorption of the antibody onto the passivated surface and that there are available ORs in the membrane of the nanosomes.
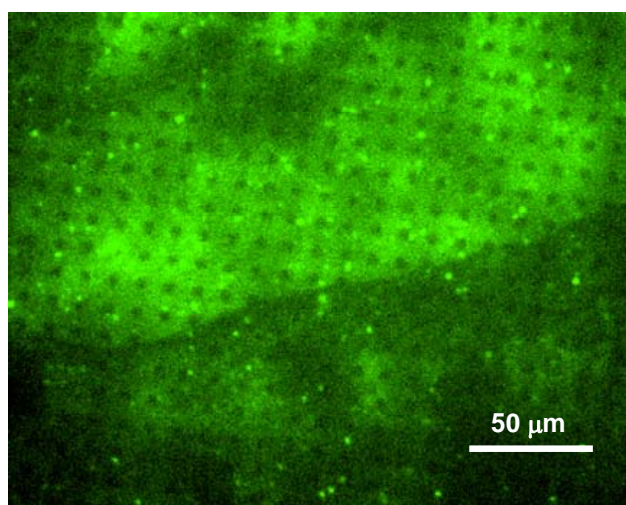

Fig. 4.18.- Fluorescence image of the adsorption of nanosomes. The black areas are the ones passivated with BSA and the rest of the surface were the nanosomes were adsorbed is stained in green through the anti-cmyc-FITC, suggesting that there are ORs available in the membranes.

Secondly, for the nanosomes immobilized through a functionalization layer, we performed another µCP experiment (Fig. 4.19). This time the functionalization was patterned onto the PLL-g-PEG-biotin coated ITO surface and stained through a TexasRed labelled oltreptavidin. After the patterning, the whole surface was incubated with the anti-c-myc-biotin antibody, and with the suspension of nanosomes, and then

blocked with BSA. To detect the presence of ORs available for molecular recognition at the nanosome surface after their immobilization, the sample was further incubated with a solution of anti-c-myc-FITC antibody. Once the sample was rinsed and dried, it was ready to be observed under the fluorescence microscope.
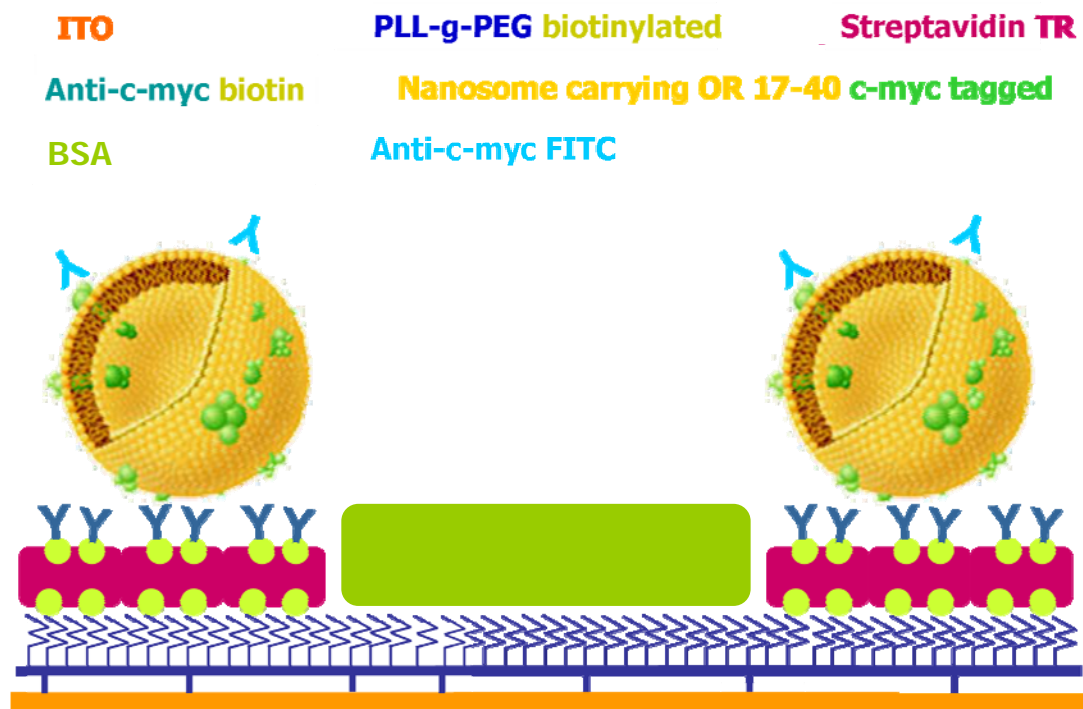

Fig. 4.19.- Squeme of a μCP experiment in which the nanosomes are immobilized onto the ITO surface through a functionalization SAM. PLL-g-PEG-biotin coated ITO was patterned with TexasRed streptavidin. After that the whole surface was incubated with the biotinilated antibody and the nanosomes. At last the surface was blocked with BSA prior to use the fluorescent antibody to identify the ORs available in the surface.

This time two steps, the streptavidin-TexasRed and the antibody-FITC, need to be investigated. The TexasRed (excited at 595 nm) and the FITC dyes were excited at the same time with the mercury lamp during 300 s, and the emitted fluorescence at 615 nm and 520 nm was recorded respectively with two band pass filters (600 to 660 nm and 510 to 550 nm).

The resulting images are shown in figure 4.20. As it can be seen, the antibody is only attached in the pattern created by the streptavidin, meaning that there is no specific adsorption of the fluorescent antibody and that there are still some ORs available in the membrane of the nanosomes.
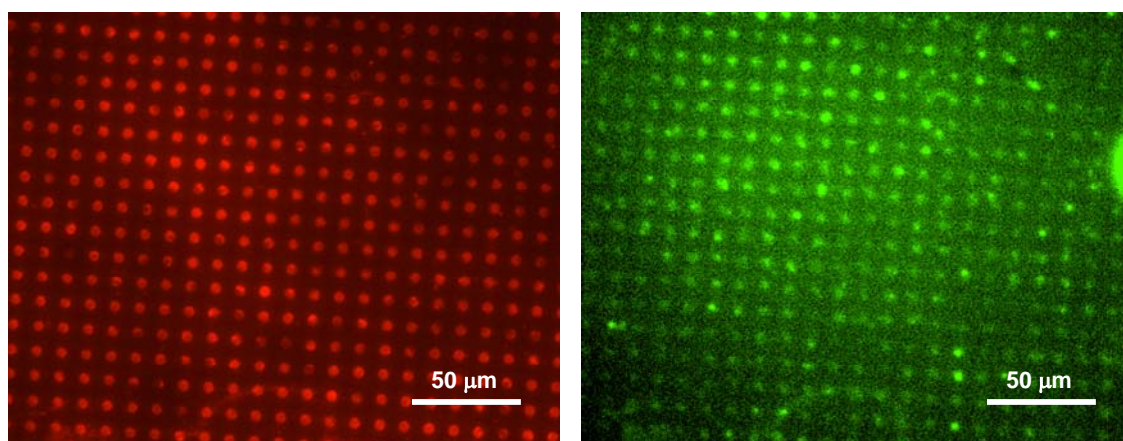
Fig. 4.20.- Fluorescence image of the immobilization of nanosomes on functionalized ITO. In the left hand side, a streptavidin pattern is stained in red. In the right hand side, we can see how the areas stained in green by the anti-cmyc-FITC coincide with the pattern previously created, and so suggesting that the nanosomes only bind onto the functionalization and that they carry available ORs in their membranes.

3.2.1 OWLS

To study in detail our functionalization approach to immobilize nanosomes carrying ORs onto sensor substrates, we have chosen the OWLS biosensing technique. Although many studies have been published that study the immobilization of nanosomes with SPR [10, 22, 30], OWLS presents several advantages when it comes to the quantification of molecules present on the sensor surface. The mathematical procedure to translate Refractive Index Units (RIU) measured by SPR into surface density is rather tedious and requires intensive modelling, while OWLS allows for a straight forward mass adsorption calculation. This is given by the fact that OWLS takes two measurements at the time during a kinetic experiment (the TE and the TM modes) while a standard imaging SPR only measures light intensity (refer to chapters 1 and 2). This handicap creates an issue when comparing different experiments, as specific normalization criteria need to be defined. Furthermore, in the long run, OWLS could be combined with electrochemistry to allow achieving a better insight into the receptor-odorant recognition process.

To get quantitative data about the immobilization steps of the nanosomes carrying olfactory receptors OR17-40 onto electrodes, we have followed the kinetics of the functionalization described in section 2.5 onto ITO waveguides (OWLS240, Microvacuum, Hungary). This process was performed in flux conditions in the OWLS

flow chamber, as described in section 2.6.4. Every immobilization step is carried out during 1 hour or longer until the signal is stable and then non-immobilized molecules are rinsed away during 10 minutes until a new baseline is achieved. Shown in figure 4.21 is an OWLS sensorgram depicting the formation of our SAM.
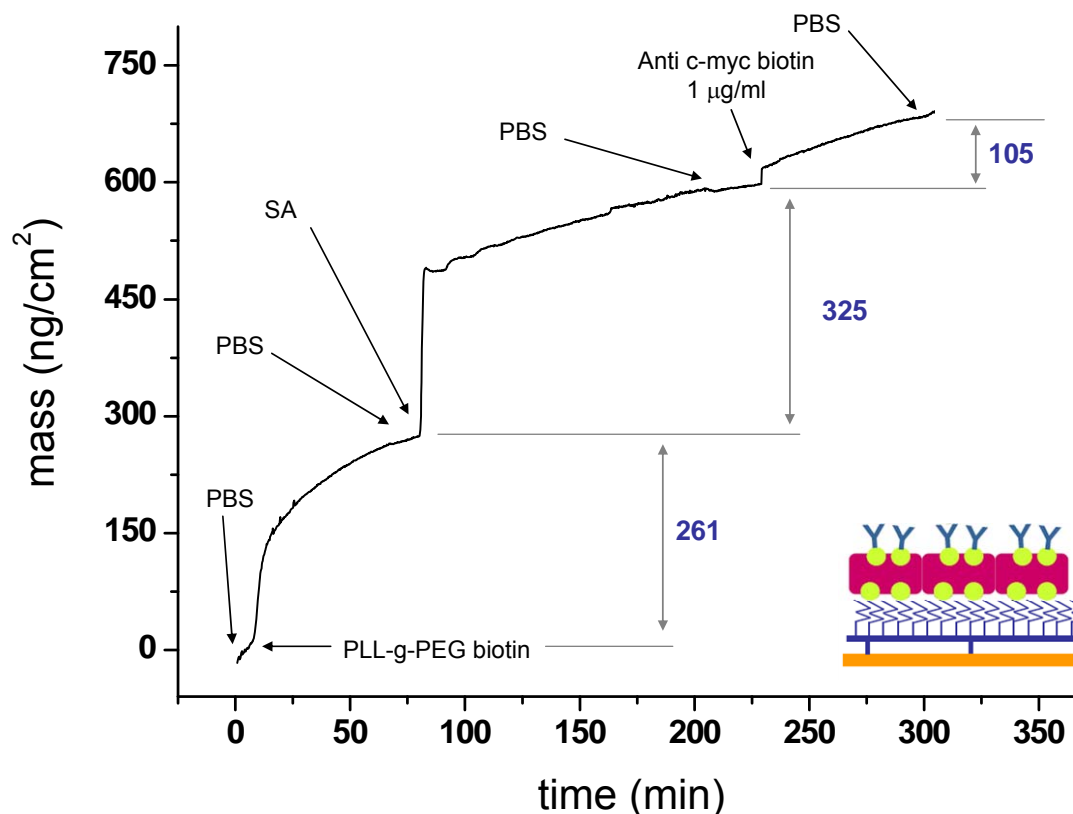

Fig. 4.21.- OWLS sensorgram depicting the kinetics of the functionalization onto an ITO grating. Firstly a PLL-g-PEG-biotin attaches to the ITO activated surface due to electrostatic interactions. Second, a monolayer of streptavidin gets immobilized onto the available biotins in the surface. Last, the biotinylated antibody is captured by the vacant streptavidin anchoring sites. A cartoon describing the different layers of the SAM is included at the bottom right. The numbers in blue represent the surface density of each layer after rinsing.

In order to quantify the efficiency of each step in the nanosome immobilizaion procedure, we need to check the pack density of perfect monolayers. According to the supplier (SuSoS, Switzerland) the surface density of a monolayer of PLL-g-PEG-biotin onto plasma activated ITO is ~ 200 ng/cm^2. Secondly, the expected density of a full packed streptavidin layer is ~ 280 ng/cm^2 [45, 46]. Last, to quantify the efficiency of biotinylated anti-c-myc antibody immobilization, we calculated the ratio of OWLS response observed for antibody relative to the streptavidin grafting. Taking into account

that the size of the streptavidin molecule is around 4.5 nm in diameter and that the hydrodynamic geometry of the antibody is commonly assumed as a sphere with average diameter of 8 nm [42-45], we have to assume a maximum linear binding ratio antibody:streptavidin of 1:3, that translates into a surface binding ratio of 1:9 (see figure 4.22). Then, considering their molecular weight (120 kDa and 60 kDa for the antibody and the streptavidin, respectively), the stoichiometric ratio should have a value of ~0.22 (Ab/SA = 1/9 * 120/60 = 2/9 = 0.22). In the experiment shown in figure 4.21, the ratio of immobilized antibody is 0.32 (after performing the experiment several times, we got the statistical average value of this ratio to be 0.23 ± 0.05). Overall our results are well in agreement with the theory, the immobilization kinetics follows a langmuir model and our functionalization provides a nice antibody monolayer.
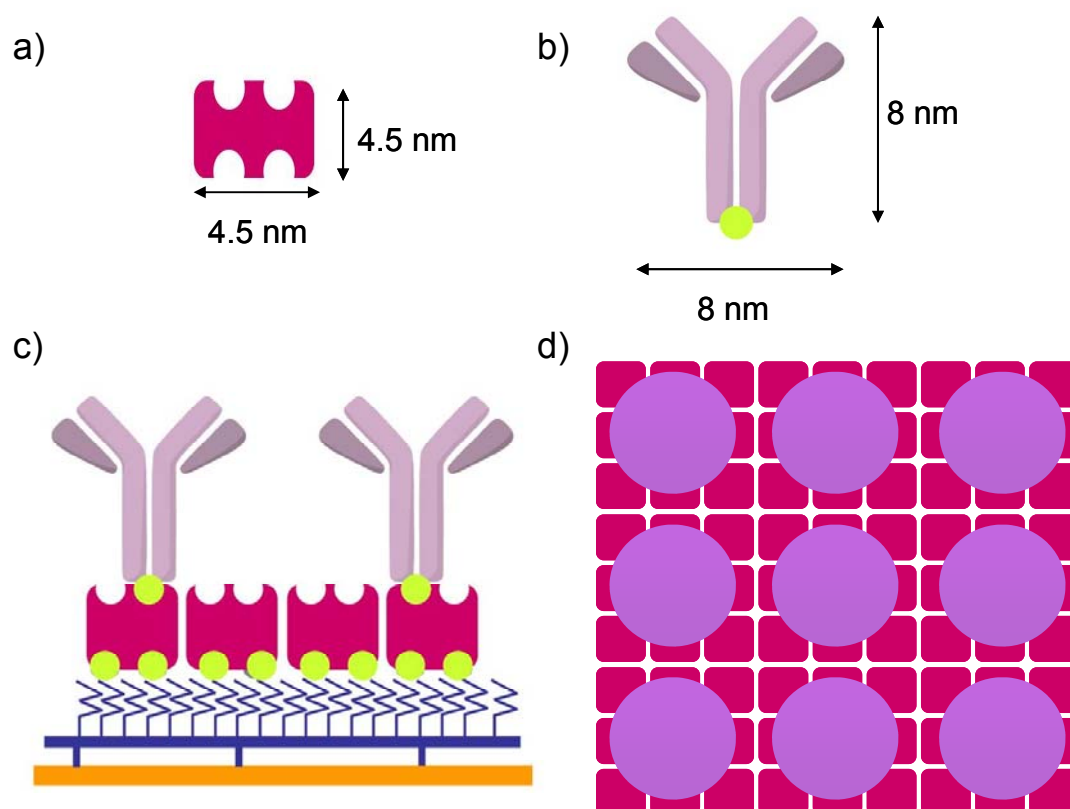

Fig. 4.22.- a) 1D drawing of the streptavidin molecule, b) 1D drawing of the biotinylated antibody, c) linear binding ratio of the pair antibody : streptavidin is 1:3, d) the pink squares represent a top view of the streptavidin molecule and the purple circles represent a top view of the antibody; the surface binding ratio of the pair antibody : streptavidin is 1:9.

Once the immobilization of the anti-cmyc antibody was performed and characterized, and being sure there were enough density of antibodies on the surface to capture the nanosomes, nanosome suspensions containing different protein concentrations where deposited and monitored in situ by OWLS. As shown in the kinetics diagram (figure 4.23), the amount of immobilized nanosomes onto the surface increases when increasing their protein concentration from 30 to 60 μg/ml, reaching the saturation at 120 μg/ml.
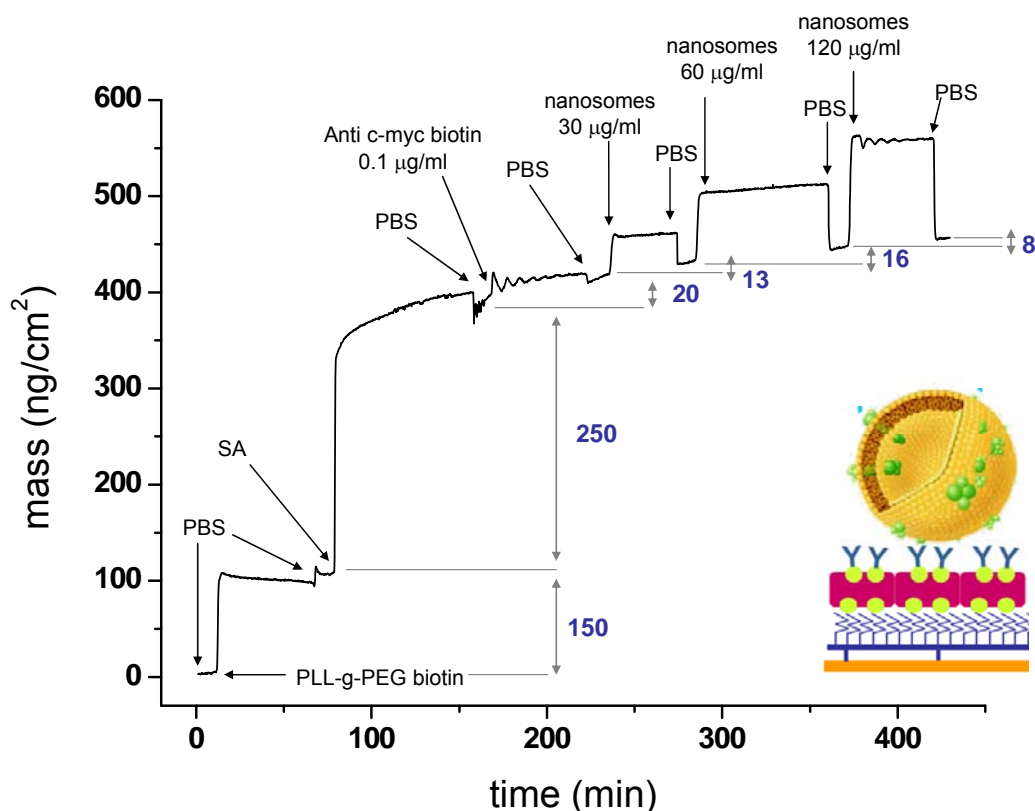

Fig. 4.23.- OWLS immobilization of different concentrations of nanosomes on functionalized ITO. The nanosomes are immobilized on the surface through the cmyc tag attached to the ORs in the membrane. This tag is specifically recognized by the antibody grafted in the SAM. A cartoon containing a sketch of the process is included at the bottom right. The numbers in blue represent the surface density of each layer after rinsing.

The amount of nanosomes used in the experiment described in figure 4.23 is hard to estimate, as we are only characterizing the nanosome solution by their total protein concentration. However, from the AFM experiments in section 3.1.3 where the functionalization was performed in flux and under the same conditions as in this section, we can assume that the surface coverage achieved when running the 60 μg/ml

nanosome solution is 23% (figure 4.15). Comparing with the OWLS sensorgram in figure 4.23 this corresponds to a mass density of 16 ng/cm^2. Now, applying this relation and using the mass densities from figure 4.23, we could imply that the surface coverage corresponding to the 30 μg/ml and 120 μg/ml is 18.7% and 11.5% respectively. Altogether this will make for a total nanosome surface coverage of 53.19%, which is a remarkably high value very close to the jamming limit of hard spheres (54.7%) and hence very close to the maximum possible coverage. This result is also very well in agreement with studies of the immobilization of nanovesicles onto hydrophilic electrodes [33]. Furthermore, the total ratio of captured receptor relative to grafted antibody is 1.86, which is much better than the highest level reported in the literature where the best value of 0.24 was achieved for a functionalization consisting on 16-mercaptohexadecanoic acid + activation + (+)-Biotinyl-3,6,9-trioxaundecamine + neutravidin + anti-cmyc-biotin [22].

Now, analogously to the μCP experiment described in figure 4.19, to elucidate whether there are available ORs in the immobilized nanosomes, we performed the OWLS experiment described in figure 4.24.
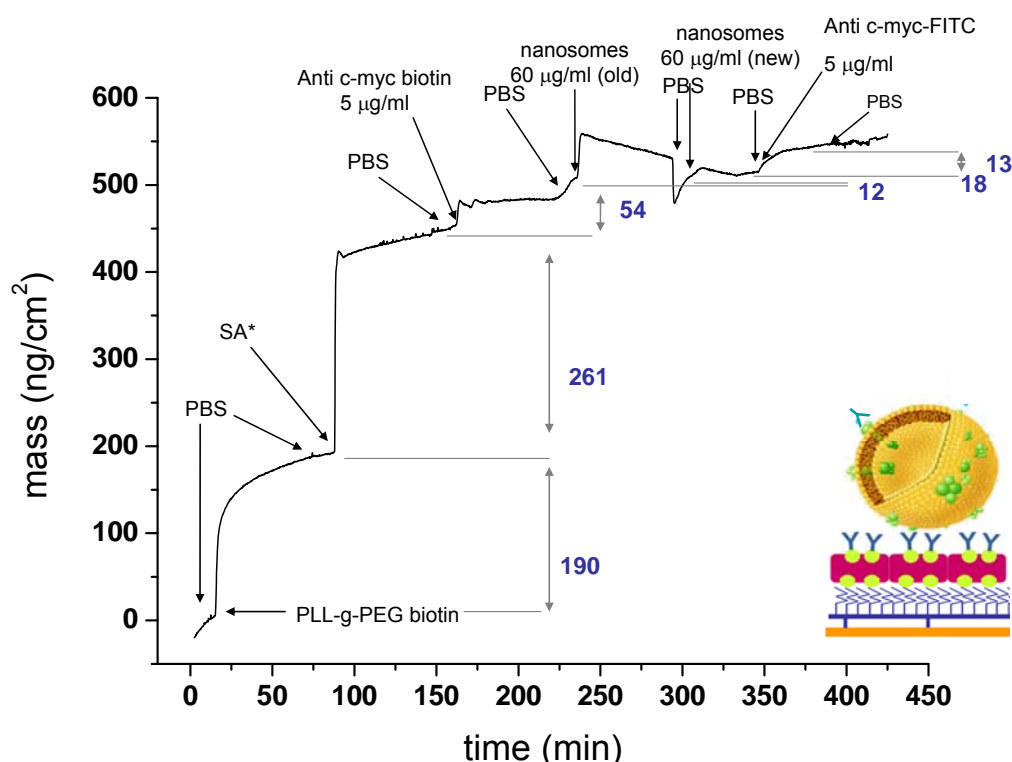

Fig. 4.24.- OWLS recognition of available ORs in the immobilized nanosome.

Again, upon activation of the ITO substrate, we functionalized the surface with PLL-g-PEG-biotin, streptavidin and anti-c-myc biotin to specifically immobilize the nanosomes. Then, to detect the presence of extra ORs in the nanosomes, a solution of 5µg/ml of anti-c-myc-FITC in PBS was left react during 1 hour. The graph showing this experiment is presented in figure 4.24. As it can be seen, some antibodies attach to the nanosomes at a density ratio of 13:30 = 0.43, suggesting that some ORs are available in the nanosomes membrane.

To discriminate whether these attached antibodies are specifically recognizing the available ORs present in the nanosomes or are being adsorbed unspecifically, we performed a control experiment, collected in figure 4.25.
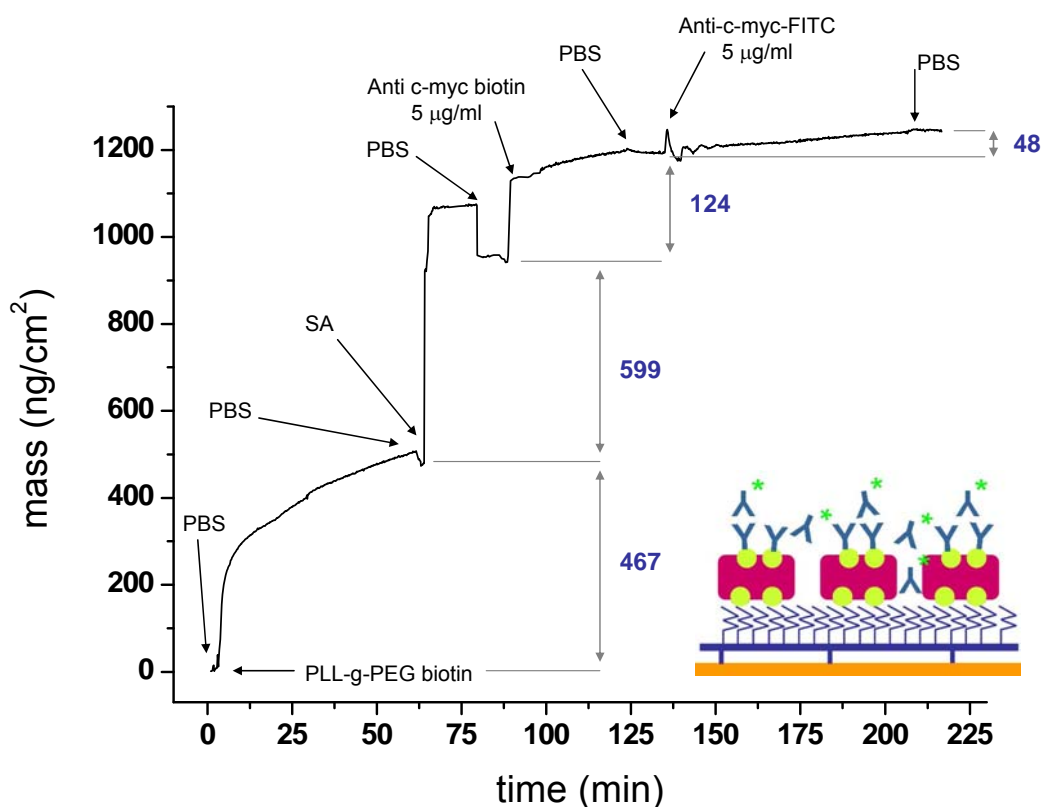
Fig. 4.25.- OWLS unspecific adsorption of secondary fluorescent antibody onto functionalized ITO.

The OWLS immobilization kinetics curve shows that indeed some antibodies react unspecifically onto the primary antibody layer, at a ratio of 48:124 = 0.39. Just to elucidate whether the FITC tag in the antibody is affecting its performance, we did another control this time with a label-free antibody (experiment presented in figure 4.26).
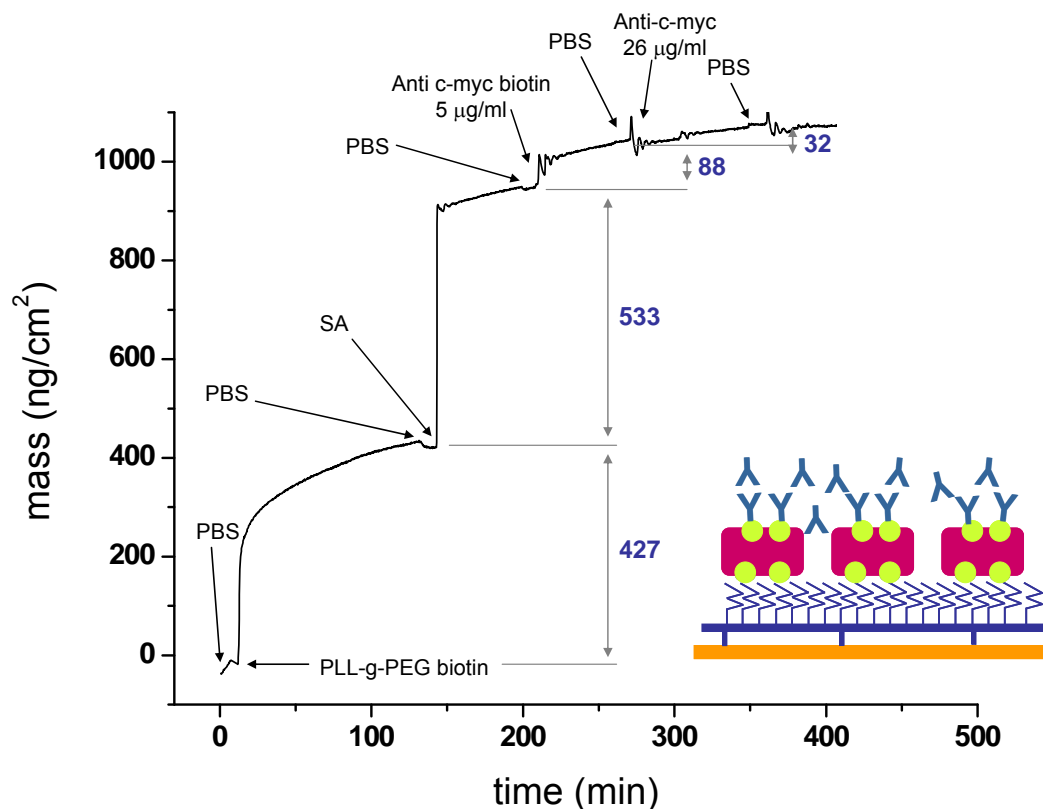
Fig. 4.26.- OWLS unspecific adsorption of secondary non-fluorescent antibodies onto functionalized ITO.

In a very similar way, the ratio of unspecific adsorption of the secondary antibody onto the primary antibody was 32:88 = 0.36. If we substract this unspecific adsorption, from the total amount of antibodies attached to the nanosomes at figure 4.24, we obtain a specific recognition of ORs in the nanosomes at a ratio of only 0.43-0.375= 0.055. This result suggests that, even though there are some olfactory receptors present and available in the nanosomes membrane, their quantity is probably too low. This problem has already been reported in the literature, where the mean value for the number of OR in a nanosome of 30 nm in diameter turned out to be less than one [33].

4 CONCLUSIONS AND FUTURE WORK

In this study, olfactory receptors carried by nanosomes were successfully immobilized onto biosensor surfaces functionalized by mixed self-assembled monolayers and biotin/streptavidin. The OR1740 receptors were grafted via a C-terminal tag (c-myc) that was adequate for preserving the receptor activity. Specific immobilization by capturing the receptors via an antibody against the c-myc tag yields a

uniform orientation of the receptor onto the surface. In addition, as a result of the in situ selection of the receptor, enrichment in membrane receptors on the biofunctionalized solid support was expected. The use of OWLS has been crucial to fully characterize the functionalization process and to understand that the enrichment in membrane receptors has not been achieved. We conclude that number of available olfactory receptors on the functionalized sensor is too low to be able to perform functionality experiments.

As future work, the number of ORs per nanosome need to be increased and further experiments need to be done to confirm that the c-myc tag is properly grafted to the olfactory receptors. Also, as the functionalization procedure has proved to be very robust, once the expression of enough number of receptors is sorted, the system is ready to perform functionality experiments. EC-OWLS will be a great candidate to get a better understanding of the processes behind the recognition of odorants by olfactory receptors, as will allow studying the relation of electrochemical impedance spectroscopy (EIS) measurements with optical measurements that provide kinetic information of the reactions taking place in the vicinity of the sensor surface.

5 REFERENCES

[1]   E. H. Oh, H. S. Song, and T. H. Park, "Recent advances in electronic and bioelectronic noses and their biomedical applications," *Enzyme and Microbial Technology,* vol. 48, pp. 427-437, 2011.

[2]   S. H. Lee and T. H. Park, "Recent advances in the development of bioelectronic nose," *Biotechnology and Bioprocess Engineering,* vol. 15, pp. 22-29, 2010.

[3]   S. H. Lee, S. B. Jun, H. J. Ko, S. J. Kim, and T. H. Park, "Cell-based olfactory biosensor using microfabricated planar electrode," *Biosensors and Bioelectronics,* vol. 24, pp. 2659-2664, 2009.

[4]   J. H. Sung, H. J. Ko, and T. H. Park, "Piezoelectric biosensor using olfactory receptor protein expressed in Escherichia coli," *Biosensors and Bioelectronics,* vol. 21, pp. 1981-1986, 2006.

[5]   J. Minic, M.-A. Persuy, E. Godel, J. Aioun, I. Connerton, R. Salesse, and E. Pajot-Augy, "Functional expression of olfactory receptors in yeast and development of a bioassay for odorant screening," *FEBS,* vol. 272, pp. 524-537, 2005.

[6]   H. J. Ko and T. Hyun Park, "Dual signal transduction mediated by a single type of olfactory receptor expressed in a heterologous system," *Biological Chemistry,* vol. 387, pp. 59-68, 2011/08/09 2006.

[7]   H. J. Ko and T. H. Park, "Functional analysis of olfactory receptors expressed in a HEK-293 cell system by using cameleons," *J. Microbiol. Biotechnol.,* vol. 17, pp. 928-933, 2007.

[8]   M. Marrakchi, J. Vidic, N. Jaffrezic-Renault, C. Martelet, and E. Pajot-Augy, "A new concept of olfactory biosensor based on interdigitated microelectrodes and immobilized yeasts expressing the human receptor OR17-40," *European Biophysics Journal,* vol. 36, pp. 1015-1018, 2007.

[9]   T.-Z. Wu, Y.-R. Lo, and E.-C. Chan, "Exploring the recognized bio-mimicry materials for gas sensing," *Biosensors and Bioelectronics,* vol. 16, pp. 945-953, 2001.

[10]   I. Benilova, V. Chegel, Y. Ushenin, J. Vidic, A. Soldatkin, C. Martelet, E. Pajot, and N. Jaffrezic-Renault, "Stimulation of human olfactory receptor 17-40 with odorants probed by surface plasmon resonance," *European Biophysics Journal,* vol. 37, pp. 807-814, 2008.

[11]   H. Song, S. Lee, E. Oh, and T. Park, "Expression, Solubilization and Purification of a Human Olfactory Receptor from <i>Escherichia coli</i&gt," *Current Microbiology,* vol. 59, pp. 309-314, 2009.

[12]   S. Katada, T. Nakagawa, H. Kataoka, and K. Touhara, "Odorant response assays for a heterologously expressed olfactory receptor," *Biochemical and Biophysical Research Communications,* vol. 305, pp. 964-969, 2003.

[13]   E. Shirokova, K. Schmiedeberg, P. Bedner, H. Niessen, K. Willecke, J.-D. Raguse, W. Meyerhof, and D. Krautwurst, "Identification of Specific Ligands for Orphan Olfactory Receptors," *The Journal of Biological Chemistry,* vol. 280, pp. 11807-11815, March 25, 2005 2005.

[14]   V. r. Matarazzo, O. Clot-Faybesse, B. Marcet, G. l. Guiraudie-Capraz, B. Atanasova, G. r. Devauchelle, M. Cerutti, P. Etiévant, and C. Ronin, "Functional Characterization of Two Human Olfactory Receptors Expressed in the Baculovirus Sf9 Insect Cell System." vol. 30, 2005, pp. 195-207.

[15]   Q. Liu, H. Cai, Y. Xu, Y. Li, R. Li, and P. Wang, "Olfactory cell-based biosensor: A first step towards a neurochip of bioelectronic nose," *Biosensors and Bioelectronics,* vol. 22, pp. 318-322, 2006.

[16]   C. Wu, P. Chen, H. Yu, Q. Liu, X. Zong, H. Cai, and P. Wang, "A novel biomimetic olfactory-based biosensor for single olfactory sensory neuron monitoring," *Biosensors and Bioelectronics,* vol. 24, pp. 1498-1502, 2009.

[17]   V. Akimov, E. Alfinito, J. Bausells, I. Benilova, I. Paramo, A. Errachid, G. Ferrari, L. Fumagalli, G. Gomila, J. Grosclaude, Y. Hou, N. Jaffrezic-Renault, C. Martelet, E. Pajot-Augy, C. Pennetta, M.-A. Persuy, M. Pla-Roca, L. Reggiani, S. Rodriguez-Segui, O. Ruiz, R. Salesse, J. Samitier, M. Sampietro, A. Soldatkin, J. Vidic, and G. Villanueva, "Nanobiosensors based on individual olfactory receptors," *Analog Integrated Circuits and Signal Processing,* vol. 57, pp. 197-203, 2008.

[18]   E. H. Oh, H. S. Song, and T. H. Park, "Recent advances in electronic and bioelectronic noses and their biomedical applications," *Enzyme and Microbial Technology,* vol. 48, pp. 427-437, May 2011.

[19]   J. Vidic, J. Grosclaude, R. Monnerie, M. A. Persuy, K. Badonnel, C. Baly, M. Caillol, L. Briand, R. Salesse, and E. Pajot-Augy, "On a chip demonstration of a functional role for odorant binding protein in the preservation of olfactory receptor activity at high odorant concentration," *Lab on a Chip,* vol. 8, pp. 678-688, 2008.

[20]   I. V. Benilova, J. Minic Vidic, E. Pajot-Augy, A. P. Soldatkin, C. Martelet, and N. Jaffrezic-Renault, "Electrochemical study of human olfactory receptor OR

Optical Grating Coupler Biosensor and Biomedical Applications

17-40 stimulation by odorants in solution," *Materials Science and Engineering: C,* vol. 28, pp. 633-639, 2008.

[21]   T. H. Kim, S. H. Lee, J. Lee, H. S. Song, E. H. Oh, T. H. Park, and S. Hong, "Single-Carbon-Atomic-Resolution Detection of Odorant Molecules using a Human Olfactory Receptor-based Bioelectronic Nose," *Advanced Materials,* vol. 21, pp. 91-94, 2009.

[22]   J. Vidic, M. Pla-Roca, J. Grosclaude, M. A. Persuy, R. Monnerie, D. Caballero, A. Errachid, Y. Hou, N. Jaffrezic-Renault, R. Salesse, E. Pajot-Augy, and J. Samitier, "Gold Surface Functionalization and Patterning for Specific Immobilization of Olfactory Receptors Carried by Nanosomes," *Analytical Chemistry,* vol. 79, pp. 3280-3290, 2007.

[23]   T.-Z. Wu, "A piezoelectric biosensor as an olfactory receptor for odour detection: electronic nose," *Biosensors and Bioelectronics,* vol. 14, pp. 9-18, 1999.

[24]   X. Zhang, O. De la Cruz, J. Pinto, D. Nicolae, S. Firestein, and Y. Gilad, "Characterizing the expression of the human olfactory receptor gene family using a novel DNA microarray." vol. 8, 2007, p. R86.

[25]   C. Moon, J.-Y. Yoo, V. r. Matarazzo, Y. K. Sung, E. J. Kim, and G. V. Ronnett, "Leukemia inhibitory factor inhibits neuronal terminal differentiation through STAT3 activation." vol. 99, 2002, pp. 9015-9020.

[26]   A. Mashukova, M. Spehr, H. Hatt, and E. M. Neuhaus, "β-Arrestin2-Mediated Internalization of Mammalian Odorant Receptors." vol. 26, 2006, pp. 9902-9912.

[27]   H. Yoon, S. H. Lee, O. S. Kwon, H. S. Song, E. H. Oh, T. H. Park, and J. Jang, "Polypyrrole Nanotubes Conjugated with Human Olfactory Receptors: High-Performance Transducers for FET-Type Bioelectronic Noses," *Angewandte Chemie International Edition,* vol. 48, pp. 2755-2758, 2009.

[28]   E. M. Neuhaus, A. Mashukova, W. Zhang, J. Barbour, and H. Hatt, "A Specific Heat Shock Protein Enhances the Expression of Mammalian Olfactory Receptor Proteins." vol. 31, 2006, pp. 445-452.

[29]   Y. Hou, N. Jaffrezic-Renault, C. Martelet, A. Zhang, J. Minic-Vidic, T. Gorojankina, M.-A. Persuy, E. Pajot-Augy, R. Salesse, V. Akimov, L. Reggiani, C. Pennetta, E. Alfinito, O. Ruiz, G. Gomila, J. Samitier, and A. Errachid, "A novel detection strategy for odorant molecules based on controlled bioengineering of rat olfactory receptor I7," *Biosensors and Bioelectronics,* vol. 22, pp. 1550-1555, 2007.

[30]   J. Minic, J. Grosclaude, M.-A. Persuy, J. Aioun, R. Salesse, and E. Pajot-Augy, "Quantitative assessment of olfactory receptors activity in immobilized nanosomes: a novel concept for bioelectronic nose," *Lab on a Chip,* pp. 1026-1032, 2006.

[31]   C. H. Wetzel, M. Oles, C. Wellerdieck, M. Kuczkowiak, G. Gisselmann, and H. Hatt, "Specificity and sensitivity of a human olfactory receptor functionally expressed in human embryonic kidney 293 cells and Xenopus Laevis oocytes," *J Neurosci,* vol. 19, pp. 7426-33, 1999.

[32]   Y. Hou, S. Helali, A. Zhang, N. Jaffrezic-Renault, C. Martelet, J. Minic, T. Gorojankina, M.-A. Persuy, E. Pajot-Augy, R. Salesse, F. Bessueille, J. Samitier, A. Errachid, V. Akimov, L. Reggiani, C. Pennetta, and E. Alfinito, "Immobilization of rhodopsin on a self-assembled multilayer and its specific

detection by electrochemical impedance spectroscopy," *Biosensors and Bioelectronics,* vol. 21, pp. 1393-1402, 2006.

[33]   I. Casuso, M. Pla-Roca, G. Gomila, J. Samitier, J. Minic, M. A. Persuy, R. Salesse, and E. Pajot-Augy, "Immobilization of olfactory receptors onto gold electrodes for electrical biosensor," *Materials Science and Engineering: C,* vol. 28, pp. 686-691, 2008.

[34]   G. Gomila, I. Casuso, A. Errachid, O. Ruiz, E. Pajot, J. Minic, T. Gorojankina, M. A. Persuy, J. Aioun, R. Salesse, J. Bausells, G. Villanueva, G. Rius, Y. Hou, N. Jaffrezic, C. Pennetta, E. Alfinito, V. Akimov, L. Reggiani, G. Ferrari, L. Fumagalli, M. Sampietro, and J. Samitier, "Advances in the production, immobilization, and electrical characterization of olfactory receptors for olfactory nanobiosensor development," *Sensors and Actuators B: Chemical,* vol. 116, pp. 66-71, 2006.

[35]   S. R. Seguí, M. Pla, J. Minic, E. Pajot-Augy, R. Salesse, Y. Hou, N. Jaffrezic-Renault, C. A. Mills, J. Samitier, and A. Errachid, "Detection of Olfactory Receptor I7 Self-Assembled Multilayer Formation and Immobilization Using a Quartz Crystal Microbalance." vol. 39: Taylor & Francis, 2006, pp. 1735 - 1745.

[36]   M. B. W. L. J. V. T. M. Kelly Bailey, "G-protein coupled receptor array technologies: Site directed immobilisation of liposomes containing the H$_1$-histamine or M$_2$-muscarinic receptors." vol. 9999, 2009, p. NA.

[37]   O. López, A. de la Maza, L. Coderch, C. López-Iglesias, E. Wehrli, and J. L. Parra, "Direct formation of mixed micelles in the solubilization of phospholipid liposomes by Triton X-100," *FEBS Letters,* vol. 426, pp. 314-318, 1998.

[38]   F. Moreno-Herrero, J. Colchero, J. Gãªmez-Herrero, and A. M. Barã³, "Atomic force microscopy contact, tapping, and jumping modes for imaging biological samples in liquids," *Physical Review E,* vol. 69, p. 031915, 2004.

[39]   I. Horcas, R. Fernandez, J. M. Gomez-Rodriguez, J. Colchero, J. Gomez-Herrero, and A. M. Baro, "WSXM: A software for scanning probe microscopy and a tool for nanotechnology." vol. 78: AIP, 2007, p. 013705.

[40]   L. Kam and S. G. Boxer, "Formation of Supported Lipid Bilayer Composition Arrays by Controlled Mixing and Surface Capture," *Journal of the American Chemical Society,* vol. 122, pp. 12901-12902, 2012/06/02 2000.

[41]   L. Feuz, "On the conformation of graft-copolymers with polyelectrolyte backbone in solution and adsorbed on surfaces," in *Swiss Federal Institute of Technology Zürich.* vol. Doctor of Sciences Zürich, 2006, p. 294.

[42]   W. H. Scouten and P. Konecny, "Reversible immobilization of antibodies on magnetic beads," *Analytical Biochemistry,* vol. 205, pp. 313-318, 1992.

[43]   R. M. Murphy, H. Slayter, P. Schurtenberger, R. A. Chamberlin, C. K. Colton, and M. L. Yarmush, "Size and structure of antigen-antibody complexes. Electron microscopy and light scattering studies," *Biophysical journal,* vol. 54, pp. 45-56, 1988.

[44]   W. K. Hartmann, N. Saptharishi, X. Y. Yang, G. Mitra, and G. Soman, "Characterization and analysis of thermal denaturation of antibodies by size exclusion high-performance liquid chromatography with quadruple detection," *Analytical Biochemistry,* vol. 325, pp. 227-239, 2004.

[45]   S. A. Darst, M. Ahlers, P. H. Meller, E. W. Kubalek, R. Blankenburg, H. O. Ribi, H. Ringsdorf, and R. D. Kornberg, "Two-dimensional crystals of

streptavidin on biotinylated lipid layers and their interactions with biotinylated macromolecules," *Biophysical Journal,* vol. 59, pp. 387-396, 1991.

[46]   L. S. Jung, K. E. Nelson, C. T. Campbell, P. S. Stayton, S. S. Yee, V. Pérez-Luna, and G. P. López, "Surface plasmon resonance measurement of binding and dissociation of wild-type and mutant streptavidin on mixed biotin-containing alkylthiolate monolayers," *Sensors and Actuators B: Chemical,* vol. 54, pp. 137-144, 1999.

Optical Grating Coupler Biosensor and Biomedical Applications

CHAPTER 5: ELECTROCHEMICAL TUNING OF THE STABILITY OF PLL/DNA MULTILAYERS

1 INTRODUCTION & STATE OF THE ART

Layer by Layer (LbL) assembly was introduced by Decher's group in 1992 for preparing structure-controlled thin films and became very popular because of the simplicity of its preparation [1, 2]. It is known that many surfaces exhibit a net negative charge in solution because of surface oxidation and hydrolysis. When immersed in a solution of positively charged polyelectrolytes and subsequently rinsed, the net surface charge becomes positive due to the overcompensation by the surface adsorbed positive polyelectrolytes. Subsequent exposure to a negatively charged polyelectrolyte solution leads to the reversal of net charge on the substrate, reversing the charge again. With such cyclic depositions, one can achieve multilayer films on the substrates with desired structures and thicknesses (figure 5.1). The LbL technique is not only applicable for polyelectrolyte/polyelectrolyte systems: almost any type of charged species, including inorganic molecular clusters, nanoparticles, nanotubes and nanowires, proteins, nucleic acids and DNA, viruses, etc. can be successfully used as components to prepare LbL films (see the comprehensive review by Kotov and coworkers) [3].
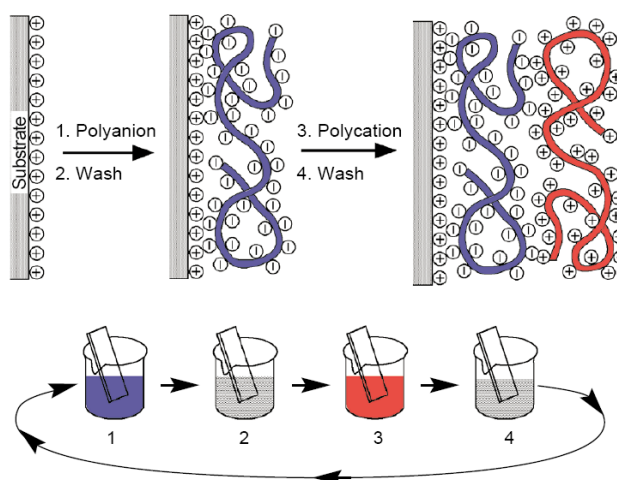

Fig. 5.1.- Schematics of a LbL film deposition process onto a positively charged surface. Steps 1 and 3 represent the adsorption of a polyanion and a polycation respectively, while steps 2 and 4 are rinsing steps. This sequence would lead to the formation of the simplest LbL film. If repeated sequencially, will lead to the formation of a multilayered film (Modified from [2]).

The LbL film deposition technique fulfils the requirement of being a simple approach to yield nanoarchitecture films with a good positioning of individual layers, but whose fabrication would be independent on the nature, size and topology of the substrate. Such versatile technique finds applications in the development of new materials with special functionalities from the combination of physical and chemical properties and high control of molecular orientation and organization at the nanoscale. This idea realizes one of the most important prerequisites for functional macroscopic devices: a fixed relation between nanoscopic order and macroscopic orientation.

The incorporation of proteins in multilayer films may lead to the application of polyelectrolyte multilayers (PEMs) as biosensors [4] or in biotechnology [5, 6] for the control of transport in multilayer films [7-9]. Multilayer films could also be built in microcapsules [10] with biomedical applications, or colloids with applications in photovoltaics [11]. They can also be used to alter the optical properties of materials [12] or even to act as membranes for gas separation purposes [13].

In regards with the biomedical applications it is possible to use the PEMs to incorporate a broad variety of bioactive components, either directly embedded into the PEM or loaded into a carrier. The PEM will provide a protective environment for the bioentities, preserving their functionality and allowing for a fine control of their localization and quantity. There is therefore a great potential for PEMs as reservoir for drugs to be used in controlled release platforms [14-17]. For biomedical applications focused on the controlled release of drugs embedded in the LbL films, the dissolution of the LbL film is the intriguing point to be investigated because the release actually corresponds with the dissolution of the film. Dissolution may be induced by changing the intrinsic properties of the environmental buffer such as pH [18], ionic-strength [19] and temperature [20], by applying external stimuli such as light [21], mechanical stress [22], or by the addition of enzymes [23]. In 2006, Vörös' group published a novel method based on electrochemistry (EC) for the dissolution of LbL films from the surface of an electrode: biodegradable and biocompatible multilayer films constituted of poly(L-lysine) (PLL) and heparin (an anti-inflammatory molecule) were used as model system on an indium tin oxide (ITO) substrate [24]. They found that the stability of the PEMs depended on the applied potential and the ionic strength of the buffer. The electrochemical method to dissolve PEMs appears indeed advantageous because of its

straightforward use, its versatility, and because of the possibility for fine tuning (as a small variation in the potential applied leads to small variations of the dissolution rate). The same year, Anzai's group published their research on the electrochemically induced dissolution of LbL films of poly(ethyleneimine) and avidin multilayer from platinum electrodes [25]. In 2008, Hammond's group reported the electrochemically induced dissolution of LbL films assembled on ITO substrates by using a nontoxic electroactive material known as Prussian Blue [26].

The success of electrochemically induced dissolution of PEMs containing biomolecules for controlled release in drug delivery, made possible to envisage other interesting applications such as genetic modification. Surface-mediated controlled delivery of DNA to cells or tissues in vitro and in vivo from the surfaces of implants and interventional devices, will provide a fantastic tool for the development of gene-based therapies. Techniques for genetic modification in molecular biology require a foreign gene to be inserted into a host cell. This is often achieved by electroporation (i.e. applying a quick voltage shock in order to temporarily disrupt areas of the membrane) [27]. Although the procedure is widely used for DNA and RNA transfection, it often has limited efficiency. But for successful gene therapy, one crucial aspect is the availability of controllable and efficient gene delivery vectors. Embedding DNA into PEMs with poly(ethylene glycol) (PEG), not only provides complexes with high colloidal stability under physiological conditions [28, 29], but also prolongs the in vivo circulation of the DNA complexes due to the high resistance to phagocytosis by macrophages in vitro [30]. LbL films were successfully employed for the transfection of DNA or RNA into cells whereby the release occurs either spontaneously or by increasing the salinity of the environmental solution [17, 31-34]. The utility of electrified surfaces for DNA or RNA transfection from LbL films was demonstrated in 2006 by the Iwata's group who succeeded in transferring genes into cells cultured on poly- (ethyleneimine) and plasmid DNA films using electrical pulsing to the ITO substrate [35]. In addition, Dong's group demonstrated that plasmid DNA collected after electrochemical dissolution from a LbL film (composed of DNA and inorganic zirconium) conserved its bioactivity by observing the expression of the corresponding fluorescent protein in cells [36].

In this chapter, we took advantage of the electrochemical Optical Waveguide Lightmode Spectroscopy technique (EC-OWLS) to study in detail the kinetics of the

surface-mediated dissolution of PEMs containing DNA, upon the application of a potential in situ. As test system, we chose an LbL film composed of poly(L-lysine) (PLL), a biodegradable polycation, and DNA. Experiments were carried out in a specially modified cell for OWLS to be operated in electrochemical (EC) conditions with a physiological HEPES buffer. The OWLS waveguides were covered with a thin layer of Indium Tin Oxide (ITO), which acted as the working electrode of a three-electrodes cell, while potentials were applied with respect of an Ag/AgCl wire (reference electrode) and the EC current was collected by a platinum wire (counter electrode). Dissolution of the PLL/DNA films was observed for potentials above 1.8 V.

2 EXPERIMENTAL

2.1 CHEMICALS AND REAGENTS

The reagents were obtained from different companies: poly(L-lysine) hydrobromide (PLL), was purchased from Sigma Aldrich (Switzerland) and prepared at 100 mg/ml in HEPES. Deoxyribonucleic acid from fish sperm (DNA) was purchased from Amresco (USA) and prepared at 100 mg/ml in HEPES. Poly(allylamine hydrochloride) (PAH) and poly(sodium 4-styrene sulfonate) (PSS) were also obtained from Sigma (Switzerland) and prepared at 100 mg/ml. The buffer solutions (HEPES150 or HEPES500) were 10 mM 4-(2-hydroxyethyl)-1-piperazine ethanesulfonic (HEPES) acid with added 150 or 500 mM sodium chloride (NaCl) respectively and pH adjusted to 7.4 with sodium hydroxide (NaOH). HEPES, NaCl and NaOH were obtained from Sigma (Switzerland).

2.2 ELECTROCHEMICAL OWLS

The EC-OWLS instrument includes an electrochemical flow cell (figure 5.2) where the working electrode is the sensor (OW 2400c Sensor Chip, MicroVacuum), a waveguide coated with ITO, the reference electrode is silver and the counter electrode a platinum wire [37]. A potentiostat/galvanostat from Uniscan Instrument (model PG580, United Kingdom) was used for the EC-OWLS experiments. The solutions were injected with a syringe during the build-up, left to react during 5 minutes and rinsed with 3 ml of buffer, and a flow rate of 30 ml/h in buffer was used during the EC dissolution process.
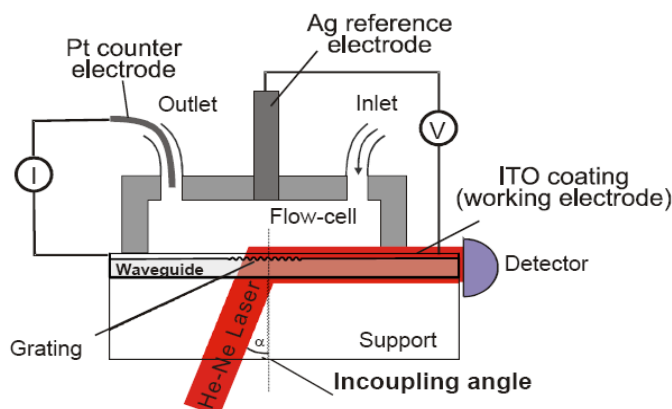
Figure 5.2.-   Schematic of EC-OWLS setup comprising a three-electrode configuration within a waveguide spectrometer with a 15 μL cell. The waveguide was coated with ITO to allow for potential control (working electrode). A silver wire inserted into the top of the cell served as a reference electrode and a platinum wire in export tubing served as a counter electrode.

2.3. ELECTROCHEMICAL ATOMIC FORCE MICROSCOPE

To observe the morphology of the film during the dissolution an electrochemical atomic force microscope (EC-AFM) was used. The EC-AFM incorporates an EC liquid cell provided with a cap with an inlet and outlet so that it is possible to fabricate and to explore LbL films without a drying step. The AFM used is the Nanowizard I BioAFM (JPK Instruments, Berlin, Germany) and the Mikromasch CSC38/noAl cantilevers both in contact and intermittent-contact modes. During the layer build-up the closed liquid-cell is filled with buffer and the solution is exchanged through the in- and outlet. After removing the cap the sample can be positioned under the AFM block without removing the liquid from the cell. As such the LbL films never undergo a drying process before and during the AFM experiment. The custom EC cell was provided with a silver wire acting as Ag/AgCl reference electrode and with a platinum wire as counter electrode. A metallic copper spring established the electrical contact with the ITO surface of the substrate so that it could be used as working electrode. Thus, the EC dissolution of the LbL films could be followed in situ. As substrates, we used glass samples coated with ITO purchased from MicroVacuum assuring the same surface as the waveguides. An AMEL potentiostat/ galvanostat (model 2053, AMEL electrochemistry, Italy) was used for EC-AFM experiments.

2.4. SAMPLE PREPARATION

LbL films were prepared according to the same procedure both for the OWLS and the AFM measurements. The ITO coated waveguides were cleaned by sonication in isopropanol followed by an O_2 plasma treatment. Polyelectrolytes were adsorbed for 5 min in HEPES150 buffer followed by 2 min rinsing, according to a procedure equivalent to the dipping method. Instead of immersing the surface in beakers containing the polyelectrolyte solutions, as in figure 5.1, a volume of 1 ml of the polyelectrolyte solution is injected into the flow cell and left react during 5 minutes, followed by an extensive rinsing with 3 ml of buffer in between each step [2, 37].

3 RESULTS

3.1 DEPOSITION AND DISSOLUTION: OWLS DATA

Fig. 5.3 shows the evolution of the adsorbed mass measured by EC-OWLS as a function of time during the fabrication and subsequent dissolution of six bilayers of PLL and DNA $(PLL/ DNA)_6$. The deposition was carried out at 0 V. The fabrication curve is characterized by the typical ''stairway'' course where every step corresponds to the injection of a polyelectrolyte.
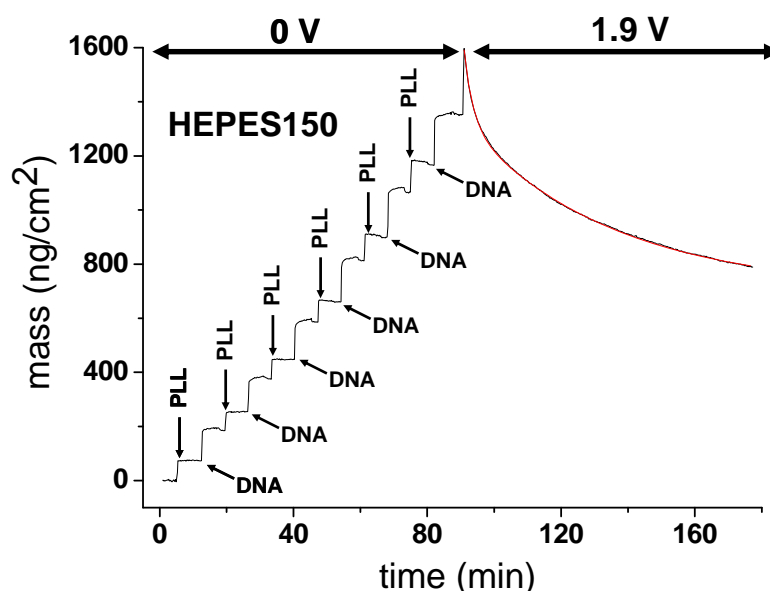

Fig. 5.3.- Adsorbed mass measured by EC-OWLS during the build-up of $(PLL/DNA)_6$ at 0 V and 1.9 V induced dissolution of multilayers in a 150 mM ionic strength buffer. A single exponential decay function was fit to the dissolution part of the curve (red line).

The obtained film is stable meaning that the adsorbed mass remains constant in the buffer solution once the fabrication is terminated. By applying a bias of $V_{diss} = 1.9$ V, the mass underwent a rapid increase and then a slow decrease. The rapid increase of the mass upon applying a voltage is due to the accumulation of ions at the ITO/buffer interface (i.e. the formation of a Stern electrical double layer) affecting the refractive index. The slow decrease is related to the dissolution of the film [24]. The time evolution of the dissolution at 1.9 V could be fitted to an exponential decay curve [24] following the next equation for the mass Γ at a given time t:

$$\Gamma = \Gamma_{\infty} + \Gamma_1 \exp^{-t/\tau} \tag{5.1}$$

with a time constant τ of 44 min and a mass percentage of remaining film Γ_{∞} of approximately 50%. This indicates that dissolution of the film indeed occurs but it is slow and only partial. It is known that pH or ionic strength of the solution can influence the dissolution speed through the destabilization of the multilayer, although we were mostly interested in taking advantage of the electrochemical control.

Fig. 5.4 shows the evolution of the adsorbed mass measured by EC-OWLS as a function of time during the fabrication and subsequent dissolution of (PLL/DNA)$_6$, as in Fig. 5.3, with the only difference that during the fabrication process a bias of $V_{dep} = 1.2$ V was applied instead of 0 V.
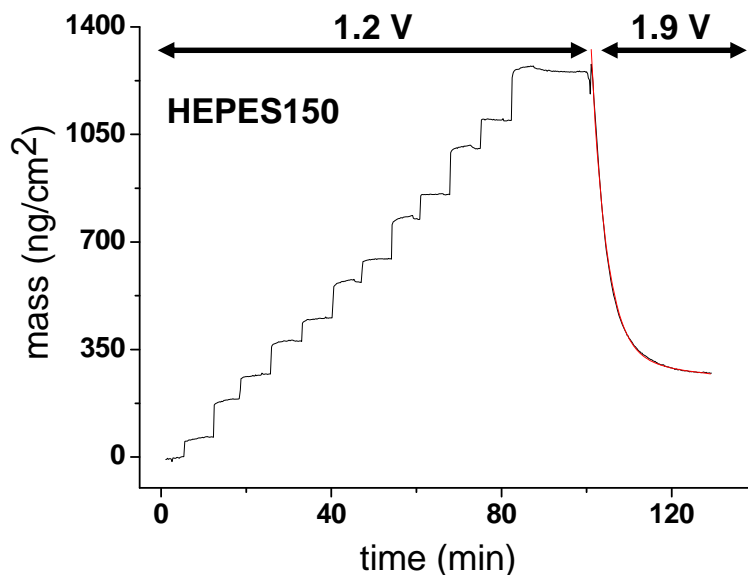

Fig. 5.4.- Adsorbed mass measured by EC-OWLS during the build-up of (PLL/DNA)$_6$ at 1.2 V and 1.9 V induced dissolution of multilayers in a 150 mM ionic strength buffer. A single exponential decay function was fit to the dissolution (red line).

While the mass of the film after deposition is unaffected by the bias, a striking difference appears for the dissolution: when a bias of 1.2 V is applied during the film deposition the dissolution occurs again with an exponential decay but it can be fitted with a much smaller time constant (5 instead of 44 min) and a much smaller mass percentage of remaining film (20% versus 50%). A comparison of the two graphs can be observed in figure 5.5. Applying a bias during the fabrication thus makes the LbL film less stable in a way that its dissolution is accelerated.
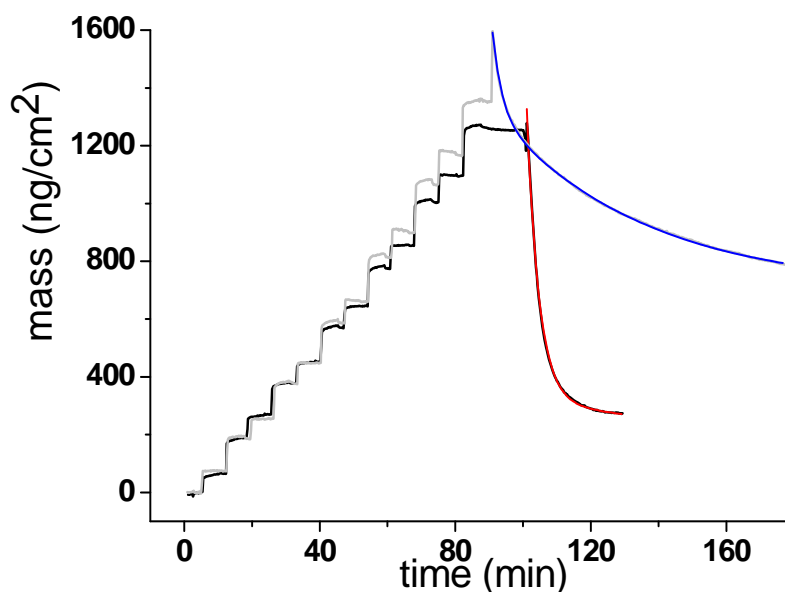

Fig. 5.5.- Adsorbed mass measured by EC-OWLS in a 150 mM ionic strength buffer during the build-up of $(PLL/DNA)_6$ at 0 V (grey line) and at 1.2 V (black line). The dissolution was induced in both cases at 1.9 V and fitted to a single exponential decay (blue line for the film built at 0 V, and red line for the film built at 1.2 V).

In an attempt to characterize in more detail this phenomenon, we studied how τ and Γ_∞ depend on V_{dep} and V_{diss}. Fig. 5.6a displays τ and Γ_∞ as a function of V_{dep} in the range between 0 and 1.2 V maintaining the value of V_{diss} at 1.9 V: both τ and Γ_∞ follow a monotonously decreasing course with increasing V_{dep}. Fig. 5.6b displays τ and Γ_∞ as a function of V_{diss} in the range between 1.8 and 2.0 V keeping constant the value of V_{dep} at 1.2 V: again the higher V_{diss} the smaller both τ and Γ_∞. In summary, the dissolution of the PEMs is faster and more efficient, the higher the potential applied.
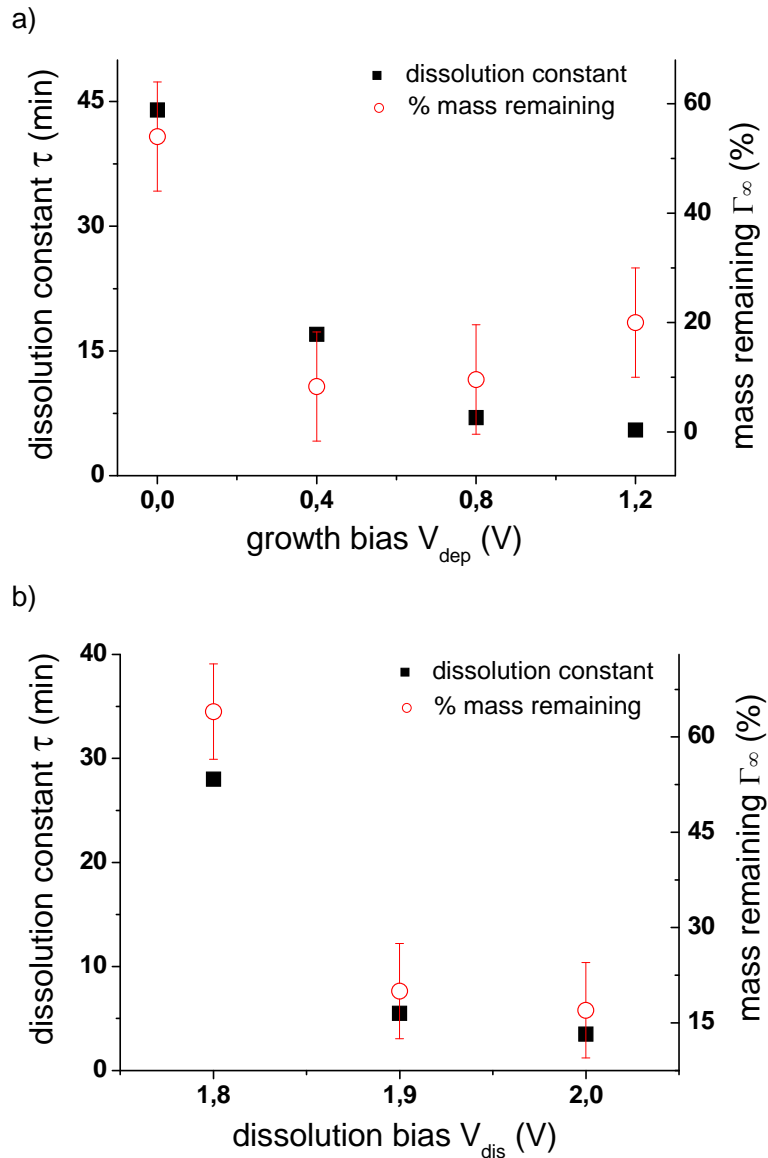
Fig. 5.6.- a) Dissolution rate at 1.9 V as determined from the fitting procedure for films fabricated at 0, 0.4, 0.8, and 1.2 V. b) Dissolution rate at different values of V_{diss} as determined from the fitting procedure for films fabricated at 1.2 V.

The effect of the ionic strength (the concentration of ions or the electrical conductivity) of the buffer solution was investigated by repeating the experiments of deposition at 0 V and 1.2 V and dissolution at 1.9 V in solutions with different salt concentration. Fig. 5.7a and 5.7b display two dissolution curves in presence of 500 mM NaCl. As in the case of 150 mM NaCl the dissolution is faster and the mass percentage of remaining film is smaller when the film is fabricated at 1.2 V than at 0 V. Incidentally, it can also be observed that the film has a lower mass [19]. Similar experiments at other salt concentrations (0 mM and 45 mM) indicated the same

behaviour. It seems the higher the ionic strength, the faster and more efficient is the dissolution.
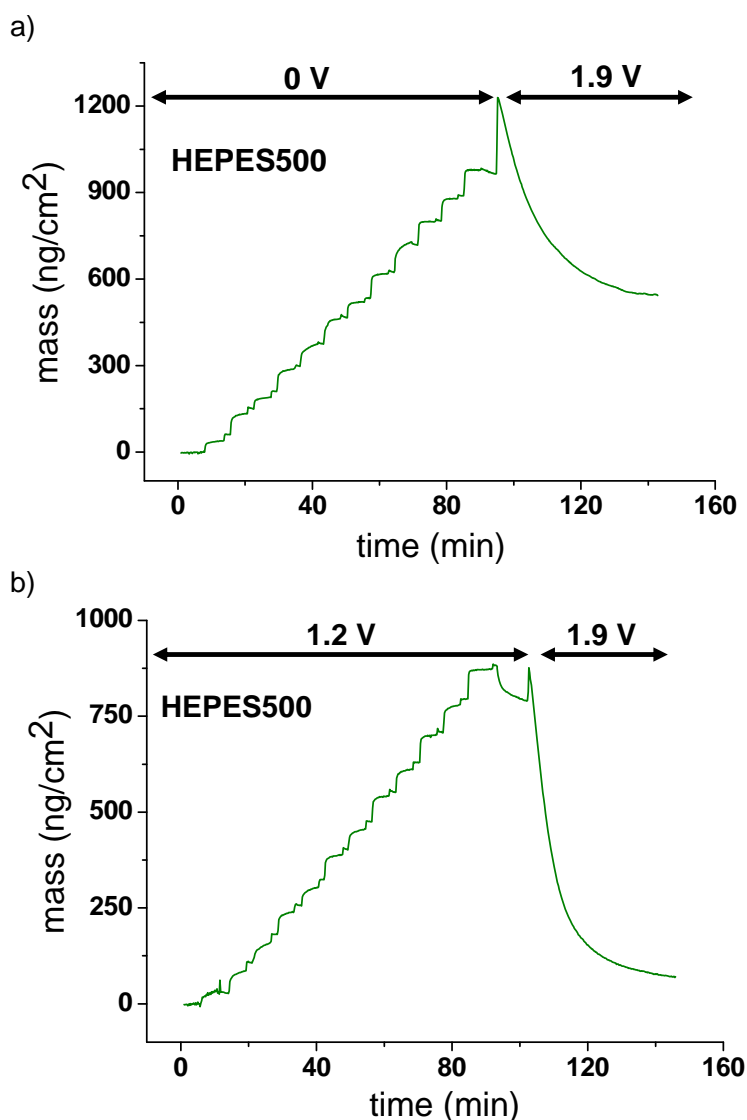

Fig. 5.7.- Adsorbed mass measured by EC-OWLS during the build-up of (PLL/DNA)$_6$ at a) 0 V, and b) 1.2 V, and 1.9 V induced dissolution of multilayer in a 500mM ionic strength buffer.

OWLS experiments carried out at higher number of bilayers (up to 15) indicated that the dissolution at 1.9 V is still quicker and more complete if a bias of 1.2 V is applied during the deposition. In figure 5.8 we can see a comparison of the dissolution of a 12 bilayer-film when built up at 0 V and at 1.2 V. When growing the film under a potential the dissolution occurs faster and results in more efficient film destruction. Applying a bias during the fabrication thus makes the LbL film less stable in a way that its dissolution is accelerated.
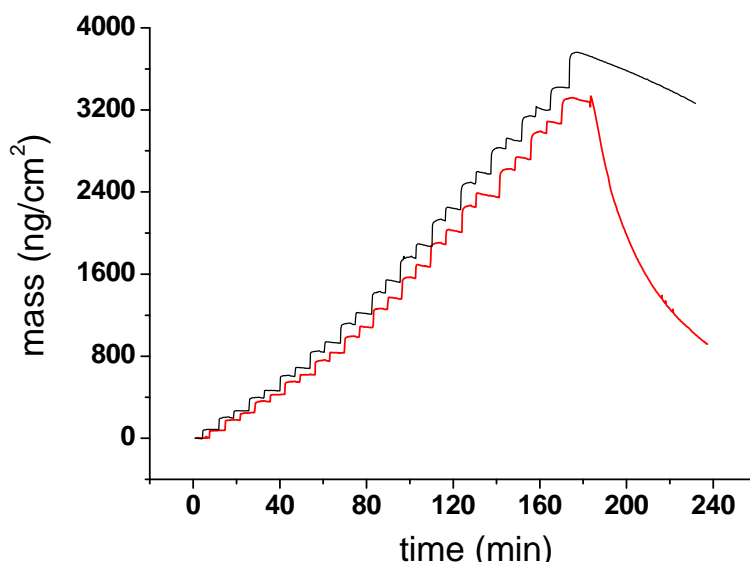
Fig. 5.8.- Adsorbed mass measured by EC-OWLS in a 150 mM ionic strength buffer during the build-up of (PLL/DNA)$_{12}$ at 0 V (black line) and at 1.2 V (red). The dissolution was induced in both cases at 1.9 V.

Finally, to be able to see if other PEMs behave the same way as the pair PLL/DNA, we have chosen to study the pair PAH/PSS. In contrast to the PLL/DNA system, PAH/PSS multilayers consist of highly charged polyelectrolytes that are known to form smooth, interdigitated layered films [38]. We studied the effect of the applied potential during the growth on the polyelectrolyte multilayer system (PAH/PSS)$_6$ in order to validate the generality of our observations. As shown in figure 5.9, the growth of the film in this case is linear with the layer number and the resulting multilayer is expected to be more stable [39].
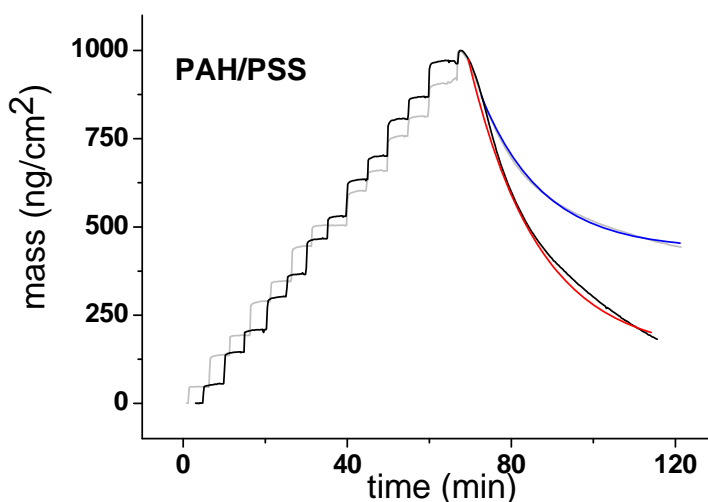

Fig. 5.9.- Adsorbed mass measured by EC-OWLS during the build-up of (PAH/PSS)$_6$ at 0 V (grey line) and at 1.2 V (black line). The dissolution was induced in both cases at 1.9 V and fitted to a single exponential decay (blue line for the film built at 0 V, and red line for the film built at 1.2 V).

Although, applying a bias during the fabrication of the film does not significantly modify the final amount of the deposited mass, but it affects the stability of the film with respect of the EC dissolution: if a bias is applied, both τ and Γ_∞ are smaller. Therefore, we can conclude that despite the major differences in their structure, with regards to potential induced dissolution, PAH/PSS multilayers behave like the PLL/DNA films at least qualitatively.

3.2 MORPHOLOGY BEFORE AND DURING THE EC DISSOLUTION: IN SITU AFM DATA

EC-AFM was used to gain complementary information about the topographical changes of the multilayers before and during the dissolution process. This topographical information will help us understand whether the dissolution starts from the top of the film of from the surface of the electrode. Fig. 5.10a is a topographical AFM image of (PLL/DNA)$_6$ fabricated at 0 V before the dissolution process. The PEM film is constituted of nanodroplets with a density of 25 μm^{-2}. The related height and size distributions of the droplets are plotted in Fig. 5.10b and 5.10c showing a mean value for the height of 27 nm and of 110 nm for the droplets size, where the size of every island was estimated from its full width at half maximum (FWHM) value. Analogously, figure 5.10d is the AFM image for the LbL film fabricated at 1.2 V, and figure 5.10e and 5.10f are the corresponding height and size distribution of the droplets. The film is constituted of nanodroplets that are directly adsorbed on the ITO surface and should not be interpreted as the top roughness of a thicker underlying film. In this case, the average height of the islands is 24 nm and the FWHM size is 108 nm. The height and size distribution are very similar to those at 0 V. Therefore, it can be stated that applying a bias during the deposition does not affect the final morphology of the film. It has to be emphasized that the PEM nanodroplets cannot be confused with ITO clusters since ITO films appear with RMS roughness of 1 nm on AFM images before PEM deposition (Figure 5.11).
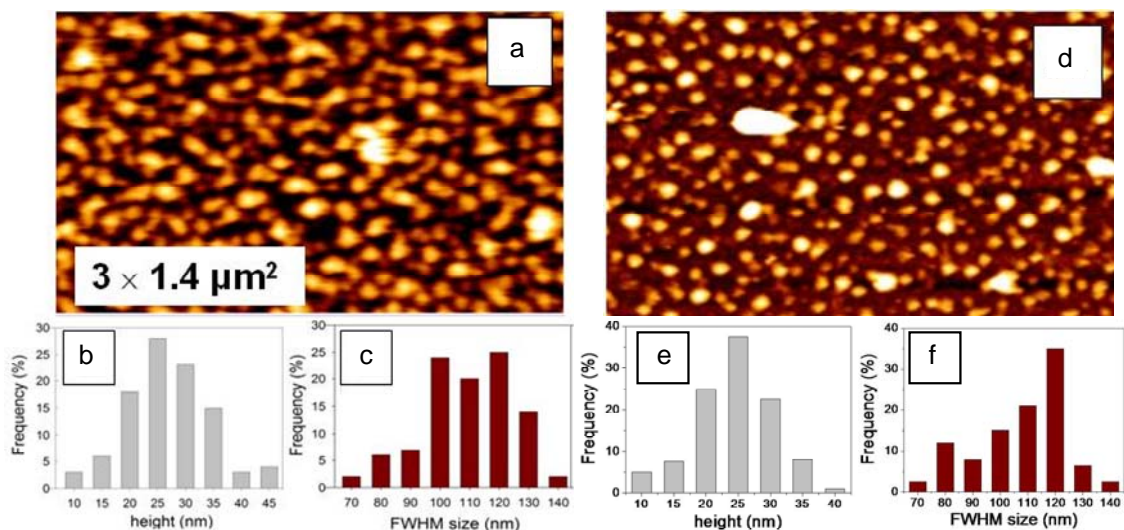
Fig. 5.10.- a) An AFM image of (PLL/DNA)$_6$ fabricated at 0 V (HEPES150, intermittent contact mode). The corresponding analysis of b) height and c) size of the islands. d) AFM image of (PLL/DNA)$_6$ fabricated at 1.2 V and e) the height and f) size analysis of the islands.
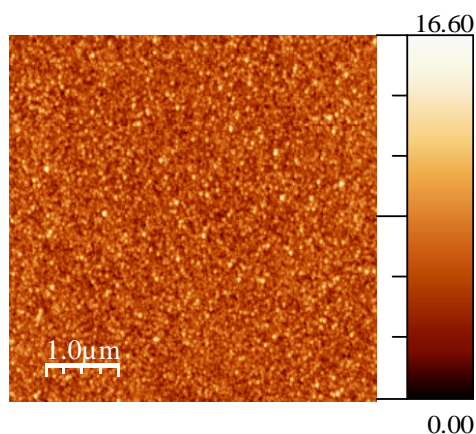

Fig. 5.11.- AFM image of a bare ITO substrate. The RMS roughness is 1nm.

To observe in situ the dissolution of the droplets, we used the EC-AFM in the LbL film fabricated at 1.2 V. Since the scanning rate is comparable with the dissolution rate we adopted the following procedure. We took an image of the film at t = 0 min. Then we retracted the tip and applied 1.9 V for a certain amount of time Δt_1. We switched off the potentiostat, approached the tip and scanned the same area obtaining the image at t = t_1 min. We retracted again the tip and repeated the cycle until the end of the dissolution process. Figures 5.12a-d are the corresponding AFM images during the dissolution 0, 15, 35 and 55 min after the beginning. Thanks to the possibility of recording images of the same area during the dissolution we could follow the time evolution of every single nanodroplet. We found that while all PEM droplets shrink in

size most of them do not completely disappear. This is in agreement with the gradual decrease of the film mass during the EC-OWLS experiments as well as with the residual mass remaining at the end of them (finite value of Γ_∞). The measured island density decreases from an initial value of 22 μm^{-2} to 17 μm^{-2}. Figures 5.12e–f are the corresponding plots of the height and size distribution at the beginning and at the end of the dissolution: the height decreases from 25 to 8 nm, while the size decreases from 110 to 65 nm. It has to be noted that the size reduction is not the same for all the droplets: indeed, some bigger island do shrink less than others. Furthermore, it has to be pointed out that the effect of the tip convolution was not taken into account, therefore the nanodroplet size is surely overestimated: the overestimation should not depend on the nanodroplet size because their height is of the same order of magnitude.
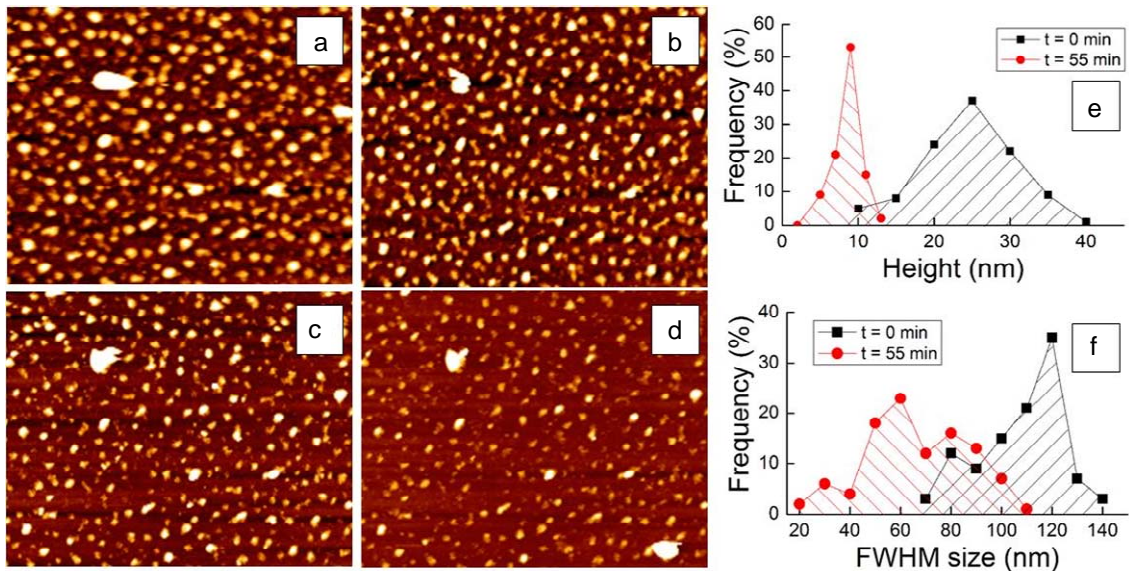

Fig. 5.12.- 3x2 μm^2 AFM images of (PLL/DNA)$_6$ fabricated at 1.2 V a) before the applying the dissolution potential of 1.9 V, b) after applying the potential for 15 min, c) 35 min and d) 55 min. The four images represent the same region. Corresponding e) height and f) size islands analysis at $t = 0$ and at $t = 55$ min.

AFM experiments were carried out increasing the number of bilayers up to 15 whereby the droplets start coalescing. We observed again the shrinking phenomenon with the particularity that all the droplets do not become smaller by the same percentage.

4 DISCUSSION

The in situ experimental AFM data showed that PLL/DNA films are constituted of nanodroplets and that the applied bias during the deposition does not affect their morphology. In situ AFM images during the EC dissolution also revealed that the nanodroplets shrink but many droplets remain on the surface at the end of the EC process (*e.g.* close to 80% in the presented case in Fig. 5.12d).

Experimental OWLS data indicate that applying a bias higher than 1.8 V after the deposition of a PLL/DNA LbL film on ITO induces its dissolution that can be fitted by an exponential decay with a satisfactory approximation. If a bias of 1.2 V is applied during the fabrication, the amount of the deposited LbL film is similar to the 0 V case, but the stability of the film is reduced in such a way that its electrochemically stimulated dissolution occurs faster and more efficiently. The delivery of DNA from PEMs can then reach a rate of 110 ng/cm^2 per minute. The EC-OWLS technique has allowed achieving quantitative information on the stability of LbL films and their dissolution in situ, permitting a better understanding of the underlying mechanisms that rule the process.

In a previous work on PLL/heparin films [24], it was suggested that the EC dissolution was stimulated by a combination of two effects: pH changes at the surface of the electrode due to the water electrolysis and ion migration into the film as consequence of the applied potential. In regards with the pH change at the electrode and in parallel with the present investigation, Vörös' group has developed a method for monitoring the electrochemically induced pH changes close to a microelectrode using the pH dependence of fluorescent dyes in solution and the desorption of fluorescent polyelectrolytes from the electrode [40]. It turned out that pH values of 4 are reached at the electrode surface for current densities of 1 A/m^2 similar to that used during the dissolution at 1.9 V and of pH 6 for current densities of 0.01 A/m^2 similar to that used during the deposition at 1.2 V. The decay of the pH gradient from the electrode surface strongly depends on the HEPES buffer concentration: in our conditions, the decay length is of the order of 1 μm. It is known from the literature that PLL starts desorbing from a SiO2 surface at pH values lower than 5.5 [41]. The ion migration mechanism also seems to play a destabilizing effect [40]: at the cathode, not only protons are produced but Cl$_2$ too, which promptly reacts with water producing HClO. HClO is

known to react with the amines of the lysine side chains forming monochloramine (R-NHCl derivatives) as described by Grisham et al [42]. Chloramines decompose to nitrogen-centered radicals or carbonyl groups. Since carbonyl can crosslink with free amine groups via Schiff base formation, amine side groups can intra- or inter-molecularly crosslink and, therefore, lose their charge, diminishing their ability to electrostatically interact with the polyanions [43]. In summary, the ions produced at the electrodes will interact with the free groups in the polyelectrolytes, reducing their electroactivity and therefore their capacity to bind to each other.

We try now to rationalise the destabilizing effect of an applied bias during the film deposition on the basis of the phenomena just listed occurring at electrodes. Figure 5.13a shows the height of the PLL deposition steps at 0 and 1.2 V derived from figures 5.3 and 5.4. A difference can be noticed in the first three steps: the PLL step height is bigger at 1.2 V than at 0 V yet levelling off by the increasing number of bilayers (#bi). Indeed, no difference occurs any more from the fourth bilayer. On the other hand, the fact that the first PLL steps are higher at 1.2 V is in agreement with the finding by Ngankam and Van Tassel on the continuous PLL adsorption under an applied potential [44]. The DNA step height is characterized by an opposite behaviour as a function of #bi (Fig. 5.13b): the DNA step height is bigger at 0 V and the difference tends to amplify with increasing #bi.
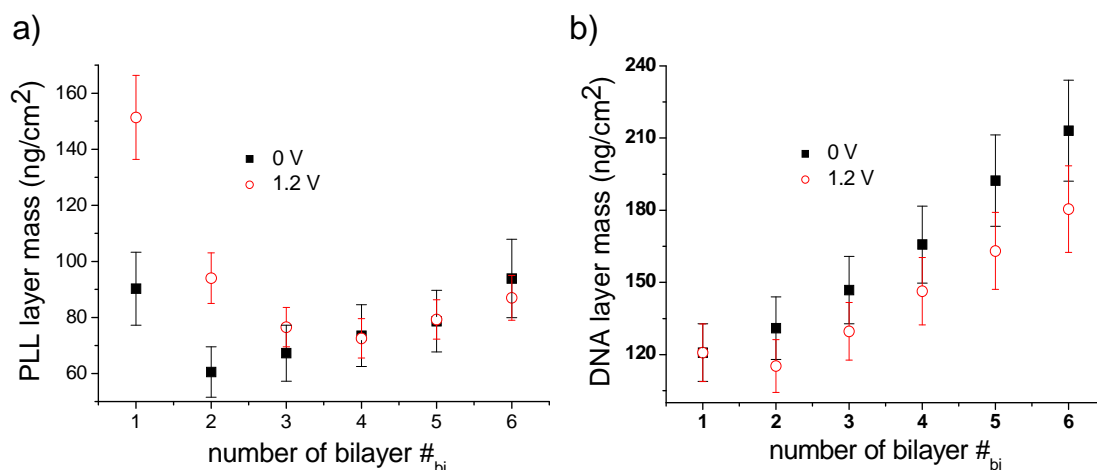

Fig. 5.13.- Height of the a) PLL and b) DNA adsorption steps at 0V and 1.2V as derived by the OWLS curves of the adsorbed mass depicted in Fig. 3 and 4.

In presence of a potential, less and less polyanion adsorbs on the film with respect to the film at 0 V whereas the amount of polycation is bigger at the beginning and similar afterwards. This means that the electrostatic overcompensation during the film deposition is altered by the presence of an applied potential: this can explain the different stability with respect to EC dissolution.
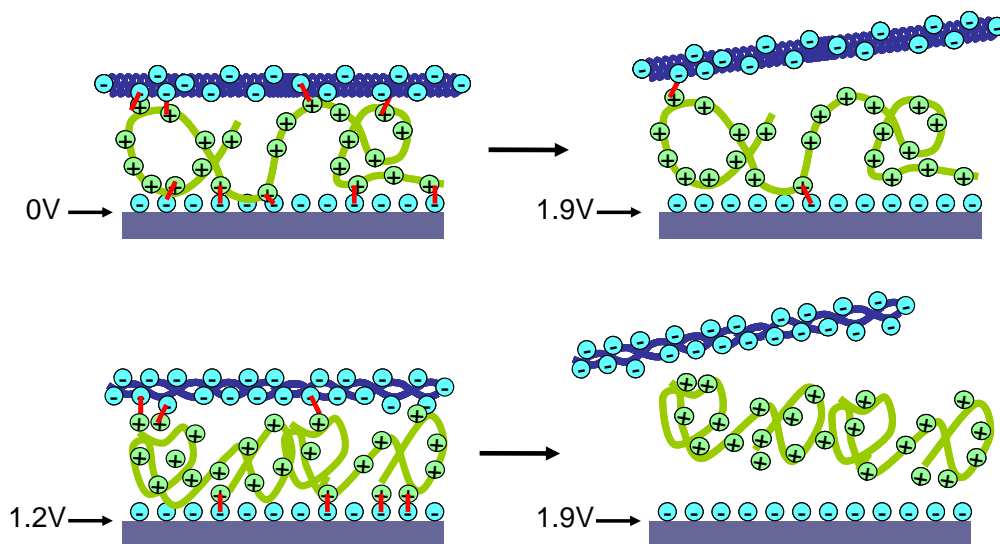

Fig. 5.14.- Scheme of the growth of the LbL film at 0V and at 1.2V and evolution of these films when applied a higher potential to promote the dissolution. In the presence of a potential, the electrostatic stability is stablished not only by a balance between the charges of the polyelectrolytes, but also the protons and chloride ions introduced at the electrodes. More polycation and less polyanion will be necessary in the biased build up. Less electrostatic bonds will be created between the layers when the film is built at 1.2 V, making the LbL less stable and easier to be released when the potential applied is increased.

The course of the dissolution rate as function of V_{diss} at constant V_{dep} and as a function of V_{dep} at fixed V_{diss} (Fig. 5.6) can be rationalized based on the pH change at the electrode: the electrochemical current (and consequently the amount of produced protons) at an electrode exponentially depends on the applied overpotential. In addition, reactive species are generated at the electrode that can alter the chemical properties of the polymers. The pK_a of amine groups is ~10, therefore acidic pH is not expected to affect the charge of the PLL. However, the amount of negative charge on the DNA is also expected to change close to the electrode when the dissolution potential is applied. Although this might explain why we see faster dissolution at higher potential, the observed difference during build-up remains unanswered. Why do we see larger PLL and smaller DNA steps at an applied 1.2 V bias? (See Fig. 5.13). A possible answer is the mentioned reaction with Cl_2: this results in less charge per PLL consequently the

PLL to DNA ratio in the layer is expected to increase to maintain charge equilibrium. A cartoon explaining the different behaviours during the deposition and dissolution at open circuit and under a potential is included in figure 5.14. OWLS data were corroborated by AFM data concerning the amount of deposited film at 0 and 1.2 V: OWLS measures the same mass for the films in the two cases while AFM shows the same density, size and height distribution for the observed nanodroplets. It can be thus excluded that the different stability of the film is originated from a different morphology of the film. Finally, a remark on the time evolution of the dissolution: The obtained good fit with a single exponential decay indicates that the amount of released molecules is directly proportional to the mass of the ''mobile'' fraction of the multilayer. Unfortunately, the time evolutions of the OWLS data and of the AFM data could not be directly compared because the geometry of the two EC-cells is different. Moreover, the EC dissolution in the OWLS cell was carried out under a constant flow of buffer while no buffer flow could be installed during AFM measurements. However, we can clearly state that the nanodroplet morphology seems to have no influence on the dissolution process.

From this study some questions remain still open regarding the EC dissolution of a LbL film. First is how it takes place: do the molecules desorb from the surface of the nanodroplets or whole droplets leave due to the broken interaction with the surface? The observed shrinking of the nanodroplets during the EC dissolution clearly indicates that the release of the polyelectrolytes occurs at the surface of the nanodroplets (Fig. 5.12). Second, could we rationalize in terms of pH changes and/or HClO formation how the applied bias during the depositions affects the stability of the multilayer? It would also be interesting to monitor and quantify the ion migration at the electrified electrode/solution interface in order to completely disentangle the mechanism of the EC dissolution. And third, why the film does not completely dissolve still remains puzzling. Are more stable polymer complexes formed inside the nanodroplets during the film deposition or during the EC dissolution? Further experiments carried out in Vörös' group have succeeded in clarifying these issues. An intensive study of various PEM systems performed with EC-OWLS and EC-AFM confirmed that the degradation of polyelectrolyte assemblies results essentially from polyelectrolyte neutralization and counter-ion condensation at the electrode/polyelectrolyte interface [45]. Two simultaneous phenomena occur at acidic pH. While counter-anions migrate into the

assembly provoking an excess of positive charges within the multilayer, the generation of protons upon water electrolysis at the electrode surface leads to the neutralization of the polyanion chains, which results in the interactions polyanion-polycation being weakened, and free polyelectrolytes can be released into the bulk, at least for the outermost layers of the film. This happens for PEMs up to 350 nm in thickness. For thicker films, the outermost part of the film is above a critical distance from the elcectrode, where the pH change is not sufficient to induce the rupture of the ionic bonds. Furthermore, the amount of residual material on the electrode after dissolution seems to correlate with the amount of amide bonds formed within the PEM [46]. Being covalent bonds formed within the assembly are unsensitive to the electrochemical stimulus and hold the polyelectrolyte chains together.

5 CONCLUSIONS

The EC-OWLS technique has allowed monitoring the kinetics of deposition and the electrochemically induced dissolution of PEMs containing DNA. The behaviour of the LbL films was confirmed by in situ EC-AFM. If the film was fabricated at 0 V, its EC dissolution at 1.9 V was slow and partial. On the contrary, if a bias up to 1.2 V was applied during the deposition, the EC dissolution at 1.9 V was much quicker and nearly complete. This effect was observed at different salt concentrations and also for other more stable systems like PAH/PSS. In situ AFM data showed that $(PLL/DNA)_6$ consists of nanodroplets and that the morphology of the film is independent on the applied bias during the deposition. The droplets were observed to shrink during the EC dissolution, indicating that the release of the polymers occurs at their surface. The process could be rationalized at the light of two phenomena occurring at the electrode under potentiostatic conditions: changes of pH and the formation of HClO reacting with the PLL amines. This study is not only relevant for applications such as local drug delivery, or DNA transfection; but also provides a new tool for biological studies. Clever cell culture systems can be envisioned where drugs or growth factors are released as wished with controlled kinetics at the required position.

6 REFERENCES

[1] G. Decher, J. D. Hong, and J. Schmitt, "Buildup of ultrathin multilayer films by a self-assembly process: III. Consecutively alternating adsorption of anionic and cationic polyelectrolytes on charged surfaces," *Thin Solid Films,* vol. 210-211, pp. 831-835, 1992.

[2] G. Decher, "Fuzzy Nanoassemblies: Toward Layered Polymeric Multicomposites," *Science,* vol. 277, pp. 1232-1237, August 29, 1997 1997.

[3] Z. Tang, Y. Wang, P. Podsiadlo, and N. A. Kotov, "Biomedical Applications of Layer-by-Layer Assembly: From Biomimetics to Tissue Engineering," *Advanced Materials,* vol. 18, pp. 3203-3224, 2006.

[4] Y. Sun, X. Zhang, C. Sun, B. Wang, and J. Shen, "Fabrication of ultrathin film containing bienzyme of glucose oxidase and glucoamylase based on electrostatic interaction and its potential application as a maltose sensor," *Macromolecular Chemistry and Physics,* vol. 197, pp. 147-153, 1996.

[5] M. Onda, Y. Lvov, K. Ariga, and T. Kunitake, "Sequential reaction and product separation on molecular films of glucoamylase and glucose oxidase assembled on an ultrafilter," *Journal of Fermentation and Bioengineering,* vol. 82, pp. 502-506, 1996.

[6] M. Onda, Y. Lvov, K. Ariga, and T. Kunitake, "Sequential actions of glucose oxidase and peroxidase in molecular films assembled by layer-by-layer alternate adsorption," *Biotechnology and Bioengineering,* vol. 51, pp. 163-167, 1996.

[7] G. B. Sukhorukov, H. Möhwald, G. Decher, and Y. M. Lvov, "Assembly of polyelectrolyte multilayer films by consecutively alternating adsorption of polynucleotides and polycations," *Thin Solid Films,* vol. 284-285, pp. 220-223, 1996.

[8] R. V. Klitzing and H. Mö̈hwald, "Transport through ultrathin polyelectrolyte films," *Thin Solid Films,* vol. 284-285, pp. 352-356, 1996.

[9] R. V. Klitzing and H. Mö̈hwald, "A realistic diffusion model for ultrathin polyelectrolyte films," *Macromolecules,* vol. 29, pp. 6901-6906, 1996.

[10] R. Pommersheim, J. Schrezenmeir, and W. Vogt, "Immobilization of enzymes by multilayer microcapsules," *Macromol. Chem. Phys.,* vol. 195, pp. 1557-1567, 1994.

[11] S. W. Keller, S. A. Johnson, E. S. Brigham, E. H. Yonemoto, and T. E. Mallouk, "Photoinduced charge separation in multilayer thin films grown by sequential adsorption of polyelectrolytes," *Journal of the American Chemical Society,* vol. 117, pp. 12879-12880, 1995.

[12] T. M. Cooper, A. L. Campbell, and R. L. Crane, "Formation of polypeptide - dye multilayers by an electrostatic self-assembly technique," *Langmuir,* vol. 11, pp. 2713-2718, 1995.

[13] P. Stroeve, V. Vasquez, M. A. N. Coelho, and J. F. Rabolt, "Gas transfer in supported films made by molecular self-assembly of ionic polymers," *Thin Solid Films,* vol. 284-285, pp. 708-712, 1996.

[14] B. G. De Geest, N. N. Sanders, G. B. Sukhorukov, J. Demeester, and S. C. De Smedt, "Release mechanisms for polyelectrolyte capsules," *Chemical Society Reviews,* vol. 36, pp. 636-649, 2007.

[15] B. Jiang, J. B. Barnett, and B. Li, "Advances in polyelectrolyte multilayer nanofilms as tunable drug delivery systems," *Nanotechnol., Sci. Appl.,* vol. 2, pp. 21-27, 2009.

[16]   D. M. Lynn, "Peeling back the layers: Controlled erosion and triggered disassembly of multilayered polyelectrolyte thin films," *Advanced Materials,* vol. 19, pp. 4118-4130, 2007.

[17]   C. M. Jewell and D. M. Lynn, "Multilayered polyelectrolyte assemblies as platforms for the delivery of DNA and other nucleic acid-based therapeutics," *Advanced Drug Delivery Reviews,* vol. 60, pp. 979-999, 2008.

[18]   A. J. Chung and M. F. Rubner, "Methods of Loading and Releasing Low Molecular Weight Cationic Molecules in Weak Polyelectrolyte Multilayer Films," *Langmuir,* vol. 18, pp. 1176-1183, 2002.

[19]   K. Ren, Y. Wang, J. Ji, Q. Lin, and J. Shen, "Construction and deconstruction of PLL/DNA multilayered films for DNA delivery: Effect of ionic strength," *Colloids and Surfaces B: Biointerfaces,* vol. 46, pp. 63-69, 2005.

[20]   J. F. Quinn and F. Caruso, "Thermoresponsive Nanoassemblies: Layer-by-Layer Assembly of Hydrophilic-Hydrophobic Alternating Copolymers," *Macromolecules,* vol. 38, pp. 3414-3419, 2005.

[21]   A. W. Jensen, N. K. Desai, B. S. Maru, and D. K. Mohanty, "Photohydrolysis of Substituted Benzyl Esters in Multilayered Polyelectrolyte Films," *Macromolecules,* vol. 37, pp. 4196-4200, 2012/06/10 2004.

[22]   D. Mertz, J. Hemmerlã©, J. r. m. Mutterer, S. Ollivier, J.-C. Voegel, P. Schaaf, and P. Lavalle, "Mechanically Responding Nanovalves Based on Polyelectrolyte Multilayers," *Nano Letters,* vol. 7, pp. 657-662, 2012/06/10 2007.

[23]   T. Serizawa, M. Yamaguchi, and M. Akashi, "Time-Controlled Desorption of Ultrathin Polymer Films Triggered by Enzymatic Degradation," *Angewandte Chemie International Edition,* vol. 42, pp. 1115-1118, 2003.

[24]   F. Boulmedais, C. S. Tang, B. Keller, and J. Vörös, "Controlled Electrodissolution of Polyelectrolyte Multilayers: A Platform Technology Towards the Surface-Initiated Delivery of Drugs," *Advanced Functional Materials,* vol. 16, pp. 63-70, 2006.

[25]   K. Sato, D. Kodama, Y. Naka, and J. i. Anzai, "Electrochemically Induced Disintegration of Layer-by-Layer-Assembled Thin Films Composed of 2-Iminobiotin-Labeled Poly(ethyleneimine) and Avidin," *Biomacromolecules,* vol. 7, pp. 3302-3305, 2006.

[26]   K. C. Wood, N. S. Zacharia, D. J. Schmidt, S. N. Wrightman, B. J. Andaya, and P. T. Hammond, "Electroactive controlled release thin films," *Proceedings of the National Academy of Sciences of the United States of America,* vol. 105, pp. 2280-2285, February 19, 2008 2008.

[27]   T. Y. Tsong, "Electroporation of cell membranes," *Biophysical Journal,* vol. 60, pp. 297-306, 1991.

[28]   K. Itaka, K. Yamauchi, A. Harada, K. Nakamura, H. Kawaguchi, and K. Kataoka, "Polyion complex micelles from plasmid DNA and poly(ethylene glycol)-poly(L-lysine) block copolymer as serum-tolerable polyplex system: Physicochemical properties of micelles relevant to gene transfection efficiency," *Biomaterials,* vol. 24, pp. 4495-4506, 2003.

[29]   K. Itaka, A. Harada, K. Nakamura, H. Kawaguchi, and K. Kataoka, "Evaluation by flourescence resonance energy transfer of the stability of nonviral gene delivery vectors under physiological conditions," *Biomacromolecules,* vol. 3, pp. 841-845, 2002.

[30] K. Riehemann, S. W. Schneider, T. A. Luger, B. Godin, M. Ferrari, and H. Fuchs, "Nanomedicine - Challenge and perspectives," *Angewandte Chemie - International Edition,* vol. 48, pp. 872-897, 2009.

[31] N. Jessel, M. Oulad-Abdelghani, F. Meyer, P. Lavalle, Y. Haïkel, P. Schaaf, and J. C. Voegel, "Multiple and time-scheduled in situ DNA delivery mediated by β-cyclodextrin embedded in a polyelectrolyte multilayer," *Proceedings of the National Academy of Sciences of the United States of America,* vol. 103, pp. 8618-8621, June 6, 2006 2006.

[32] F. Meyer, V. Ball, P. Schaaf, J. C. Voegel, and J. Ogier, "Polyplex-embedding in polyelectrolyte multilayers for gene delivery," *Biochimica et Biophysica Acta (BBA) - Biomembranes,* vol. 1758, pp. 419-422, 2006.

[33] M. Dimitrova, Y. Arntz, P. Lavalle, F. Meyer, M. Wolf, C. Schuster, Y. Haïkel, J. C. Voegel, and J. Ogier, "Adenoviral Gene Delivery from Multilayered Polyelectrolyte Architectures," *Advanced Functional Materials,* vol. 17, pp. 233-245, 2007.

[34] J. Zhang, S. I. Montañez, C. M. Jewell, and D. M. Lynn, "Multilayered Films Fabricated from Plasmid DNA and a Side-Chain Functionalized Poly(β-amino Ester): Surface-Type Erosion and Sequential Release of Multiple Plasmid Constructs from Surfaces," *Langmuir,* vol. 23, pp. 11139-11146, 2012/06/10 2007.

[35] F. Yamauchi, K. Kato, and H. Iwata, "Layer-by-Layer Assembly of Poly(ethyleneimine) and Plasmid DNA onto Transparent Indium-Tin Oxide Electrodes for Temporally and Spatially Specific Gene Transfer," *Langmuir,* vol. 21, pp. 8360-8367, 2012/06/10 2005.

[36] F. Wang, D. Li, G. Li, X. Liu, and S. Dong, "Electrodissolution of Inorganic Ions/DNA Multilayer Film for Tunable DNA Release," *Biomacromolecules,* vol. 9, pp. 2645-2652, 2012/06/10 2008.

[37] J. P. Bearinger, J. Vörös, J. A. Hubbell, and M. Textor, "Electrochemical optical waveguide lightmode spectroscopy (EC-OWLS): A pilot study using evanescent-field optical sensing under voltage control to monitor polycationic polymer adsorption onto indium tin oxide (ITO)-coated waveguide chips," *Biotechnology and Bioengineering,* vol. 82, pp. 465-473, 2003.

[38] A. Izquierdo, S. S. Ono, J. C. Voegel, P. Schaaf, and G. Decher, "Dipping versus Spraying: Exploring the Deposition Conditions for Speeding Up Layer-by-Layer Assembly," *Langmuir,* vol. 21, pp. 7558-7567, 2012/06/10 2005.

[39] P. Lavalle, C. Gergely, F. J. G. Cuisinier, G. Decher, P. Schaaf, J. C. Voegel, and C. Picart, "Comparison of the Structure of Polyelectrolyte Multilayer Films Exhibiting a Linear and an Exponential Growth Regime: An in Situ Atomic Force Microscopy Study," *Macromolecules,* vol. 35, pp. 4458-4465, 2012/06/10 2002.

[40] M. Gabi, T. Sannomiya, A. Larmagnac, M. Puttaswamy, and J. Voros, "Influence of applied currents on the viability of cells close to microelectrodes," *Integrative Biology,* vol. 1, pp. 108-115, 2009.

[41] T. M. Blättler, S. Pasche, M. Textor, and H. J. Griesser, "High Salt Stability and Protein Resistance of Poly(l-lysine)-g-poly(ethylene glycol) Copolymers Covalently Immobilized via Aldehyde Plasma Polymer Interlayers on Inorganic and Polymeric Substrates," *Langmuir,* vol. 22, pp. 5760-5769, 2012/06/10 2006.

[42] M. B. Grisham, M. M. Jefferson, D. F. Melton, and E. L. Thomas, "Chlorination of endogenous amines by isolated neutrophils. Ammonia-dependent bactericidal,

cytotoxic, and cytolytic activities of the chloramines," *Journal of Biological Chemistry,* vol. 259, pp. 10404-10413, August 25, 1984 1984.

[43]   C. L. Hawkins, D. I. Pattison, and M. J. Davies, "Hypochlorite-induced oxidation of amino acids, peptides and proteins," *Amino Acids,* vol. 25, pp. 259-274, 2003.

[44]   A. P. Ngankam and P. R. Van Tassel, "Continuous polyelectrolyte adsorption under an applied electric potential," *Proceedings of the National Academy of Sciences of the United States of America,* vol. 104, pp. 1140-1145, January 23, 2007 2007.

[45]   O. Guillaume-Gentil, N. Graf, F. Boulmedais, P. Schaaf, J. Vörös, and T. Zambelli, "Global and local view on the electrochemically induced degradation of polyelectrolyte multilayers: from dissolution to delamination," *Soft Matter,* vol. 6, pp. 4246-4254, 2010.

[46]   O. Guillaume-Gentil, D. Abbruzzese, E. Thomasson, J. Vörös, and T. Zambelli, "Chemically Tunable Electrochemical Dissolution of Noncontinuous Polyelectrolyte Assemblies: An In Situ Study Using ecAFM," *ACS Applied Materials & Interfaces,* vol. 2, pp. 3525-3531, 2012/06/10 2010.

GENERAL CONCLUSIONS

Taking advantage of the last advances in nanotechnology, the versatility of an Optical Grating Coupler Biosensor has been investigated.

In the technological part of this thesis and after an extensive study on how the film thickness and refractive index affects the sensitivity of waveguides, a polymer-based grating sensor chip has been designed and fabricated by Nano Imprint Lithography. This polymer grating will be the substrate for an ITO waveguide featuring high sensitivity. Also, gold coated commercial gratings have been fabricated with good optical characteristics, but poor adhesion. A waveguide with a silicon nitride grating surface has been fabricated by coating a diffraction grating with a 10 nm thin layer of Si_3N_4 by sputtering deposition. The adsorbed mass of protein on the surface can be easily measured, giving extra information about the molecular interactions processes compared with the previous detection techniques. The potential of the Si_3N_4 covered grating sensor chips opens new ways in biosensing, allowing the integration of optical biosensors with microelectronics.

A new calibration protocol has been established for experiments requiring high precision measurements. This routine includes an individual modelling of each sensor chip and considers, in a very precise way, parameters that are normally not taken into account, such as the buffer's nature, its composition and the working temperature. In this way, the particular refractive indices of buffer solutions can be measured with great accuracy before each experiment regardless the working conditions, ensuring high precision of the kinetics measurements and in the further analysis of an adsorbed layer.

Looking at the biomedical applications, taking advantage of the grating coupler biosensor, olfactory receptors carried by nanosomes were successfully immobilized onto biosensor surfaces functionalized by mixed self-assembled monolayers. The use of our biosensor has been crucial to fully characterize the functionalization process and to understand that the enrichment in membrane receptors has not been achieved. The combination of the grating coupler with electrochemistry has allowed monitoring the kinetics of deposition and the electrochemically induced dissolution of polyelectrolyte multilayers containing DNA.

APPENDIX: EXPERIMENTAL

1 FABRICATION TECHNIQUES

1.1 SOFT LITHOGRAPHY

In technology, soft lithography refers to a family of techniques for fabricating or replicating structures using elastomeric stamps, molds, and conformable photomasks [2]. It is called soft because it uses elastomeric materials most notably PDMS. Soft lithography is generally used to construct features measured on the micrometer to nanometer scale.

PDMS stamps are pieces of polydimethylsiloxane (PDMS) that have been patterned usually against a master to form a relief pattern. This PDMS stamp can be used in either its current form as a relief surface for techniques such as Micro Contact Printing or can also be attached to an external source by tubing so that liquid may be past through channels on its surface. Alternatively a PDMS stamp can be laminated to a second piece of PDMS to form a contained device, as shown in figure A.1. It is possible to pattern PDMS to micrometer scale. Many techniques have been developed to modify the basic setups to perform a range of tasks such as assays on small volumes. These kinds of devices are often referred to as microfluidic devices. Because of the dimensions of these devices flow is laminar not turbulent which can lead to many useful properties however it reduces the ability of fluid streams to mix.
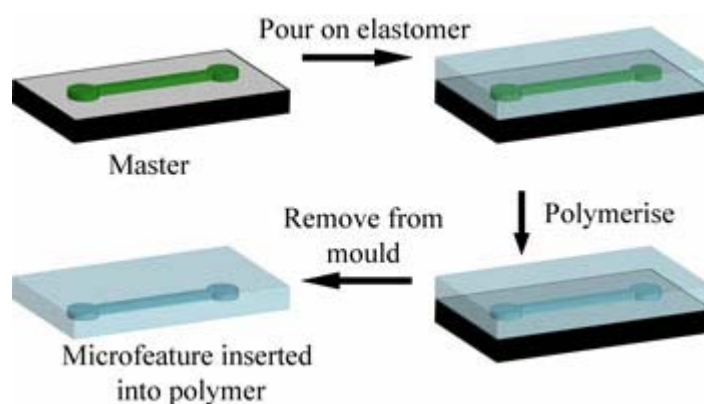

Figure A.1.- Fabrication of a microfluidics chip by soft lithography with PDMS.

1.2 NANO-IMPRINT LITHOGRAPHY

Nanoimprint lithography is a method of fabricating nanometer scale patterns. It is a simple nanolithography process with low cost, high throughput and high resolution. It creates patterns by mechanical deformation of imprint resist and subsequent processes. The imprint resist is typically a monomer or polymer formulation that is cured by heat or UV light during the imprinting. Adhesion between the resist and the template is controlled to allow proper release.

In a standard Thermoplastic-NIL process, a thin layer of imprint resist (thermoplastic polymer) is spin coated onto the sample substrate. Then the mold, which has predefined topological patterns, is brought into contact with the sample and they are pressed together under certain pressure. When heated up above the glass transition temperature of the polymer, the pattern on the mold is pressed into the softened polymer film [3]. After being cooled down, the mold is separated from the sample and the pattern resist is left on the substrate (figure A.2). Not only polymer coated samples can be used, but also polymer sheets which do not need a substrate support.
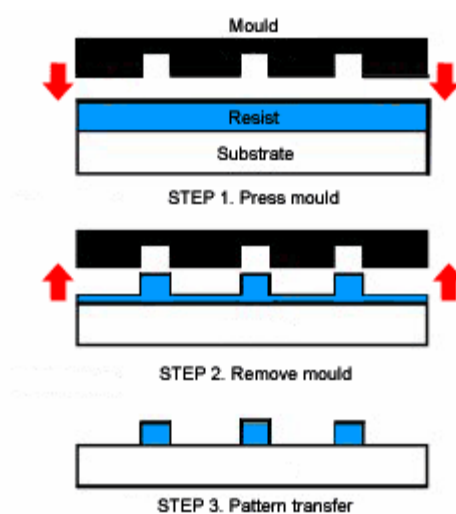

Figure A.2.- Schematic diagram of the steps involved in the nano-imprint lithographic process

1.3 SPUTTERING

Sputtering is a process whereby atoms are ejected from a solid target material due to bombardment of the target by energetic particles [4]. It is commonly used for

thin-film deposition, etching and analytical techniques. A schematic representation is shown in figure A.3.
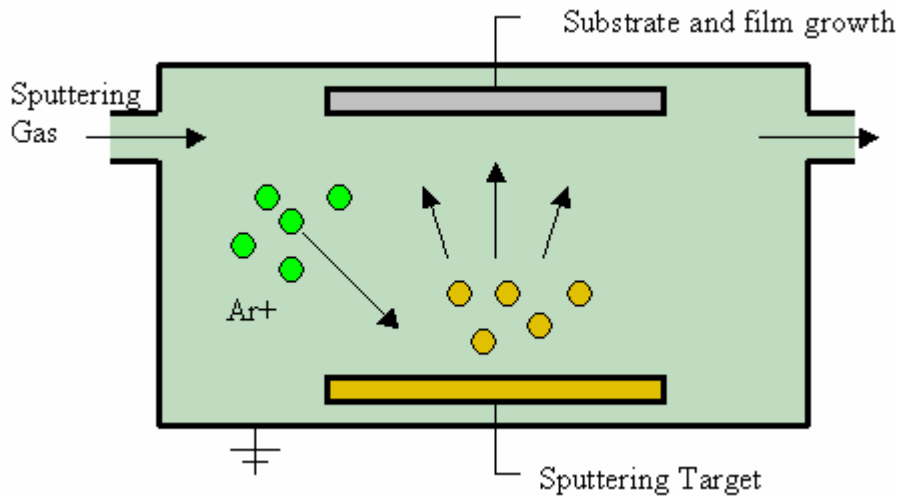

Figure A.3.- Basis of the sputtering process.

Physical sputtering is driven by momentum exchange between the ions and atoms in the material, due to collisions.

The incident ions set off collision cascades in the target. When such cascades recoil and reach the target surface with energy above the surface binding energy, an atom can be ejected. If the target is thin on an atomic scale the collision cascade can reach the back side of the target and atoms can escape the surface binding energy in transmission. The average number of atoms ejected from the target per incident ion is called the sputter yield and depends on the ion incident angle, the energy of the ion, the masses of the ion and target atoms, and the surface binding energy of atoms in the target. For a crystalline target the orientation of the crystal axes with respect to the target surface is relevant.

The primary particles for the sputtering process can be supplied in a number of ways, for example by plasma, an ion source, an accelerator or by a radioactive material emitting alpha particles.

1.4 LOW PRESSURE CHEMICAL VAPOR DEPOSITION

Chemical vapor deposition (CVD) is a chemical process used to produce high-purity, high-performance solid materials. The process is often used in the semiconductor industry to produce thin films. In a typical CVD process, the wafer (substrate) is exposed to one or more volatile precursors, which react and/or decompose on the substrate surface to produce the desired deposit. Frequently, volatile by-products are also produced, which are removed by gas flow through the reaction chamber.

Microfabrication processes widely use CVD to deposit materials in various forms, including: monocrystalline, polycrystalline, amorphous, and epitaxial.

Low-pressure CVD (LPCVD) are standard CVD processes at subatmospheric pressures (fig. A.4). Reduced pressures tend to reduce unwanted gas-phase reactions and improve film uniformity across the wafer.
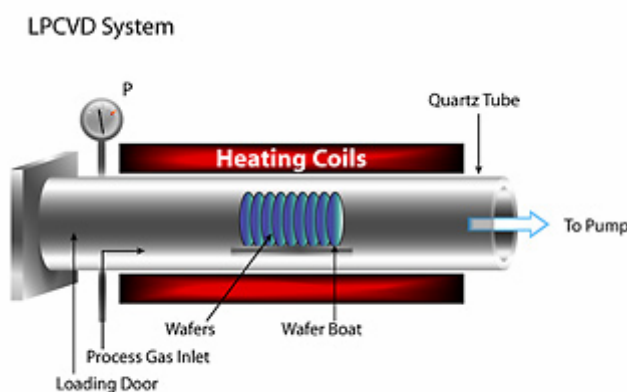

Figure A.4.- LPCVD system.

1.5 ELECTRON-BEAM

Electron beam lithography (often abbreviated as e-beam lithography) is the practice of scanning a beam of electrons in a patterned fashion across a surface covered with a resist [5], (exposing the resist, figure A.5) and of selectively removing either exposed or non-exposed regions of the resist (developing). The purpose, as with photolithography, is to create very small structures in the resist that can subsequently be transferred to the substrate material, often by etching. It was developed for manufacturing integrated circuits, and is also used for creating nanotechnology artifacts.

The primary advantage of electron beam lithography is that it is one of the ways to beat the diffraction limit of light and make features in the nanometer regime. This

form of maskless lithography has found wide usage in photomask-making used in photolithography, low-volume production of semiconductor components, and research & development.

On the other hand, the key limitation of electron beam lithography is throughput, i.e., the very long time it takes to expose an entire silicon wafer or glass substrate. A long exposure time leaves the user vulnerable to beam drift or instability which may occur during the exposure. Also, the turn-around time for reworking or re-design is lengthened unnecessarily if the pattern is not being changed the second time.
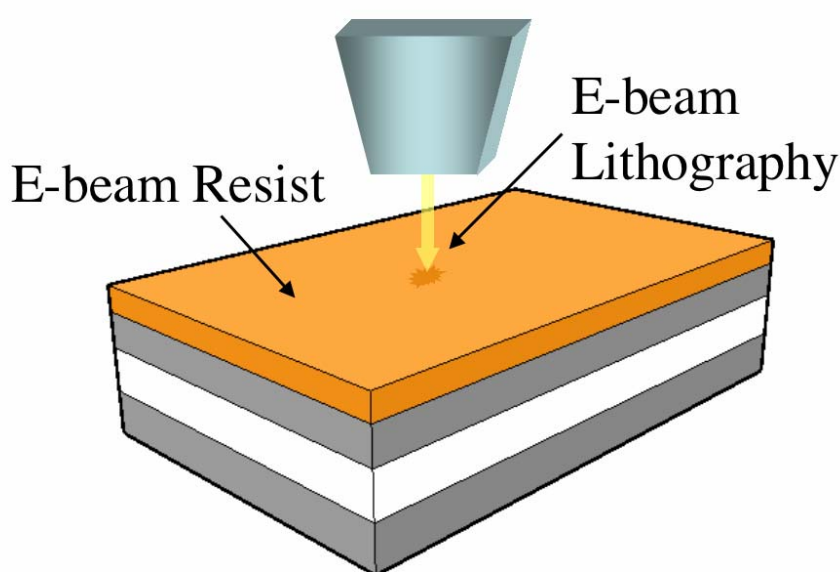
Figure A.5.- e-beam lithography

1.6 REACTIVE ION ETCHING

Reactive ion etching (RIE) is an etching technology used in microfabrication. It uses chemically reactive plasma to remove material deposited on wafers (figure A.6). The plasma is generated under low pressure (vacuum) by an electromagnetic field. High-energy ions from the plasma attack the wafer surface and react with it.

A typical parallel plate RIE system consists of a cylindrical vacuum chamber, with a wafer platter situated in the bottom portion of the chamber. The wafer platter is electrically isolated from the rest of the chamber, which is usually grounded. Gas enters through small inlets in the top of the chamber, and exits to the vacuum pump system

through the bottom. The types and amount of gas used vary depending upon the etch process; for instance, sulphur hexafluoride is commonly used for etching silicon. Gas pressure is typically maintained in a range between a few millitorr and a few hundred millitorr by adjusting gas flow rates and/or adjusting an exhaust orifice.
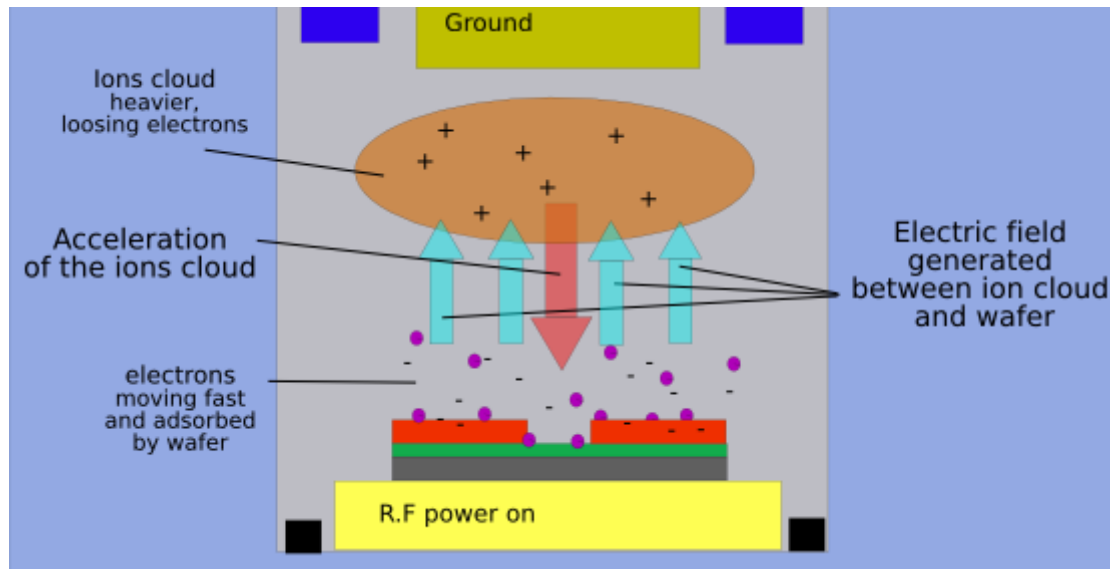

Figure A.6.- Schematics of the RIE effect

1.7 MICRO CONTACT PRINTING

In the field of (bio)chemical patterning systems for biosensing applications, a lot of effort is put into the development of substrates for the detection and analysis of biorecognition processes with high sensitivity and selectivity [6]. In literature different patterning techniques have been described to immobilize (bio)molecules onto surfaces with high precision [7-10]. Among them, soft-lithography techniques [11] have demonstrated to create surfaces with high degree of performance for (bio)medical applications [12].

Microcontact printing (µCP) is the most representative soft-lithography technique. It uses a patterned silicone stamp to print over a large surface area the desired pattern by physical contact between the stamp and a substrate [13, 14]. It is a well-known technique, very effective, fast to functionalize, inexpensive, easy-to-use, and no special laboratory equipment is required and it has been demonstrated to be a useful

technique in the patterned functionalization of certain chemicals or biological samples onto a wide range of different surfaces.

The stamps used for µCP are made of a silicone elastomer - PDMS – that molds with very high fidelity to a patterned template. PDMS is a liquid prepolymer at room temperature due to its low melting point (about -50ºC) and glass transition temperature (about -120ºC). The stamps were replicated from a silicon (or silicon nitride) mould structured by deep reactive ion etching (DRIE) (601 DRIE, Alcatel, France) with circular features 0.8 µm deep. The mould was first cleaned by submersing it in a 50:50 ethanol:isopropanol solution (Panreac Química) and then ultrasonicating it for 10 minutes to remove any PDMS present from previous mouldings. If necessary, the master was further cleaned using Piranha solution (70:30, H_2SO_4–H_2O_2) (Merck) for 10 minutes. In each case, the mold was thoroughly rinsed several times with deionized water (Milli-Q, 18.2 MΩ·cm resistivity). Finally, the mold was ultrasonicated in fresh deionized water for 2–3 minutes. The mold was then silanized to avoid PDMS adhesion with a monolayer of trichlorofluorosilane (Cl_3FSi 153.44 g/mol; Aldrich Chemical Co.). One drop of the silane was placed inside a small vial and introduced into a vacuum desiccator with the mold for 1 hour. Prior to use, the mold was rinsed with ethanol (96%) and dried under a N_2 flow.

To fabricate patterned PDMS stamps, the prepolymer is mixed with the curing agent in a ratio of 10:1, degassed in a desiccator to remove the bubbles present and poured over the patterned master (Figure A.7 (1a)) with the features to be replicated (Figure A.7 (2)). Then, it is cured at 90ºC in the oven to crosslink the polymer. After cooling, the stamp is simply manually demolded from the mold, ready for use (Figure A.7 (3b)). Then, the PDMS stamp is submerged into the desired ink (Figure A.7 (4c)) and any excess is removed under an N_2 flow. Then, the stamp is placed in contact with the substrate (Figure A.7 (5)). A small amount of pressure is applied manually before removing the stamp, leaving the pattern on the substrate (Figure A.7 (6d)).

The use of elastomeric stamps also presents a number of advantages [15]. For instance, PDMS is reusable after cleaning; it is durable, nontoxic, chemically inert, and environmentally safe; it deforms reversibly allowing it to conformally contact a substrate; it is optically transparent down to 300 nm (in the UV-visible region); it has a low thermal expansion; it is hydrophobic (although it can be made temporarily hydrophilic using a plasma treatment); it is permeable to gas (e.g., CO_2 and O_2); and it

can be moulded with high fidelity using a mould. However, the main disadvantage of using PDMS for microcontact printing stamps is that the stamps suffer deformation under pressure due to the inherent elasticity of PDMS [16, 17] during stamping this can cause expansion of the pattern being printed, and thus, limit the possible resolution. However, with a new submerged microcontact printing (SµCP) method [18] where µCP is carried out in a water environment using stamps with aspect ratios unsuitable for conventional µCP, these problems are solved.
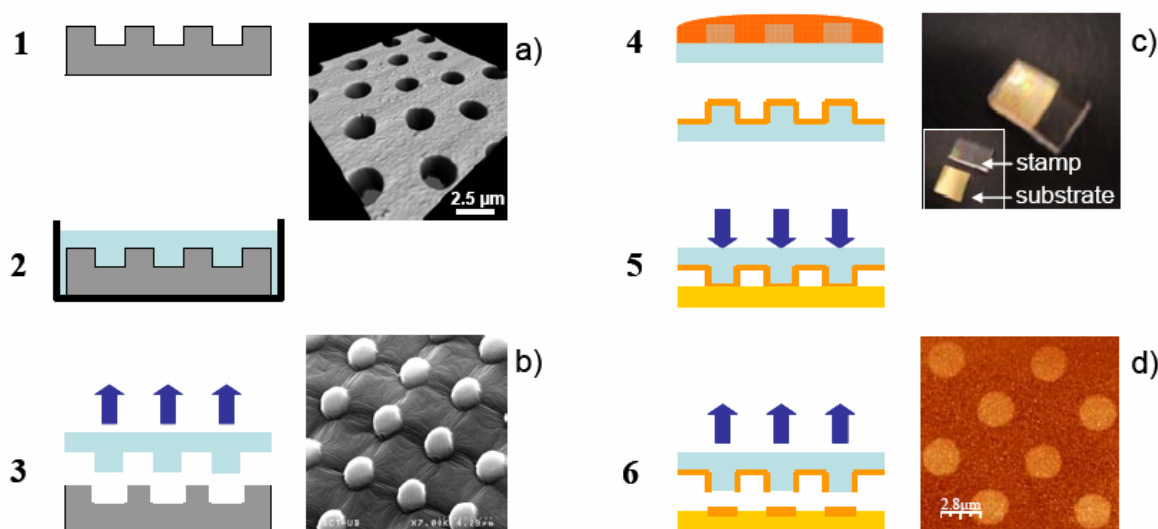
Figure A.7.- Microcontact Printing Technique. The patterned master **(1)** is placed in the bottom of a container and the PDMS is poured over it **(2)**. The stamp is peeled from the master **(3)** and soaked with the desired ink removing the excess **(4)**. The ink is transferred to a substrate by stamping **(5)** reproducing the pattern of the PDMS stamp **(6)**. Image **(a)** shows an AFM image of a silicon master; image **(b)** shows a SEM image of a PDMS stamp; image **(c)** is a picture of the stamping procedure and image **(d)** shows an AFM image of a transferred pattern.

2 CHARACTERIZATION TECHNIQUES

2.1 INTERFEROMETRY

White light interferometry is an extremely powerful tool for optical measurements of surface topography and for height profile measurement of objects [19]. In contrast to classical interferometry, this method can be used for measurement of objects with rough surface even in the case of speckle imaging. The white light interferometry is in principle a Michelson interferometer [20] with a broad-band light source and a CCD (charge-couple device) camera as a detector. The measured object is

placed in one arm of the Michelson interferometer instead of one of the mirrors. Due to the reflection on the rough surface, a speckle pattern arises in the detector plane. This pattern is superimposed on the reference wave. The phase in the individual speckle is random, but it remains approximately constant within one speckle. This renders the white light interference observable, if the optical path lengths of the two arms differ less than the coherence length. The measured object is translated in the longitudinal direction. Gradually, as parts of the object surface fulfil the requirement that the optical path difference between both interferometer arms is comparable to the coherence length, the white light interference is observable in the corresponding speckles. A typical white light correlogram is sampled for each pixel in the course of the movement. In this way, the longitudinal coordinates of a large number of points on the object surface is gained. This longitudinal coordinates together with the corresponding lateral coordinates describe the geometrical shape of the measured object (Figure A.8). The main drawback of the technique is the error produced when imaging samples with surfaces of different materials and so, with different refractive indexes.
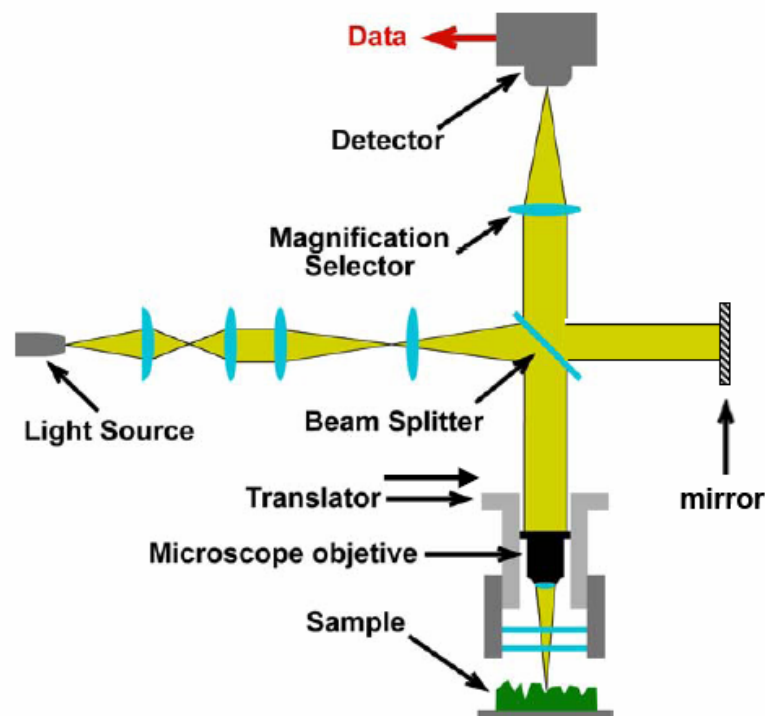

Figure A.8.- White light interferometer: The measured object is placed in one arm of the Michelson interferometer which varies the light path for measurement of a rough surface.

2.2 PROFILOMETRY

Profilometer is a measuring instrument used to measure the profile of a surface, in order to quantify its roughness (figure A.9). Vertical resolution is usually in the nanometre level, though lateral resolution is usually poorer.

In contact profilometers, a diamond stylus is moved vertically in contact with a sample and then moved laterally across the sample for a specified distance and specified contact force. A profilometer can measure small surface variations in vertical stylus displacement as a function of position. A typical profilometer can measure small vertical features ranging in height from 10 nanometres to 1 millimetre. The height position of the diamond stylus generates an analog signal which is converted into a digital signal stored, analyzed and displayed. The radius of diamond stylus ranges from 20 nanometres to 25 μm, and the horizontal resolution is controlled by the scan speed and data signal sampling rate. The stylus tracking force can range from less than 1 to 50 milligrams.
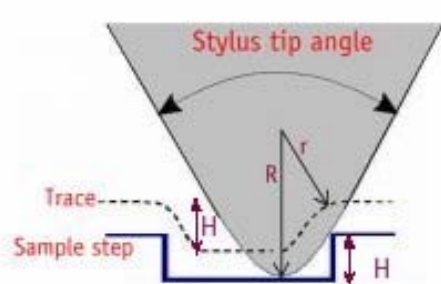

Figure A.9.- A profilometer is a basic tool that allows to quickly measure the physical thickness of films

2.3 ELLYPSOMETRY

Ellipsometry is a powerful tool for the characterization of thin films and multilayer semiconductor structures. Linearly polarised light is reflected from the surface of a material. The reflected light becomes elliptically polarized the degree of ellipticity being determined by the optical properties of the solid being probed. Instruments measure the shape of this polarization ellipse, hence the names ellipsometry.

There are two special polarization directions for which the reflected light is plane polarized. We will define the plane of incidence as that containing the incident beam and the normal to the surface of the solid. Light polarized parallel (p-polarized

light) and perpendicular (s-polarized light) to this plane will remain plane polarized on reflection (figure A.10). The ellipsometer will measure the ratio of the reflected p- and s-components (*tan ψ*) and the phase difference between these two components (*cos Δ*). These two parameters are related to the fundamental physical properties of the reflecting surface such as the optical constants (refractive index *n* and extinction coefficient *k*) and the thickness of the material. Since ellipsometers measure the ratio of the reflected intensities of two mutually-perpendicularly polarised light beams, it does not need a reference beam. This makes ellipsometry highly accurate and very reproducible. Ellipsometry can determine thin film thickness, optical constants for bulk and thin film materials, and often both thickness and optical constants of the film simultaneously. It can measure other parameters such as surface roughness, degree of crystallinity, void fractions etc. [21]
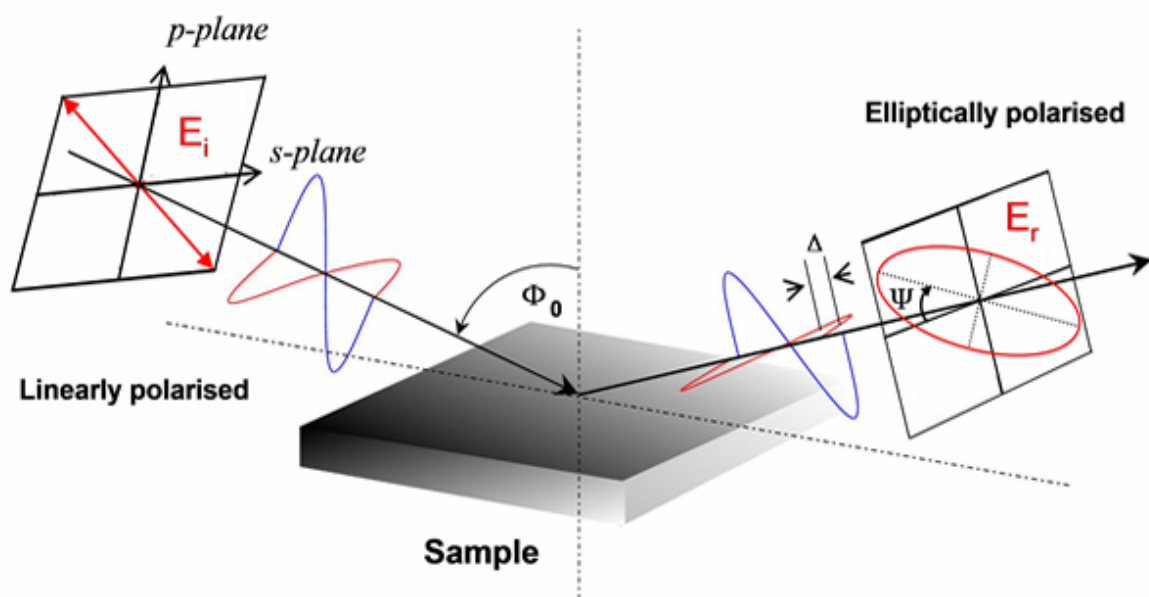

Figure A.10.- Ellipsometry technique principle.

2.4 REFRACTOMETRY

Refractometry is the method of measuring the refractive index (RI) of a substance. Although refractometers are best known for measuring liquids, they are also used to measure gases and solids. In figure A.11 a picture of a Abbe refractometer, special to measure in liquid, is shown.

The RI of a substance is strongly influenced by temperature and the wavelength of light used to measure it, therefore, care must be taken to control or compensate for temperature differences and wavelength. RI measurements are usually reported at a reference temperature of 20 degrees Celsius, which is considered to be room temperature. A reference wavelength of 589.3 nm (the sodium D line) is most often used.
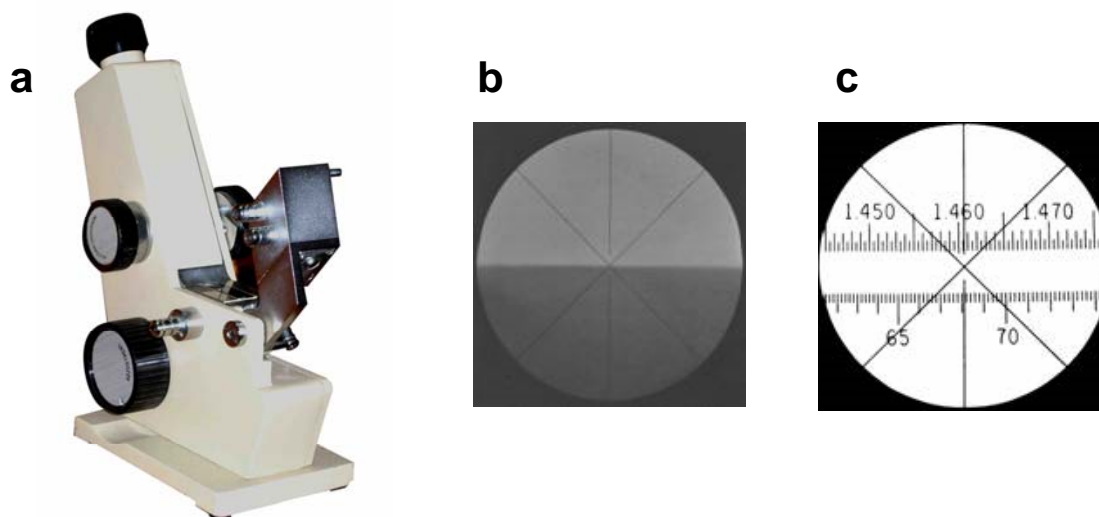

Figure A.11.- Abbe refractometer. When the separation line between light and dark is clear and centered, the value that appears in the scale is the refractive index of the analysed liquid.

2.5 SHEET RESISTANCE

The sheet resistance is a measure of resistance of thin films that have a uniform thickness. It is commonly used to characterize materials made by semiconductor doping, metal deposition, resistive paste printing, and glass coating.

The utility of sheet resistance, as opposed to resistance or resistivity, is that it is directly measured using a four-terminal sensing measurement (also known as a four-point probe measurement).

The van der Pauw method (figure A.12) is a commonly used technique to measure the sheet resistance of a material. A four point probe is used to avoid contact resistance, which can often be the same magnitude as the sheet resistance. Typically a constant current is applied to two probes and the potential on the other two probes is

measured with a high impedance voltmeter. A geometry factor needs to be applied according to the shape of the four point array. Two common arrays are square and in-line.
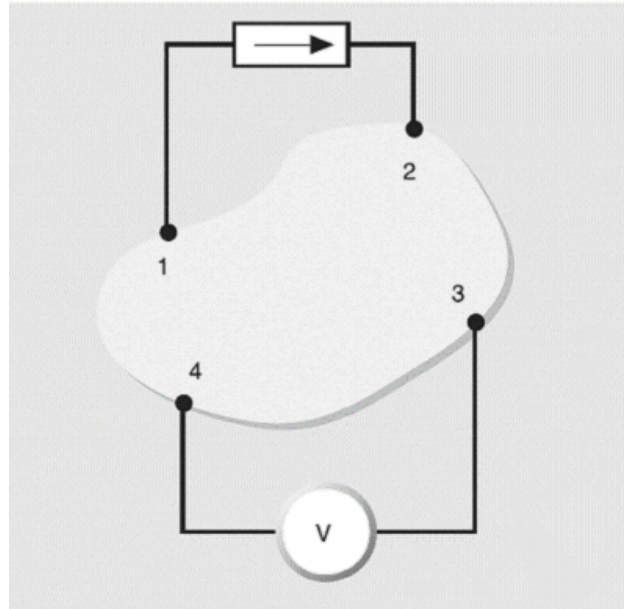
Figure A.12.- Van der Pauw method to measure sheet resistance.

A very crude two point probe method is to measure resistance with the probes close together and the resistance with the probes far apart. The difference between these two resistances will be the order of magnitude of the sheet resistance.

2.6 ATOMIC FORCE MICROSCOPY

The AFM is a very high-resolution type of scanning probe microscope, which is mainly used to image, measure and manipulate matter at the nanoscale, or even at the sub-nanometer level, and for the measurement of interaction forces.

Scanning probe microscopy (SPM) [22] is a branch of microscopy that forms images of surfaces using a small sharp probe that scans the sample. An image of the surface and other fundamental information is obtained by mechanically moving the probe in a raster scan and the interaction with the surface is recorded in each pixel to form an image of the probe-surface interaction.

In Atomic Force Microscopy (AFM) [23, 24], a cantilever with a very sharp tip is scanned over the surface and, using the van der Waals forces or contact forces between a tip and the sample, is able to measure the sample topography or to record information about the mechanical properties (figure A.13). Basically, the theory and operation of an AFM is similar to a stylus profiler but with much higher lateral and vertical resolution. The working principle of an AFM is very similar and simply. It is based on a force sensitive probe composed of a cantilever which holds a very sharp tip at its end. The interaction force between the sample and the probe is monitored and maintained constant and used by the AFM system to control the vertical position of the probe while the probe is raster scanned across the surface. By monitoring the motion of the probe as it is scanned across the surface, a 3D image of the surface is constructed. As shown in Figure 5, an AFM consists of 5 basic elements: (1) a microsized cantilever with a sharp tip at its end (probe) used for sample scanning, (2) a laser beam that reflects on the backside of the cantilever, (3) a photodetector to monitor the cantilever deflection and measure the force applied to the sample, and (4) a feedback system connected to a (5) piezoelectric scanner or nanopositioner for accurate and precise scanning.
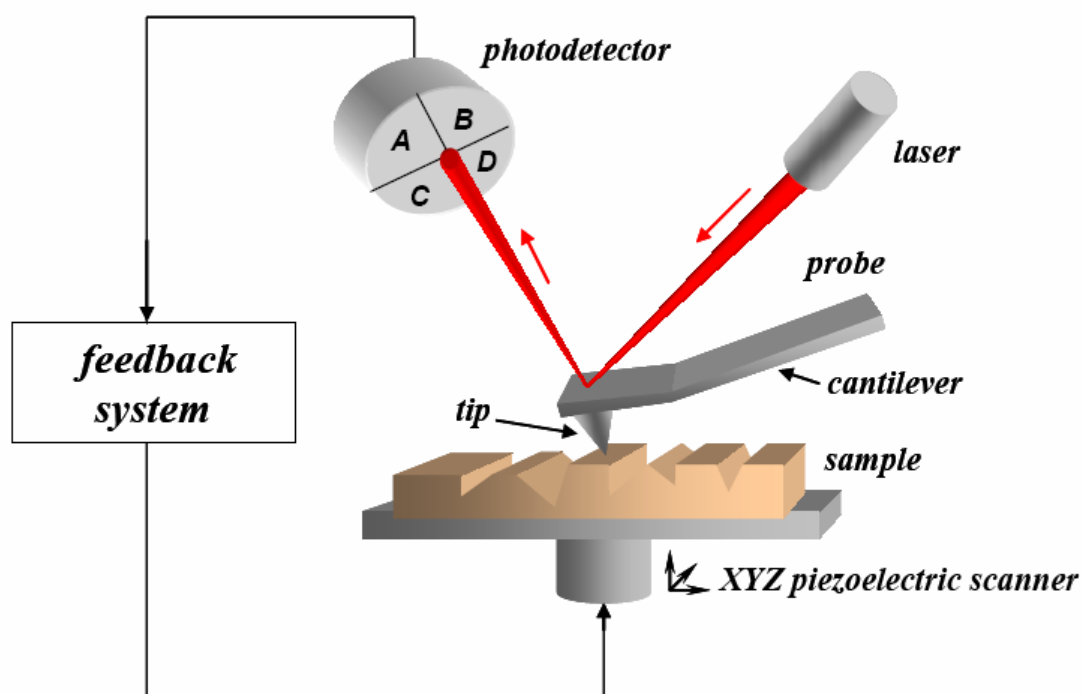
Figure A.13.- Schematics of the basic compounds of an atomic force microscope.

2.7 TRANSMISSION ELECTRON MICROSCOPY

Transmission electron microscopy (TEM) is a microscopy technique whereby a beam of electrons is transmitted through an ultra thin specimen, interacting with the specimen as it passes through (figure A.14). An image is formed from the interaction of the electrons transmitted through the specimen; the image is magnified and focused onto an imaging device, such as a fluorescent screen, on a layer of photographic film, or to be detected by a sensor such as a CCD camera.
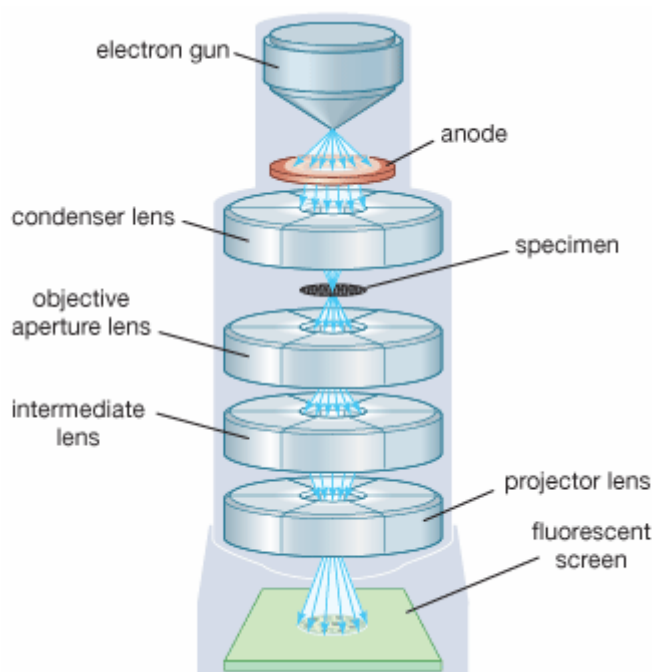

Figure A.14.- Transmission Electron Microscope.

TEMs are capable of imaging at a significantly higher resolution than light microscopes, owing to the small de Broglie wavelength of electrons. This enables the instrument's user to examine fine detail—even as small as a single column of atoms, which is tens of thousands times smaller than the smallest resolvable object in a light microscope. TEM forms a major analysis method in a range of scientific fields, in both physical and biological sciences. TEMs find application in cancer research, virology, materials science as well as pollution and semiconductor research.

At smaller magnifications TEM image contrast is due to absorption of electrons in the material, due to the thickness and composition of the material. At higher magnifications complex wave interactions modulate the intensity of the image, requiring expert analysis of observed images. Alternate modes of use allow for the TEM

to observe modulations in chemical identity, crystal orientation, electronic structure and sample induced electron phase shift as well as the regular absorption based imaging.

2.8 SCANNING ELECTRON MICROSCOPY

The scanning electron microscope (SEM) is a type of electron microscope that images the sample surface by scanning it with a high-energy beam of electrons in a raster scan pattern. The electrons interact with the atoms that make up the sample producing signals that contain information about the sample's surface topography, composition and other properties such as electrical conductivity. Figure A.15 shows the working principle of the microscope.
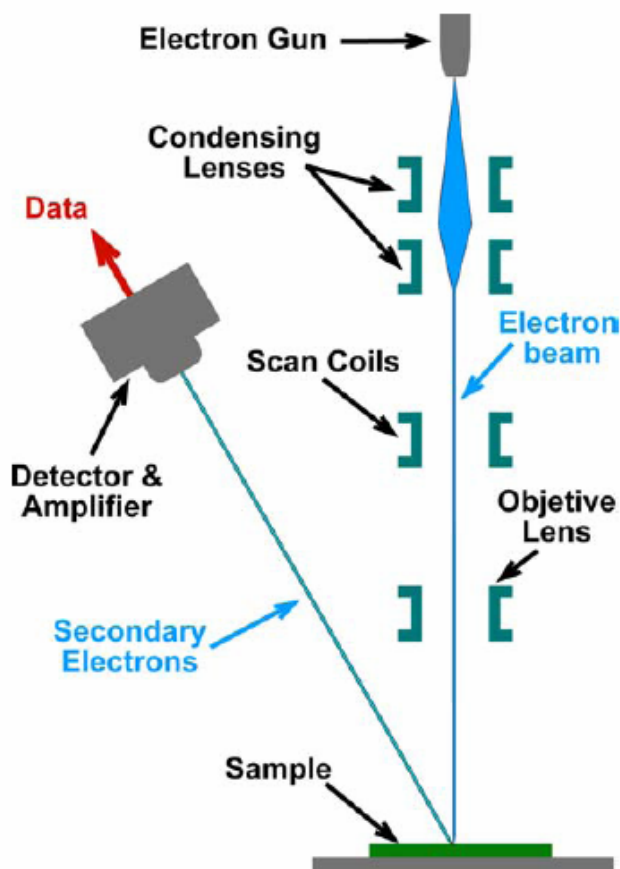

Figure A.15.- Scanning Electron Microscope. The primary electron beam is condensed and rasterized over the sample. The secondary electrons are captured and amplified to obtain a digital image.

In a SEM, electrons are emitted from a tungsten anode and accelerated to the cathode with energies ranging from a few to hundreds of keV. The free electrons are

condensed and focused in a spot of ~0.5 nm diameter. The beam is deflected by a set of magnetic coils in the X and Y direction in a similar fashion to that of the cathode ray tube, producing a raster pattern over the sample surface.

The types of signals produced by an SEM include secondary electrons, back-scattered electrons (BSE), characteristic X-rays, light (cathodoluminescence), specimen current and transmitted electrons. Secondary electron detectors are common in all SEMs, but it is rare that a single machine would have detectors for all possible signals.

The signals result from interactions of the electron beam with atoms at or near the surface of the sample. In the most common or standard detection mode, secondary electron imaging or SEI, the SEM can produce very high-resolution images of a sample surface, revealing details about less than 1 to 5 nm in size. Due to the very narrow electron beam, SEM micrographs have a large depth of field yielding a characteristic three-dimensional appearance useful for understanding the surface structure of a sample. A wide range of magnifications is possible, from about 10 times (about equivalent to that of a powerful hand-lens) to more than 500,000 times, about 250 times the magnification limit of the best light microscopes.

The SEM has compensating advantages, though, including the ability to image a comparatively large area of the specimen; the ability to image bulk materials (not just thin films or foils); and the variety of analytical modes available for measuring the composition and nature of the specimen. However, the main difficulties of this technique arise from requiring extreme conditions to achieve the measurements. High degree of vacuum is required. Thus, biological samples must be treated for visualizing before introducing them into the microscope to avoid the destruction of them. Charging of the sample is another problem. It must be properly grounded, otherwise the detection will be impossible. This is specially important for non-conducting samples, as biological ones. They must be coated with a conductive layer (gold, carbon...) to avoid charging effects, as well as other special treatments, as dehydratation or fixation.

2.9 FLUORESCENCE MICROSCOPY

A fluorescence microscope (colloquially synonymous with epifluorescence microscope) is an optical microscope used to study properties of organic or inorganic

substances using the phenomena of fluorescence and phosphorescence instead of, or in addition to, reflection and absorption [28, 29].

In most cases, a component of interest in the specimen can be labeled specifically with a fluorescent molecule called a fluorophore. The specimen is illuminated with light of a specific wavelength (or wavelengths) which is absorbed by the fluorophores, causing them to emit light of longer wavelengths (i.e. of a different color than the absorbed light). The illumination light is separated from the much weaker emitted fluorescence through the use of a spectral emission filter. Typical components of a fluorescence microscope are the light source (xenon arc lamp or mercury-vapor lamp), the excitation filter, the dichroic mirror (or dichromatic beamsplitter), and the emission filter (see figure A.16). The filters and the dichroic are chosen to match the spectral excitation and emission characteristics of the fluorophore used to label the specimen. In this manner, the distribution of a single fluorophore (color) is imaged at a time. Multi-color images of several types of fluorophores must be composed by combining several single-color images [28].
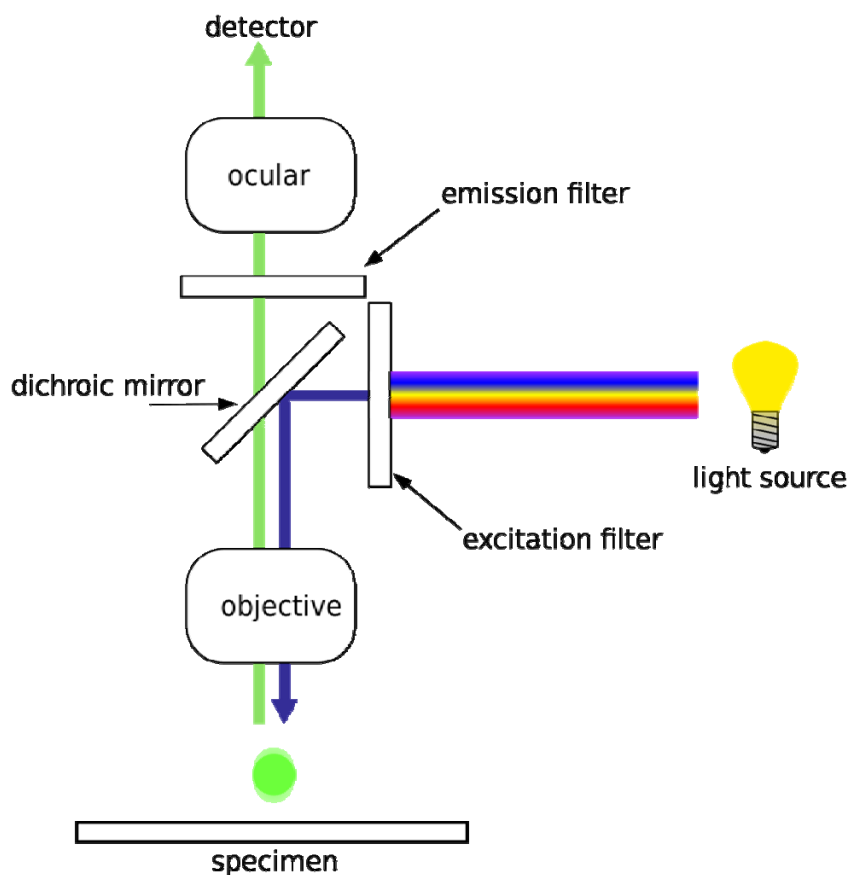

Figure A.16.- Schematic of a fluorescence microscope

Most fluorescence microscopes in use are epifluorescence microscopes (i.e. excitation and observation of the fluorescence are from above (epi–) the specimen). These microscopes have become an important part in the field of biology, opening the doors for more advanced microscope designs, such as the confocal microscope and the total internal reflection fluorescence microscope (TIRF).

Fluorophores lose their ability to fluoresce as they are illuminated in a process called photobleaching. Special care must be taken to prevent photobleaching through the use of more robust fluorophores, by minimizing illumination, or by introducing a scavenger system to reduce the rate of photobleaching.

2.10 DYNAMIC LIGHT SCATTERING

Scattering of light or other electromagnetic radiation is the deflection of rays in random directions by irregularities in the propagation medium, or in a surface or interface between two media. Scattering from a surface or interface can also be called diffuse reflection.

Rayleigh scattering is the elastic scattering of light or other electromagnetic radiation by objects or surfaces much smaller than the wavelength of the incoming light. It often can occur when light travels in transparent solids and liquids, but is more prevalent in gases. This type of scattering is responsible of the blue color of the sky during the day. Rayleigh scattering is inversely proportional to the fourth power of wavelength, which means that the shorter wavelength of blue light will be scattered more intensely than the longer wavelengths (e.g. green and red).

Mie scattering is scattering of light by spherical particles. Rayleigh scattering is Mie scattering in the special case where the diameter of the particles is much smaller than the wavelength of the light.

Dynamic light scattering (also known as Photon Correlation Spectroscopy or Quasi-Elastic Light Scattering) is a technique in physics, which can be used to determine the size distribution profile of small particles in suspension (chemistry) or polymers in solution (see figure A.17). It can also be used to probe the behavior of complex fluids such as concentrated polymer solutions.
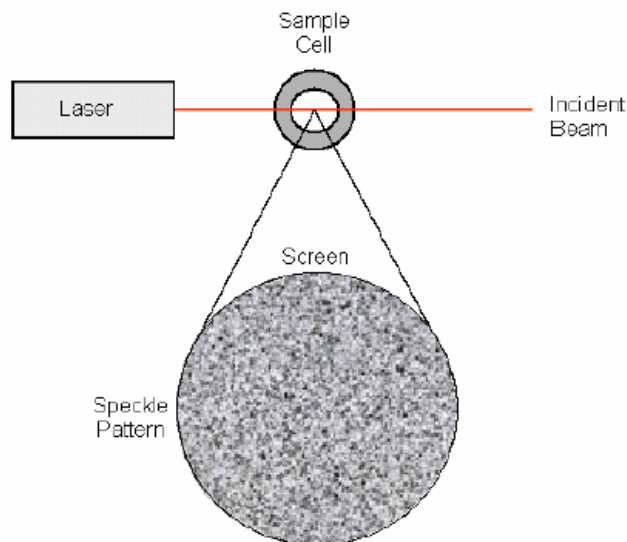
Figure A.17.- Dynamic light scattering basis

When light hits small particles the light scatters in all directions (Rayleigh scattering) so long as the particles are small compared to the wavelength (below 250 nm). If the light source is a laser, and thus is monochromatic and coherent, then one observes a time-dependent fluctuation in the scattering intensity. These fluctuations are due to the fact that the small molecules in solutions are undergoing Brownian motion and so the distance between the scatterers in the solution is constantly changing with time. This scattered light then undergoes either constructive or destructive interference by the surrounding particles and within this intensity fluctuation, information is contained about the time scale of movement of the scatterers.

From the Mie theory, when the size of the particles becomes roughly equivalent to the wavelength of the illuminating light, then a complex function of maxima and minima with respect to angle is observed. If the distribution of particles by intensity is a single fairly smooth peak, then there is little point in doing the conversion to a volume distribution using the Mie theory. If the plot shows a substantial tail, or more than one peak, then Mie theory can make use of the input parameter of sample refractive index to convert the intensity distribution to a volume distribution. This will then give a more realistic view of the importance of the tail or second peak present.

3 REFERENCES

[1]   D.C. O'Shea, T.J. Suleski, A.D. Kathman, and D.W. Prather, Diffractive Optics. Design, Fabrication and Test., 2004.

[2]   Rogers, J. A. & Nuzzo, R. G. (2005, February). Recent progress in soft lithography. In Materials today, 8, 50 – 56.

[3]   Chou, S.Y.; Krauss, P.R.; Renstrom, P.J. (1996). "Imprint Lithography with 25-Nanometer Resolution". Science 272 (5258): 85–7

[4]   R. Behrisch (ed.) (1981). Sputtering by Particle bombardment:. Springer, Berlin. ISBN 978-3540105213.

[5]   McCord, M. A.; M. J. Rooks (2000). SPIE Handbook of Microlithography, Micromachining and Microfabrication.
        http://www.cnf.cornell.edu/cnf_spietoc.html.

[6]   Mrksich, M. and G.M. Whitesides, Patterning self-assembled monolayers using microcontact printing: A new technology for biosensors? Trends in Biotechnology, 1995. **13**(6): p. 228-235.

[7]   Hong, S., J. Zhu, and C.A. Mirkin, Multiple Ink Nanolithography: Toward a Multiple-Pen Nano-Plotter. Science, 1999. **286**(5439): p. 523-525. [8]   Lange, S.A., et al., Microcontact Printing of DNA Molecules. Anal. Chem., 2004. **76**(6): p. 1641-1647.

[9]   Hoff, J.D., et al., Nanoscale Protein Patterning by Imprint Lithography. NanoLett., 2004. **4**(5): p. 853-857.

[10]   Gates, B.D., et al., Unconventional nanofabrication. Annual Review of Materials Research, 2004. **34**(1): p. 339-372.

[11]   Xia, Y. and G.M. Whitesides, Soft Lithography. Angewandte Chemie International Edition, 1998. **37**(5): p. 550-575.

[12]   Ruiz, S.A. and C.S. Chen, Microcontact printing: A tool to pattern. Soft Matter, 2007. **3**(2): p. 168-177.

[13]   Caballero, D., et al., Atomic Force Microscopy Characterization of a Microcontact Printed, Self Assembled Thiol Monolayer for Use in Biosensors. Analytical Letters, 2006. **39**(8): p. 1721 - 1734.

[14]   Bernard, A., et al., Microcontact Printing of Proteins. Advanced Materials, 2000. **12**(14): p. 1067-1070.

[15]   Lötters, J.C., et al., The mechanical properties of the rubber elastic polymer polydimethylsiloxane for sensor applications. Journal of Micromechanics and Microengineering, 1997. **7**(3): p. 145.

[16]   Lauer, L., C. Klein, and A. Offenhäusser, Spot compliant neuronal networks by structure optimized micro-contact printing. Biomaterials, 2001. **22**(13): p. 1925-1932.

[17]   Hsia, K.J., et al., Collapse of stamps for soft lithography due to interfacial adhesion. Applied Physics Letters, 2005. **86**(15): p. 154106.

[18]   Bessueille, F., et al., Submerged Microcontact Printing (SμCP): An Unconventional Printing Technique of Thiols Using High Aspect Ratio, Elastomeric Stamps. Langmuir, 2005. **21**(26): p. 12060-12063.

[19]   Conor, O., et al., Characterization of micromechanical structures using whitelight interferometry. Measurement Science and Technology, 2003. **14**(10): p. 1807.

[20]   Michelson, A.A., Determination experimentale de la valeur du metre en longuers d'ondes lumineuses. Trav. Mem. Bur. Int. Poids Mes, 1895. **11**: p. 1-42.

[21]   Fujiwara, H., Spectroscopic Ellipsometry: Principles and Applications. 2007, ISBN:0-470-01608-6: John Wiley & Sons Inc.

[22]   Lillehei, P.T. and L.A. Bottomley, Scanning Probe Microscopy. Anal. Chem., 2000. **72**(12): p. 189-196.

[23]   Binnig, G., C.F. Quate, and C. Gerber, Atomic Force Microscope. Physical Review Letters, 1986. **56**(9): p. 930.

[24]   Binnig, G., et al., Atomic resolution with atomic force microscope. Surface Science, 1987. **189-190**: p. 1-6.

[25]   Amzallag A., Vaillant C., Jacob M., Unser M., Bednar J., Kahn J., Dubochet J., Stasiak A. and John H. Maddocks, A (2006). "3D reconstruction and comparison of shapes of DNA minicircles observed by cryo electron microscopy" Nucleic Acids Research **34** (18): e125.

[26]   Echlin P (1992) Low Temperature Microscopy and Analysis. Plenum Publishing Corporation, New York

[27]   Dubochet J, Adrian M, Chang J-J, Homo J-C, Lepault J, McDowall AW, Schulz P (1988) Cryo-electron microscopy of vitrified specimens, Quarterly Review of Biophysics 21, 129-228

[28]   Spring KR, Davidson MW. "Introduction to Fluorescence Microscopy". http://www.microscopyu.com/articles/fluorescence/fluorescenceintro.html. Retrieved 2008-09-28.

[29]   "The Fluorescence Microscope". Microscopes Help Scientists Explore Hidden Worlds.
http://nobelprize.org/educational_games/physics/microscopes/fluorescence/. Retrieved 2008-09 28.

Optical Grating Coupler Biosensor and Biomedical Applications

Optical Grating Coupler Biosensor and Biomedical Applications

RESUMEN EN CASTELLANO

Los biosensors son hoy en día una herramienta muy eficaz para permitir la detección de interacciones biológicas específicas y para evaluar la relación de la respuesta con la concentración. Un biosensor consiste normalmente de tres partes: la muestra a medir, el transductor y el sistema electrónico que amplifica la señal, analiza los datos y presenta un resultado al usuario final. El transductor incluye el bioreceptor (que interacciona específicamente con la muestra) y la interfaz que transforma el reconocimiento del bioreceptor en una señal medible. Cuando el analito interacciona con el bioreceptor, el transductor envía una señal que es procesada por la electrónica. Todo este proceso ocurre de un modo eficiente, rápido fácil, simple y específico. Dependiendo del tipo de tansductor, los biosensors pueden ser electroquímicos, ópticos, acústicos, magnéticos o termométricos; pero en general los biosensores más potentes son los biosensores ópticos y, entre ellos, el *grating coupler* (acoplador por red de difracción). Como técnica para investigar procesos en la interfaz sólido-líquido, presenta alta estabilidad mecánica, inmunidad a interferencias electromagnéticas y lleva la sensibilidad a niveles incluso más altos que otras técnicas. Además, permite monitorizar directamente la adsorción de macromoléculas en la superficie del sensor. Aprovechando los últimos avances en nanotecnología, el objetivo de ésta tesis es estudiar la versatilidad del *Optical Grating Coupler Biosensor*. Para lograr éste objetivo, nuevos sensores más robustos serán diseñados y fabricados en distintos materiales presentando alta sensibilidad, respuesta rápida, estabilidad, reproducibilidad, pequeño tamaño y bajo coste. Este será el objetivo del capitulo 2. En el tercer capítulo, un nuevo método de calibración para caracterizar individualmente los sensores, los analitos y las soluciones buffer previamente a realizar los experimentos de biosensado, será investigado. En el capítulo cuarto, el potencial de la técnica de *grating coupler* se aplica para optimizar la inmovilización de liposomas que expresan receptores olfativos en la superficie de un sensor. Por último, en el capítulo número cinco, el biosensor de *grating coupler* se combinará con técnicas electroquímicas para conseguir un mejor entendimiento en los mecanismos predominantes en la estabilidad de multicapas de poliectrolito.

CAPÍTULO 1: BIOSENSORES

1 INTRODUCCIÓN

Los biosensores, y en particular los inmunosensores, se usan para estudiar interacciones antígeno-anticuerpo y resultan en una herramienta de análisis prometedora debido a su especificidad y sensibilidad. La alta especificidad se consigue por el reconocimiento molecular de los analitos blanco (normalmente antígenos) por parte de los anticuerpos para formar un complejo estable en la superficie del inmunosensor. Para explotar esta interacción específica a través del bioreconocimiento, la arquitectura superficial del sensor debe suprimir cualquier interacción no-específica. En investigación es mucho el esfuerzo que está siendo invertido en encontrar formas de modificar las superficies para permitir interacciones específicas durante largos periodos de tiempo y en líquido.

Las figuras de mérito para evaluar el éxito en el funcionamiento de un biosensor son la sensibilidad y el límite de detección (LOD). El LOD es la minima concentracción de analito que es detectable con precision y reproducibilidad, y la sensibilidad es la variación en la concentración más pequeña que el biosensor es capaz de detectar. El rango en el que el sensor es sensible se llama el rango dinámico.

2 BIOSENSORES PIEZOELÉCTRICOS

De los biosensores piezoelectricos, el más conocido es la balanza de cuarzo (QCM). Una QCM detecta cambios en la masa adsorbida por unidad de area de un electrodo, midiendo cambios en la frequencia de resonancia del cristal de cuarzo. Con la balanza de cuarzo se mueden medir densidades de masa por debajo de 1 μg/cm^2. Además de medir frecuencias frecuentemente se mide también la disipación, para ayudar en el análisis de datos. La disipación es un parámetro que mide el amortiguamiento en el sistema y está relacionado con las propiedades viscoelásticas de la muestra.

3   BIOSENSORES ELECTROQUÍMICOS

Los inmunosensores electroquímicos, en los que un electrodo se usa como transductor, representan una subclase muy importante de entre los inmunosensores bioquímicos. Estos dispositivos lideran la lista de sensores comerciales y tienen aplicaciones en clínica, industria, medio ambiente y agricultura. Se dice que la detección electroquímica de interacciones anticuerpo-antígeno resuelve los problemas relacionados con otros métodos, como son la velocidad de detección, simplicidad, precio y límites de detección. Además, la electroquímica en un proceso de interfaz, y precisamente las reacciones relevantes tienen lugar en la interfaz electrodo-solución. De entre las técnicas electroquímicas, las más comunes son la voltametría cíclica, la amperometría, la potenciometría y la espectroscopia de impedancias.

4   BIOSENSORES ÓPTICOS

Como casi todos los fenómenos ópticos que ocurren en una superficie (absorción, fluorescencia, cambios en el índice de refracción, etc) pueden ser utilizados como elementos transductores en un biosensor, los inmunosensores ópticos son considerados la alternative más prometedora a los ensayos tradicionales usados en diagnóstico clínico y análisis medioambiental. Los biosensors ópticos presentan las siguientes ventajas: usan radiación electromagnética en el visible, su medio de operación es no destructivo, la generación de señal es muy rápida, son inmunes a interferencias electromagnéticas, se pueden usar en ambientes agresivos y tienen muy alta sensibilidad. En los transductores ópticos, el estímulo químico o biológico produce cambios en las características del medio en contacto con el camino óptico, como pueden ser cambios en las propiedades de emisión o absorción (luminiscencia, fluorescencia) o en el índice de refracción. Esta desviación modificará la propagación de la luz (longitude de onda, polarización, velocidad de fase, etc) y este cambio podrá ser medido con diversas técnicas.

De entre los biosensors ópticos, los basados en la técnica de onda evanescente usan el campo evanescente para sondear la superficie de un sensor, buscando la presencia de analitos adsorbidos. Las guías de onda son el elemento básico de estos sensores, ya que proporcionan estucturas para la propagación de la luz. Una guía de

ondas está formada por una capa central de un material (guía) con un cierto índice de refacción rodeado de dos medios con índices de refracción menores. La luz queda confinada en la guía, debido al fenómeno de reflexión total interna (TIR). Pero aunque la luz viaja confinada dentro de la guía, hay una parte de luz guiada (la cola evanescente) que viaja a través de la interfaz penetrando unos cientos de nanómetros en el medio externo. Cuando se produce un cambio en las características ópticas del medio externo (por ejemplo, un cambio en el índice de refracción), la velocidad de propagación de la luz se altera.

4.1 Surface Plasmon Resonance

Una de las técnicas ópticas más relevantes para biosensores es el cambio en las propiedades de la resonancia de plasmones superficiales (SPR). SPR es una poderosa técnica para medir las interacciones biomoleculares en tiempo real en un entorno *label-free*. La resonancia de plasmón superficial es un proceso físico que puede ocurrir cuando luz polarizada llega a una película de metal en condiciones de TIR. Cuando un haz de luz golpea un metal (generalmente oro), la mayor parte de la luz incidente se refleja. Sin embargo, en los ángulos de incidencia mayores que el ángulo crítico, toda la luz entrante es reflejada. Cuando en una situación de TIR la energía cuántica de los fotones es la correcta, los fotones se convierten en plasmones, dejando un "vacío" en la intensidad de la luz reflejada (Figura 1). Los plasmones crean un campo evanescente que se extiende unos 300 nm en el medio a cada lado de la película. La velocidad de los plasmones cambia cuando lo hace la composición del medio. Y debido al cambio en el la propagación del plasmón, el ángulo de resonancia cambia.
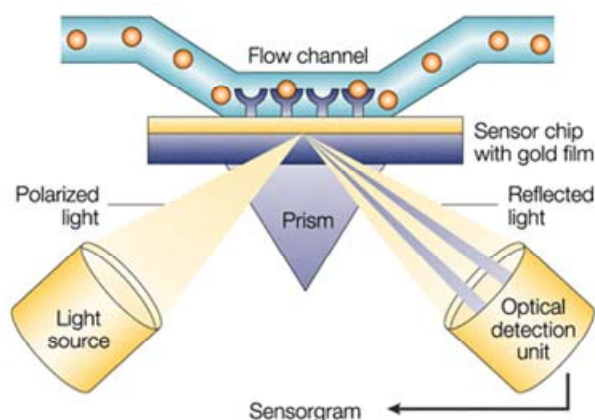

Figura 1.- Principio de funcionamiento de un biosensor SPR.

4.2 Interferómetro Mach-Zehnder

En un interferómetro de Mach Zehnder (MZI) dos haces de luz de igual intensidad se hacen viajar a través de dos áreas de una guía de ondas (una es el sensor y el otro es el de referencia) y finalmente se combinan, creando un patrón de interferencia (Figura 2).
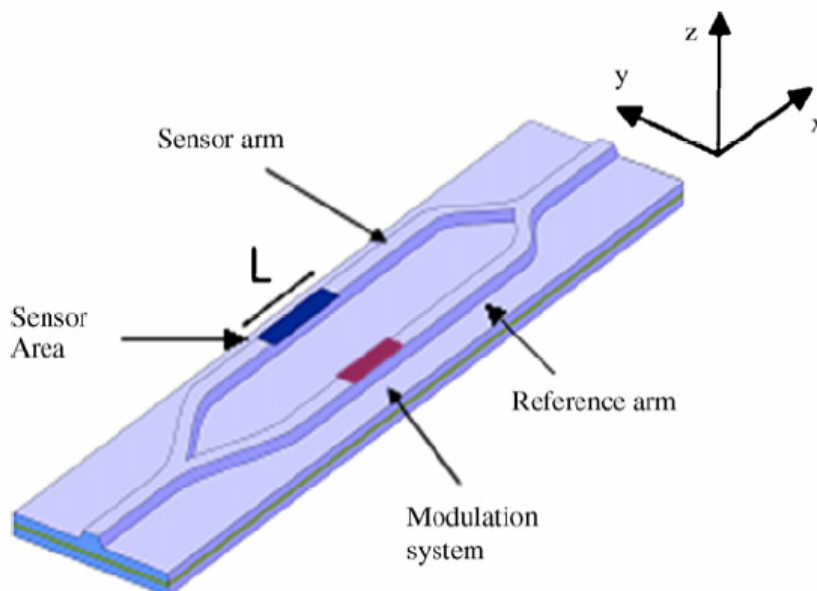

Figura 2.- Interferómetro de Mach-Zehnder.

El sensor interferométrico es muy sensible y es la única técnica que proporciona una referencia interna para la compensación de las fluctuaciones del índice de refracción y la adsorción inespecífica. Los sensores interferométricos tienen un rango dinámico más amplio que la mayoría de los otros tipos de sensores y muestran una mayor sensibilidad en comparación con otros biosensores ópticos integrados.

4.3. Grating coupler

Utilizando la física de una red de difracción, un *grating coupler* (GC) mide la concentración de un analito mediante la detección de cambios en el ángulo en el que la luz se acopla en una guía de ondas, a medida que el analito se deposita en su superficie. Receptores biológicos sobre la superficie de la guía de ondas capturan las moléculas de interés, que afectan el índice de refracción visto por la onda evanescente en la vecindad de la superficie del sensor (Figura 3).
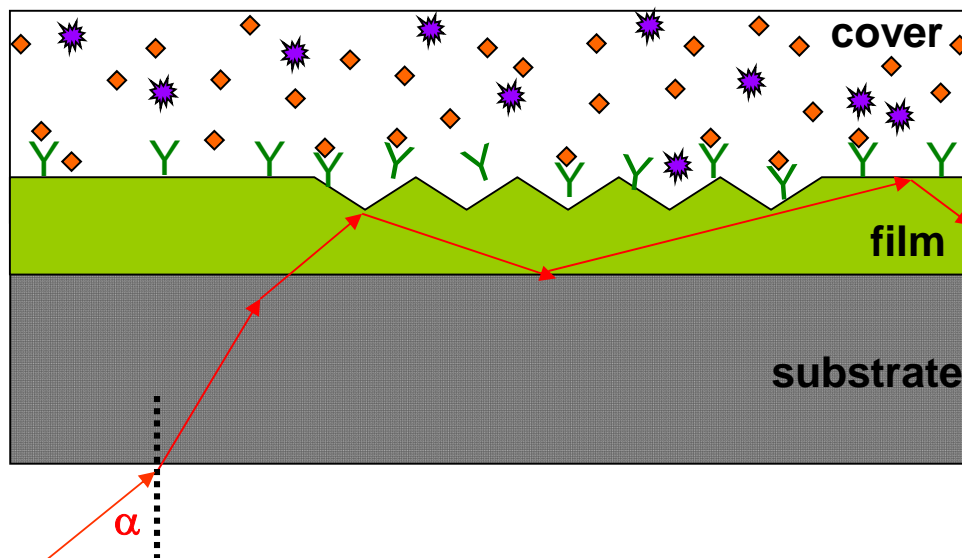
Figura 3.- Esquema de un grating coupler. Cuando un analito se adsorbe en la superficie del sensor, el ángulo al que la luz se acopla varia.

El índice de refracción efectivo, N_{eff} del GC cambiará dependiendo de la concentración de partículas dentro de una muestra. Para determinar el N_{eff}, hay que monitorizar el ángulo de acoplo. El espesor y el índice de refracción de capas homogéneas adsorbidas pueden ser determinados a partir de los cambios en el ángulo de acoplo. Dado que el índice de refracción es una función lineal de la concentración o densidad de masa, la cantidad absoluta de las moléculas adsorbidas se puede calcular usando la fórmula Feijter. La técnica de GC ofrece una resolución de 10^{-6} en el cambio de índice de refracción efectivo, es por tanto altamente sensible (~ 1 ng/cm^2) y permite seguir directamente la cinética de adsorción.

5 COMPARATIVA

De todos los biosensores descritos anteriormente, los biosensores ópticos son un candidato excelente para estudiar y el desarrollar, ya que presentan una alta sensibilidad, alta estabilidad mecánica, son inmunes a las interferencias electromagnéticas y no admiten mediciones destructivas. Mientras que la QCM mide masa húmeda depositada sobre la superficie, SPR y GC detectan masa seca adsorbida sobre el sensor; lo que discrimina de efecto del analito de los efectos de la solución. Por otro lado, los sensores electroquímicos son tan sensibles a cualquier cambio que ocurre en la superficie del electrodo, que hace muy difícil diferenciar la influencia individual de eventos

independientes. Los biosensores interferométricos son altamente sensibles y proporcionan una referencia interna para la compensación de las fluctuaciones del índice de refracción y la adsorción inespecífica. Además tienen un rango dinámico más amplio que la mayoría de sensores y muestran una mayor sensibilidad (incluso con moléculas pequeñas: hasta 0,1 ng/ml con contaminantes medioambientales). El límite de detección que se puede lograr es de 10^{-7} en el índice de refracción, pero la técnica está limitada por el ruido electrónico y mecánico, la deriva térmica, las inestabilidades de la fuente de luz y el ruido químico. Aunque el Mach-Zehnder parece ser uno de los conceptos más prometedores para la detección de baja concentración de moléculas pequeñas *label-free* (10^{-12} M o incluso inferior), el principal problema en la comercialización y desarrollo posible del dispositivo MZI es la complejidad de los ajustes de diseño, fabricación y óptica. El procedimiento general para su fabricación es bastante laborioso y requiere guías de onda monomodo, aumentando aún más la complejidad de la tecnología. La principal ventaja del GC sobre el SPR se encuentra en los grados de libertad para el diseño del sensor. En ambas tecnologías, la zona de alta sensibilidad depende de la profundidad de penetración de la onda evanescente. Para los sistemas de SPR, este parámetro está dado por las propiedades del material, con una profundidad de penetración típico de alrededor de 200 nanómetros. En el caso de las guías de ondas dieléctricas planas, esta propiedad puede ser elegida por el diseño, abriendo nuevos campos de aplicación para la detección de entidades relativamente grandes, tales como las células. Además, la ausencia de una capa de metal puede ser una ventaja, por ejemplo, en casos en que se quiera combinar la técnica con detección luminiscente. La transferencia de energía a la capa de oro (*quenching*) hace que la combinación de luminiscencia y SPR sea casi imposible, mientras que las guías de onda se utilizan con éxito para mejorar la sensibilidad de los sensores fluorescentes. Otra ventaja de los GC es su idoneidad para la construcción de arrays de sensores con un elevado número de diferentes regiones de detección presentes en el mismo chip. Esto facilita la detección de varios tipos de moléculas presentes simultáneamente en una solución, que es un requisito fundamental para los sensores bioquímicos en todos los campos de aplicación. Por todas estas razones, los biosensores basados en guías de onda con acoplo por redes de difracción será nuestra técnica de elección para los estudios y desarrollos llevados a cabo en esta tesis.

CAPÍTULO 2:   DISEÑO Y FABRICACIÓN DE SENSORES GRATING COUPLER

1 INTRODUCCIÓN

Una guía de ondas óptica es una estructura que limita y guía al haz de luz por el proceso de reflexión total interna. La guía de ondas más simple es la guía de ondas plana que consta de una capa delgada (de índice de refracción n_F) intercalado entre dos materiales de índice de refracción ligeramente inferiores. Estas guías de onda planas son componentes importantes en óptica integrada con aplicaciones en sensores y en comunicaciones ópticas. Este capítulo tiene como objetivo diseñar y fabricar diferentes guías de onda que presenten una red de difracción en su superficie, para ser sensores *grating coupler*. Hemos investigado la replicación de redes de difracción óptica en substratos de polímero, para conseguir nuevos sensores de bajo coste. También hemos estudiado el recubrimiento de sensores comerciales con diferentes materiales por técnicas de *sputtering* y evaporación, para permitir rápidos estudios cuantitativos de la adsorción de biomoléculas sobre sus superficies, para ser utilizados en la calibración de otras técnicas.

2 DISEÑO DE UN GRATING COUPLER BASADO EN POLÍMERO

El parámetro principal a tener en cuenta al diseñar un biosensor de guía de ondas es su sensibilidad, que se define como la capacidad para detectar las variaciones del índice de refracción del medio cubierta. Cuando se forma una capada de biomoléculas adsorbida sobre la superficie del sensor (*adlayer*), la sensibilidad está definida por la dependencia del índice de refracción efectivo en el índice de refracción del medio cubierta (*buffer*) y en el índice de refracción y espesor del adlayer. Para el caso particular en que el adlayer esté formado por una sola sustancia, la sensibilidad depende sólo del índice del buffer y del espesor del adlayer. La sensibilidad de una guía de ondas se puede ajustar cambiando los parámetros de fabricación.

2.1 Polímero sobre vidrio

El PMMA es un polímero termoplástico transparente. Su baja temperatura de transición vítrea, a 105 º C, lo convierten en un gran candidato para las técnicas de replicado por impresión. Estas características permiten fabricar una fina capa de PMMA para ser utilizado como la capa guía en una guía de ondas óptica, y donde se estampa la red de difracción con técnicas de réplica-molde. Sin embargo, el índice de refracción del PMMA, 1.492, es bastante bajo en comparación con el del vidrio, 1.453, haciendo que las guías de onda de PMMA sobre el vidrio no sean muy sensibles. A pesar de la baja sensibilidad, el PMMA es todavía una buena opción para el replicado de la red. Usando el PMMA como sustrato sobre el que se deposita otra capa con mayor contraste de índice de refracción, permitiría el fabricado fácil de la red y, al mismo tiempo, garantizaría una buena sensibilidad.

2.2 ITO sobre PMMA

Hay varios dieléctricos transparentes con alto índice de refracción que podrían actuar como guía, pero para biosensores *label-free*, una combinación de espectroscopia óptica y técnicas electroquímicas ofrece una mayor sensibilidad y versatilidad para la detección de biomoléculas. Los óxidos conductores transparentes son capas delgadas transparentes en la región visible del espectro electromagnético (> 80%) y conductores de corriente eléctrica ($<10^{-3}\Omega$cm) y, por lo tanto plantean una alternativa interesante a las capas delgadas de metales transparentes, debido a su alta transparencia y buena conductividad. En la figura 4 una simulación muestra la sensibilidad de una guía de ondas de ITO sobre PMMA con el espesor del adlayer, contra el espesor de la guía. En este caso se ha elegido un valor constante para el índice de buffer de 1.33.
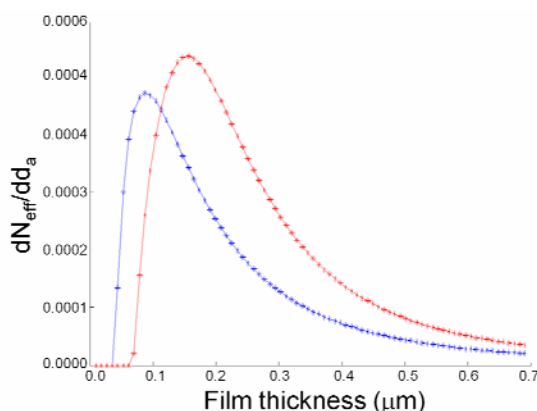

Figura 4.- Sensibilidad de la guía de ITO sobre PMMA a cambios en el espesor del adlayer, con respecto a el grosor de la guía. Modos acoplados TE (azul) y TM (rojo).

Para conocer el espesor de guía óptimo para construir una guía de ondas monomodo, tenemos que buscar el espesor de capa que da la mejor sensibilidad a la estructura. Según la figura 4, el espesor óptimo debe ser entre 120 a 200 nm. También es importante asegurarse de que, en el espesor de capa elegido la guía de ondas es monomodo. Si consideramos la guía de ondas compuesta por agua, ITO y PMMA y calculamos los espesores de guía en los que aparecen los modos TE y TM fundamentales, veremos que el modo TE fundamental será excitado cuando el espesor de la película es de 40.5 nm, y el TM cuando es 69.8 nm. El primer modo TE no aparecerá si la guía es más delgada de 295.7 nm. De esta manera podemos estar seguros de que una guía de 120 nm de ITO sobre PMMA será sensible y monomodo.

2.3 Replicado de la red de difracción en polímero

Para integrar una guía de ondas de polímero en un biosensor óptico se necesita replicar la red de difracción sobre la superficie del polímero, reduciendo los costes de fabricación y por lo tanto, lograr la fabricación de chips de desechables de un sólo uso. Una capa gruesa de 3 μm de PMMA se fabrica por *spin coating* sobre sustratos de vidrio utilizados como soporte. Después de curar la muestra a 180 º C durante 60 segundos, ya está lista para la impresión. Como másters hemos utilizado redes de difracción (20 nm de profundidad, 0.5 μm de periodo y 50% de ciclo de trabajo) en nitruro fabricadas por RIE y eBeam. El proceso de litografía por nano-impresión (NIL) se lleva a cabo en dos etapas: del máster de nitruro a una lámina de 125 μm de poli(naftalato de etileno) (PEN), y de la réplica de PEN al PMMA.
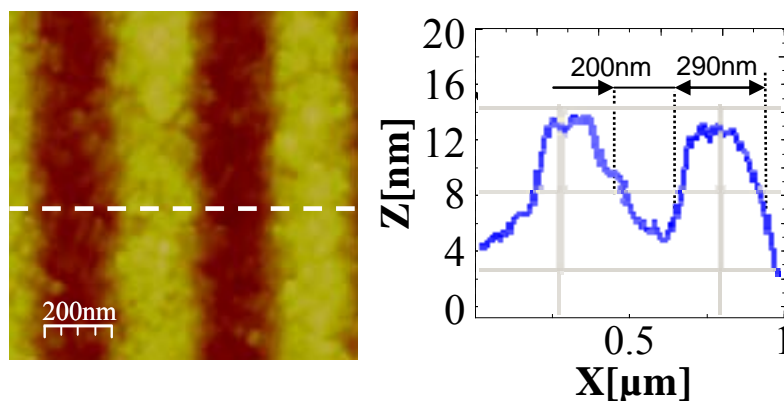

Figura 5.- Imagen de AFM de la red de difracción replicada en los sustratos de PMMA.

En la figura 5 se muestra una imagen de AFM de la red replicada en polímero. Es posible concluir que NIL es adecuado para replicar estructuras sobre substratos de polímero con buena definición dimensional. No sólo la replica es exitosa cuando se trata de su geometría, sino que las redes de polímero también son capaces de acoplar la luz, como se muestra claramente en la figura 6.
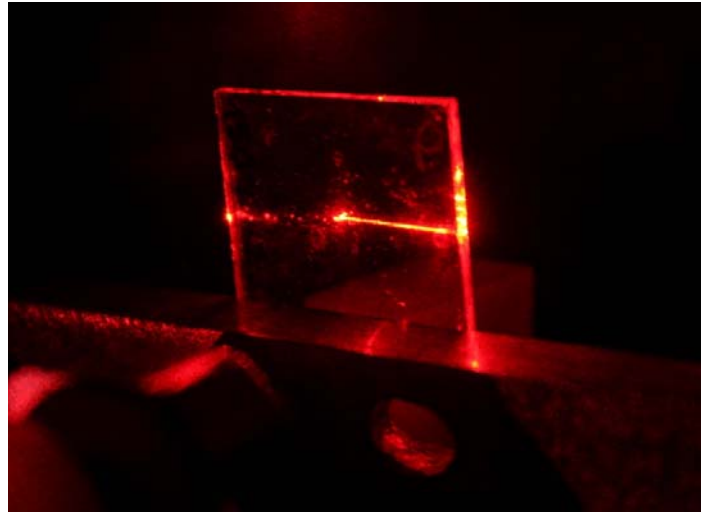

Figura 6.- Un láser de He-Ne se acopla en la guía de PMMA mediante la red replicada, en el banco óptico

2.4 Recubrimiento de ITO por sputtering

Óptimas capas delgadas de 120 nm de ITO amorfo sobre PMMA se depositaron a temperatura ambiente a una velocidad de 0,4 nm/s con un contenido de oxígeno de 0,5 SCCM durante 300 segundos. La resistencia laminar de capa de ITO obtenida fue $7.12 \cdot 10^{-4}$ Ω/cm. La capa de ITO muestra una transmitancia de aproximadamente 80% en 632.8nm y un índice de refracción de 1.932. El espesor de capa se confirmó con SEM alrededor de 110 nm. Una vez que los parámetros de depósito fueron optimizados, una capa de 120 nm de ITO se depositó sobre las redes de PMMA. La calidad de la superficie de la guía se comprobó con AFM (figura 7). Se comprobó que el período de la red se mantiene a 500 nm con una profundidad aparente de 10 nm, mientras que la rugosidad es aproximadamente de sólo 1.3nm.
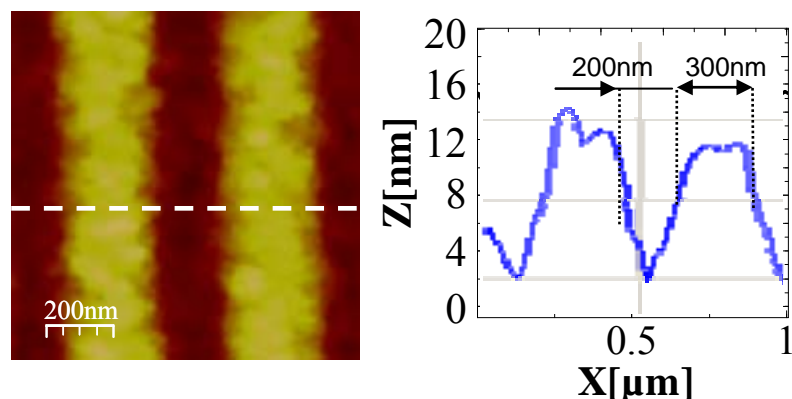
Figura 7.- Imagen de AFM de la red de difracción de PMMA recubierta con ITO.

2.5. Caracterización de las guías de polímero recubiertas de ITO

Una vez fabricado el chip de ITO/PMMA, estudiamos su rendimiento con el OWLS (figura 8).
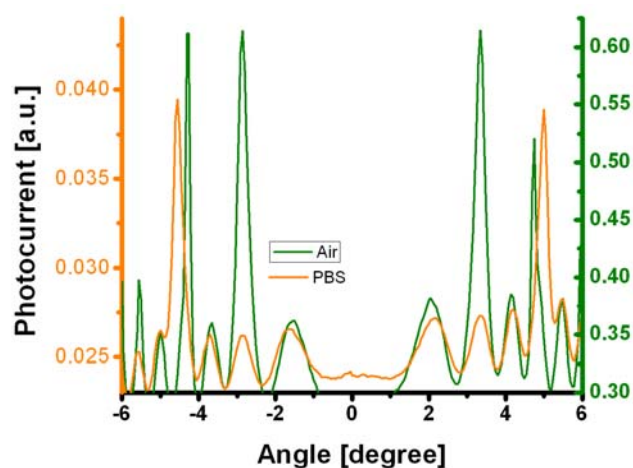

Figura 8.- El haz laser se acopla en la guía a diferentes ángulos. La línea verde muestra el espectro de acoplo del chip ITO/PMMA en aire, y la línea naranja en PBS.

A pesar de que el chip de polímero presenta un buen rendimiento en aire, sólo dos picos se encuentran cuando se prueba en PBS. Esto podría ser debido al hecho de que las pérdidas por acoplamiento son tan altas que no se pueden excitar los modos TE y TM al mismo tiempo. Cuando la luz se polariza a 0 º y 90 º somos capaces de encontrar los modos TE y TM respectivamente, pero su intensidad es aún muy baja. Para resolver este problema sería necesario reducir las pérdidas por acoplamiento. Una forma de lograr este propósito sería disminuir aún más la rugosidad de la capa de polímero.

3 GRATING COUPLERS RECUBIERTOS DE CAPAS FINAS

Con el fin de adaptar los sensores a los requerimientos de aplicaciones específicas, podemos fabricar guías de ondas con recubrimientos de capas finas de distintos materiales transparentes, sin afectar su sensibilidad y permitiendo simular las propiedades de la superficie del material de interés. El recubrimiento de sensores comerciales de óxido de titanio en silicio con diferentes materiales permitirá rápidos estudios cuantitativos de la adsorción de biomoléculas sobre sus superficies, para ser utilizado en la calibración de otras técnicas.

3.1 Evaporación térmica de oro

Capas finas y transparentes de oro son depositadas en los chips comerciales utilizando evaporación térmica. La transmitancia de la capa de oro disminuye con el tiempo de depósito, es decir, disminuye a medida que aumenta el espesor de oro. Después de optimizar los parámetros para producir una capas de oro con una transmitancia del 83,43% en 632.8nm, se depositan capas delgadas de oro sobre los sensores comerciales durante 25 segundos. La topografía de los sensores recubiertos de oro se evaluó mediante AFM y los resultados se presentan en la figura 9. La rugosidad de la capa de oro aumenta hasta 2 nm, haciendo que la profundidad de la red sea un poco más pequeño, alrededor de 5 nm.
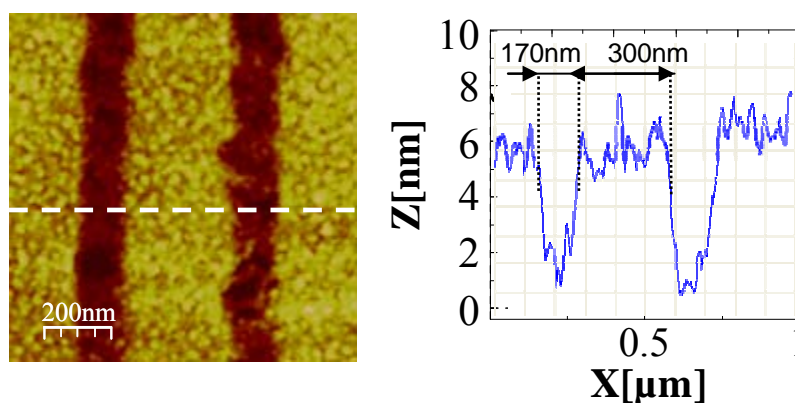

Figura 9.- Imagen de AFM image de la red de difracción recubierta por una fina capa de oro.

El rendimiento del sensor en aire fue comprobado mediante OWLS. La figura 10 confirma el funcionamiento de la red recubierta de oro en aire, mostrando picos bien definidos para TE y TM. Desafortunadamente, la adherencia de la capa de oro sobre el sensor es pobre y se desprende de la superficie cuando se pone en contacto con la

solución buffer. Trabajo adicional debe hacerse con el fin de mejorar la adherencia de los nanocapas de oro en el sensor. Esto podría hacerse depositando una capa muy delgada de aproximadamente 5 nm de cromo antes de la deposición de oro.
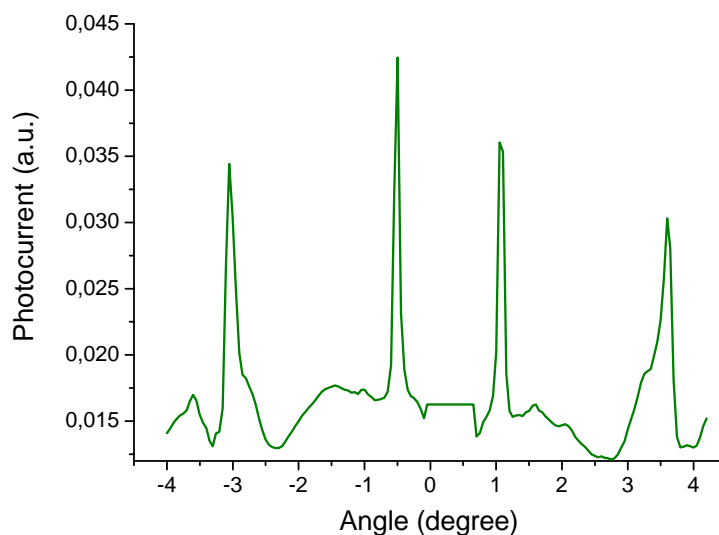

Figura 10.- La gráfica de OWLS muestra el espectro de acoplamiento en aire de la guía recubierta de oro.

3.2 Sputtering de Nitruro de Silicio

Capas delgadas de nitruro de silicio fueron depositadas por sputtering sobre las redes de difracción comerciales. El tiempo de depósito y la polarización aplicada en el proceso de bombardeo iónico se optimizaron para obtener una capa de nitruro con alta transmitancia en el visible y baja rugosidad. Después del depósito, el grosor y el índice de refracción del nitruro medidos por elipsometría resultaron 10.3 nm y 2.22, respectivamente. En la Figura 11 se puede notar que después del depósito de nitruro la rugosidad de la superficie ha aumentado hasta 2.6 nm, mientras que la estructura de la red se mantuvo apenas alterado (período de 450 nm y profundidad aparente de 7 nm).
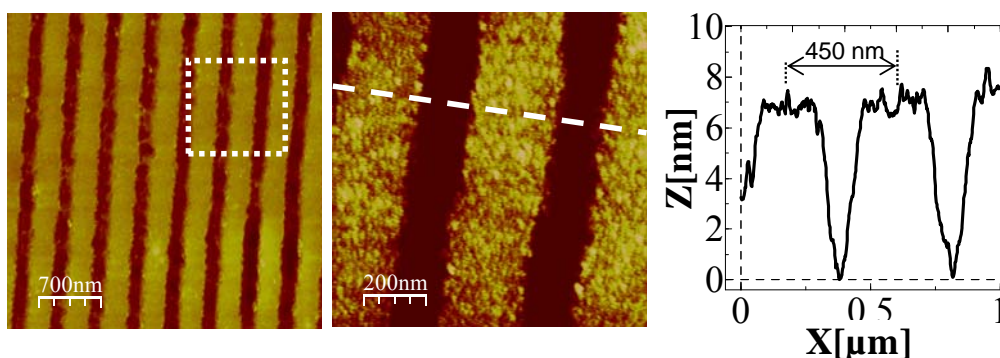

Figura 11.- Imagen de AFM de la red de difracción después del depósito de una fina capa de nitruro.

Una vez fabricado el chip recubierto de nitruro de silicio, se comprobó su rendimiento en OWLS. La figura 12 muestra los espectros de acoplo después del depósito de la capa de nitruro. Se puede observar que tanto TE como TM son perfectamente visibles. Para poner a prueba la capacidad de las nuevas estructuras para trabajar como un inmunosensor, experimentos estándar antigeno-anticuerpo se llevaron a cabo. Para este propósito se seleccionó como modelo el par anti-HSA/HSA. La figura 12 también incluye el espectro de acoplo después de que el chip haya sido funcionarizado con una capa de anticuerpo anti-HSA.
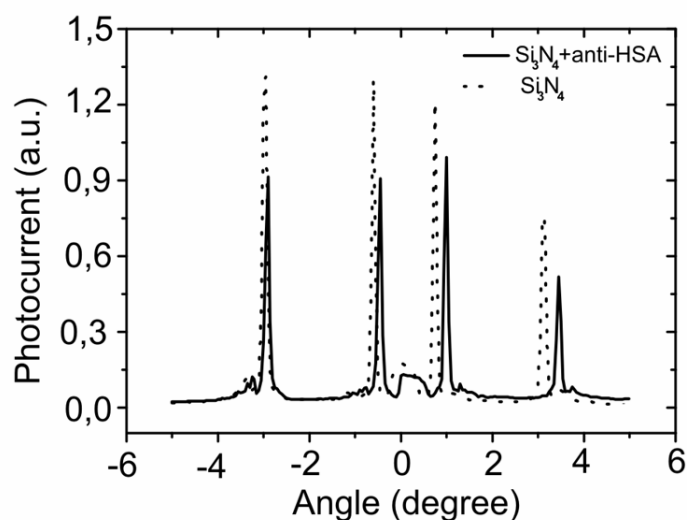

Figura 12.- El laser se acopla dentro de la guía para diferentes ángulos de acoplo (dependiendo del recubrimiento del chip). La línea de puntos muestra el espectro del chip recubierto de nitruro, mientras que la línea continua representa el espectro después de la funcionalización.

Se realizaron experimentos de detección de la proteina HSA con el fin de establecer la viabilidad biosensora de todo el sistema desarrollado. HSA fue reconocida por el anticuerpo anti-HSA unido a las guías recubiertas de nitruro. El sistema resultó ser estable y la relación entre la masa de proteína adsorbida y la concentración de HSA se muestra en la figura 13. Los valores experimentales de masa adsorbida se ajustaron utilizando un ajuste sigmoidal con un factor de correlación R^2 de 0.9969. La gráfica también sugiere un ajuste lineal dentro del intervalo de 10^{-3} M a 10^{-6} M con un valor de R^2 de 0.9969. La sensibilidad del sistema en el rango dinámico es de 34 ng/cm^2 para la detección de HSA. Estos resultados muestran un sistema biosensor con un rango dinámico muy adecuado diseñado para la aplicación específica, con un límite de detección que, a pesar de no llegar a los valores reportados por otros estudios similares,

es tres órdenes de magnitud mejor de lo necesario para el diagnóstico de hiper/hipoalbuminemia y es mucho más estable. Además, nuestro sistema presenta muy buena sensibilidad y la posibilidad de extraer los valores de masa adsorbida.
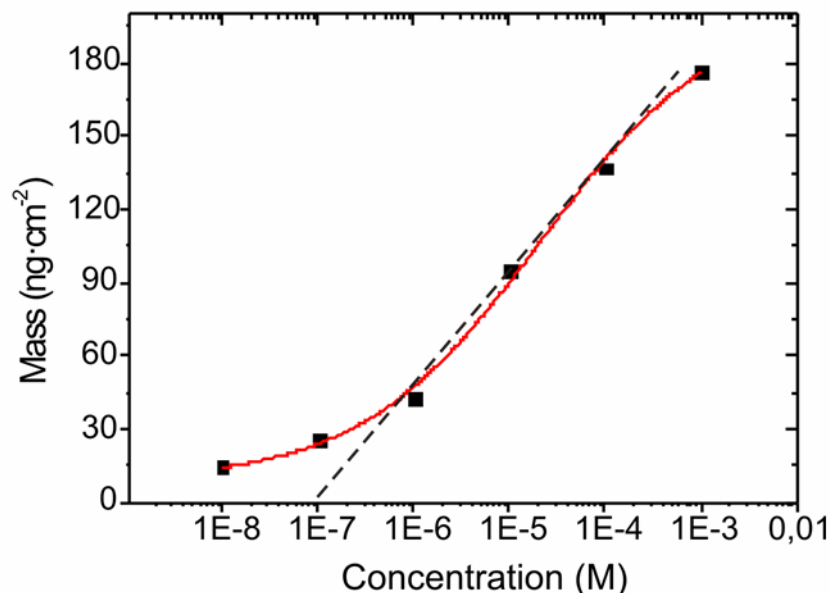

Figura 13.- Relación entre la masa de HSA adsorbida en la superficie del sensor y la concentración de HSA en solución.

Este modelo de estudio de la detección y cuantificación de la HSA demuestra el potencial de las redes de difracción recubiertas de nitruro.

4 CONCLUSIONES

Después de un extenso estudio de la sensibilidad de las guías de polímero, un grating coupler basado en polímero ha sido fabricado mediante NIL y usado como sustrato para la fabricación de una guía de ITO con alta sensibilidad. A pesar de haber optimizado su sensibilidad, las pérdidas por acoplo interfieren en el rendimiento de la guía de ondas polimérica. También se han fabricado guías recubiertas de oro con buenas características ópticas, pero pobre adherencia. A pesar de haber demostrado la validez de estos nuevos enfoques, es necesario seguir investigando para lograr una prueba de concepto más sólida. Por otro lado también se han fabricado guías recubiertas de una capa fina de nitruro. Los resultados muestran que la masa adsorbida en la superficie de estos sensores se puede medir fácilmente, dando información adicional sobre los procesos de interacciones moleculares en comparación con las anteriores técnicas de detección.

CAPÍTULO 3: EFECTO DEL ÍNDICE DE REFRACCIÓN DEL BUFFER EN BIOSENSORES DE ONDA EVANESCENTE

1 INTRODUCCIÓN

Como se indica en el capítulo 2, un grating coupler, como el utilizado en la técnica owls, por lo general consiste en tres capas diferentes: sustrato, guía y cubierta (figura 14). La cubierta es la solución muestra, que está formada por una solución buffer que contiene las biomoléculas que se adsorberán sobre la superficie del sensor. Cuando se crea en la superficie del sensor una capa adsorbida, las condiciones de acoplo varían, lo que permite seguir la inmovilización tiempo real. Por otro lado, la variación del índice de refracción de la capa adsorbida sobre la superficie del chip se traduce en concentración superficial de la molécula adsorbida. Es importante tener en cuenta que la capa adsorbida no es una capa seca compuesta únicamente por biomoléculas, sino que la adlayer está también hidratada por el buffer.
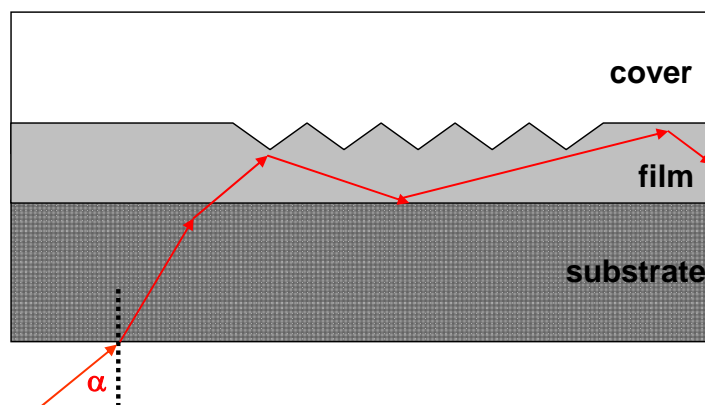

Figura 14.- Esquema de un grating coupler de tres capas. La guía está atrapada entre el sustrato y la cubierta.

Con el fin de obtener medidas cuantitativas precisas de la adlayer y su dependencia con el buffer y otros parámetros externos, es de crucial importancia una caracterización previa de los parámetros de la guía de onda (espesor e índice de refracción de la guía). Esto es debido a que estos parámetros pueden variar ligeramente dependiendo de las condiciones de fabricación. También las condiciones de trabajo, tales como la temperatura, pueden influir en las medidas y por lo tanto deben ser evaluadas antes de cada experimento. En este capítulo, se describe un nuevo método de calibración para caracterizar de forma individual cada sensor y cada solución buffer

antes de realizar las medidas de biosensado con la técnica owls. Este nuevo protocolo permitirá la realización de experimentos cinéticos con gran precisión, sin tener en cuenta las condiciones de trabajo. En primer lugar, para un chip sensor específico, el ángulo de acoplo se midió en aire y en agua para obtener, después de simulaciones, los parámetros intrínsecos de la guía (índice de refracción, n_F, y espesor, d_F, de la guía). Una vez que los parámetros están calibrados, los podemos establecer como constantes en la ecuación de dispersión. Entonces, al medir el ángulo de acoplo, será posible calcular el índice de refracción de buffers, n_C, desconocidos y su variación con las condiciones externas. Una vez que todo el sistema esté caracterizado, podemos usar nuestro modelo para controlar con gran precisión un experimento de adsorción. Todo este trabajo sienta las bases para la calibración de cualquier biosensor óptico con red de difracción.

2   MEDIDA DEL ÍNDICE DE REFRACCIÓN DEL BUFFER

Una vez que el chip se ha calibrado se han calculado sus parámetros intrínsecos, es posible calcular directamente el índice de refracción del buffer sólo mediante la medición del ángulo de acoplo del sistema y aplicando el modelo de tres capas a la inversa. Como se muestra en la figura 15, al saber los parámetros reales del chip, es posible establecer un ajuste lineal entre el ángulo de acoplo y el índice de refracción de los diferentes buffers.
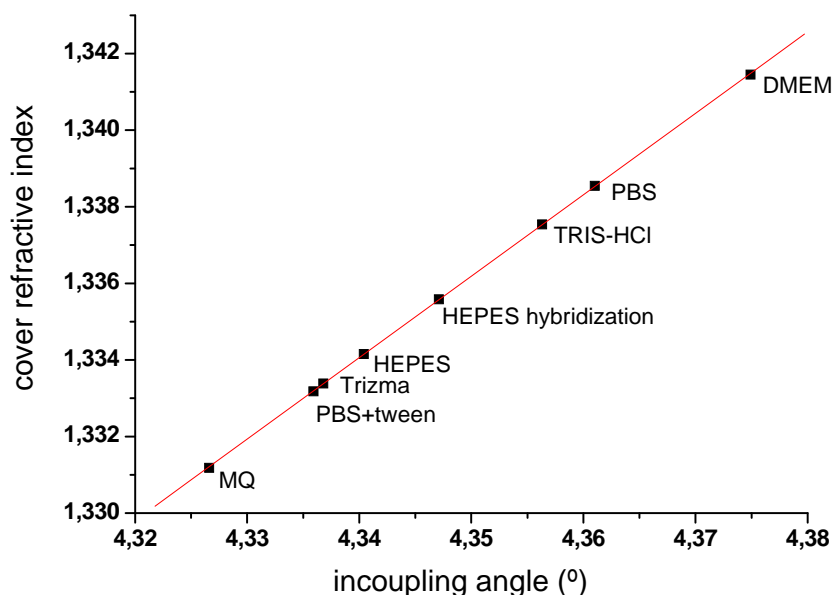

Figura 15.- Índice de refracción de los buffers más communes medidos con OWLS. El ajuste lineal da el índice de refracción de la cubierta para cada ángulo de acoplo.

Combinanas las mediciones de OWLS junto con nuestra calibración son capaces de distinguir soluciones con la precisión requerida de 10^{-6} en el índice de refracción. El OWLS garantiza la precisión de 10^{-6} precision y la calibración asegura que la diferencia relativa entre una medición y otra se debe sólo a la solución buffer. Nuestra definición precisa del índice de refracción nos permitirá distinguir entre diferentes proteínas en las soluciones, o concentraciones diferentes de la misma proteína, aún cuando la variación del índice de refracción sea muy leve. Otra cuestión es que la misma solución preparada en condiciones diferentes, en un día diferente, o a una temperatura diferente, tendrá un índice de refracción diferente. Esta calibración permite calcular, no el índice de refracción absoluto, pero el índice de refracción particular justo antes del experimento. Este control preciso del buffer, independientemente de las condiciones de trabajo, asegura una alta precisión en el análisis posterior de una capa adsorbida.

3   DEPENDENCIA DEL ÍNDICE DE REFRACCIÓN DEL BUFFER CON LA CONCENTRACIÓN SALINA

Dado que algunas propiedades de los buffers, tales como la concentración salina, la temperatura o el pH cambian dependiendo del experimento llevado a cabo, es de gran interés obtener un modelo que describa la variación del índice de refracción del buffer como una función de estos parámetros.
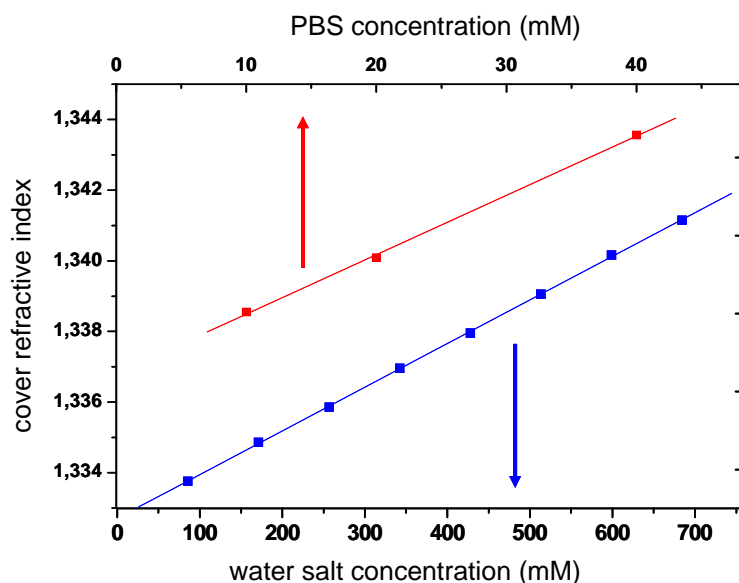

Figura 16.- Índice de refracción del PBS a distintas concentraciones (10 mM, 20 mM and 40 mM) medido a 25ºC (valores experimentales) y variación del índice de refracción del agua con el contenido en sal (valor obtenido de la bibliografía).

La figura 16 muestra la variación del índice de refracción del agua con la concentración salina medido a 18 ºC (línea azul). Para probar si otros buffers seguirían un comportamiento similar, se ha medido distintas concentraciones de PBS (10 mM, 20 mM y 40 mM) a a 25 ºC (línea roja). Se obtubo la dependencia lineal esperada con R^2 mejor que 0.999. Estos resultados se pueden utilizar para calcular fácilmente la influencia de la concentración de sal del buffer en un experimento de adsorción, y para discriminar este efecto de la cinética real de adsorción.

4   DEPENDENCIA DEL ÍNDICE DE REFRACCIÓN DEL BUFFER CON LA TEMPERATURA

Otro parámetro externo, importante a tener en cuenta a la hora de realizar experimentos de biosensado es la temperatura. Las dos temperaturas típicas de trabajo son la temperatura ambiente (25 ºC) y la fisiológica (37 ºC). En la figura 17, se presenta un estudio de la evolución del índice de refracción de varios buffers (agua MilliQ, PBS y HEPES) con variaciones de la temperatura en este rango.
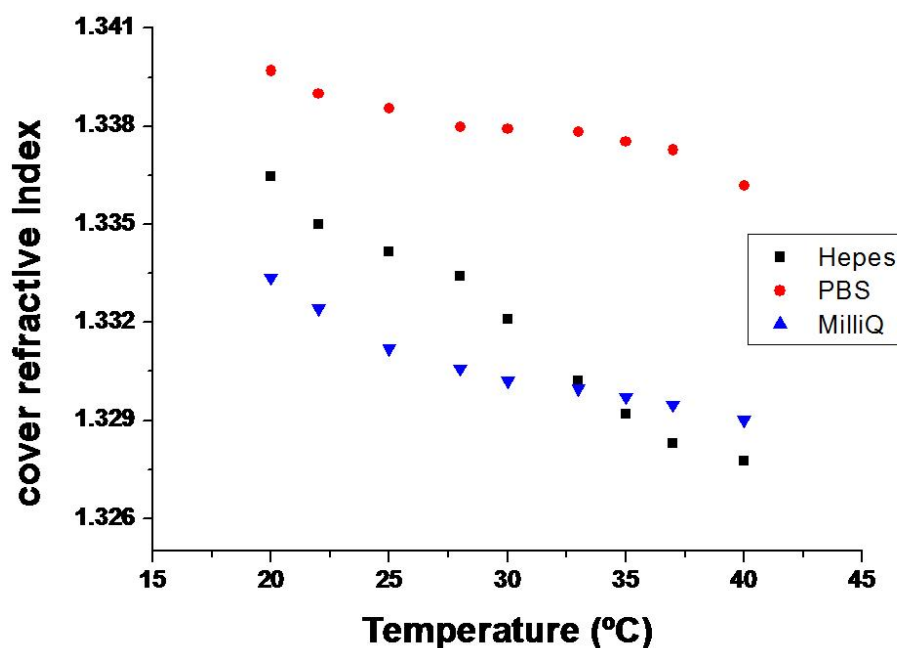

Figura 17.- Índice de refracción de varios buffers (agua, PBS y HEPES) medidos a diferentes temperaturas.

5 CONCLUSIONES

En este capítulo se ha establecido un nuevo protocolo de calibración para experimentos que requieren medidas de alta precisión. Esta rutina incluye un modelado individual de cada sensor y considera, en una manera muy precisa, los parámetros que normalmente no son tenidos en cuenta, tales como la naturaleza del buffer, su composición y la temperatura de trabajo. De esta manera, los índices de refracción particulares de las soluciones buffer se pueden medir con gran precisión antes de cada experimento, independientemente de las condiciones de trabajo, asegurando una alta precisión de las mediciones cinéticas y en el análisis posterior de una capa adsorbida.

CAPÍTULO 4: MONITORIZANDO LA INMOVILIZACIÓN DE RECEPTORES OLFATIVOS EN SUPERFICIES SENSORAS

1 INTRODUCCIÓN

En este capítulo se ha caracterizado la inmovilización de liposomas (provenientes de levaduras) conteniendo receptores olfativos (ORs) en la superficie de un sensor por medio de OWLS. El objetivo de este trabajo es optimizar la estrategia de funcionalización de la superficie del sensor, que conduce a la unión efectiva de los liposomas.

2 CARACTERIZACIÓN DE LOS LIPOSOMAS

Para estudiar el tamaño de los nano-liposomas (nanosomas) y la homogeneidad de su solución, hemos realizado medidas de DLS. Una muestra no tratada muestra nanosomas con un tamaño promedio de alrededor de 400 nm de diámetro, pero con una polidispersidad muy alta de 178 nm. Lo ideal sería tener una población homogénea de nanosomas con un diámetro medio inferior a 100 nm, de manera que los ORs no queden demasiado lejos de la superficie de detección. Con el fin de reducir el tamaño de los nanosomas y para homogeneizar la población, hemos sonicado (50 W, 40 Hz) la suspensión nanosomas en agua helada durante 2 y 20 minutos. La variación del diámetro de los nanosomas y de la polidispersidad de la muestra con el tiempo de sonicación se muestran en la figura 18. Cuando la solución se sonicó durante 2 minutos (cuadrados negros) el tamaño de los nanosomas es mucho más pequeño y homogéneo que en la muestra no tratada, con un diámetro promedio nanosomas de 110 nm y una polidispersidad (círculos huecos) baja de 34 nm. Pero cuando la solución se sonicó durante 20 minutos el diámetro medio de los nanosomas disminuyó hasta 66 nm y la polidispersidad es sólamente 18 nm. Hay por tanto una gran disminución en el diámetro medio de los nanosomas y un avance masivo en la homogeneidad de la muestra cuando ésta se sonica durante 2 minutos. Esta tendencia se acentúa aún más cuando la muestra es sometida a ultrasonidos durante tiempos más largos. Como la medida de la polidispersidad de la muestra sonicada durante 2 minutos es aceptable y el diámetro de los nanosomas, ~ 100 nm, es lo suficientemente bueno para nuestra aplicación, este es el

parámetro elegido para la etapa de homogeneización. Un tiempo de sonicación inferior permitirá la preparación de muestras más rápido, al mismo tiempo que garantizará que los ORs se vean menos afectados. Como conclusión, de acuerdo con los resultados DLS, las muestras de nanosomas producidas por 2 minutos de sonicación en agua helada tienen buenas características en términos de tamaño y polidispersidad y serán los utilizados de aquí en adelante.
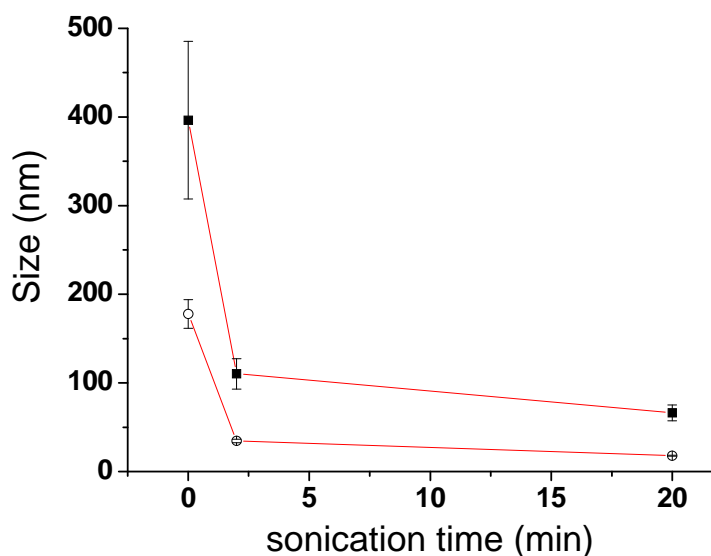

Figura 18.- Evolution del diámetro de los nanosomas (cuadrados negros) y de la polidispersidad de la muestra (círculos huecos) con el tiempo de sonicación.

Para investigar más a fondo la morfología de los nanosomas en solución, usamos la técnica de criofractura-TEM. Dos conjuntos de muestras fueron estudiados, suspensión de nanosomas sin tratar (figura 19) y suspensión sonicada durante 2 minutos (figura 20). El examen de las imágenes muestra que en la suspensión sin tratar coexisten liposomas con diámetros que oscilan desde 200 nm a 2 μm, mientras que en la muestra tratada las vesículas muestran un diámetro homogéneo justo por encima de 100 nm, con una densidad estimada de nanosomas en la superficie de 1 nanosoma por 3 μm^2. Las micrográficas de TEM también muestran la presencia de proteínas de unos 5 nm en la membrana de las nanovesículas, independientemente del tratamiento de la muestra. Algunas de estas proteínas de membrana son receptores olfativos.
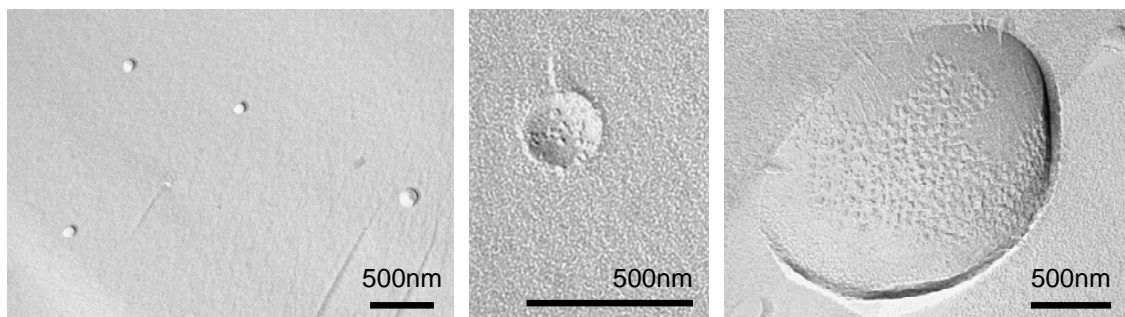
Figura 19.- Imagenes de cryo-TEM de una suspension de nanosomas sin tartar. Se pueden apreciar proteínas de membrana en los liposomas. Los nanosomas presentan tamaños muy variados.
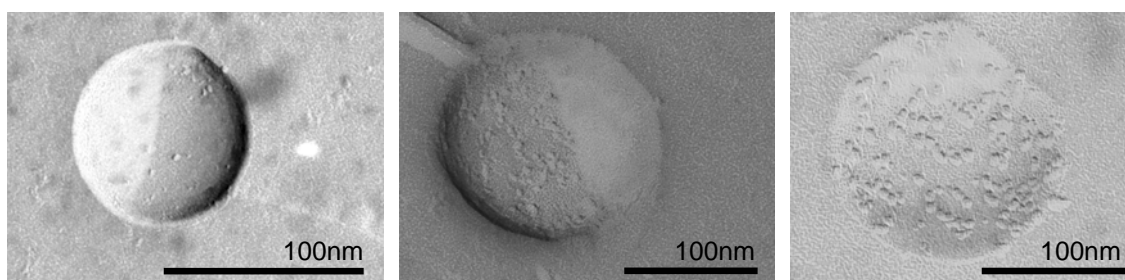

Figura 20.- Micrográficas de cryo-TEM de una suspension de nanosomas sonicada durante 2 minutos. Todavía podemos ver las proteinas de membrana a pesar del tratamiento de ultrasonidos. El diámetro de los nanosomas parece ser homogéneo, con un diámetro de unos 100 nm.

Estos resultados son consistentes con los datos de DLS y confirman que nuestro tratamiento para homogeneizar la suspensión de nanosomas tiene éxito.

3 INMOVILIZACIÓN DE LOS NANOSOMAS

3.1 Adsorción física

Para estudiar la distribución de los nanosomas sobre una superficie y explorar si mantienen la misma forma y proporciones que en líquido, se han caracterizado primero los nanosomas adsorbidos sobre una superficie de ITO. Para ello, hemos depositado la suspensión nanosomas sobre el sustrato y dejado reaccionar durante una hora. Después de eliminar nanosomas no enganchados con PBS, tomamos imágenes con AFM en líquido. Como se puede ver en la figura 21, sólo unos pocos nanosomas se sientan sobre la superficie y, además no mantienen una estructura esférica, sino que se extienden formando un "huevo frito " con una relación de aspecto 1:6.
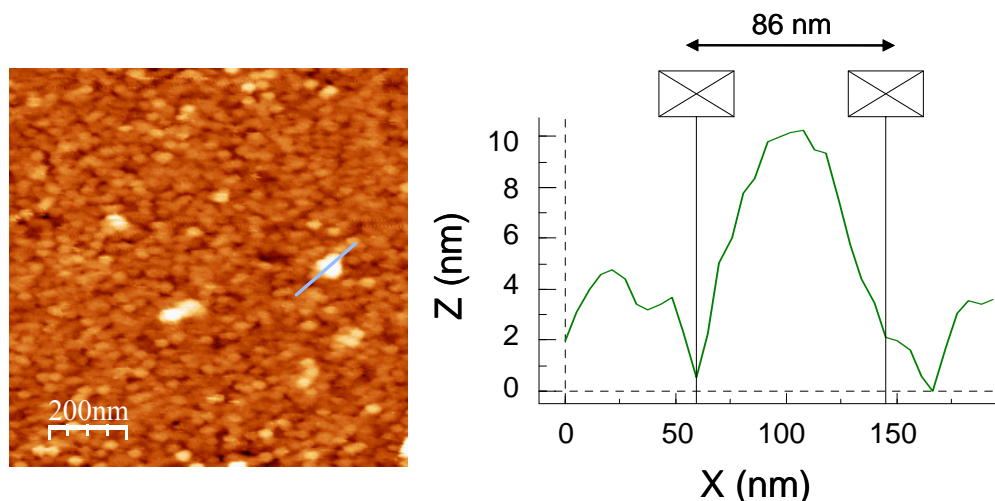
Figura 21.- Imagen de AFM de los nanosomas adsorbidos sobre ITO.

En conclusión, la estructura de los nanosomas se aplana al inmovilizarse debido a las fuerzas de interacción con la superficie; sin embargo, esas fuerzas no son lo suficientemente fuertes para provocar la apertura del nanosoma. La hidrofilicidad de la superficie juega un papel importante en la cobertura de la superficie, pero no afecta a la naturaleza de los nanosomas una vez son adsorbidos. Aún así, la adsorción física de los nanosomas sobre la superficie del sensor no proporciona una buena metodología para la inmovilización de los nanosomas, ya que proporciona una cobertura superficial muy baja que influiría negativamente en la respuesta del potencial sensor.

3.2 Reconocimiento molecular específico

Como la densidad superficial de los nanosomas adsorbidos sobre ITO es muy baja, diseñamos un procedimiento de funcionalización para promover el anclaje de nanosomas en superficies por mecanismos de reconocimiento molecular. Este proceso debería aumentar la cobertura de la superficie y mantener la forma esférica de los nanosomas. De esta manera, los nanosomas se inmovilizarían específicamente sobre la superficie a través de una "etiqueta" c-myc que está acoplada al receptor olfativo expresado en la membrana de los nanosomas. Para el procedimiento de funcionalización, la superficie de ITO es activada por plasma de oxígeno y luego se sumerge en PLL-g-PEG-biotina para formar una monocapa. Después de enjuagar con PBS, la muestra se sumerge en una solución de estreptavidina y por último en una solución de anticuerpo anti-cmyc biotilinizado. Después de la incubación del anticuerpo, la muestra está lista para reaccionar con el cmyc unido a las proteínas de

membrana presentes en los nanosomas. Un esquema del proceso de funcionalización se incluye en la figura 22.
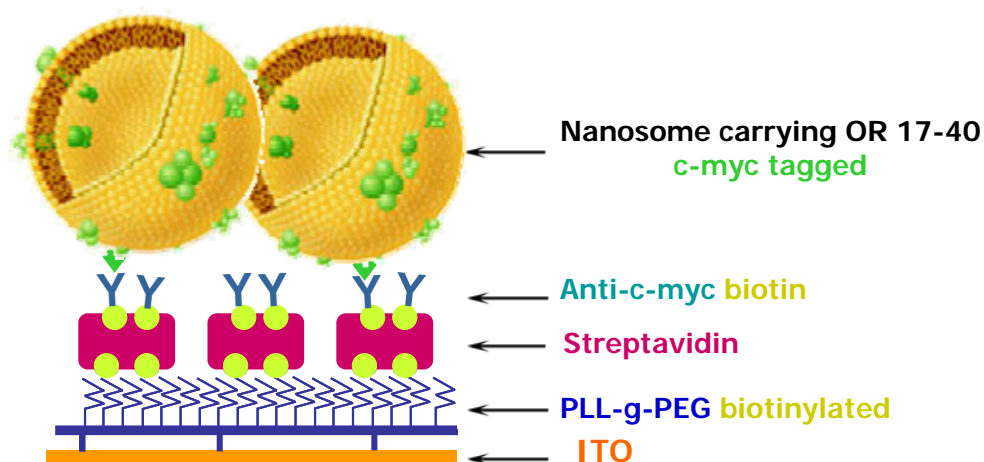

Figura 22.- Esquema de la funcionalización del sustrato de ITO.

El proceso completo de funcionalización se realizó en una celda de flujo y, una vez que la capa de funcionalización se ha caracterizado, se depositó encima una suspensión de nanosomas y dejó reaccionar en flujo durante 1 hora. La muestra resultante fue analizada por AFM, como se muestra en la figura 23. La imagen sugiere que el número de nanosomas presentes sobre la superficie ha aumentado a un recubrimiento superficial de aproximadamente 23%, aunque la relación de aspecto se ha incrementado aún más a 1:20.
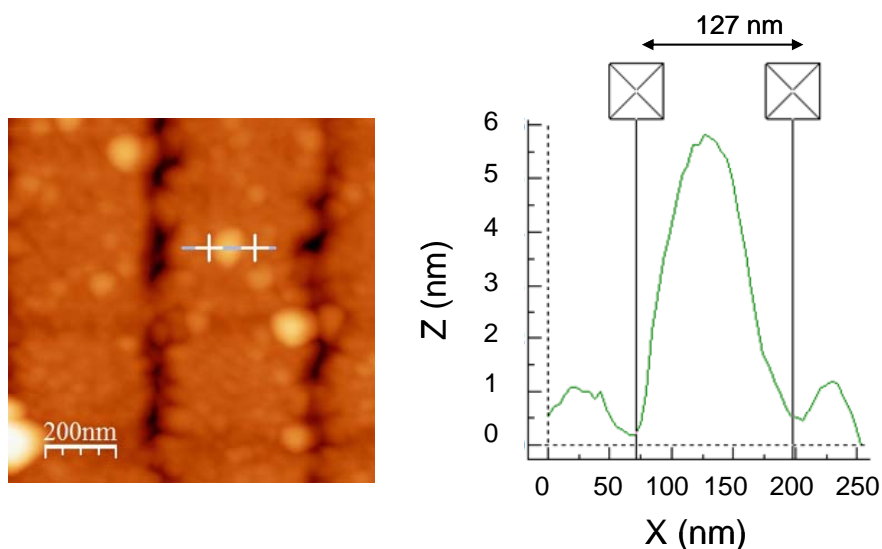

Figura 23.- Imagen de AFM de los nanosomas inmovilizados sobre la funcionalización en la superficie de ITO (un grating coupler de OWLS). La funcionalización se realizó en flujo.

Para comprender plenamente la causa de que los nanosomas colapsen aún más en las muestras funcionalizadas, y discriminar si este efecto es un artefacto inducido por la punta del AFM durante la exploración de las muestras, se decidió investigar las muestras con la técnica de criofijado-SEM. Los resultados muestran que el diámetro de los nanosomas es de alrededor de 100 nm, lo que sugiere que el efecto de colapso que apareció en las imágenes de AFM es un artefacto causado por la punta del AFM en sí.

4 NÚMERO DE RECEPTORES POR NANOSOMA

A la vista de los resultados obtenidos sobre el proceso de inmovilización de nanosomas, la cobertura de la superficie se revela como un tema crítico. Como el procedimiento utilizado para anclar los nanosomas sobre la superficie funcionalizada se basa en la captura de "etiquetas" cmyc, incorporadas en los receptores olfativos, a través del anticuerpo anti-cmyc inmovilizado en la superficie; habría que preguntarse si el número de receptores olfativos por nanosoma es uniforme y, en caso afirmativo, si este número es demasiado bajo como para impedir la inmovilización de nanosomas. Como la técnica de μCP permite llevar a cabo experimentos de fluorescencia incluyendo el control al mismo tiempo y en el mismo sustrato, se realizó un experimento de μCP para evaluar la disponibilidad de ORs en nanosomas funcionarizados sobre ITO (figura 24).
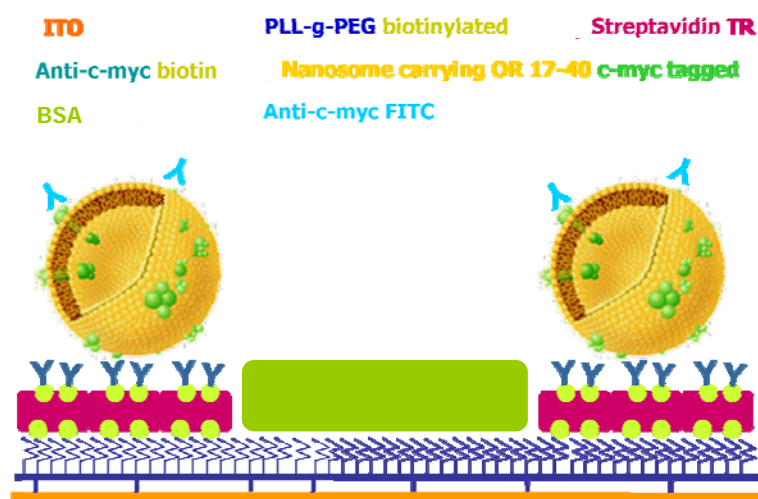

Figura 24.- Esquema del experimento de μCP en el que los nanosomas se inmovilizan sobre el ITO funcionalizado. Se creó un patrón de estreptavidina-TexasRed sobre la superficie de ITO recubierta de PLL-g-PEG-biotin. Después la superficie se incubó con los anticuerpos y los nanosomas. Por último, la superficie se bloqueó con BSA antes de usar un anticuerpo secundario-FITC para identificar los ORs libres en la superficie.

Las imágenes resultantes se muestran en la figura 25. Como puede verse, el anticuerpo sólo se adjunta en el patrón creado por la estreptavidina, lo que significa que no hay adsorción inespecífica del anticuerpo fluorescente y que todavía hay algunos ORs disponibles en la membrana de los nanosomas.
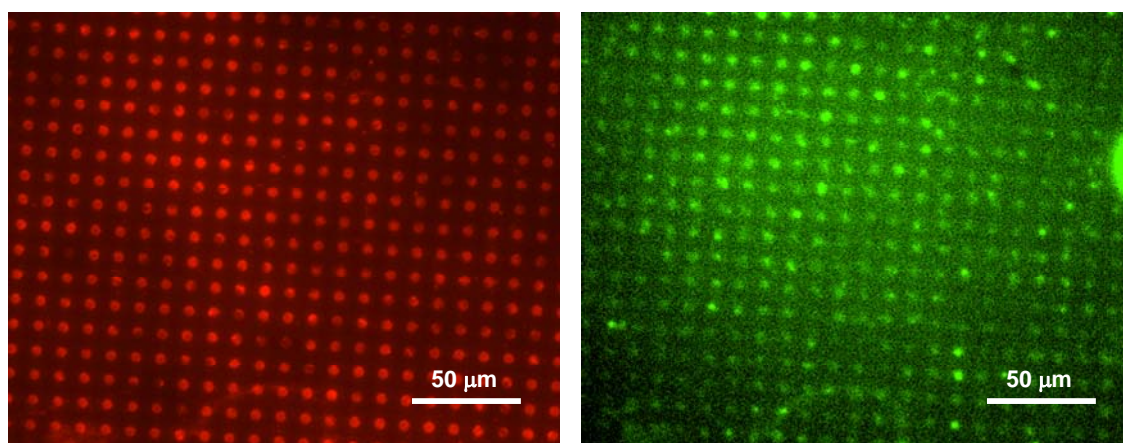

Figura 25.- Imagen de flourecencia de la inmovilización de nanosomas sobre ITO funcionalizado. En la izquierda, el patron de estreptavidina está marcado en rojo. En la derecha, podemos ver como las areas marcadas en verde por el anticuerpo secundario coinciden con el patron creado previamente, sugiriendo que los nanosomas solo se inmovilizan sobre la funcionalización y que tienen Ors disponibles en sus membranes.

5 OWLS

Para estudiar en detalle nuestra funcionalización para inmovilizar nanosomas sobre sustratos de sensores, hemos elegido la técnica de OWLS. Una vez que la inmovilización del anticuerpo anti-cmyc fue caracterizada y que nos hemos asegurado de que hay suficiente densidad de anticuerpos en la superficie, suspensiones de nanosomas que contienen diferentes concentraciones de proteína son depositadas en la superficie y monitorizadas in situ por OWLS. Como se muestra en el diagrama cinético (figura 26), la cantidad de nanosomas inmovilizados sobre la superficie aumenta al aumentar su concentración de proteína, llegando incluso a la saturación.
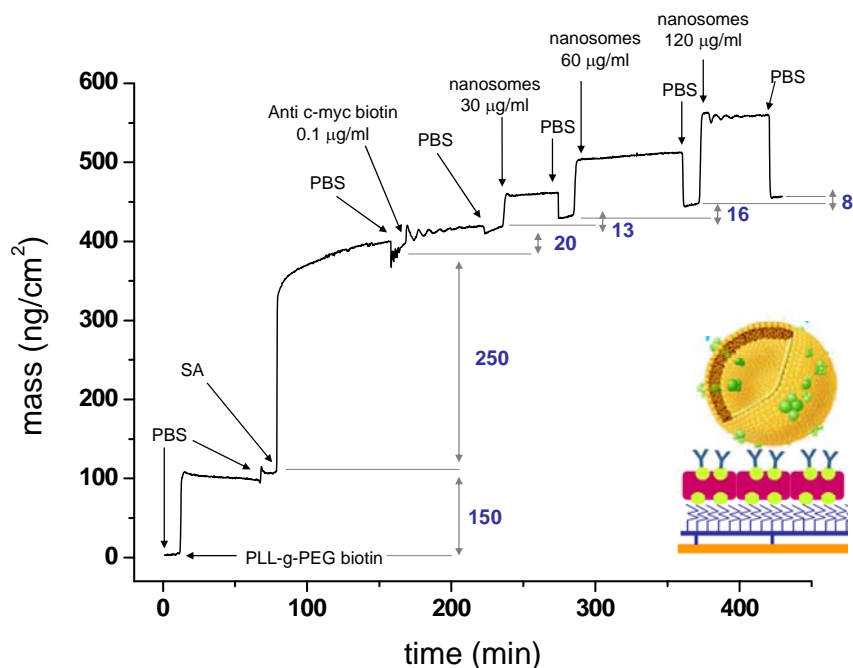
Figura 26.- Inmovilización de diferentes concentraciones de nanosomas sobre ITO funcionalizado. Los nanosomas se anclan a la superficie mediante la etiqueta cmyc enganchada a los ORs en la membrane. Esta "etiqueta" es reconocida específicamente por los anticuerpos inmovilizados en la superfice. Un esquema del proceso se incluye en la esquina inferior derecha. Los números en azul representan la densidad superficial de cada capa después del lavado.

La cantidad de nanosomas adsorbidos en el experimento descrito en la figura 26 corresponden a una cobertura de la superficie total de nanosomas de un 53.19%, que es un valor notablemente elevado muy cerca del límite de interferencia de esferas rígidas (54.7%) y por lo tanto muy cercano al máximo posible de cobertura. Además, la relación total de receptores capturados en relación con el anticuerpo inmovilizado es de 1.86, que es mucho mejor que el nivel más alto que hemos encontrado en la literatura.

Para dilucidar si hay ORs disponibles en los nanosomas inmovilizados, se realizó un experimento OWLS donde, análogamente al experimento de µCP, un anticuerpo secundario reconoce los ORs libres en los nanosomas. Algunos anticuerpos se unen a los nanosomas en una relación de densidad de 13:30 = 0.43, lo que sugiere que algunos ORs están disponibles en la membrana nanosomas. Sin embargo, cuando se realiza un experimento de control para discriminar si estos anticuerpos reconocen específicamente los ORs en los nanosomas o están siendo absorbidos inespecíficamente, la cinética muestra que, efectivamente, algunos anticuerpos reaccionan inespecíficamente sobre la capa primaria de anticuerpos, en una relación de 48:124 = 0.39. Si restamos esta adsorción inespecífica a la cantidad total de anticuerpos unidos a

los nanosomas, se obtiene un reconocimiento específico de ORs en los nanosomas en una proporción de sólo 0.43-0.39 = 0,04. Este resultado sugiere que, a pesar de que hay algunos receptores olfativos presentes y disponibles en la membrana de los nanosomas, su cantidad es probablemente demasiado baja. El mismo problema se encontró en la literatura, donde el valor medio para el número de ORs en un nanosoma de 30 nm de diámetro resultó ser menor que uno.

4 CONCLUSIONES

En este estudio, los receptores olfativos transportados por nanosomas fueron inmovilizados con éxito en las superficies de biosensores funcionalizados. La inmovilización específica de los nanosomas mediante la captura de los receptores a través de un anticuerpo contra la "etiqueta" c-myc produce una orientación uniforme del receptor en la superficie. Además, como resultado de la selección in situ del receptor, era esperado un enriquecimiento en el número de ORs inmovilizados en la superficie biofuncionalizada. El uso de OWLS ha sido crucial para caracterizar completamente el proceso de funcionalización y para entender que el enriquecimiento de los receptores de membrana no se ha logrado. Se concluye que el número de receptores olfativos disponibles en el sensor funcionalizado es demasiado bajo para ser capaz de realizar experimentos de funcionalidad.

CAPÍTULO 5: MODIFICACIÓN ELECTROQUÍMICA DE LA ESTABILIDAD DE MULTICAPAS DE PLL/DNA

1 INTRODUCCIÓN

En este capítulo, se aprovechó la técnica de OWLS electroquímico (EC-OWLS) para estudiar en detalle la cinética de la disolución de multicapas de polielectrolito (PEM) que contienen DNA cuando se les aplica un potencial. Como sistema de prueba, se eligió el sistema de *Layer-by-Layer* (LbL) compuesto de PLL, un policatión biodegradable, y el DNA. Los experimentos se llevaron a cabo en una celda especialmente modificado para poder hacer electroquímica en el OWLS. Las guías de ondas usadas están recubiertas con una capa delgada del ITO que actua como el electrodo de trabajo de una celda de tres electrodos, mientras que los potenciales se aplica con respecto de un alambre de Ag/AgCl (electrodo de referencia) y la corriente se recogió por un alambre de platino (contraelectrodo). La disolución de los *films* PLL/DNA se observó para potenciales por encima de 1.8 V.

2 DEPÓSITO Y DISOLUCIÓN: EC-OWLS

Cuando un film (PLL/DNA)$_6$ se deposita a 0 V, el film obtenido es estable y la masa adsorbida se mantiene constante en la solución buffer una vez que la fabricación se termina. Aplicando una polarización de 1.9 V, la masa en el sensor comienza a disminuir lentamente debido a la disolución del film. La evolución en el tiempo de la disolución a 1.9 V se puede ajustar a una curva de decaimiento exponencial con una constante de tiempo τ de 44 minutos y un porcentaje de masa de film restante Γ_∞ de aproximadamente el 50%. Esto indica que la disolución del film se produce, pero es lenta y solamente parcial. Se sabe que el pH o la fuerza iónica de la solución puede influir en la velocidad de disolución a través de la desestabilización de la multicapa, aunque nuestro interés se centra principalmente en el aprovechamiento del control electroquímico. Cuando el film se crece a 1.2 V y se aplican 1.9 V para la disolución, ésta se ajusta de nuevo con una curva exponencial pero con una constante de tiempo

mucho menor (5 min en lugar de 44) y con un porcentaje de masa residual menor (20% versus 50%). En la figura 27 se recogen los dos experimentos.
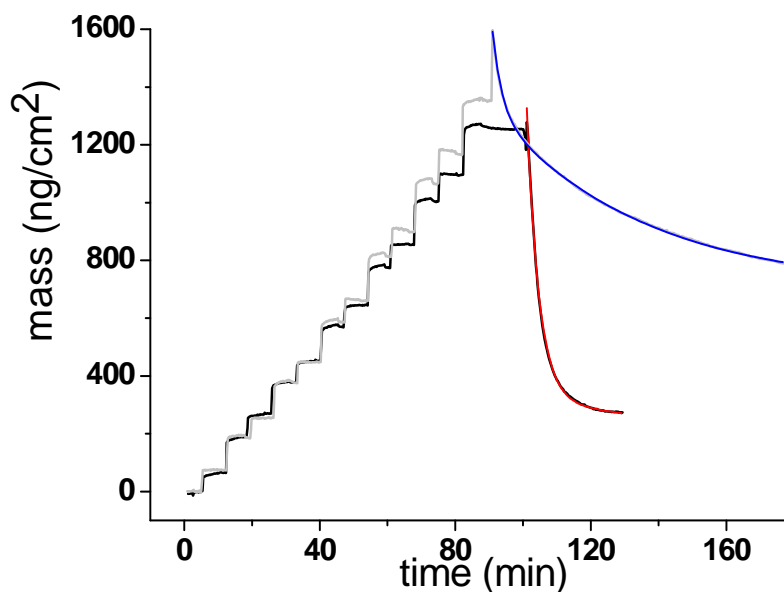

Figura 27.- Masa adsorbida medida con EC-OWLS en un buffer con fuerza iónica 150 mM durante el crecimiento de un film (PLL/DNA)$_6$ a 0 V (línea gris) y a 1.2 V (línea negra). La disolución se provocó en ambos casos a 1.9 V y se ajustó a un decaimiento exponencial (línea azul para el film crecido a 0 V, y línea roja para el film crecido a 1.2 V).

En un intento de caracterizar con mayor detalle este fenómeno, hemos estudiado cómo τ y Γ_∞ dependen de los potenciales de depósito y disolución. En resumen, la disolución de las PEM es más rápida y más eficiente cuanto mayor es el potencial aplicado.

El efecto de la fuerza iónica (la concentración de iones o la conductividad eléctrica) del buffer se investigó mediante la repetición de los experimentos de depósito y disolución en buffers con una concentración de sal diferente. Como en el caso de la figura 27 (150 mM de NaCl) la disolución es más rápida y el porcentaje de masa residual menor cuando la película se fabrica a 1.2 V. Al parecer, cuanto mayor la fuerza iónica, más rápida y más eficiente es la disolución.

Experimentos de OWLS también se llevaron a cabo para films con mayor o menor número de bicapas (hasta 15). Igualmente, la disolución del film es aún más rápida y completa si se aplica un potencial durante el depósito. En la figura 28 podemos ver una comparación de la disolución de un film formado por 12 bicapas cuando es construido a 0 V y a 1.2 V. Cuando el crecimiento del film se desarrolla bajo un potencial, la disolución se produce más rápido y resulta en una destrucción del film más

eficaz. En definitiva, aplicar un potencial durante la fabricación hace que el film sea menos estable y que su disolución se acelere.
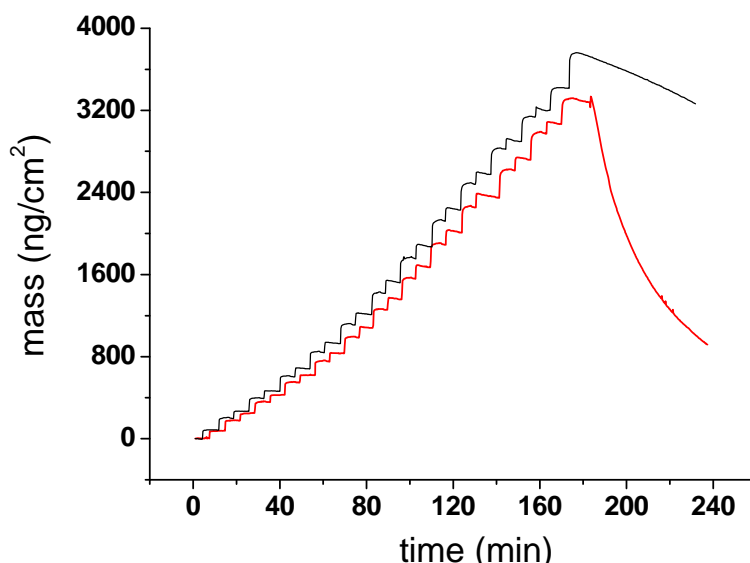

Figura 28.- Masa adsorbida medida con EC-OWLS en un buffer con fuerza iónica 150 mM durante el crecimiento de un film (PLL/DNA)$_{12}$ a 0 V (línea gris) y a 1.2 V (línea negra). La disolución se provocó en ambos casos a 1.9 V.

3 MORFOLOGÍA ANTES Y DURANTE LA DISOLUCIÓN: EC-AFM

Usamos un AFM electroquímico (EC-AFM) para obtener información complementaria acerca de los cambios topográficos de las multicapas antes y durante el proceso de disolución. Esta información topográfica nos ayudará a comprender si la disolución se inicia desde la parte superior del film o desde la superficie del electrodo. Comparando una imagen topográfica de AFM (PLL/ADN)$_6$ fabricada a 0 V y a 1.2 V antes del proceso de disolución, se deduce que ambas películas están constituidas de nanoislas que están directamente adsorbidas sobre la superficie de ITO, con altura media y tamaño FWHM muy similar en ambos casos. Por lo tanto, se puede afirmar que la aplicación de una polarización durante el depósito no afecta a la morfología final del film.

Para observar in situ la disolución de las islas, se utilizó el EC-AFM en un film fabricado a 1.2V. Las figuras 29a-d son las imágenes de AFM correspondientes a los minutos 0, 15, 35 y 55 min después del comienzo de la disolución. Se encontró que mientras que todas las nanoislas disminuyen de tamaño, la mayoría no desaparecen por completo. Esto está de acuerdo con la disminución gradual de la masa del film y con el porcentaje de masa residual que observábamos en los experimentos de EC-OWLS. La

densidad media de islas disminuye desde un valor inicial de 22 μm^{-2} a 17 μm^{-2}. Las figuras 29e-f son las correspondientes a la altura y la distribución de tamaño de las islas, al principio y al final de la disolución: la altura disminuye de 25 a 8 nm, mientras que el tamaño disminuye de 110 a 65 nm.
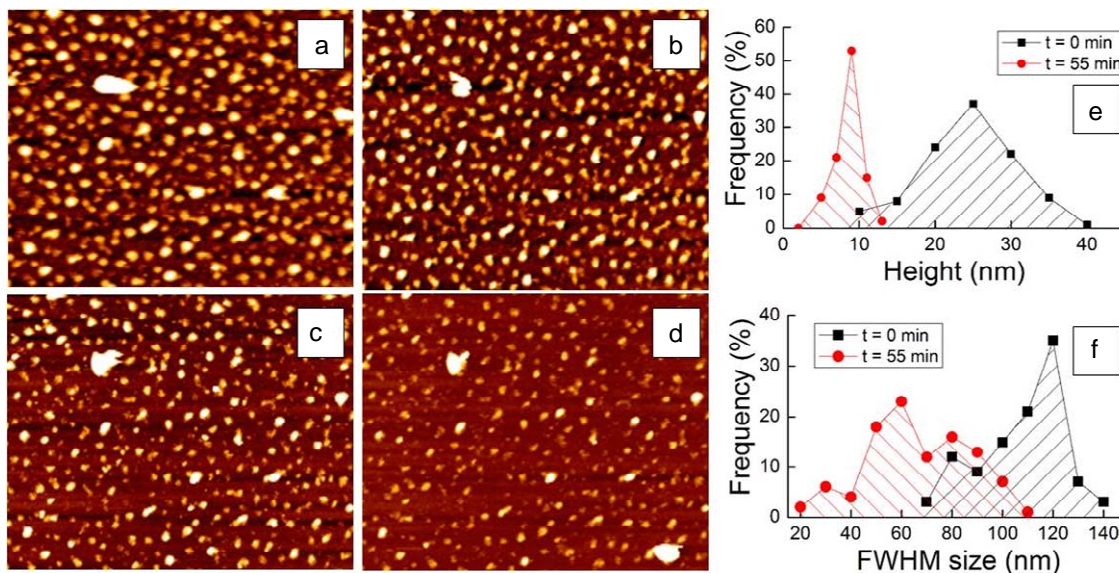

Figura 29.- Imágenes de AFM (3x2 μm^2) de (PLL/DNA)$_6$ fabricado a 1.2 V a) antes de aplicar el potencial de disolución potential de 1.9 V, b) después de aplicar el potencial durante 15 min, c) 35 min y d) 55 min. Las cuatro imágenes representan la misma región. Análisis de e) la altura y f) el tamaño de las islas a t = 0 y a t = 55 min.

4 DISCUSIÓN

Los datos experimentales mostraron que los films de PLL/DNA están constituidos por nanogotas y que la polarización aplicada durante el depósito no afecta a su morfología. Las imágenes de AFM durante la disolución también reveló que las nanoislas se retraen, pero muchas permanecen en la superficie al final del proceso de disolución. La interpretación de los resultados de OWLS nos lleva a concluir que, en presencia de un potencial, se adsorbe menos polianión que en el film depositado a 0 V, mientras que la cantidad de policatión es mayor al principio y similar después. Esto significa que la compensación electrostática durante el depósito del film se ve alterada por la presencia de un potencial aplicado: esto puede explicar el cambio en la estabilidad de los films.

5 CONCLUSIONES

La técnica de EC-OWLS ha permitido el seguimiento de la cinética del depósito y la disolución electroquímicamente inducida de PEMs que contienen DNA. El comportamiento de las multicapas fue confirmado por in situ EC-AFM. Si el film se fabrica a 0 V, la disolución es lenta y parcial. Por el contrario, si un potencial de hasta 1,2 V se aplica durante el depósito, la disolución es mucho más rápida y casi completa. Este efecto se observó a diferentes concentraciones de sal y también para otros sistemas más estables como PAH/PSS. Los datos de AFM in situ mostraron que los films $(PLL/DNA)_6$ constan de nanogotas y que la morfología del film es independiente de la polarización aplicada durante el depósito. Se observó como las nanogotas se contraen durante la disolución, indicando que la liberación de los polímeros se produce desde su superficie. El proceso podría ser racionalizado a la luz de dos fenómenos que tienen lugar en el electrodo en condiciones potenciostáticas: cambios de pH y la formación de HClO que reaccionan con las aminas del PLL. Este estudio no sólo es relevante para aplicaciones tales como la administración local de fármacos, o de transfección de DNA, sino que también proporciona una nueva herramienta para los estudios biológicos. Se podrían imaginar sistemas inteligentes de cultivo celular, donde las drogas o factores de crecimiento son liberados con una cinética controlada y en la posición deseada.

UNIVERSITY OF BARCELONA
08028 Barcelona, Spain
Telephone: (+34) 934 021 100
www.ub.edu

INSTITUT FOR BIOENGINEERING OF CATALONIA
08028 Barcelona, Spain
Telephone: (+34) 934 039 706
www.ibecbarcelona.eu

Biosensors are nowadays a powerful tool to enable the detection of specific biological interactions and to evaluate the concentration dependence in the response. A biosensor usually consists of three different parts: the sample to be measured, the transducer and the electronic system that amplifies the signal, analyzes the data and brings a result to the final user. The transducer includes the bioreceptor (which specifically interacts with the sample) and the interface that transforms the recognition from the bioreceptor into a measurable signal. When the analyte interacts with the bioreceptor, the transducer sends a signal that is processed by the electronic signal. All this process occurs in a efficient, quick, cheap, easy, simple and specific way. Regarding the type of the transductor, the biosensors can be electrochemical, optical, acoustic, magnetic or thermometric; but overall the most powerful ones are the optical biosensors, and among them the grating coupler. As a technique for investigating processes at the solid/liquid interface, presents high mechanical stability, immunity to electromagnetic interferences and pushes the sensitivity to levels even higher than other techniques and allows for the direct monitoring of macromolecular adsorption. Taking advantage of the last advances in nanotechnology, the goal of this thesis is to study the versatility of an Optical Grating Coupler Biosensor. The design of new grating sensor chips will be investigated, a new calibration technique for the sensors will be proposed and, taking advantage of the technique, different biomedical scenarios will be tested.

Lorena Diéguez Moure
Electronics Department, UB
Nanobioengineering, IBEC

ldieguez@el.ub.es